

Electronic Thesis and Dissertation Repository

4-28-2023 10:00 AM

Flow Characterization over Biomimetic Fish Scale Arrays

Isaac NR Clapp Mr., *Western University*

Supervisor: Siddiqui, Kamran, *The University of Western Ontario*

A thesis submitted in partial fulfillment of the requirements for the Master of Engineering Science degree in Mechanical and Materials Engineering

© Isaac NR Clapp Mr. 2023

Follow this and additional works at: <https://ir.lib.uwo.ca/etd>



Part of the [Aerodynamics and Fluid Mechanics Commons](#)

Recommended Citation

Clapp, Isaac NR Mr., "Flow Characterization over Biomimetic Fish Scale Arrays" (2023). *Electronic Thesis and Dissertation Repository*. 9254.

<https://ir.lib.uwo.ca/etd/9254>

This Dissertation/Thesis is brought to you for free and open access by Scholarship@Western. It has been accepted for inclusion in Electronic Thesis and Dissertation Repository by an authorized administrator of Scholarship@Western. For more information, please contact wlsadmin@uwo.ca.

Abstract

The contributions of drag to energy consumption in the transportation sector are significant and often unavoidable. Biomimetic surfaces are promising as passive drag reduction mechanisms. Among them, fish scale arrays are beneficial in the laminar and transitional flow regimes but lack fundamental understanding. This research addressed this need and investigated the underlying flow mechanisms over fish scale arrays. Experimental measurements revealed the presence of flow recirculation, streamwise velocity streaks, spanwise velocity fluctuations, and wall normal vorticity streaks, all of which play a role in the near wall flow behaviour. Numerical simulations revealed the superior friction drag reduction capabilities of the diamond scale shape. The findings highlight how the surface variations contribute to the formation of flow behaviours which influence the skin friction and contribute to delaying the transition to turbulence. The improved understanding of underlying processes from this study will aid the optimization of scale shape to reduce drag.

Keywords

Biomimetic, Fish Scales, Particle Imaging Velocimetry, Computational Fluid Dynamics, Drag Reduction, Hydrodynamics, Bio-Inspired Fluid Mechanics

Summary for Lay Audience

The interaction between solid surfaces and surrounding fluids is common in our everyday lives. Whether it be in a car or on a plane, the interaction between the vehicle and the surrounding fluid generates drag forces. These drag forces lead to excessive energy consumption and consequently greenhouse gas emissions, especially in the transportation sector. The shear drag associated with the near wall boundary layer can often account for between 20-50% of the drag force depending on the mode of transportation. Several approaches to friction drag reduction have been tested with varying results. Biomimetic surface modifications such as shark skin inspired riblets and hydrophobic microstructures have shown promising drag reduction capabilities in turbulent flow. Biomimetic fish scale arrays are another technique which have shown promising results in the laminar and transitional flow regimes. However, the lack of understanding of how the fish scale arrays interact with the fluid raises questions about how they function as a drag reduction mechanism. Thus, a deeper understanding of how fish scale arrays interact with the surrounding flow is needed to understand the underlying friction drag reduction mechanisms. This deeper understanding will help inform the design of structured surfaces which target drag reduction in commercial applications.

The current study uses both experimental and numerical techniques to evaluate and understand the unique flow patterns in the near wall boundary layer over biomimetic fish scale arrays. Experimental measurements provide an in-depth analysis of the near wall flow behaviour and highlight four mechanisms which are generated due to the unique scale pattern. Flow recirculation, streamwise velocity streaks, spanwise velocity fluctuations, and wall normal vorticity streaks are all found to play an important role in changing the friction forces the surface experiences and delaying the transition from laminar to turbulent flow. Numerical simulations explored the impact of scale shape, highlighting the superior capabilities of the diamond scale shape for improved drag reduction. This work provides new contributions in terms of the understanding of the mechanisms driving the flow behaviour over fish scales and potential techniques for optimization of the drag reduction behaviour.

Co-Authorship Statement

This master's thesis is organized in an integrated article formation with four chapters, two of which are planned to be co-authored papers by Isaac Clapp and Kamran Siddiqui. The work related to the execution of the experiments and/or simulations, data collection, data processing, data analysis, and manuscript writing was conducted by Isaac Clapp. This accounted for 90% of the work for each chapter. Kamran Siddiqui provided resources, technical support, guidance, and manuscript editing accounting for 10% of the work for each chapter. The following chapters are planned to be submitted for publication in peer-reviewed journals in 2023.

- Chapter 2 includes the detailed experimental analysis and characterization of the flow over a biomimetic fish scale array. Planned to be submitted to *Experimental Thermal and Fluid Science*.
- Chapter 3 explores the influence of scale shape on the flow behaviour over biomimetic fish scale arrays using numerical techniques. Planned to be submitted to *International Journal of Heat and Fluid Flow*.

Acknowledgments

I would like to acknowledge and thank the Natural Sciences and Engineering Research Council of Canada (NSERC), the province of Ontario, and the University of Western Ontario for their funding support.

I would also like to thank my supervisor Kamran Siddiqui for his invaluable guidance, expertise, and patience throughout this process. I am sincerely grateful for my friends and colleagues who have encouraged, challenged, and inspired me along the way. My time here would not have been the same without you.

Finally, I would not have been able to do this without the continued support of my family. I am forever grateful for their constant words of encouragement, endless support, and inspiration that allowed me to explore my interests and become the person I am today.

To all that helped me along the way, it means more than you know – Thank you!

Table of Contents

Abstract.....	ii
Summary for Lay Audience.....	iii
Co-Authorship Statement.....	iv
Acknowledgments.....	v
Table of Contents.....	vi
List of Tables.....	x
List of Figures.....	xii
List of Appendices.....	xxii
Nomenclature.....	xxiii
Chapter 1.....	1
1 Introduction.....	1
1.1 Background.....	1
1.1.1 The Boundary Layer.....	2
1.1.2 Laminar Flow.....	4
1.1.3 Transition to Turbulence.....	6
1.1.4 Turbulent Flow.....	9
1.2 Friction Drag Reduction Techniques.....	12
1.2.1 Active Methods.....	13
1.2.2 Passive Methods.....	17
1.2.3 Fish Scales.....	24
1.2.4 Knowledge Gaps.....	28
1.3 Research Objectives.....	29
1.3.1 Objectives of the Current Work.....	29
1.3.2 Thesis Organization.....	31

Bibliography.....	32
Chapter 2.....	41
2 Experimental Investigation into the Fundamental Flow Behaviour over Biomimetic Fish Scale Arrays	41
2.1 Introduction.....	41
2.2 Motivation and Objectives.....	45
2.3 Methodology.....	45
2.3.1 Experimental Setup.....	45
2.3.2 Surface Design.....	47
2.3.3 PIV Technique	51
2.3.4 Channel Flow Results	56
2.4 Results and Discussion	60
2.4.1 Flat Plate Upstream Flow Characterization	60
2.4.2 Vertical Plane Results.....	65
2.4.3 Horizontal Plane Results.....	86
2.4.4 Discussion of 3D Flow Behaviour.....	105
2.4.5 Drag Reduction Mechanisms.....	109
2.5 Impact of Reynolds Number.....	113
2.6 Conclusion	119
Bibliography.....	122
Chapter 3.....	129
3 Numerical Investigation into the Influence of Scale Shape on the Hydrodynamic Performance of Biomimetic Fish Scale Arrays.....	129
3.1 Introduction.....	129
3.2 Objectives and Scope.....	132
3.3 Methodology.....	132
3.3.1 Scale Design.....	133

3.3.2	Numerical Models.....	137
3.3.3	Grid Independence.....	140
3.3.4	Model Validation.....	144
3.3.5	Simulation Parameters.....	150
3.4	Results and Discussion.....	151
3.4.1	Vertical Profiles.....	154
3.4.2	Recirculation Zone.....	160
3.4.3	Streamwise Velocity.....	164
3.4.4	Spanwise Velocity.....	169
3.4.5	Wall Normal Vorticity.....	175
3.4.6	Drag Analysis.....	179
3.4.7	Overall Impact of Scale Geometry.....	190
3.4.8	Impact of Reynolds Number.....	193
3.5	Conclusion.....	203
	Bibliography.....	206
Chapter 4	211
4	Conclusions.....	211
4.1	Problem Overview.....	211
4.2	Chapter 2.....	211
4.3	Chapter 3.....	213
4.4	Summary.....	215
4.5	Novel Contributions.....	218
4.6	Future Recommendations.....	219
Appendix A:	Experimental Facilities Development.....	221
	Original Design.....	221
	Outlet Modifications.....	224

Inlet Modifications	225
Sample Mounting Modifications.....	228
Final Design	231
Bibliography.....	233
Appendix B: PIV Uncertainties	234
Bibliography.....	236
Curriculum Vitae	237

List of Tables

Table 1: Description of common flow instabilities.....	7
Table 2: Scale Geometry Parameters	50
Table 3: Repeatability mean and 95% confidence intervals for channel velocity measurements.....	57
Table 4: Average reattachment lengths and confidence intervals	72
Table 5: Displacement thickness, momentum thickness, and shape factor over scale $S_{0,5}$	74
Table 6: Displacement thickness, momentum thickness, and shape factor for different values of ϕ over scale $S_{0,5}$ in the overlapping plane.	85
Table 7: Free-stream velocity and non-dimensional values for experiments at all flow conditions.....	114
Table 8: Different scale geometries and their key parameters (Wainwright & Lauder, 2016)	136
Table 9: Mesh refinement parameters.....	138
Table 10: Simulation Parameters for all cases	151
Table 11: Reattachment length and associated 95% confidence interval for each geometry	162
Table 12: Total skin friction coefficient over a single scale ($S_{0,5}$) along centerline and overlapping regions.....	184
Table 13: Total skin friction coefficient over scale arrays along centerline and overlapping regions.....	186
Table 14: Total friction drag for all geometries at the experimental flow condition.....	187
Table 15: Reattachment length and associated 95% confidence interval for each geometry and flow condition.	200

Table 16: Friction drag coefficients for all geometries under different flow conditions.....	201
Table 17: Percentage reduction in the friction drag coefficient compared to the flat plate..	202
Table 18: Contraction Section Parameters.....	227

List of Figures

Figure 1: Velocity boundary layer development on a flat plate. Adapted from Bergman & Lavine (2017).....	4
Figure 2: Sketch of flat plate boundary layer transition (White, pp.377, 2006).....	8
Figure 3: The turbulent boundary layer profile obtained from Kundu et al. (2016) which shows data replotted from Oweis et al. (2010) for three Reynolds numbers. The dashed lines indicate the bounds of each of the regions within the turbulent boundary layer.	10
Figure 4: Local skin friction coefficient for various Reynolds numbers based on both the laminar and turbulent theory.....	12
Figure 5: Formation of streamwise velocity streaks behind an isolated roughness element (Joseph et al., 2022)	21
Figure 6: Different scale shapes (Sudo et al., 2002).....	24
Figure 7: 3D Biomimetic fish scale replicating the overlapping nature of the fish scales.	26
Figure 8: Schematic of the water channel. 1) Outlet water reservoir; 2) 2-hp Pump; 3) Inlet settling chamber; 4) Inlet; 5) Contraction and flow conditioning section; 6) Test section; 7) Diffusion outlet section; 8) Weir gate.....	46
Figure 9: Schematic of the sample mounting arm.	47
Figure 10: Different scale shapes (Sudo et al., 2002).....	48
Figure 11: (Left) CAD model of scale array and (Right) photograph of the 3D printed scale array used for testing.....	51
Figure 12: PIV Laser and camera setup for (A) vertical plane and (B) horizontal plane measurements.....	52
Figure 13: Locations of measurement planes. Green lines represent the spanwise locations of vertical planes: Centerline ($z = 0$ cm), Overlapping ($z = 1$ cm), and Midline ($z = 0.7$ cm).	

The coloured dashed boxes represent the overlapping fields of view in the horizontal plane measurements: 1 – Leading Edge, 2 – Scales Upstream, 3 – Scales Downstream..... 53

Figure 14: Locations of measurement planes. Green lines represent the vertical locations of horizontal planes varying from 1.3 mm to 5 mm from the surface. The coloured dashed boxes represent the overlapping fields of view in the vertical plane measurements: A – Leading Edge, B – Leading Edge 5 cm, C – Leading Edge 7.5 cm, D – Leading Edge 10 cm, E – Scales #1, F – Scales #2, G – Scales #3, H – Scales #4..... 53

Figure 15: Profiles of the (A) mean streamwise velocity and (B) turbulent intensity, in the mid-vertical plane (at $z = 0$ cm) in the channel (in the absence of the surface). The virtual location of the surface is marked with the dashed line. 58

Figure 16: Profiles of the (A) mean streamwise velocity and (B) turbulent intensity, in the horizontal plane at the height of 5 cm from the channel base in the absence of the surface, which corresponds to the virtual location of the surface ($y = 0$ cm). The virtual locations of the surface edges are marked with dashed black lines. (C) The plan view of the structured surface schematic. The dash-dotted lines in (A, B and C) correspond to the region over the surface not impacted by the boundary layers on the channel walls ($z = -2.6$ cm to $z = 2.6$ cm)..... 59

Figure 17: Non-dimensional streamwise velocity profiles at 5 cm, 7.5 cm, and 10 cm from the leading edge ($z = 0$ cm) compared to Blasius solution..... 61

Figure 18: Non-dimensional streamwise velocity profiles 10 cm from the leading edge at $z = 0$ cm, $z = 0.7$ cm, and $z = 1$ cm, corresponding to the centerline, midline, and overlapping planes respectively..... 62

Figure 19: (A) Streamwise and (B) spanwise RMS velocity colourmaps over the leading edge at a wall normal distance of 1.3 mm. Flow is from left to right. 64

Figure 20: Coordinate system over the scale array. The blue arrow shows the scale length ($l_{sl} = 16$ mm), the orange arrow shows the scale width ($l_{sw} = 26.65$ mm), and the scale height is shown by the green arrow ($l_{sh} = 0.8$ mm). The varying height of the surface (y_0) along with the upstream position of the scale (x_0) are also shown. Scales are identified using

double subscript notation where the first subscript corresponds to the spanwise row (-1, 0, 1), and the second subscript corresponds to the streamwise scale number (1-9)..... 66

Figure 21: Colormap of the streamwise mean velocity in the mid-vertical plane ($\xi = 0$) over $S_{0,4}$ and $S_{0,5}$. Flow is from left to right. 67

Figure 22: Non-dimensional wall normal mean streamwise velocity profiles for values of ϕ along the length of scale $S_{0,5}$. The velocity profile from the Blasius solution is also plotted for reference..... 68

Figure 23: Non-dimensional wall normal mean streamwise velocity profiles over scale length ($S_{0,5}$) for various values of ϕ . The mean velocity profile from the Blasius solution is also plotted for reference. 69

Figure 24: Non-dimensional wall normal mean streamwise velocity profiles in the separation region of scale $S_{0,5}$ at various values of ϕ . The mean velocity profile from the Blasius solution is also plotted for reference. 70

Figure 25: Mean velocity vector plot showing the flow recirculation over $S_{0,5}$. Flow is from left to right..... 71

Figure 26: Non-dimensional reattachment length (ϕ) for scales along centerline plane..... 71

Figure 27: Colourmap of the mean wall normal velocity in the near wall region of scale $S_{0,5}$ over the centerline plane ($\xi = 0$). Flow is from left to right. 76

Figure 28: (A) Location of midline region over scale array; (B) Image showing blocked area along the midline plane ($\xi = 0.26$) over scale $S_{0,5}$ 77

Figure 29: Mean wall normal velocity colormap in the near wall region over scale $S_{0,5}$ along the midline plane ($\xi = 0.26$). Flow is from left to right..... 78

Figure 30: Non-dimensional wall normal mean streamwise velocity profiles for various values of ϕ over the length of scale $S_{0,5}$ along the midline plane ($\xi = 0.26$). The Blasius velocity profile is also plotted for comparison. 79

Figure 31: Near wall non-dimensional mean streamwise velocity profiles for various values of ϕ over the length of scale $S_{0,5}$ along the midline plane ($\xi = 0.26$). The Blasius velocity profile is also plotted for comparison.	80
Figure 32: (A) Location of overlapping region over scale array; (B) Image showing blocked area along overlapping plane ($\xi = 0.375$) for scale $S_{0,5}$	82
Figure 33: Mean wall normal velocity colourmap in the near wall region over scale $S_{0,5}$ in the overlapping region. Flow is from left to right.....	82
Figure 34: Non-dimensional wall normal streamwise velocity profiles along the overlapping plane over scale $S_{0,5}$ for various values of ϕ	83
Figure 35: Colormap of the mean streamwise velocity at wall normal distance of $\lambda_1 = 2.5$. Flow is from left to right.....	87
Figure 36: Non-dimensional mean streamwise velocity variation at different non-dimensional wall normal distances at a streamwise location of $\phi_t = 4.5$. (A) wall normal positions are plotted as a fraction of the boundary layer thickness (λ_2); (B) wall normal positions are plotted as the number of scale heights from the wall (λ_1).	89
Figure 37: Non-dimensional streamwise velocity variation (ψ) at a wall normal position of $\lambda_1 = 2.5$ for streamwise locations of $\phi_t = 2.5, 4.5, 6.5,$ and 8.5	91
Figure 38: Average streamwise streak amplitude between $\xi = -1$ and 1 for the length of the array ($\phi_t = 1.5 - 9$).	92
Figure 39: Colormap of the mean spanwise velocity at wall normal distance of $\lambda_1 = 2.5$. Flow is from left to right.....	94
Figure 40: Schematic showing bounds of overlapping region (blue dashed lines) and center of overlapping region (or overlapping plane – green lines).....	95
Figure 41: Convergence plot for square median filter size showing the average peak ω for $\xi = \pm 0.375$ at $\lambda_1 = 2.5$ between $\phi_t = 1.5$ to 9	96

Figure 42: Filtered spanwise velocity field revealing the background spanwise velocity trends at a wall normal location of $\lambda_1 = 2.5$. Flow is from left to right.....	96
Figure 43: Resultant unbiased spanwise velocity field for a wall normal location of $\lambda_1 = 2.5$. Flow is from left to right.	97
Figure 44: Spanwise velocity component along a streamwise line in the overlapping region ($\xi = -0.375$) at a wall normal distance of $\lambda_1 = 2.5$	98
Figure 45: Schematic showing spanwise velocity patterns in the overlapping region.	99
Figure 46: Non-dimensional spanwise velocity variation (ω) at all measured wall normal locations (λ_1) along a streamwise direction in the overlapping plane ($\xi = 0.375$).	99
Figure 47: Average peak spanwise velocity amplitude (ω) for all peaks between $\phi_t = 1.5$ and 9 at spanwise locations of $\xi = \pm 0.375$ for each wall normal height (λ_1). The 95% confidence interval is plotted as error bars.	100
Figure 48: Colourmap of the mean wall-normal vorticity at wall normal distance of $\lambda_1 = 2.5$. Flow is from left to right.	102
Figure 49: Wall-normal vorticity profiles across the array at a streamwise position of $\phi_t = 4.5$ for different wall normal distances (λ_1).	103
Figure 50: Average peak wall-normal vorticity value (for ξ between -1 and 1) plotted at four streamwise locations ($\phi_t = 2.5, 4.5, 6.5, \text{ and } 8.5$) and all wall normal heights (λ_1).	105
Figure 51: Colormap of the non-dimensional mean streamwise velocity over the scale array at free-stream velocities of (a) 0.028 m/s (b) 0.036 m/s (c) 0.066 m/s (d) 0.083 m/s (e) 0.12 m/s (f) 0.14 m/s (g) 0.18 m/s. Flow is from top to bottom.	114
Figure 52: Non-dimensional streamwise velocity variation (ψ) at a wall normal distance of $\lambda_1 = 2.5$ and streamwise position $\phi_t = 4.5$, for varying flow conditions.	115

Figure 53: Non-dimensional streamwise velocity variation (ψ) at a streamwise position of $\phi_t = 4.5$ for different wall normal distances (λ_2) based on varying free-stream velocity conditions.....	116
Figure 54: Colormap of the non-dimensional normalized mean spanwise velocity for all measured speeds over the scale array (a) 0.028 m/s (b) 0.036 m/s (c) 0.066 m/s (d) 0.083 m/s (e) 0.12 m/s (f) 0.14 m/s (g) 0.18 m/s. Flow is from top to bottom.....	117
Figure 55: Non-dimensional spanwise velocity (ω) at a wall normal location of $\lambda_1 = 2.5$ and spanwise position $\xi = 0.375$ for all flow conditions.	118
Figure 56: Different scale shapes (Sudo et al., 2002).....	133
Figure 57: Circular geometry fluid domain for mesh independence.	137
Figure 58: Horizontal Streamwise 2 mm – $y = 2$ mm and $z = 0$ cm; Horizontal Streamwise 4 mm – $y = 4$ mm and $z = 0$ cm; Vertical Leading Edge 5 cm – $x = 5$ cm and $z = 0$ cm; Vertical Leading Edge 10 cm – $x = 10$ cm and $z = 0$ cm; Vertical Centerline 23.6 cm – $x = 23.6$ cm and $z = 0$ cm; Vertical Overlapping 23.6 cm – $x = 23.6$ cm and $z = 1$ cm.....	140
Figure 59: Streamwise velocity profiles for mesh independence study: A - Vertical Leading Edge 10 cm ($x = 10$ cm and $z = 0$ cm); B - Horizontal Spanwise 2 mm ($x = 23.6$ cm and $y = 2$ mm).....	141
Figure 60: RMS error convergence graphs for all vertical (A) and horizontal (B) streamwise velocity profiles. RMS error was taken with respect to the finest mesh (13M) as the base case.....	143
Figure 61: New model domain with experimental boundary layer inlet profile 5 cm upstream of the scale array.	144
Figure 62: Model validation locations: -2.5 cm ($z = 0$ cm) Upstream, 0 cm ($z = 0$ cm) Upstream, Centerline 7.2 cm ($z = 0$ cm), Overlapping 7.2 cm ($z = 1$ cm), Centerline 13.6 cm ($z = 0$ cm), Overlapping 13.6 cm ($z = 1$ cm), Centerline 16 cm ($z = 0$ cm), and Overlapping 16 cm ($z = 1$ cm).....	145

Figure 63: Validation of non-dimensional wall normal streamwise velocity profiles -2.5 cm (A), and 0 cm (B) upstream of the scale array over the flat plate. 146

Figure 64: Nondimensional vertical velocity validation plots: A – Centerline 7.2 cm; B – Overlapping 7.2 cm; C – Centerline 13.6 cm; D – Overlapping 13.6 cm. 148

Figure 65: Centerline (A) and overlapping (B) vertical velocity profile validation 13 cm from the entrance of the scale array. 149

Figure 66: Coordinate system for discussion of results over scale array. The blue arrow shows the scale length ($l_{sl} = 16$ mm), the orange arrow shows the scale width ($l_{sw} = 26.65$ mm), and the scale height is shown by the green arrow ($l_{sh} = 0.8$ mm). The varying height of the surface (y_0) along with the upstream position of the scale (x_0) are also shown. Scales are identified using double subscript notation where the first subscript corresponds to the spanwise row (-1, 0,1), and the second subscript corresponds to the streamwise scale number (1-9). 153

Figure 67: Non-dimensional wall normal streamwise velocity profiles at (A) $\phi_t = 4.5$ and (B) $\phi_t = 8.5$ along the scales centerline ($\xi = 0$) for all three geometries. The theoretical Blasius profile is also plotted as reference. 154

Figure 68: Non-dimensional wall normal streamwise velocity profile for different values of ϕ over a single scale $S_{0,7}$ at $\xi = 0$ for (A) flat back shaped scale and (B) Circular shaped scale. 156

Figure 69: Non-dimensional wall normal streamwise velocity profiles for different values of ϕ over scale $S_{0,7}$ at $\xi = 0$ for the diamond scale. 157

Figure 70: Non-dimensional wall normal streamwise velocity profiles at (A) $\phi_t = 4.5$ and (B) $\phi_t = 8.5$ in the scales overlapping region ($\xi = 0.375$) for all three scale geometries. 159

Figure 71: Colourmap plot showing regions of negative streamwise velocity over all scale geometries in 1 mm increments from the centerline plane ($\xi = 0$) to the overlapping plane ($\xi = 0.375$). 161

Figure 72: Colourmap of the streamwise velocity at a wall normal distance of $\lambda_1 = 2$ for all geometries. The flow is from top to bottom.	164
Figure 73: Size of overlapping region for each scale shape.	165
Figure 74: Streamwise velocity variation (ψ) for all geometries at a streamwise position of $\phi_t = 4.5$ and wall normal locations of (A) $\lambda_1 = 2.5$ and (B) $\lambda_1 = 5$	166
Figure 75: Streamwise velocity variation (ψ) for all geometries at a streamwise position of $\phi_t = 8.5$ for wall normal heights corresponding to (A) $\lambda_1 = 2.5$ and (B) $\lambda_1 = 5$	168
Figure 76: Colourmap of the spanwise velocity at a wall normal distance of $\lambda_1 = 2$ for all geometries. Flow is from top to bottom.	170
Figure 77: Non-dimensional spanwise velocity (ω) in the overlapping region ($\xi = 0.375$) at wall normal heights of (A) $\lambda_1 = 2.5$ and (B) $\lambda_1 = 5$ for all three geometries.	171
Figure 78: Colourmap of the spanwise velocity over scale $S_{0.5}$ at a wall normal distance of (A) $\lambda_1 = 1.25$ and (B) $\lambda_1 = 0.625$ for all geometries. Flow is from left to right.	173
Figure 79: Colourmap of the wall normal vorticity at a wall normal distance of $\lambda_1 = 2$ for all geometries. Flow is from top to bottom. The positive values correspond to clockwise rotation, whereas negative values correspond to anticlockwise rotation.	175
Figure 80: Spanwise profiles of the wall-normal vorticity for all geometries at a streamwise location of $\phi_t = 4.5$ and wall normal heights (A) $\lambda_1 = 2.5$ and (B) $\lambda_1 = 5$	177
Figure 81: Colourmap of the skin friction coefficient along the surface for all geometries.	179
Figure 82: Skin friction coefficient along scale $S_{0.5}$ in the (A) centerline ($\xi = 0$) and (B) overlapping ($\xi = 0.375$) regions for all three scale geometries.	182
Figure 83: Skin friction coefficient along a streamwise line located at $\xi = 0$ (A) and $\xi = 0.375$ (B) over the surface. The skin friction coefficient for a classical flat plate laminar boundary layer is also presented for comparison.	185

Figure 84: Non-dimensional wall normal streamwise velocity profiles for the circular geometry at a streamwise distance of $\phi_t = 8.5$ in the (A) centerline ($\xi = 0$) and (B) overlapping ($\xi = 0.375$) regions for the circular geometry. The classical laminar Blasius profile is plotted for reference..... 194

Figure 85: Non-dimensional wall normal streamwise velocity profiles in the centerline plane along the length of scale $S_{0,7}$ in the circular geometry at a $\theta_{ratio} = 10.6$. The classical laminar Blasius solution is plotted for reference. 195

Figure 86: Non-dimensional streamwise velocity variation (ψ) for all flow conditions at a streamwise distance of $\phi_t = 8.5$ for three wall normal locations corresponding to (A) $\lambda_1 = 2.5$, (B) $\lambda_1 = 5.0$, and (C) $\lambda_1 = 6.25$ for the circular geometry. 196

Figure 87: Non-dimensional streamwise velocity variation (ψ) at streamwise distance of $\phi_t = 8.5$ for $\theta_{ratio} = 10.6$ at several wall normal locations (λ_1) for the circular geometry. 198

Figure 88: Non-dimensional spanwise velocity (ω) in the streamwise direction at a spanwise location of $\xi = 0.375$ and wall normal heights of (A) $\lambda_1 = 2.5$ and (B) $\lambda_1 = 5.0$, for all flow conditions over the circular geometry..... 199

Figure 89: Original water channel CAD model. Inlet on the left, water flowing through the test section and into the outlet section of the right..... 221

Figure 90: Closed circuit water channel layout. 1) Outlet reservoir; 2) Pump; 3) Inlet and contraction section; 4) Flow Conditioning; 5) Test Section; 6) Outlet and Diffusion Section 222

Figure 91: Original stilling plate design. Units are in mm. 223

Figure 92: Sample Mounting Apparatus..... 223

Figure 93: New flume outlet 224

Figure 94: Vertical Inlet Configuration 225

Figure 95: Stages 2, 3, and 4 show the water path through the pump into the inlet settling reservoir before entering the inlet and contraction section from below.	226
Figure 96: 3D Printed Inlet Contraction Section	227
Figure 97: Final inlet configuration with two stages of flow conditioning and curved contraction section.	228
Figure 98: Streamwise velocity colourmap in the horizontal plane 1 mm from the surface in the region of the sharp leading edge. Highlights the flow separation happening over the sharp leading edge. Flow is from the left to the right.	229
Figure 99: Curved leading-edge mould.	230
Figure 100: Streamwise velocity colourmap in the horizontal plane 1 mm from the surface in the region of the curved leading edge. Flow is from the left to the right.	230
Figure 101: Schematic of Experimental Facility. 1) Outlet Reservoir 2) 2-hp Centrifugal Pump 3) Inlet Settling Reservoir 4) Inlet Contraction Section 5) Flow Conditioning 6) Test Section 7) Outlet Diffuser Section 8) Weir Gate	232
Figure 102: Schematic of the sample mounting structure including the curved leading edge, 10 cm flat plate, 16 cm structured sample, and 3D printed mounting arm.	232

List of Appendices

Appendix A: Experimental Facilities Development.....	221
Appendix B: PIV Uncertainties.....	234

Nomenclature

A_{st} = Amplitude of the streamwise velocity variations (% of U_{∞})

A_c = Cross-sectional area (m^2)

$C_{f,lam}$ = Laminar skin friction coefficient

$C_{f,turb}$ = Turbulent skin friction coefficient

$C_{D,friction}$ = Friction drag coefficient

D_h = Hydraulic diameter (m)

H = Shape factor

H_{inlet} = Half height of the inlet of the contraction section (m)

H_{outlet} = Half height of the outlet of the contraction section (m)

l_{sl} = Scale length (m)

l_{sw} = Scale width (m)

l_{sh} = Scale height (m)

L = length (m)

P_w = Wetted perimeter (m)

Re_{BL} = Reynolds number based on boundary layer thickness

Re_x = Reynolds number based on distance from leading edge

U_{∞} = Free-stream velocity ($\frac{m}{s}$)

u = x -velocity ($\frac{m}{s}$)

$u_{max,y}$ = Maximum streamwise velocity at a given height ($\frac{m}{s}$)

u_{min} = Minimum streamwise velocity at a given height ($\frac{m}{s}$)

u_t = Friction velocity ($\frac{m}{s}$)

v = y-velocity ($\frac{m}{s}$)

w = z-velocity ($\frac{m}{s}$)

x_0 = Upstream end of an individual scale (x -coordinate, m)

x = x -coordinate distance (m)

y_0 = Varying height along a single scale (y -coordinate, m)

y = y -coordinate distance (m)

z = z -coordinate distance (m)

ϕ = Non-dimensional length along scale in x -direction (using l_{sl})

ϕ_t = Non-dimensional length along scale array in x -direction (using l_{sl})

λ_1 = Non-dimensional length along scale in y - direction (using l_{sh})

λ_2 = Non-dimensional length along scale in y -direction (using δ_{99})

ψ = Non-dimensional streamwise velocity variation (% of U_∞)

δ_{99} = Boundary layer thickness (m)

δ^* = Displacement thickness (m)

μ = Dynamic viscosity ($\frac{kg}{ms}$)

ρ = Density ($\frac{kg}{m^3}$)

θ = Momentum thickness (m)

θ_{ratio} = Boundary layer thickness to scale height ratio

τ_w = Wall shear stress (Pa)

ν = Kinematic Viscosity ($\frac{m^2}{s}$)

ω = Non-dimensional spanwise velocity variation (% of U_∞)

ξ = Non-dimensional length along scale in z -direction (using l_{sw})

Chapter 1

1 Introduction

1.1 Background

Fluid interaction at the solid-fluid interface is an important area in fluid mechanics with a wide spectrum of applications. Whether it be vehicles, boats, planes, or buildings, many of our everyday activities undergo this fundamental interaction. The fluid behaviour which evolves due to this interaction is heavily influenced by the geometry of the solid surface, which despite being an active research area for decades, is still not well understood for a range of surface geometries. Hence, there is a motivation to develop a deeper understanding of the fluid flow behaviour over different surface patterns to understand why certain surfaces perform better than others.

Whenever there is relative motion between the fluid and the solid, the solid surface experiences a force exerted by the fluid known as “drag.” The two primary contributors of the drag force are the pressure drag (or form drag) and the friction drag. The pressure drag arises due to the finite thickness or shape of the body that causes the surrounding fluid to compress, creating a non-uniform pressure distribution (White, p. 476, 2016). Pressure drag is often reduced by changing the shape of the body in a process known as ‘streamlining.’ On the other hand, the friction drag arises due to the viscosity of the fluid and the no-slip boundary condition at the solid interface (Schlichting & Gersten, pp. 25-50, 2018). This creates a fluid shearing effect in the near wall region and generates a force acting against the relative motion. It is important to note that each drag component is generated by unique mechanisms. Drag forces play a major role in several engineering applications such as the transportation sector, construction sector, etc.

Drag is sometimes desirable, for example when airplanes are required to slow down before landing, or for a vertical axis drag type turbine which uses blades with an increased frontal area to generate rotational motion. However, for the vast majority of applications, drag is undesirable, and engineers are often tasked with reducing the drag experienced by a body. For example, the complex wind loading conditions on buildings

and bridges are a result of drag and can cause catastrophic failure if not accounted for in design. Another application that is negatively impacted by the phenomenon of drag is transportation. While the movement of people and goods accounts for about 28% (U.S. Energy Information Administration, 2022) and 23% (Government of Canada, *Energy Production*, 2022) of energy consumption in the United States and Canada respectively, Wood (2004) estimated that 16% of the energy consumed in the US is used to overcome aerodynamic drag in the transportation sector. Despite advancements in technology, energy consumption in the US transportation sector has remained stagnant around 28% since 2001 (United States Department of Transportation, 2022), while the transportation sector in Canada saw a 5% increase in consumption in 2021 (Government of Canada, *Energy Supply and Demand*, 2022). These figures highlight that the demand for energy in the transportation sector remains high and aerodynamic drag is a significant contributor to energy consumption in the transportation sector.

While aerodynamic drag is composed of both friction drag and pressure drag, it has been estimated that friction drag accounts for about 20% of total vehicular drag (Wood, 2004), about 50% of aircrafts drag (Abbas et al., 2017; Malik et al., 2015), and up to 80% of a slow-moving ship's total resistance (Sindagi & Vijayakumar, 2020). Thus, it is evident that friction drag accounts for a significant portion of the total drag in different modes of transportation. While several modifications have been made to streamline the shape of transport vehicles to reduce the pressure drag, little has been done to reduce the friction drag. As refinements to vehicular shape become limited, methods targeting friction drag reduction have become ever more important. Given that friction drag is related to the shear forces close to the fluid surface, first an introduction to the theory behind the generation of friction drag in various flow regimes is presented.

1.1.1 The Boundary Layer

The classification of flow regimes defined by Reynolds in 1894, would serve as pillar of modern fluid mechanics (Schlichting & Gersten, pp. XXI-XXV, 2018). The orderly flow, known as “laminar flow,” and disorderly flow, known as “turbulent flow,” were classified based on a non-dimensional quantity known as the “Reynolds Number.” The

Reynolds number represents a ratio between the inertial and viscous forces of the fluid and can be calculated using equation 1.1 (White, p. 25, 2016).

$$Re_x = \frac{\rho U_\infty x}{\mu} \quad (1.1)$$

For small values of the Reynolds number, the viscous forces are large in comparison to the inertial forces and instabilities within the flow can be suppressed. As the Reynolds number increases in the streamwise direction, the inertial forces begin to grow relative to the viscous forces and flow instabilities are amplified by the inertial forces leading to the transition to turbulence (Schlichting & Gersten, pp. 418-419, 2018). This transition process happens over a range of Reynolds numbers, however, for simplicity and calculation purposes, a critical Reynolds number is often defined as the transition point between laminar and turbulent flow.

As mentioned previously, friction drag is generated by the fluid viscosity and no-slip condition at the solid interface. In 1904, Prandtl suggested that the flow over a solid body could be divided into two regions consisting of a thin layer close to the surface (boundary layer) where viscosity is important, and the remaining region outside this thin layer, where viscous effects could be neglected (Schlichting & Gersten, pp. XXI-XXV, 2018). It was Prandtl's understanding and the theoretical model of the Prandtl boundary layer that helped explain the influence of viscosity and the "fluid sticking effect" when considering friction drag. This thin layer later became known as the "boundary layer."

Given the fundamental differences in the flow behaviour of the laminar and turbulent flow regimes, the viscous (or friction) forces and the boundary layer characteristics are found to be different in the two flow regimes. Figure 1 shows the flow over a flat plate illustrating the boundary layer development from the laminar to turbulent flow regimes. The following sections will explore the theory governing flow in the different flow regimes.

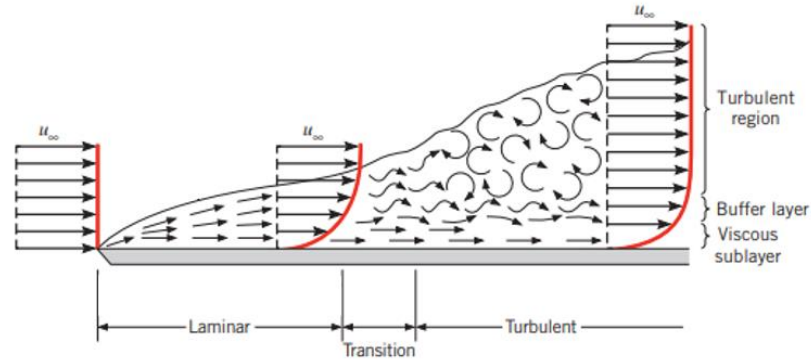


Figure 1: Velocity boundary layer development on a flat plate. Adapted from Bergman & Lavine (2017)

1.1.2 Laminar Flow

The laminar flow regime is characterized by smooth and organized flow. Near the solid boundary, viscous effects dominate and a Prandtl boundary layer is formed in which fluid layers shear over each other. The boundary layer maintains the condition of “no-slip” at the solid boundary, and the thickness of the boundary layer continues to grow in the downstream direction. For laminar flow over a flat plate in the absence of an external pressure gradient, H. Blasius proposed a solution to the boundary layer equations (momentum and continuity equations). Using a constant free-stream velocity and a coordinate transformation, Blasius was able to simplify the boundary layer equations to a single third-order nonlinear ordinary differential equation (Blasius solution) which could be solved numerically. The Blasius solution gives a non-dimensional solution for the shape of the velocity profile throughout a laminar boundary layer (White, p. 459, 2016).

The Blasius solution also allows the computation of some important theoretical correlations. The boundary layer thickness is defined as the distance away from the wall at which 99% of the free-stream velocity has been recovered and can be calculated using equation 1.2 (White, p. 459, 2016). The wall shear stress and local skin friction coefficient are also defined in equations 1.3 and 1.4 (White, p. 460, 2016) and are quantities which can be used to characterize the friction drag force the plate experiences.

$$\delta_{99} \approx \frac{5x}{\sqrt{Re_x}} \quad (1.2)$$

$$\tau_w = 0.332\mu U_\infty \sqrt{\frac{U_\infty}{\nu x}} \quad (1.3)$$

$$C_{f,lam} = \frac{0.664}{\sqrt{Re_x}} \quad (1.4)$$

Given the importance of the boundary layer to friction drag, there are a few additional parameters which can be used to describe the boundary layer. The displacement thickness is a measure of the mass flow deficit in the boundary layer and can be generally described by equation 1.5 (Duncan et al., 1985; White, p. 455, 2016). The momentum thickness is a measure of the momentum deficit caused by the boundary layer and is generally described by equation 1.6 (Duncan et al., 1985; White, p. 453, 2016). Given that the momentum thickness defines the momentum deficit caused by the boundary layer, it is expected that the momentum thickness distribution along the plate will be closely linked with the pressure and skin friction distributions (Duncan et al., 1985). Finally, the ratio of displacement to momentum thickness defines the shape factor (equation 1.7) (White, p. 461, 2016). The shape factor is a measure of the velocity deficit within the boundary layer where larger values represent a greater velocity deficit.

$$\delta^* = \int_0^\delta \left(1 - \frac{u}{U_\infty}\right) dy \quad (1.5)$$

$$\theta = \int_0^\delta \frac{u}{U_\infty} \left(1 - \frac{u}{U_\infty}\right) dy \quad (1.6)$$

$$H = \frac{\delta^*}{\theta} \quad (1.7)$$

When considering the laminar boundary layer over a flat plate (Blasius solution), the displacement thickness and momentum thickness can be calculated using equation 1.8 (White, p. 460, 2016) and 1.9 (White, p. 461, 2016) based on the distance from the leading edge of the plate. Given the shape factor measures the velocity deficit within the boundary layer, the ratio of the displacement thickness to the momentum thickness for the Blasius solution yields a shape factor of 2.59 (White, p. 461, 2016). While the Blasius solution considers a zero-pressure gradient flow, the shape factor can also give an indication of the pressure gradient present within the boundary layer by comparison to

the shape factor of the Blasius solution. Thus, values of H smaller than 2.59 describe a favourable pressure gradient and values of H larger than 2.59 describe an adverse pressure gradient (White, p. 471, 2016).

$$\delta^* = \frac{1.721x}{\sqrt{Re_x}} \quad (1.8)$$

$$\theta = \frac{0.664x}{\sqrt{Re_x}} \quad (1.9)$$

These theoretical correlations derived through the analysis of the Blasius solution provide good information for the bulk characterization of the laminar boundary layer, where the wall shear stress and skin friction coefficients provide an estimation of the friction drag experienced by the surface. Due to the orderly nature of laminar flow and the convenience of the Blasius solution, the friction forces and equations defining the flow behaviour in a laminar boundary layer over a flat plate are well established. However, the transition process and the turbulent flow domain are not yet fully understood. In the next sections, the theory behind the transitional and turbulent flow regimes will be explored.

1.1.3 Transition to Turbulence

As the laminar boundary layer continues to grow downstream over a flat plate, the inertial forces begin to dominate the viscous forces and instabilities become amplified as opposed to suppressed by viscous dissipation. This leads to the transition from laminar to turbulent flow. This transition process is often quite complex and can take many different forms depending on the characteristics of the flat plate and the conditions of the oncoming flow. Ultimately, the transition process is associated with instabilities inside the boundary layer growing in both space and time until they lead to the breakdown of the laminar boundary layer. While the understanding of the transition from laminar to turbulent flow is an active field of research, this section will explore some of the possible instabilities which lead to the breakdown of laminar flow.

The process by which these instabilities are introduced into the boundary layer from external perturbations is known as “receptivity.” Common receptivity mechanisms include surface vibrations, surface roughness, and steady free-stream vortices (Kachanov,

2006). These receptivity mechanisms are associated with either the flat plate boundary or the oncoming flow and lead to small perturbations in the near wall flow.

The instabilities which are formed from these receptivity mechanisms can take many forms and are generally categorized as follows: convective (grow in space), absolute (grow in time), and global (grow in both space and time) (Kachanov, 2006). The type of instability that is generated is a function of both the receptivity mechanism and the level of disturbance in the flow. The instabilities of primary concern are convective instabilities as they only grow in space and are unable to become neutrally stable in the streamwise direction. There are several types of convective instabilities including Tollmien-Schlichting (TS) waves, Görtler vortices, streaky structures, and crossflow vortices to name a few (Kachanov, 2006). Table 1 contains a description of each of these instabilities.

Table 1: Description of common flow instabilities

Instability	Description
TS-Waves	2D streamwise travelling waves that often grow to become 3D instabilities and are very common in the traditional transition to turbulence (Kachanov, 2006).
Görtler vortices	Steady streamwise vortices that appear due to the combined influence of wall curvature on the wall normal mean velocity gradient (Kachanov, 2006).
Streaky structures	Represent a non-modal mechanism of transient growth often connected with the “lift-up” effect, which uses a small amount of streamwise vorticity to move low momentum fluid away from the surface (and high momentum towards the surface) (Kachanov, 2006; Cossu & Brandt, 2004).
Crossflow vortices	Often only observed in 3D boundary layers and represent an instability similar to TS-waves but occur on the spanwise component of the mean velocity profile (Kachanov, 2006).

The traditional transition to turbulence follows the linear growth of convective instabilities in the boundary layer until they start to interact with each other and reach a critical amplitude. These interactions result in secondary instabilities and the non-linear growth phase of the boundary layer (Kachanov, 2006). The non-linear growth of secondary instabilities dictates the transition to turbulence which can either be suppressed, accelerated, or triggered immediately (Kachanov, 2006). Drag reduction mechanisms which target a delay in transition to turbulence focus on suppressing the growth of secondary instabilities. Finally, in the late stages of the transition to turbulence, the instability modes begin transforming into intense concentrated vortices often known as “turbulent spots.” The size and number of the turbulent spots begin growing in space and time leading to full breakdown of the laminar boundary layer (Kachanov, 2006). Figure 2 shows the schematic of the turbulent breakdown process for Tollmien-Schlichting waves which result in streamwise velocity streaks as a secondary instability (characteristic of spanwise vorticity) and eventual breakdown to turbulent flow.

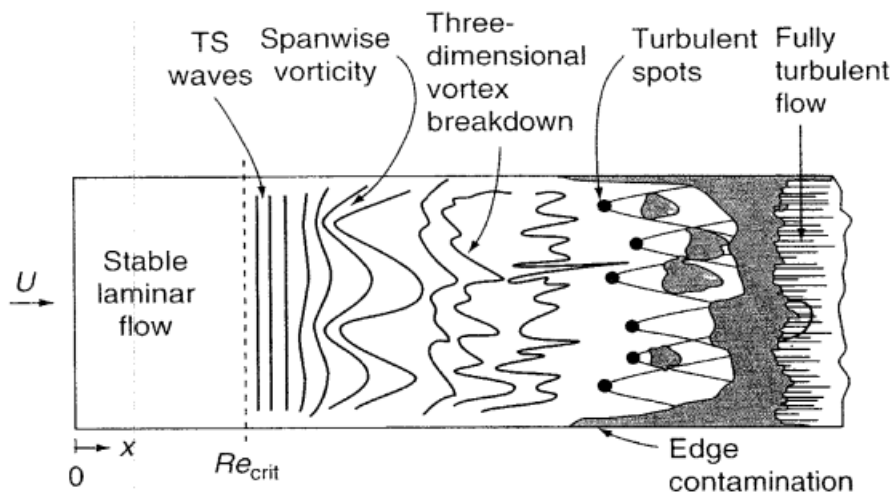


Figure 2: Sketch of flat plate boundary layer transition (White, p. 377, 2006)

When large unstable disturbances are present in the boundary layer, the transition to turbulence can be triggered immediately, in what is referred to as the “transient growth” process (Reshotko & Tumin, 2006). In this process, large amplitude unstable disturbances interact with the linear instabilities early in the transition process leading directly to secondary instabilities or causing direct breakdown to turbulence via the “bypass

mechanism.” This “bypass mechanism” contains very large amplitude forcing and often has no linear regime (Reshotko & Tumin, 2006). The transition route which dominates is characterized by the conditions of the flow, surface boundaries, and instabilities which develop in the flow.

As was outlined above, the transition process from laminar to turbulent flow is highly complex and not yet fully understood. While not everything about the transition process is yet understood, a basic understanding of the type of instabilities and paths of transition to turbulence provides a necessary background for understanding how to prevent and control this process. Many methods of friction drag reduction target the control of flow over surfaces to prevent, trip, or strategically modify the transition process. The next section will focus on the turbulent flow regime.

1.1.4 Turbulent Flow

Once in the fully turbulent flow regime, the boundary layer profile and mechanisms for boundary layer growth differ from those in the laminar regime. The turbulent boundary layer consists of various layers including the viscous sublayer, buffer layer, and logarithmic (overlap) layer (see Figure 3). The friction velocity and kinematic viscosity are often used to normalize the velocity and wall normal distance, respectively. The friction velocity is calculated using the wall shear stress in equation 1.10 (White, p. 354, 2016), and the normalized velocity and wall normal distance are calculated according to equations 1.11 (White, p. 354, 2016) and 1.12 (White, p. 356, 2016).

$$u_t = \sqrt{\frac{\tau_w}{\rho}} \quad (1.10)$$

$$u^+ = \frac{u}{u_t} \quad (1.11)$$

$$y^+ = \frac{yu_t}{\nu} \quad (1.12)$$

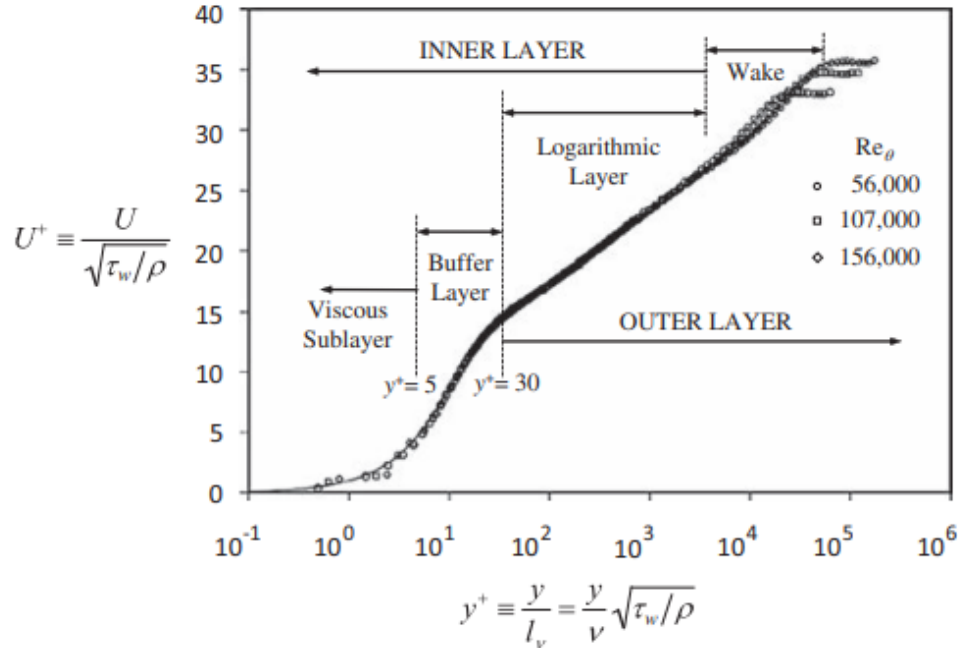


Figure 3: The turbulent boundary layer profile obtained from Kundu et al. (2016) which shows data replotted from Oweis et al. (2010) for three Reynolds numbers. The dashed lines indicate the bounds of each of the regions within the turbulent boundary layer.

Similar to a laminar boundary layer, the viscous sublayer is governed by viscous forces. The viscous sublayer extends to $y^+ = 5$, and it is said to have a linear relationship with velocity according to equation 1.13 (White, p. 356, 2016). Far away from the wall there exists the logarithmic layer (overlap layer) which has significant turbulent effects. The relationship describing the velocity in this layer is given by the log-law in equation 1.14 where $\kappa = 0.41$ and $C = 5.0$ (White, p. 355, 2016). The limits of the log-layer are often described over a range corresponding to $40 - 70 \leq y^+ \leq 500 - 1000$. Between the viscous sublayer and the log-layer lies the buffer layer where both turbulent and viscous effects are important. The buffer layer exists for $5 \leq y^+ \leq 40 - 70$ and is often modeled using experimental data to connect the viscous sublayer to the logarithmic overlap layer. Above the log-layer lies the wake or bulk flow region where the pressure effects become significant and turbulent shear dominates (White, p. 354, 2016).

$$u^+ = y^+ \quad (1.13)$$

$$u^+ = \frac{1}{\kappa} \ln(y^+) + C \quad (1.14)$$

While the above set of equations describes the velocity relationship in each layer of the turbulent boundary layer, Prandtl suggested a simpler one-seventh power law expression (equation 1.15) which can be used to approximate the entire turbulent boundary layer profile (White, p. 464, 2016).

$$\frac{u}{U_\infty} = \left(\frac{y}{\delta}\right)^{\frac{1}{7}} \quad (1.15)$$

The complex structure of the turbulent boundary layer generally results in a greater friction drag than a laminar boundary layer. The additional turbulent stresses often referred to as the “Reynolds stresses” are representative of the mixing phenomenon and continuous transport of energy to larger eddies within the boundary layer (Schlichting & Gersten, p. 499, 2018). These turbulent stresses contribute to an overall greater skin friction coefficient in the turbulent boundary layer, which can be approximated using Prandtl’s one-seventh power law approximation in equation 1.16 (White, p. 465, 2016).

$$C_{f,turb} = \frac{0.027}{Re_x^{\frac{1}{7}}} \quad (1.16)$$

This expression highlights the differences in friction drag between the laminar and turbulent regimes as the turbulent skin friction coefficient relies on $\frac{1}{Re_x^{\frac{1}{7}}}$ and the laminar skin friction coefficient relies on $\frac{1}{\sqrt{Re_x}}$ (equation 1.4). Figure 4 shows the resulting skin friction coefficients at various Reynolds numbers based on the laminar and turbulent theory, highlighting the difference in friction drag between the two flow regimes.

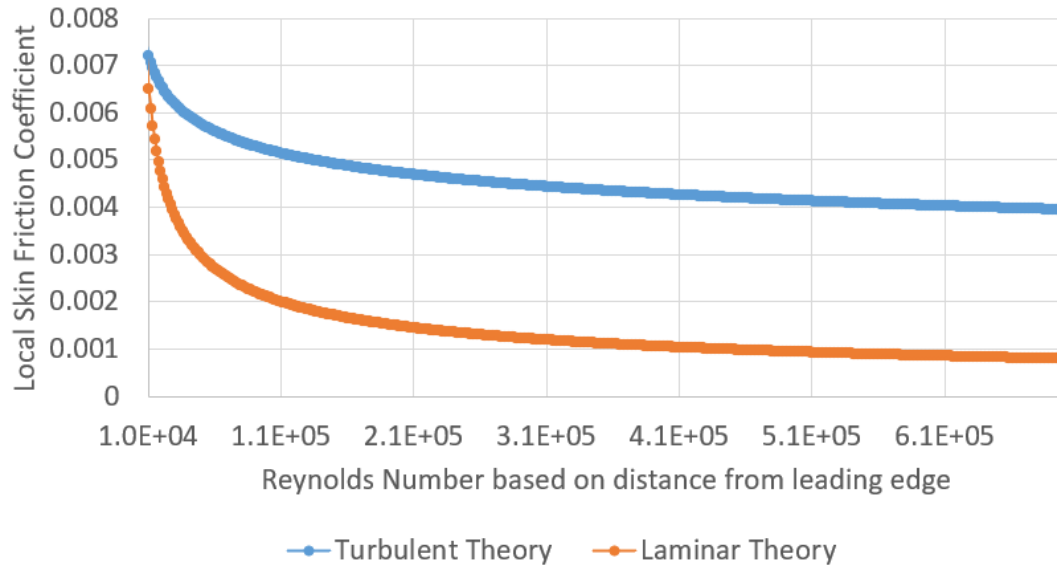


Figure 4: Local skin friction coefficient for various Reynolds numbers based on both the laminar and turbulent theory.

Despite the higher skin friction coefficient, the turbulent boundary layer carries a smaller shape factor (H), equal to 1.3 (White, p. 465, 2016), indicating a lower velocity deficit. The delay in transition to turbulence is often desired as the lower skin friction coefficient associated with the laminar boundary layer results in an overall reduction in drag (Figure 4).

Given the differing boundary layer profiles and growth mechanisms between the laminar, transitional, and turbulent flow regimes, methods targeting drag reduction in each regime are likely to vary. The following section will focus on methods of friction drag reduction that result in both the delay in transition to turbulence and modification of the friction drag directly.

1.2 Friction Drag Reduction Techniques

Several drag reduction techniques have utilized the replication of features or processes found in nature. These applications are often referred to as “biomimetic applications” which utilize the optimized features from nature. Some examples of biomimetic applications include Velcro which is derived from the action of the hooked seeds of the burdock plant (Velcro, 1955), dry adhesive tape which was inspired from the adhesion

mechanism of gecko feet (Geim et al., 2003), and the small surface properties of lotus leaves that have been applied to various surfaces and paints to achieve self-cleaning characteristics (Barthlott & Neinhuis, 1997). Each of these examples made use of the unique properties found in nature to achieve better performance in everyday applications.

Within the field of fluid mechanics, some examples of biomimetic features include the unique feathers around penguin beaks which introduce a turbulent boundary layer over the swimming bird (Parfitt & Vincent, 2005), shark skin inspired riblets which have been found to reduce drag in turbulent flow (Dean & Bhushan, 2010), and the tubercles found on the flippers of humpback whales which have been studied for their role in reducing drag and improving lift (Fish et al., 2011). Replicating these specific biological features is a particularly useful process because it allows for the underlying physics to be applied to engineered surfaces for the purpose of exploiting the benefits in performance.

While several drag reduction techniques have utilized biomimetic replication, they have largely focused on active and passive methods of drag reduction. Active methods often require some form of control, whereas passive methods rely solely on the passive interaction between the fluid and the surface (Ghaemi, 2020). The following section will explore drag reduction techniques in each of these fields with a focus on understanding the mechanisms driving the drag reduction.

1.2.1 Active Methods

1.2.1.1 Stationary Surfaces

The first group of active drag reduction techniques modify the surface boundary directly without any active motion. These include micro-blowing, electromagnetic actuation, and thermal heating.

Micro-blowing or sometimes called jet actuators, introduce air (or another fluid) into the near wall boundary layer through small holes placed on the surface. These actuation streams are often oriented perpendicular to the flow (in the spanwise direction) and are operated in a periodic manner. Abbas et al. (2017) discusses the success of this technique and highlights that a 20-30% reduction in the turbulent fluctuations can be achieved.

Additionally, Zhang et al. (2020) cites Choi and Clayton (2001) and Karniadakis and Choi (2003) who describe the mechanism as the reduction and elimination of streamwise vorticity and low-speed streaky structures within the boundary layer which are often unstable and add additional shear in turbulent boundary layers. The main drawback of this technique is that it requires physical holes in the surface in addition to control components responsible for the blowing motion that is not practical in all applications.

Similar spanwise forcing in the near wall region can be achieved by electromagnetic actuation. The electromagnetic actuation uses the speed and charge of the fluid particles to induce a spanwise fluid motion within the boundary layer. The magnets arranged in an alternating pattern have been used to induce alternating forces within the boundary layer (Zhang et al., 2020 from Berger et al., 2000; Lee and Sung, 2005; Breuer et al., 2004; and Pang and Choi, 2004). Xu and Choi (2008) and Du and Karniadakis (2000) studied the oscillations induced by the Lorentz force and found that a drag reduction rate of 28-30% could be achieved. They also suggest this technique targets a similar mechanism to micro-blowing where the disruption of instabilities within the boundary layer reduces the shear stress associated with the turbulent boundary layer. While this method does not require holes in the surface, it relies on the magnetic charge associated with the fluid particles which may not be realistic in all practical situations.

While spanwise forcing is common, similar methods can be applied in the streamwise direction. Tong et al. (2008) found a maximum drag reduction rate of 46% when oscillating waves were induced by the Lorentz force in the streamwise direction. Additionally, Huang et al. (2010) suggests the mechanism for drag reduction in the streamwise direction is the formation of a generalized Stokes layer. A Stokes layer is the oscillating motion of the fluid usually induced by the wall motion (Quadrio & Ricco, 2011). The oscillating flow behaviour in the streamwise direction leads to the disruption of turbulence regeneration mechanisms such as bursting and can prevent the growth of instabilities (Huang et al., 2010). This highlights that drag reduction via streamwise and spanwise fluid motion can be achieved largely through the disruption of near wall instabilities that produce additional shear stress in turbulent boundary layers.

Finally, Fuaad et al. (2016) showed that thermal heating patterns could be utilized in both the streamwise and spanwise directions to obtain a drag reduction of 8% through thermal buoyancy. In a similar fashion to electromagnetic forcing, thermal heating changes the local buoyancy of the fluid. This results in the prevention of crossflow fluctuations restraining the transient growth of the velocity streaks. While periodic heating requires the consumption of energy, there is no discussion of the net energy benefit. Additionally, periodic heating is complex and impractical in many applications including transportation, limiting the ability for its use.

These active methods have focused on introducing fluid motion in the near wall boundary layer (over stationary surface) and targeted the disruption of turbulence regeneration mechanisms decreasing the shear stresses associated with the turbulent boundary layer. The ability for these methods to introduce stabilizing flow patterns that result in the suppression of instabilities suggests these methods could also be applied in the transitional flow regime. Suppressing the growth of instabilities throughout the transition to turbulence often results in a delay in transition location and extension of the smaller friction drag associated with the laminar boundary layer.

1.2.1.2 Moving Surfaces

The other group of active drag reduction techniques involves those which require moving surfaces. These active methods include wall motion and wall deformation.

Wall motion is a common drag reduction technique in turbulent flows and is applied predominantly in the spanwise direction. Zhang et al. (2020) provides a comprehensive summary of the studies which have explored drag reduction through spanwise wall motion indicating that up to a 45% drag reduction rate can be achieved (Choi et al., 1998; Laadhari et al., 1994). The mechanisms driving this drag reduction are related to the generation of a transverse Stokes layer (or oscillating boundary layer in the spanwise direction). Leschziner (2020) highlights the effectiveness of the Stokes layer in disrupting the turbulence regeneration mechanisms when confined to the viscous sublayer. Choi and Clayton (2001) also highlighted that the spanwise oscillations resulted in a thicker

viscous sublayer and a reduction in the turbulent fluctuations. These findings show that within a turbulent boundary layer, spanwise wall motion can result in drag reduction.

While this method proved useful in reducing drag in the turbulent boundary layer, Ricco (2011) studied the impact of spanwise wall forcing in laminar flows and found that the amplitude of unsteady velocity streaks within the boundary layer could be modified by varying the amplitude of wall forcing. The streamwise velocity streak intensity is found to decrease when the spanwise wavelength is of the same order as the theoretical laminar boundary layer thickness (Blasius solution). This highlights that the transverse Stokes layer that is formed within the near wall region of the boundary layer has the ability to modify the near wall flow structures in both laminar and turbulent flows when it is limited in the spanwise and wall normal directions, respectively.

Another variation on the traditional spanwise wall motion is to have the spanwise motion travel downstream or upstream over the plate, adding a streamwise dependency to the spanwise motion. Quadrio and Ricco (2009) and Auteri et al. (2010) found that a reduction in the skin friction drag is always observed when spanwise waves travel in the direction opposite to the flow. While the flow behaviour is similar to the spanwise wall motion mentioned above, Quadrio and Ricco (2009) found a maximum drag reduction of 48% using direct numerical simulations (DNS). The additional benefits of the spanwise motion traveling in the streamwise direction does not drastically improve the drag reduction rate and instead adds unnecessary complexity. In general, spanwise wall motion is proven to be effective at reducing drag, however, is once again complex and impractical in many real-world scenarios.

Active wall deformation is another technique to achieve drag reduction. This technique requires a more complex set of actuators and a compliant surface material which allows for periodic deformations in the surface. Deformations have been applied in both the spanwise and streamwise directions, indicating up to 13% drag reduction for spanwise deformations (Tamano & Itoh., 2012), and 70% for streamwise travelling waves (Nakanishi et al., 2012). While streamwise travelling wall deformation is found to be more effective at reducing the drag than the active wall motion techniques described

previously, its implementation is significantly more complicated. The spanwise wall deformations were found to induce a secondary flow in between waves that moved the streamwise vortices away from the surface (Tomiyama & Fukagata, 2013). They were also found to reduce the vorticity fluctuations in the viscous sublayer and lead to a decrease in the momentum exchange in the near wall region (Klump et al., 2010 and 2011; Roggenkamp et al., 2015). Different from wall motion, spanwise wall deformation physically pushes the turbulent flow structures away from the surface reducing the impact they have on the surface drag.

Streamwise wall deformations are shown to have a higher drag reduction than the spanwise deformations and better performance when the waves propagate along the flow direction (Nakanishi et al., 2012). Streamwise travelling waves were suggested to reduce crossflow velocity fluctuations (Ahmad et al., 2015), and introduce roller-like vortices between waves which reduce skin friction through velocity slip (Mamori & Fukagata, 2011). These mechanisms are fundamentally different from the spanwise wall deformation and result in a greater reduction of friction drag in turbulent flows.

Overall, the active drag reduction techniques discussed above are focused largely on drag reduction in the turbulent regime. Modification of the near wall flow behaviour was the primary mechanism driving the drag reduction. This included suppressing streamwise velocity streaks, preventing crossflow vortices, and reducing turbulent fluctuations within the near wall boundary layer. While these methods focused on the turbulent flow regime, a strong case can be made that they may also play a role in delaying the transition to turbulence as the suppression of instabilities is a key feature related to delaying transition. The main drawback with active drag reduction systems is they often require complex control mechanisms and additional energy input making them difficult to apply in practical applications. As such, the next section will focus on passive methods of friction drag reduction.

1.2.2 Passive Methods

Passive drag reduction methods have the benefit of interacting naturally with the fluid, leading to drag reduction without any additional control. This section will focus on

passive drag reduction mechanisms which target the fluid interface and those which carry unique surface modifications.

1.2.2.1 Fluid Interface

The two primary techniques identified which modify the fluid interface are fluid additives and hydrophobic surfaces.

Fluid additives refers to the addition of small amounts of polymer to the surrounding fluid. This technique has been tested for several different polymer solutions and has shown a drag reduction potential up to 80% (Asidin et al., 2019; Lumley, 1969; Virk, 1975). This method has been implemented successfully in crude oil transportation where it resulted in an increase in crude oil production by up to 30% (Liu & Ma, 2022; Burger et al., 1982). The comprehensive review provided by Xi (2019) discusses that polymer additives result in a solution with viscoelastic properties which in the onset of drag reduction have the ability to absorb energy and suppress flow instabilities common in the turbulence regeneration process. They describe two competing theories that argue the drag reduction behaviour is caused by either the extensional viscosity associated with the elongated polymers in the solution (Lumley, 1973), or the elastic energy being stored in the individual polymer chains contributing to the drag reduction (Tabor & de Gennes, 1986). Despite the debate over which is the governing mechanism, there is strong evidence that polymer additives are effective as a passive drag reduction technique. While this method has been found to be successful in reducing drag, it requires modification of the surrounding fluid which is impractical in most of the applications including the transportation sector.

The other drag reduction technique which targets the fluid-solid interface is hydrophobic surfaces. Hydrophobic surfaces are classified as surfaces with a water contact angle greater than 90° . They have a high surface free energy and do not exhibit wetting behaviour (Liu & Ma, 2022). The surface of Lotus leaves was found to contain unique microstructures which led to a large water contact angle (Feng et al., 2002). Similar microstructures have since been replicated by Ou et al. (2004) in a microchannel where they observed a decrease in the surface drag under laminar flow conditions. These

surfaces are often called superhydrophobic surfaces, where the driving mechanism leading to drag reduction is the modification of the surface boundary condition resulting in fluid slip (Ou & Rothstein, 2005). It is the presence of entrapped air in the microstructures that leads to a nearly shear-free condition at the boundary, where the total shear stress is dominated by the tops of the surface structures (Ybert et al., 2007). Park et al. (2014) adjusted the geometric parameters of the microstructures on a superhydrophobic surface to demonstrate a 75% drag reduction compared to a smooth surface. These methods show promising results; however, the fine microstructures present some unique challenges.

The two major drawbacks of superhydrophobic surfaces are the diffusion of entrapped air over time and the strength of the microstructures (Liu & Ma, 2022). While entrapped air drives the drag reduction over the surface, the diffusion of this air over time requires that it be replenished to maintain drag reduction over long periods. Additionally, given the entrapped air is supported by fine microstructures, the durability and strength of these features is critical for maintaining the ability to reduce drag. Despite these challenges, Xu et al. (2020) demonstrated that a 30-40% drag reduction could be achieved using superhydrophobic surfaces on a realistic boat in open water.

Overall, superhydrophobic surfaces present the best passive drag reduction technique discussed thus far. Although polymer additives showed promising results, it is impractical to modify the surrounding fluid in many applications. While the discussion of passive mechanisms has focused on the fluid interface, the following section will explore surface modifications which have shown promising drag reduction results.

1.2.2.2 Surface Modifications

Surface modifications are a passive drag reduction technique which involve introducing unique geometric patterns on the surface to influence the near wall flow behaviour in such a way as to modify the flow structures or wall shear stress so that the drag reduction can be achieved. These techniques include riblets, finite amplitude velocity streaks, and fish scales.

Several studies have found that the microstructures on shark skin are successful in reducing friction drag in the turbulent flow regime (Liu et al., 2020; Liu & Ma, 2022; Dean & Bhushan, 2010). Riblet optimization studies have shown that sawtooth riblets with a height to spacing ratio of 0.5 achieved 11% drag reduction numerically (Heidarian et al., 2018), scalloped riblets with a height to spacing ratio of 0.7 resulted in 6.5% drag reduction numerically (Heidarian et al., 2018), and blade riblets with a height to spacing ratio of 0.5 could achieve 9.9% drag reduction experimentally (Bechert et al., 1997). Riblets are predominantly implemented in the streamwise direction; however, Koeltzsch et al. (2002) explored the impact of converging and diverging riblet patterns experimentally to find that diverging patterns resulted in an increased mean flow velocity and a reduction in turbulent fluctuations. Additionally, Chen et al. (2013) studied the herringbone riblet patterns from bird feathers experimentally and found that these riblet patterns contributed about 16% higher drag reduction than traditional riblet patterns. Thus, the unique arrangements of traditional riblets presents a strong case for additional drag reduction. Overall, these results highlight that shark-skin inspired riblets are a successful technique to achieve passive drag reduction.

There exist two theories for the drag reduction mechanism over riblet surfaces, with neither being conclusive. The first is the protruding height theory which argues that since the riblets contain a small spacing and protrude into the boundary layer, turbulent vortices are effectively lifted away from the surface and only interact with the tips of the riblets. This effectively increases the thickness of the viscous sublayer and suggests that although there is an increase in the wetted area, the turbulent stresses are reduced as the vortices only interact with the riblet tips (Bechert & Bartenwerfer, 1989; Bechert et al., 2000; Liu et al., 2020; Dean & Bhushan, 2010). The second is the secondary vortex theory which suggests that secondary vortices are formed in the riblet valleys, weakening the uplifting and turbulent bursting that happens in turbulent boundary layer (Liu et al., 2020). The contribution of the interaction between these secondary vortices and the surface of the riblet valleys is small and these vortices contribute to rolling friction with the outer flow resulting in a decreased friction drag (Fu et al., 2017). While it is likely that both mechanisms are present in the flow over riblet surfaces, it is the effective lifting and

pinning of vortices, along with the reduction of turbulent stresses in the near wall region that contributes to the overall drag reduction.

While riblet surfaces have shown benefits in drag reduction, their main drawback is the difficulty and cost of manufacture (Liu & Ma, 2022). The small and precise nature of the riblet size, shape, and spacing presents a unique challenge in manufacturing. Despite this, Yang et al. (2021) numerically explored the impact of sawtooth riblets on airfoils and found that a 15% drag reduction could be achieved for an optimal riblet length of 0.8 chords. Shark skin inspired riblets have also successfully been applied to Speedo swimsuits where they claim to reduce the drag by 4% for men and 3% for women (Krieger, 2004). While riblets have shown success in reducing friction drag, the increased wetted area results in a drag increase under laminar flow conditions when turbulent vortices are no longer present (Bixler & Bhushan, 2013).

The second technique which focuses on friction drag reduction in laminar and transitional flows is the formation of steady streamwise velocity streaks within the boundary layer. These velocity streaks may be introduced through various methods including mini-vortex generators (Fransson & Talamelli, 2012) or cylindrical roughness elements (Fransson et al., 2005). Figure 5 shows a schematic of the formation of streamwise velocity streaks behind an isolated roughness element and their eventual breakdown to turbulent flow.

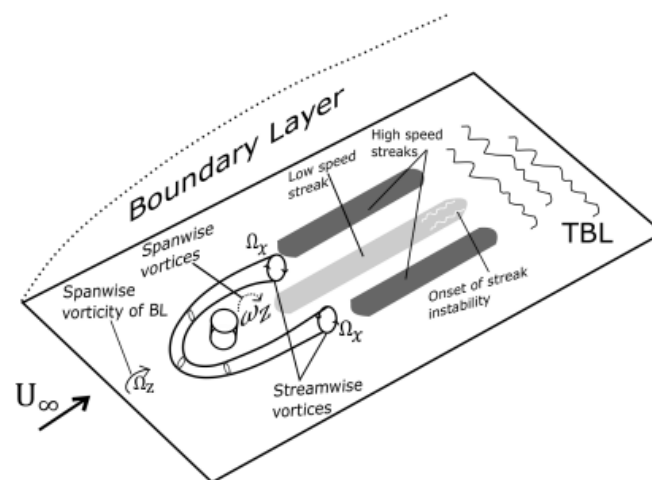


Figure 5: Formation of streamwise velocity streaks behind an isolated roughness element (Joseph et al., 2022)

Fransson et al. (2005) showed experimentally and Schlatter et al. (2010) showed numerically that the formation of finite amplitude streamwise velocity streaks within the boundary layer resulted in the suppression of Tollmien-Schlichting waves, which are often amplified in the transition process to turbulence. In addition to this, Shahinfar et al. (2014) also demonstrated experimentally that the passive introduction of these velocity streaks via mini-vortex generators resulted in the attenuation of other three-dimensional instabilities such as single and pair oblique waves. The stabilizing effect of these finite amplitude steady velocity streaks is found to increase with the streak amplitude (Fransson et al., 2005; Cossu & Brandt, 2004). While streamwise velocity streaks eventually lead to the transition to turbulence, the stabilizing effect of these steady finite amplitude streaks occurs as a result of the spanwise shear associated with the velocity streaks working against the kinetic energy production of the instabilities (Cossu & Brandt, 2004). The important characteristics of this drag reduction mechanism is that the velocity streaks are steady and of finite amplitude.

Andersson et al. (2001) studied the transition to turbulence through the development of natural disturbances over a flat plate using DNS and found that once the amplitude of the streamwise velocity streaks reached 26% of the free-stream velocity, breakdown to turbulence was imminent. While these results relate to the natural formation of velocity streaks over a flat plate, Fransson et al. (2005) studied experimentally, the formation of velocity streaks using cylindrical roughness elements and found that stable streaks could only be formed up to a streak amplitude of 12% of the free-stream velocity. Amplitudes above this resulted in the vortex shedding from the roughness elements to become unsteady and lead to the onset of turbulence. To avoid this, Fransson and Talamelli (2012) studied the experimental formation of velocity streaks using mini-vortex generators and found that stable streaks could be formed with amplitudes exceeding 30% without any indication of instability amplification. This highlights that while finite amplitude velocity streaks lead to drag reduction, the critical streak amplitude before the amplification to turbulence is linked to the underlying streak generation mechanism.

Given the viscous effects in a laminar boundary layer tend to suppress instabilities, the streak behaviour tends to weaken in the streamwise direction, unless perturbed by

secondary instabilities causing amplification. Fransson (2015) describes this behaviour as being the natural recovery of the velocity streaks which occurs exponentially in the streamwise direction. Fransson and Talamelli (2012) conducted experiments which showed that the placement of a second mini-vortex generator array downstream results in the reinforcement of the velocity streaks within the boundary layer leading to further delay in transition. These findings highlight that although the passive formation of streamwise velocity streaks within the boundary layer results in significant delay in transition, without continued forcing these benefits dissipate quickly. Reinforcement of the streamwise velocity streaks in the streamwise direction has significant benefits in terms of the stability of the flow behaviour and can lead to further delay in transition. These streamwise velocity streaks are a unique passive technique which requires fine tuning of the generation mechanisms and streak amplitudes.

Another technique which has been a recent topic of research is the potential for fish scale surfaces to reduce drag in laminar and transitional flow regimes. Most recently, a study by Muthuramalingam et al. (2019) gave numerical evidence of the unique flow patterns that are observed over a biomimetic fish scale array. The formation of high- and low-streamwise velocity streaks were validated qualitatively using experimental visualizations. While they briefly discuss the potential mechanisms for drag reduction, Muthuramalingam et al. (2020) demonstrated experimentally the ability for fish scale arrays to delay transition far downstream of the scale array. A visualization technique and velocity measurements were employed to determine the delay in transition location. Further, a theoretical estimation of the drag reduction due to this delay in transition highlighted a potential for 27% reduction in skin friction drag. Given fish scale arrays present a unique streak generation mechanism with little fundamental understanding, the detailed results of these studies and others focused on fish scales as a technique for drag reduction will be explored in the next section.

1.2.3 Fish Scales

1.2.3.1 Fish Skin Classification

Fish scales come in many shapes and sizes and can be generally classified into the four categories shown in Figure 6.

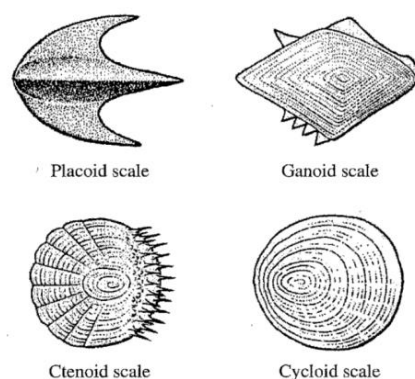


Figure 6: Different scale shapes (Sudo et al., 2002).

This categorization highlights four distinct scale shapes along with unique surface microstructures for each scale type. Placoid scales contain a raised riblet aligned with the flow and have been proven to reduce drag in turbulent flow (Dean & Bhushan, 2010). Ctenoid scales have an oval shape and contain Ctenii (or spiny features) located on the rear portion of the scale exposed to the flow (Wainwright & Lauder, 2017). Cycloid scales are circular and contain prominent circuli (or rings) around the scale (Wainwright & Lauder, 2017). Finally, while the ganoid scale does not have any distinct surface features, it contains a unique diamond scale shape different from all the others. While the influence of these surface microstructures on the flow remains unknown, Wainwright and Lauder (2017) suggest they may play an important role in the retention of mucus and the near wall flow interactions.

The importance of fish scales as a drag reduction technique has only been explored recently, however, fish scales have historically been studied from an evolutionary perspective exploring how factors such as species, environment, and age effect the overall size and shape of the scales present on the fish surface (Kuusipalo, 1998; Sudo et

al., 2002; Ibañez et al., 2009; Wainwright et al., 2022). Wainwright et al. (2017) and Wainwright and Lauder (2016) presented a new GelSight characterization technique and provided an in-depth characterization of the surface of Bluegill sunfish. This detailed characterization highlighted that scale size and shape is also found to vary across the surface of a single fish, raising questions about how scale shape can affect the flow over the fish surface.

While Wainwright and Lauder (2017) suggest the potential structural benefits that fish scales may play in creating an armor like surface, they also highlighted the limited knowledge about the hydrodynamic importance of fish scales. While variations in both scale size and shape have been found through the detailed characterization of the Bluegill sunfish (Wainwright & Lauder, 2016), the importance of these variations can only be understood after a detailed understanding of fish scale arrays themselves is developed. The following section will explore the research related to the drag reduction potential of fish scales and highlight studies focused on understanding their functional significance.

1.2.3.2 Drag Reduction

With the recent success of shark skin riblets leading to drag reduction, the topic of fish scales resurfaced as a potential technique for reducing friction drag. Wainwright and Lauder (2017) highlight that early work was largely theoretical with little quantitative analysis (Walters, 1963; Hamner, 1979; Burdak, 1986). Starting in 2008, Sagong et al. studied V-shaped protrusions experimentally in turbulent flow and found there to be no significant drag reduction outside of the experimental uncertainty. Despite this, Dou et al. (2012) demonstrated experimentally that micron-scale caves spontaneously distributed on the surface resulted in a drag reduction of about a 10% at 13.1 m/s. These authors took a multiphase approach to the simulation of flow over their bionic fish scales and found that entrapped air contributed to modification of the surface boundary condition (similar to superhydrophobic surfaces). While these experiments showed promising results, the method for surface replication consisted of spray-painting, which does not accurately capture the important features of the fish skin but rather creates more of a distributed roughness. Capturing a more accurate scale geometry, Wu et al. (2017 & 2018) numerically and experimentally studied the crescent-shaped microstructures of grass carp

and found that they produced a surface wetting behaviour that trapped water and contributed to a ~3% drag reduction at 0.66 m/s. While these studies have highlighted some success and potential drag reduction mechanisms, the replication of fish scale surfaces up to this point has comprised of individual scale features distributed on a surface and ignored how the scales interact with each other.

The work of Muthuramalingam et al. (2019) provided significant advancements in the field of hydrodynamic research on fish scales as it modelled the 3D overlapping nature of the scales into a biomimetic fish scale array. Figure 7 shows a biomimetic fish scale array with overlapping scale features characteristic of real fish skin.



Figure 7: 3D Biomimetic fish scale replicating the overlapping nature of the fish scales.

Muthuramalingam et al. (2019) simulated laminar flow over the scale arrays and found the formation of streamwise velocity streaks within the boundary layer that produced a maximum velocity difference of 9% of the free-stream velocity. They validated the formation of these velocity streaks using visualization techniques over both real fish skin and a biomimetic fish scale array. While the simulation results showed a net drag reduction for small scale heights relative to the boundary layer thickness, their conclusions are based largely on the physics identified from numerical simulations with little experimental validation. To the best of the author's knowledge, this is the only study to date that explores, in some detail, the fundamental mechanisms driving the flow behaviour over these overlapping biomimetic fish scale arrays.

To further their work of 2019, Muthuramalingam et al. (2020) studied experimentally the impact of a fish scale array on the transition to turbulence and found that downstream of

the scale array over a flat surface, the induced velocity streaks have the ability to suppress Tollmien-Schlichting waves and delay the transition to turbulence. They theoretically estimated that this delay in transition would result in about a 27% reduction in drag by maintaining a laminar boundary layer for 55% farther compared to without the scale array upstream. While this study presents a strong case for the benefit of fish scale arrays in the transition to turbulence, they only speculate about the driving mechanisms which contribute to the stabilizing flow behaviour and delay in transition.

Since the work of Muthuramalingam et al. in 2019 and 2020, Mosghani et al. (2021) simulated the impact of Ctenoid shaped scales on a cylindrical rod and found a total net drag reduction of 20% in a turbulent flow. While the pressure drag had a significant impact, it was the reduction in friction drag and large contribution of the friction component to the total drag that resulted in the drag reduction. Additionally, Hou et al. (2021) studied the impact of different arrangements of isolated fish scale pits and found that a drag reduction of up to 6% was driven by the vortex cushioning effect which converts sliding friction to rolling friction over the pits. While these studies focused on numerical simulations, they once again highlight the potential for fish scale arrays as a technique for drag reduction beyond just the delay in transition.

Another aspect of fish scale research that has received little attention is the influence of the undulatory swimming motion on the flow over the fish. Early theories by Lighthill (1971) suggested that the undulatory motion causes alternating thin boundary layers with higher shear stress compared to a rigid plate. Anderson (2001) studied the boundary layer at several locations over two fish species with different undulatory motions and found that when swimming in still water, the boundary layer always suggested a laminar profile with no separation. Additionally, Yanase and Saarenrinne (2016) examined the unsteady boundary layer of a swimming rainbow trout and found that laminar flow was maintained over the entire length of the fish, and flow separation was delayed until the vortex shedding occurred in the rear region of the fish. Finally, Lauder et al. (2016) highlighted the importance of dynamic testing of fish scale surfaces and used a dynamic controller with 2D foil cut outs of scale features allowed to “pop-up.” This study showed that the 2D foil cut-outs did not perform as well as the smooth control. While the undulatory

motion of fish adds another complexity to the problem of hydrodynamics over fish, a detailed understanding of the interactions over stationary fish skin surfaces is required before considering the impact of undulatory motion.

Overall, the recent interest in the hydrodynamic performance of fish skin has resulted in several studies investigating the drag reduction performance of fish skin surfaces. While advances in the replication of the fish scales resulted in the modeling of overlapping scale arrays, the fundamental understanding of how fish scale arrays modify the flow behaviour is still very limited. The current foundational studies are those of Muthuramalingam et al. (2019) and (2020) which largely rely on numerical simulations with little experimental validation.

1.2.4 Knowledge Gaps

Based on the literature review in preceding sections regarding friction drag reduction mechanisms, it is evident that while several mechanisms have been proposed, many are impractical for application in the transportation sector. Many techniques focused on drag reduction in the turbulent flow regime, with only a few focusing on drag reduction in laminar and transitional flow. Thus, there is a need to identify and understand drag reduction techniques which can target both the laminar and transitional flow regimes. Given the recent focus on fish scales as a drag reduction technique and the promising drag reduction results in both the laminar and transitional flow regimes, the critical knowledge gaps in the field of research focused on fish scales are discussed here.

While little work has been done to understand the underlying physical mechanisms, numerical simulations have dominated this field of study. There is a particular need to demonstrate and quantify the observed flow behaviour over the scale arrays experimentally as this would deepen our understanding of the governing flow behaviour over these scale arrays.

The current research on fish scales also highlights that each study considers a unique scale geometry. While variations in scale size and shape detailed by Wainwright and Lauder (2016) suggests the potential impact of scale shape on the performance of the

scale arrays, no reported study has explored this hypothesis. Hence, there is a need to standardize the current fish scale geometries and evaluate the performance of different scale shapes. This will help inform how scale shape affects the observed flow behaviour and lead to further optimization of fish scale arrays for better performance.

Further, there is a need to understand the importance of the small microstructures found on fish scales (Ctenii and circuli). While Wainwright and Lauder (2017) speculate about the role they play in the near wall flow behaviour, there is no conclusive evidence suggesting their hydrodynamic function.

Finally, there exists a gap in the understanding of how the undulatory swimming motion of fish impacts the near wall flow behaviour. While it is suggested that the boundary layer remains in the laminar and transitional flow regimes, the impact on the near wall shear stress and vortex shedding behaviour is not fully understood. Understanding how the swimming motion impacts the observed near wall flow behaviour is a complex and challenging task that will give a deeper physical understanding into the flow over real fish.

1.3 Research Objectives

The background and literature review have provided a detailed understanding of different flow regimes and several methods of active and passive friction drag reduction. Due to the significant benefits of passive applications, a focus on passive surface modifications leading to friction drag reduction revealed the potential benefits and lack of understanding in fish scales as a mechanism for drag reduction. While several knowledge gaps in the field of fish scale research have been identified, the objectives of the current work are described as follows.

1.3.1 Objectives of the Current Work

1.3.1.1 Fundamental experimental investigation

While Wainwright and Lauder (2017) highlighted a significant gap in the understanding of flow over fish scales, recent research by Muthuramalingam et al. (2019) has sought to fill this gap only with certain limitations. The work of Muthuramalingam et al. (2019)

derives their conclusions from a numerical simulation with only a qualitative experimental validation. They identify certain underlying flow structures but lack the detailed exploration of the variations across the scale array that are needed to fully understand the mechanics of the underlying flow behaviour. They only describe the velocity results in a small region over the scale array. As such, a comprehensive in-depth experimental investigation of the near wall boundary layer flow is required to advance the knowledge and understanding of the formation mechanisms related to the unique flow structures, and determine the role these flow behaviours have on potential surface drag reduction.

The specific scope of this objective is to:

- Develop an experimental facility for measuring the flow behaviour over structured surfaces.
- Provide an in-depth experimental analysis of the velocities and flow structures formed over a circular scale array.
- Determine the fundamental mechanisms driving the unique flow behaviour.

1.3.1.2 Impact of scale shape

Fish skin characterization techniques have been successful in detailing the variations in scale size and shape as they are linked to various factors including species, flow environment, and region on the fish body. Research on the drag reduction potential of fish scale surfaces has largely focused on individual scale geometries replicated from nature by the respective authors. The lack of geometry standardization in the current fish scale drag reduction research, and the gap in the physical understanding of scale shape variations highlighted by Wainwright and Lauder (2017) motivates this topic of research. Understanding how fish scale geometry impacts the observed flow behaviours is the first step in optimization of fish scale design.

Thus, the specific scope of this objective is to:

- Develop and validate a numerical model for simulation of flow over biomimetic fish scale array surfaces.

- Explore the impact of scale shape on the flow behaviours and array performance.
- Evaluate the impact of Reynolds number on the flow over fish scale arrays.

1.3.2 Thesis Organization

This thesis is structured in an integrated article format such that Chapter 2 and Chapter 3 are standalone papers which will be submitted for publication. The content of this thesis is structured as follows:

- Chapter 1 provides a background into the importance of drag reduction research and discusses the theory involved in the laminar, transitional, and turbulent flow regimes. A summary of friction drag reduction techniques using both active and passive approaches is provided. A more detailed exploration of fish scales as a technique for drag reduction highlights potential areas for improvement. The knowledge gaps in the current scientific literature are discussed, which is followed by the outline of the objectives of the present research work.
- Chapter 2 details the experimental work investigating the fundamental physics of the near wall flow behaviour over the fish scale array. This includes a short introduction highlighting the background and relevant literature, the development of the experimental testing facility, description of the measurement technique, and the detailed analysis of the velocity results over the scale array to reveal the physics of the underlying flow behaviours. Finally, exploratory work investigating the impact of Reynolds number on the flow patterns is presented.
- Chapter 3 contains the numerical exploration of the influence of scale geometry on the observed flow behaviours. This includes a short introduction with the relevant background and literature, description and validation of the numerical model, details of different scale geometries, an analysis of the impact of scale geometry, and finally a discussion on the impact of varying Reynolds number on the performance of the scale arrays.
- Chapter 4 summarizes the findings from this research and provides recommendations for future work.

Bibliography

- Abbas, A., Bugada, G., Ferrer, E., Fu, S., Periaux, J., Pons-Prats, J., Valero, E., & Zheng, Y. (2017). Drag reduction via turbulent Boundary Layer Flow Control. *Science China Technological Sciences*, *60*(9), 1281–1290. <https://doi.org/10.1007/s11431-016-9013-6>
- Ahmad, H., Baig, M. F., & Fuaad, P. A. (2015). Numerical investigation of turbulent-drag reduction induced by active control of streamwise travelling waves of wall-normal velocity. *European Journal of Mechanics - B/Fluids*, *49*, 250–263. <https://doi.org/10.1016/j.euromechflu.2014.09.004>
- Anderson, E. J., McGillis, W. R., & Grosenbaugh, M. A. (2001). The boundary layer of swimming fish. *Journal of Experimental Biology*, *204*(1), 81–102. <https://doi.org/10.1242/jeb.204.1.81>
- Andersson, P., Brandt, L., Bottaro, A., & Henningson, D. S. (2001). On the breakdown of boundary layer streaks. *Journal of Fluid Mechanics*, *428*, 29–60. <https://doi.org/10.1017/s0022112000002421>
- Asidin, M. A., Suali, E., Jusnukin, T., & Lahin, F. A. (2019). Review on the applications and developments of drag reducing polymer in turbulent pipe flow. *Chinese Journal of Chemical Engineering*, *27*(8), 1921–1932. <https://doi.org/10.1016/j.cjche.2019.03.003>
- Auteri, F., Baron, A., Belan, M., Campanardi, G., & Quadrio, M. (2010). Experimental assessment of drag reduction by traveling waves in a turbulent pipe flow. *Physics of Fluids*, *22*(11), 115103. <https://doi.org/10.1063/1.3491203>
- Barthlott, W., & Neinhuis, C. (1997). Purity of the sacred Lotus, or escape from contamination in biological surfaces. *Planta*, *202*(1), 1–8. <https://doi.org/10.1007/s004250050096>
- Bechert, D. W., & Bartenwerfer, M. (1989). The viscous flow on surfaces with longitudinal ribs. *Journal of Fluid Mechanics*, *206*, 105–129. <https://doi.org/10.1017/s0022112089002247>
- Bechert, D. W., Bruse, M., & Hage, W. (2000). Experiments with three-dimensional riblets as an idealized model of shark skin. *Experiments in Fluids*, *28*(5), 403–412. <https://doi.org/10.1007/s003480050400>
- Bechert, D. W., Bruse, M., Hage, W., Van Der Hoeven, J. G., & Hoppe, G. (1997). Experiments on drag-reducing surfaces and their optimization with an adjustable geometry. *Journal of Fluid Mechanics*, *338*, 59–87. <https://doi.org/10.1017/s0022112096004673>
- Berger, T. W., Kim, J., Lee, C., & Lim, J. (2000). Turbulent boundary layer control utilizing the Lorentz force. *Physics of Fluids*, *12*(3), 631–649. <https://doi.org/10.1063/1.870270>
- Bergman, T. L., & Lavine, A. S. (2017). Laminar and Turbulent Flow. In *Fundamentals of heat and mass transfer* (8th ed., p. 353). Wiley.

- Bixler, G. D., & Bhushan, B. (2013). Fluid drag reduction with shark-skin riblet inspired microstructured surfaces. *Advanced Functional Materials*, 23(36), 4507–4528. doi:10.1002/adfm.201203683
- Breuer, K. S., Park, J., & Henoeh, C. (2004). Actuation and control of a turbulent channel flow using Lorentz forces. *Physics of Fluids*, 16(4), 897–907. https://doi.org/10.1063/1.1647142
- Burdak, V. D. (1986). Morphologie fonctionnelle du tegument ecailleux des poissons. *Cybiurn*, 10, 1-128.
- Burger, E. D., Munk, W. R., & Wahl, H. A. (1982). Flow increase in the Trans Alaska pipeline through use of a polymeric drag-reducing additive. *Journal of Petroleum Technology*, 34(02), 377–386. https://doi.org/10.2118/9419-pa
- Chen, H., Rao, F., Shang, X., Zhang, D., & Hagiwara, I. (2013). Biomimetic drag reduction study on herringbone riblets of Bird Feather. *Journal of Bionic Engineering*, 10(3), 341–349. https://doi.org/10.1016/s1672-6529(13)60229-2
- Choi, K.-S., & Clayton, B. R. (2001). The mechanism of turbulent drag reduction with wall oscillation. *International Journal of Heat and Fluid Flow*, 22(1), 1–9. https://doi.org/10.1016/s0142-727x(00)00070-9
- Choi, K.-S., DeBisschop, J.-R., & Clayton, B. R. (1998). Turbulent boundary-layer control by means of spanwise-wall oscillation. *AIAA Journal*, 36, 1157–1163. https://doi.org/10.2514/3.13948
- Cossu, C., & Brandt, L. (2004). On Tollmien–Schlichting-like waves in streaky boundary layers. *European Journal of Mechanics - B/Fluids*, 23(6), 815–833. https://doi.org/10.1016/j.euromechflu.2004.05.001
- Dean, B., & Bhushan, B. (2010). Shark-skin surfaces for fluid-drag reduction in turbulent flow: A Review. *Philosophical Transactions of the Royal Society A: Mathematical, Physical and Engineering Sciences*, 368(1929), 4775–4806. https://doi.org/10.1098/rsta.2010.0201
- Dou, Z., Wang, J., & Chen, D. (2012). Bionic research on fish scales for drag reduction. *Journal of Bionic Engineering*, 9(4), 457–464. https://doi.org/10.1016/s1672-6529(11)60140-6
- Du, Y., & Karniadakis, G. E. (2000). Suppressing wall turbulence by means of a transverse traveling wave. *Science*, 288(5469), 1230–1234. https://doi.org/10.1126/science.288.5469.1230
- Duncan, W. J., Thom, A. S., & Young, A. D. (1985). *Mechanics of Fluids*. Arnold.
- Feng, L., Li, S., Li, Y., Li, H., Zhang, L., Zhai, J., Song, Y., Liu, B., Jiang, L., & Zhu, D. (2002). Super-hydrophobic surfaces: From natural to Artificial. *Advanced Materials*, 14(24), 1857–1860. https://doi.org/10.1002/adma.200290020
- Fish, F. E., Weber, P. W., Murray, M. M., & Howle, L. E. (2011). The tubercles on humpback whales' flippers: Application of bio-inspired technology. *Integrative and Comparative Biology*, 51(1), 203–213. https://doi.org/10.1093/icb/icr016

- Fransson, J. H. M. (2015). Transition to turbulence delay using a passive flow control strategy. *Procedia IUTAM*, *14*, 385–393. <https://doi.org/10.1016/j.piutam.2015.03.018>
- Fransson, J. H., & Talamelli, A. (2012). On the generation of steady streamwise streaks in flat-plate boundary layers. *Journal of Fluid Mechanics*, *698*, 211–234. <https://doi.org/10.1017/jfm.2012.80>
- Fransson, J. H., Brandt, L., Talamelli, A., & Cossu, C. (2005). Experimental study of the stabilization of Tollmien–Schlichting waves by finite amplitude streaks. *Physics of Fluids*, *17*(5), 054110. <https://doi.org/10.1063/1.1897377>
- Fuaad, P. A., Baig, M. F., & Khan, B. A. (2016). Turbulent drag reduction using active control of buoyancy forces. *International Journal of Heat and Fluid Flow*, *61*, 585–598. <https://doi.org/10.1016/j.ijheatfluidflow.2016.07.003>
- Geim, A. K., Dubonos, S. V., Grigorieva, I. V., Novoselov, K. S., Zhukov, A. A., & Shapoval, S. Y. (2003). Microfabricated adhesive mimicking gecko foot-hair. *Nature Materials*, *2*(7), 461–463. <https://doi.org/10.1038/nmat917>
- Ghaemi, S. (2020). Passive and active control of turbulent flows. *Physics of Fluids*, *32*(8), 080401. <https://doi.org/10.1063/5.0022548>
- Government of Canada. (2022, July 28). *Energy Production*. Provincial and Territorial Energy Profiles – Canada. Retrieved January 30, 2023, from <https://www.cer-rec.gc.ca/en/data-analysis/energy-markets/provincial-territorial-energy-profiles/provincial-territorial-energy-profiles-canada.html>
- Government of Canada. (2022, December 6). *Energy Supply and demand, 2021*. The Daily. Retrieved January 30, 2023, from <https://www150.statcan.gc.ca/n1/daily-quotidien/221206/dq221206e-eng.htm>
- Hamner, W. M. (1979). [Review of *Nekton.*, by Y. G. Aleyev]. *Limnology and Oceanography*, *24*(6), 1173–1175. <http://www.jstor.org/stable/2835593>
- Heidarian, A., Ghassemi, H., & Liu, P. (2018). Numerical Analysis of the effects of riblets on drag reduction of a flat plate. *Journal of Applied Fluid Mechanics*, *11*(3), 679–688. <https://doi.org/10.29252/jafm.11.03.28344>
- Hou, J.-M., Shi, G.-F., Li, L., Li, Hong-da, & Xia, Mingqiang. (2021). Analysis of the influence of pit unit arrangement on the drag reduction performance of fish-scale pits. *Journal of Physics: Conference Series*, *1885*(2), 022029. <https://doi.org/10.1088/1742-6596/1885/2/022029>
- Huang, L., Fan, B., & Dong, G. (2010). Turbulent drag reduction via a transverse wave traveling along streamwise direction induced by Lorentz force. *Physics of Fluids*, *22*(1), 015103. <https://doi.org/10.1063/1.3291071>
- Ibañez, A. L., Cowx, I. G., & O'Higgins, P. (2009). Variation in elasmoid fish scale patterns is informative with regard to taxon and swimming mode. *Zoological Journal of the Linnean Society*, *155*(4), 834–844. <https://doi.org/10.1111/j.1096-3642.2008.00465.x>

- Joseph, R., Kumar, P. P., & Diwan, S. S. (2022). Characterization of streak development for boundary layer transition caused by isolated and distributed roughness. <https://doi.org/10.21203/rs.3.rs-1940022/v1>
- Kachanov, Y. S. (2006). Routes of boundary-layer transition. *Solid Mechanics and Its Applications*, 95–104. https://doi.org/10.1007/978-1-4020-4150-1_9
- Karniadakis, G. E., & Choi, K.-S. (2003). Mechanisms on transverse motions in turbulent wall flows. *Annual Review of Fluid Mechanics*, 35(1), 45–62. <https://doi.org/10.1146/annurev.fluid.35.101101.161213>
- Klumpp, S., Meinke, M., & Schröder, W. (2010). Drag reduction by Spanwise Transversal Surface Waves. *Journal of Turbulence*, 11. <https://doi.org/10.1080/14685248.2010.494606>
- Klumpp, S., Meinke, M., & Schröder, W. (2011). Friction drag variation via Spanwise Transversal Surface Waves. *Flow, Turbulence and Combustion*, 87(1), 33–53. <https://doi.org/10.1007/s10494-011-9326-3>
- Koeltzsch, K., Dinkelacker, A., & Grundmann, R. (2002). Flow over convergent and divergent wall riblets. *Experiments in Fluids*, 33(2), 346–350. <https://doi.org/10.1007/s00348-002-0446-3>
- Kundu, P. K., Dowling, D. R., & Cohen, I. M. (2016). *Fluid mechanics* (6th ed.). Elsevier.
- Kuusipalo, L. (1998). Scale morphology in malawian cichlids. *Journal of Fish Biology*, 52(4), 771–781. <https://doi.org/10.1111/j.1095-8649.1998.tb00819.x>
- Laadhari, F., Skandaji, L., & Morel, R. (1994). Turbulence reduction in a boundary layer by a local spanwise oscillating surface. *Physics of Fluids*, 6(10), 3218–3220. <https://doi.org/10.1063/1.868052>
- Lauder, G. V., Wainwright, D. K., Domel, A. G., Weaver, J. C., Wen, L., & Bertoldi, K. (2016). Structure, biomimetics, and fluid dynamics of fish skin surfaces. *Physical Review Fluids*, 1(6). <https://doi.org/10.1103/physrevfluids.1.060502>
- Lee, J.-H., & Sung, H. J. (2005). Response of a spatially developing turbulent boundary layer to a spanwise oscillating Electromagnetic Force. *Journal of Turbulence*, 6. <https://doi.org/10.1080/14685240500293977>
- Leschziner, M. A. (2020). Friction-drag reduction by transverse wall motion – A Review. *Journal of Mechanics*, 36(5), 649–663. <https://doi.org/10.1017/jmech.2020.31>
- Lighthill, M. J. (1971). Large-amplitude elongated-body theory of fish locomotion. *Proceedings of the Royal Society of London. Series B. Biological Sciences*, 179(1055), 125–138. <https://doi.org/10.1098/rspb.1971.0085>
- Liu, G., Yuan, Z., Qiu, Z., Feng, S., Xie, Y., Leng, D., & Tian, X. (2020). A brief review of bio-inspired Surface Technology and application toward underwater drag reduction. *Ocean Engineering*, 199, 106962. <https://doi.org/10.1016/j.oceaneng.2020.106962>

- Liu, M., & Ma, L. (2022). Drag reduction methods at solid-liquid interfaces. *Friction*, *10*(4), 491–515. <https://doi.org/10.1007/s40544-021-0502-8>
- Lumley, J. L. (1969). Drag reduction by Additives. *Annual Review of Fluid Mechanics*, *1*(1), 367–384. <https://doi.org/10.1146/annurev.fl.01.010169.002055>
- Lumley, J. L. (1973). Drag reduction in turbulent flow by polymer additives. *Journal of Polymer Science: Macromolecular Reviews*, *7*(1), 263–290. <https://doi.org/10.1002/pol.1973.230070104>
- Malik, M., Liao, W., Li, F., & Choudhari, M. (2015). Discrete-roughness-element-enhanced swept-wing natural laminar flow at high Reynolds Numbers. *AIAA Journal*, *53*(8), 2321–2334. <https://doi.org/10.2514/1.j053637>
- Mamori, H., & Fukagata, K. (2011). Drag reduction by streamwise traveling wave-like Lorenz Force in channel flow. *Journal of Physics: Conference Series*, *318*(2), 022030. <https://doi.org/10.1088/1742-6596/318/2/022030>
- Mosghani, M. M., Alidoostan, M. A., & Binesh, A. (2021). Numerical analysis of drag reduction of fish scales inspired ctenoid-shape microstructured surfaces. *Chemical Engineering Communications*, 1–16. <https://doi.org/10.1080/00986445.2021.1992398>
- Muthuramalingam, M., Puckert, D. K., Rist, U., & Bruecker, C. (2020). Transition delay using biomimetic fish scale arrays. *Scientific Reports*, *10*(1). <https://doi.org/10.1038/s41598-020-71434-8>
- Muthuramalingam, M., Villemin, L. S., & Bruecker, C. (2019). Streak formation in flow over biomimetic fish scale arrays. *Journal of Experimental Biology*. <https://doi.org/10.1242/jeb.205963>
- Nakanishi, R., Mamori, H., & Fukagata, K. (2012). Relaminarization of turbulent channel flow using traveling wave-like wall deformation. *International Journal of Heat and Fluid Flow*, *35*, 152–159. <https://doi.org/10.1016/j.ijheatfluidflow.2012.01.007>
- Ou, J., Perot, B., & Rothstein, J. P. (2004). Laminar drag reduction in microchannels using ultrahydrophobic surfaces. *Physics of Fluids*, *16*(12), 4635–4643. <https://doi.org/10.1063/1.1812011>
- Ou, J., & Rothstein, J. P. (2005). Direct velocity measurements of the flow past drag-reducing ultrahydrophobic surfaces. *Physics of Fluids*, *17*(10), 103606. <https://doi.org/10.1063/1.2109867>
- Oweis, G. F., Winkel, E. S., Cutbrith, J. M., Ceccio, S. L., Perlin, M., & Dowling, D. R. (2010). The mean velocity profile of a smooth-flat-plate turbulent boundary layer at high Reynolds number. *Journal of Fluid Mechanics*, *665*, 357–381. <https://doi.org/10.1017/s0022112010003952>
- Pang, J., & Choi, K.-S. (2004). Turbulent drag reduction by Lorentz force oscillation. *Physics of Fluids*, *16*(5). <https://doi.org/10.1063/1.1689711>

- Parfitt, A. R., & Vincent, J. F. (2005). Drag reduction in a swimming Humboldt penguin, *Spheniscus humboldti*, when the boundary layer is turbulent. *Journal of Bionic Engineering*, 2(2), 57-62. doi:10.1007/bf03399481
- Quadrio, M., & Ricco, P. (2011). The laminar generalized stokes layer and turbulent drag reduction. *Journal of Fluid Mechanics*, 667, 135–157. <https://doi.org/10.1017/s0022112010004398>
- Quadrio, M., Ricco, P., & Viotti, C. (2009). Streamwise-travelling waves of spanwise wall velocity for turbulent drag reduction. *Journal of Fluid Mechanics*, 627, 161–178. <https://doi.org/10.1017/s0022112009006077>
- Reshotko, E., & Tumin, A. (2006). Application of transient growth theory to bypass transition. *Solid Mechanics and Its Applications*, 83–93. https://doi.org/10.1007/978-1-4020-4150-1_8
- Ricco, P. (2011). Laminar streaks with spanwise wall forcing. *Physics of Fluids*, 23(6), 064103. <https://doi.org/10.1063/1.3593469>
- Roggenkamp, D., Jessen, W., Li, W., Klaas, M., & Schröder, W. (2015). Experimental investigation of turbulent boundary layers over transversal moving surfaces. *CEAS Aeronautical Journal*, 6(3), 471–484. <https://doi.org/10.1007/s13272-015-0155-2>
- Sagong, W., Kim, C., Choi, S., Jeon, W.-P., & Choi, H. (2008). Does the sailfish skin reduce the skin friction like the shark skin? *Physics of Fluids*, 20(10), 101510. <https://doi.org/10.1063/1.3005861>
- Schlatter, P., Deusebio, E., de Lange, R., & Brandt, L. (2010). Numerical Study of the stabilisation of boundary-layer disturbances by finite amplitude streaks. *International Journal of Flow Control*, 2(4), 259–288. <https://doi.org/10.1260/1756-8250.2.4.259>
- Schlichting (Deceased), H., & Gersten, K. (2018). Fundamentals of Boundary-Layer Theory. In *Boundary-layer theory* (9th ed., pp. 29–50). Springer Berlin.
- Schlichting (Deceased), H., & Gersten, K. (2018). Fundamentals of Turbulent Flows. In *Boundary-layer theory* (9th ed., p. 499). Springer Berlin.
- Schlichting (Deceased), H., & Gersten, K. (2018). Introduction. In *Boundary-layer theory* (9th ed., pp. XXI - XXV). Springer Berlin.
- Schlichting (Deceased), H., & Gersten, K. (2018). Onset of Turbulence (Stability Theory). In *Boundary-layer theory* (9th ed., pp. 418 - 419). Springer Berlin.
- Shahinfar, S., Sattarzadeh, S. S., & Fransson, J. H. M. (2014). Passive boundary layer control of oblique disturbances by finite-amplitude streaks. *Journal of Fluid Mechanics*, 749, 1–36. <https://doi.org/10.1017/jfm.2014.211>
- Sindagi, S., & Vijayakumar, R. (2020). Succinct review of MBDR/BDR technique in reducing ship's drag. *Ships and Offshore Structures*, 16(9), 968–979. <https://doi.org/10.1080/17445302.2020.1790296>

- Sudo, S., Tsuyuki, K., Ito, Y., & Ikohagi, T. (2002). A Study on the Surface Shape of Fish Scales. *JSME International Journal Series C*, 45(4), 1100-1105. doi:10.1299/jsmec.45.1100
- Tabor, M., & Gennes, P. G. (1986). A cascade theory of drag reduction. *Europhysics Letters (EPL)*, 2(7), 519–522. <https://doi.org/10.1209/0295-5075/2/7/005>
- Tamano, S., & Itoh, M. (2012). Drag reduction in turbulent boundary layers by spanwise traveling waves with wall deformation. *Journal of Turbulence*, 13. <https://doi.org/10.1080/14685248.2012.655743>
- Tomiyaama, N., & Fukagata, K. (2013). Direct numerical simulation of drag reduction in a turbulent channel flow using spanwise traveling wave-like wall deformation. *Physics of Fluids*, 25(10), 105115. <https://doi.org/10.1063/1.4826887>
- Tong, Q., Peng, G., Nan-Sheng, L., & Xi-Yun, L. (2008). Turbulent boundary layer control via a streamwise travelling wave induced by an external force. *Chinese Physics Letters*, 25(10), 3700–3703. <https://doi.org/10.1088/0256-307x/25/10/050>
- U.S. Energy Information Administration. (2022, June 28). *Energy use for transportation*. Use of energy for transportation in depth. Retrieved February 1, 2023, from <https://www.eia.gov/energyexplained/use-of-energy/transportation-in-depth.php> U.S. Energy
- United States Department of Transportation. (2022, Sept. 8). *U.S. energy consumption by the transportation sector*. Bureau of Transportation Statistics. Retrieved February 1, 2023, from <https://www.bts.gov/content/us-energy-consumption-transportation-sector>
- Velcro, S. A. (1955). Improvements in or relating to a method and a device for producing a velvet type fabric. Patent no. 721 338 Switzerland.
- Virk, P. S. (1975). Drag reduction fundamentals. *AIChE Journal*, 21(4), 625–656. <https://doi.org/10.1002/aic.690210402>
- Wainwright, D. K., & Lauder, G. V. (2016). Three-dimensional analysis of scale morphology in bluegill sunfish, *Lepomis macrochirus*. *Zoology*, 119(3), 182–195. <https://doi.org/10.1016/j.zool.2016.02.006>
- Wainwright, D. K., & Lauder, G. V. (2017). Mucus matters: The slippery and complex surfaces of fish. *Biologically-Inspired Systems*, 223–246. https://doi.org/10.1007/978-3-319-74144-4_10
- Wainwright, D. K., Karan, E. A., & Collar, D. C. (2022). Evolutionary patterns of scale morphology in damselfishes (Pomacentridae). *Biological Journal of the Linnean Society*, 135(1), 138–158. <https://doi.org/10.1093/biolinlean/blab140>
- Walters, V. (1963). The trachipterid integument and an hypothesis on its hydrodynamic function. *Copeia*, 1963(2), 260. <https://doi.org/10.2307/1441341>
- White, F. M. (2016). Flow Past Immersed Bodies. In *Fluid mechanics* (8th ed., p. 453). McGraw-Hill.

- White, F. M. (2016). Flow Past Immersed Bodies. In *Fluid mechanics* (8th ed., p. 455). McGraw-Hill.
- White, F. M. (2016). Flow Past Immersed Bodies. In *Fluid mechanics* (8th ed., p. 459). McGraw-Hill.
- White, F. M. (2016). Flow Past Immersed Bodies. In *Fluid mechanics* (8th ed., p. 460). McGraw-Hill.
- White, F. M. (2016). Flow Past Immersed Bodies. In *Fluid mechanics* (8th ed., p. 461). McGraw-Hill.
- White, F. M. (2016). Flow Past Immersed Bodies. In *Fluid mechanics* (8th ed., p. 462). McGraw-Hill.
- White, F. M. (2016). Flow Past Immersed Bodies. In *Fluid mechanics* (8th ed., p. 465). McGraw-Hill.
- White, F. M. (2016). Flow Past Immersed Bodies. In *Fluid mechanics* (8th ed., p. 471). McGraw-Hill.
- White, F. M. (2016). Flow Past Immersed Bodies. In *Fluid mechanics* (8th ed., p. 476). McGraw-Hill.
- White, F. M. (2006). The Stability of Laminar Flows. In *Viscous Fluid Flow* (3rd ed., p. 377). McGraw-Hill.
- White, F. M. (2016). Viscosity and Other Secondary Properties. In *Fluid mechanics* (8th ed., p. 25). McGraw-Hill.
- White, F. M. (2016). Viscous Flow in Ducts. In *Fluid mechanics* (8th ed., p. 342). McGraw-Hill.
- White, F. M. (2016). Viscous Flow in Ducts. In *Fluid mechanics* (8th ed., p. 354). McGraw-Hill.
- White, F. M. (2016). Viscous Flow in Ducts. In *Fluid mechanics* (8th ed., p. 355). McGraw-Hill.
- White, F. M. (2016). Viscous Flow in Ducts. In *Fluid mechanics* (8th ed., p. 356). McGraw-Hill.
- Wood, R. M. (2004). Impact of advanced aerodynamic technology on Transportation Energy Consumption. *SAE Technical Paper Series*. <https://doi.org/10.4271/2004-01-1306>
- Wu, L. Y., Jiao, Z. B., Song, Y. Q., Ren, W. T., Niu, S. C., & Han, Z. W. (2017). Water-trapping and drag-reduction effects of fish ctenopharyngodon idellus scales and their simulations. *Science China Technological Sciences*, *60*(7), 1111–1117. <https://doi.org/10.1007/s11431-016-0630-x>
- Xi, L. (2019). Turbulent drag reduction by polymer additives: Fundamentals and recent advances. *Physics of Fluids*, *31*(12), 121302. <https://doi.org/10.1063/1.5129619>
- Xu, M., Grabowski, A., Yu, N., Kerezyte, G., Lee, J.-W., Pfeifer, B. R., & Kim, C.-J. (2020). Superhydrophobic drag reduction for turbulent flows in Open water.

Physical Review Applied, 13(3).

<https://doi.org/10.1103/physrevapplied.13.034056>

- Xu, P., & Choi, K.-S. (2008). Boundary layer control for drag reduction by Lorentz forcing. *IUTAM Symposium on Flow Control and MEMS*, 259–265. https://doi.org/10.1007/978-1-4020-6858-4_31
- Yanase, K., & Saarenrinne, P. (2016). Boundary Layer Control by a fish: Unsteady laminar boundary layers of rainbow trout swimming in turbulent flows. *Biology Open*, 5(12), 1853–1863. <https://doi.org/10.1242/bio.020008>
- Yang, X., Wang, J., Jiang, B., Li, Z., & Xiao, Q. (2021). Numerical study of effect of sawtooth riblets on low-Reynolds-number airfoil flow characteristic and aerodynamic performance. *Processes*, 9(12), 2102. <https://doi.org/10.3390/pr9122102>
- Ybert, C., Barentin, C., Cottin-Bizonne, C., Joseph, P., & Bocquet, L. (2007). Achieving large slip with superhydrophobic surfaces: Scaling laws for generic geometries. *Physics of Fluids*, 19(12), 123601. <https://doi.org/10.1063/1.2815730>
- Zhang, L., Shan, X., & Xie, T. (2020). Active control for wall drag reduction: Methods, mechanisms and performance. *IEEE Access*, 8, 7039–7057. <https://doi.org/10.1109/access.2020.2963843>

Chapter 2

2 Experimental Investigation into the Fundamental Flow Behaviour over Biomimetic Fish Scale Arrays

2.1 Introduction

All objects moving through a surrounding fluid will generate a boundary layer close to the fluid-surface interface. This boundary layer arises due to the viscosity of the fluid and the no-slip condition at the surface boundary or ‘the wall’ (Schlichting & Gersten, 2018). An object’s frictional resistance to motion is dictated by the wall shear stress that exists within the boundary layer at the wall (Schlichting & Gersten, 2018). Additionally, the conditions of the boundary layer (laminar or turbulent) are found to influence the velocity gradient at the wall, the stability of the boundary layer against flow separation, and the additional shear stresses within the boundary layer which all contribute to the friction drag experienced by the object (Schlichting & Gersten, 2018). In many cases, a reduction in the friction drag is desirable as this will decrease the energy required to keep the object in motion.

Given a laminar boundary layer contains a lower wall shear stress and skin friction coefficient compared to a turbulent boundary layer, a delay in the transition to turbulence is often desired to reduce friction drag. The benefits of decreased skin friction often outweigh the greater resistance to flow separation which is intrinsic in a turbulent boundary layer (Schlichting & Gersten, 2018). Thus, when targeting drag reduction in the laminar and transitional flow regimes, mechanisms consist of either delaying the transition to turbulence or modifying the wall shear stress component directly.

The transportation sector accounts for about 28% (U.S. Energy Information Administration, 2022) and 23% (Government of Canada, *Energy Production*, 2022) of energy consumption in the United States (US) and Canada, respectively. Despite technological advances in fuel efficiency, energy consumption by the transportation sector in the US has remained stagnant around 28% since 2001 (United States Department of Transportation, 2022), while the transportation sector in Canada saw a 5%

increase in consumption in 2021 (Government of Canada, *Energy Supply and Demand*, 2022). While there are several factors contributing to energy consumption in transportation, Wood (2004) estimated that 16% of the total energy consumed in the United States is used to overcome aerodynamic drag in transportation systems. Further to this, it is estimated that frictional drag accounts for about 20% of total vehicular aerodynamic drag (Wood, 2004), about 50% of an aircraft's drag (Abbas et al., 2017; Malik et al. 2015), and up to 80% of a ship's total resistance (Sindagi & Vijayakumar, 2020). As such, it is evident that methods to reduce friction drag have the potential to provide significant reductions in energy consumption in the transportation sector.

Many researchers have focused on methods of friction drag reduction through the development of either active or passive mechanisms (Abbas et al., 2017; Zhang, 2020; Fish & Lauder, 2006). Active methods such as jet- or plasma-actuators, wall-motion, wall deformation, and micro-vibrations have shown the potential to reduce friction drag by up to approximately 20-30% (Abbas et al., 2017), 30-40% (Leschziner, 2020), 70% (Nakanishi et al., 2012), and 50% (Bai et al., 2014), respectively. Although these drag reduction methods have shown promising results, the drawback of active systems is that they require active control and additional energy input. In contrast, passive drag reduction methods interact naturally with the surrounding fluid, often making them a desirable solution.

Passive and active methods of drag reduction also often draw inspiration from nature, utilizing the fundamental physics associated with intricate biomimetic features. For example, the use of hydrophobic materials entraps air bubbles at the wall boundary resulting in fluid slip and a reduction in the shear stress and net drag on the body (Ou et al., 2004 from Yu et al. 2020). Hydrophobic coatings were inspired by the lotus effect found on lotus leaves and provide additional self-cleaning properties beneficial for anti-fouling applications (Bhushan et al., 2009). Other examples of biomimetic features include the unique feathers around the beak of penguins that have been investigated for their role in inducing a turbulent boundary layer (Parfitt & Vincent, 2005), and the tubercles on the flippers of Humpback whales which have been found to induce vortices within the boundary layer and improve swimming performance (Fish et al., 2011).

Further work understanding the purpose of biological features has the potential to reveal promising findings that can inform the design of engineered surfaces focused on drag reduction.

One example of this is the application of shark skin denticles for drag reduction in turbulent flow (Dean & Bhushan, 2010; Bixler & Bhushan, 2013; Heidarian et al., 2018). Dean and Bhushan (2010) summarized research investigating optimal riblet geometries and size to spacing ratios which showed that a drag reduction of 9.9% was achieved experimentally in an open channel flow with blade riblets (Bechert et al., 1997). Additionally, Koeltzsch et al. (2002) examined the effect of converging and diverging riblet patterns on the bulk flow behaviors and found that a divergent riblet pattern results in an increased mean flow velocity and decreased velocity fluctuations. Bixler and Bhushan (2013) and Dean and Bhushan (2010) both discuss one mechanism by which shark skin riblets reduce drag as the lifting and pinning of vortices within the turbulent boundary layer, decreasing the wetted area over which these vortices interact. More recently, Heidarian et al. (2018) completed a numerical analysis comparing blade, sawtooth, and scalloped riblets with different spacing ratios and found that smaller riblets produced greater drag reduction due to their ability to prevent vortices from falling in the riblets valleys. They also highlight that a maximum drag reduction of 11% could be achieved using a sawtooth riblet with a height to spacing ratio of 0.5. Yang et al. (2021) explored the application of sawtooth riblets on airfoils numerically and found that the most effective riblet length was 0.8 chords and led to a maximum drag reduction of 15% under all angles of attack studied. While the research on shark skin riblets has shown promising results in turbulent flow, little work has been done on the biomimetic features of smaller and slower fish to understand the significance of their surface topographies in laminar boundary layers.

Fish skin characterization techniques have been used to develop a deeper understanding of the fish scale size and shape between species and different regions on an individual fish (Wainwright et al., 2022; Sudo et al., 2002; Ibañez et al., 2009). Wainwright and Lauder (2016) utilized a novel GelSight technology to develop 3D topographical images of the Bluegill Sunfish and found that scale height, size, and shape can vary significantly

in different regions of the fish. They also highlight that while little work has focused on the hydrodynamic significance of fish scales, the variations in size and shape may play a fundamental role in modifying the flow behaviour over the fish skin.

Wainwright and Lauder (2017) highlighted that early work on fish scales was largely hypothetical (Walters, 1963; Hamner, 1979; Burdak, 1986) with little quantitative results. More recently, Sagong et al. (2008) explored numerically, the possibility that sailfish skin could reduce drag under turbulent flow conditions. They found that while the skin friction was reduced in some cases, the total drag was found to be larger than a smooth surface. Dou et al. (2012) explored the drag reduction over a bionic surface with micro-scale caves modeled after fish scales. They found a 10% drag reduction experimentally and explored the mechanism of entrapped air using a multiphase flow simulation. Additionally, Wu et al. (2017) reported a drag reduction of about 2.8% compared to a flat plate when simulating crescent-like ridges (modeled after the grass carp fish scales), in a laminar boundary layer numerically. They hypothesized the crescent-like structures created a water-trapping effect leading to a spread-wetting phenomenon that played a role in the drag reduction. While these studies focused on modelling fish scales as individual features, they often misrepresent the physical nature of the scales on a fish.

Muthuramalingam et al. (2019) identified the need to explore the fish scale shapes not as individual elements but rather as 3D overlapping arrays. They modeled their scale array after the European seabass and completed a numerical analysis, validated only using flow visualization techniques. Their simulation results revealed evidence of near wall velocity streaks aligned with the scales and they hypothesized their role in delaying the transition to turbulence. To test this hypothesis, Muthuramalingam et al. (2020) studied the effect of these scale arrays on the downstream transition to turbulence using induced Tollmien-Schlichting (T-S) waves. They found that the scale arrays resulted in the attenuation of TS waves and the ability to delay the transition to turbulence leading to a maximum theoretical friction drag reduction of about 27%. They speculated that the velocity streaks formed over the scale array contribute to the stabilizing effect of the boundary layer through a smaller spanwise averaged shape factor, with little explanation as to how the spanwise averaged shape factor was calculated. Additionally, their fundamental

understanding of the streaky base flow that is generated over the scale arrays is largely based on numerical results. To the authors' knowledge, there has been no fundamental experimental analysis of the flow over the fish scale arrays, seeking to understand how the velocity streaks are generated.

2.2 Motivation and Objectives

Thus, the present study aims to use a 3D biomimetic fish scale array with overlapping features to experimentally investigate the flow behaviour and near wall velocity streaks within the boundary layer over the scale array. The detailed analysis over the scale array will provide insight into the mechanisms leading to the observed flow behaviors and provide a foundational understanding of the flow over these scale arrays. The motivation for this work is driven by the lack of understanding of the hydrodynamic function of these 3D fish scale arrays and the desire to utilize their fundamental mechanisms in commercial drag reduction applications such as those targeting the transportation sector.

2.3 Methodology

The following methodology section will describe the experimental setup, surface design, and Particle Imaging Velocimetry (PIV) technique used for this analysis. The final part of the methodology section will show the results characterizing the background channel flow without the structured surface.

2.3.1 Experimental Setup

The experimental facility used to conduct these experiments consisted of a recirculating water channel with a 2-hp centrifugal pump capable of producing flow rates up to 130 GPM. An open channel allows for a free surface flow to develop through the test section which contains a total cross-sectional area of $10\text{ cm} \times 15\text{ cm}$ and length of 90 cm. This cross-sectional area allows for channel velocities up to about 0.5 m/s. The bottom and sides of the test section are made from clear acrylic for optical access, and a schematic of the water channel is shown in Figure 8.

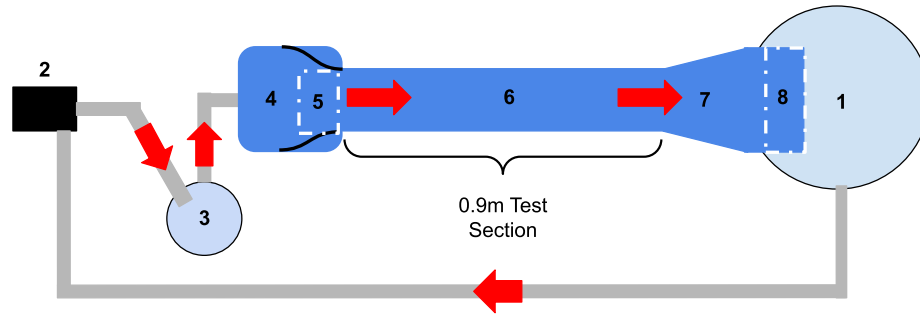


Figure 8: Schematic of the water channel. 1) Outlet water reservoir; 2) 2-hp Pump; 3) Inlet settling chamber; 4) Inlet; 5) Contraction and flow conditioning section; 6) Test section; 7) Diffusion outlet section; 8) Weir gate.

A two-stage inlet labeled as 3 and 4 in Figure 8, was adopted to dissipate turbulent fluctuations introduced in the pump and allow the flow in the channel to be driven by gravity. The first stage of the inlet (labeled 3) is filled from above by the pump and flows to the second stage of the inlet (labeled 4) from a height of about 5 cm above the channel bottom. The second stage of the inlet (labeled 4) extends 28 cm below the height of the channel bottom and is filled from below. Within the second stage of the inlet, a contraction section using a 5th order polynomial (equation 2.1) profile (Lakshman & Basak, 2018 from Bell and Mehta, 1988) was used to reduce the cross-sectional area of the flow while maintaining flow uniformity and preventing flow separation. Flow conditioning consisted of a combination of 20 & 80 mesh per inch wire screens placed before the contraction section, and a 0.5-inch-thick honeycomb core with 0.125-inch cell size along with a 20 mesh per inch wire screen after the contraction section (shown in region labeled 5 in Figure 8). A 6 cm weir gate was located at the end of the outlet section (labeled 8 in Figure 8) to maintain a water height of 8 cm within the test section.

$$y(x) = H_{inlet} - (H_{inlet} - H_{outlet}) * \left[6 \left(\frac{x}{L} \right)^5 - 15 \left(\frac{x}{L} \right)^4 + 10 \left(\frac{x}{L} \right)^3 \right] \quad (2.1)$$

Within the 90 cm test section, a sample mounting arm (shown in Figure 9) was used to hold the structured sample within the channel from above. The sample mounting arm consists of an upright support that holds a curved leading edge, a 10 cm long flat plate entrance length, and the 16 cm long structured surface. This mounting arm was secured

onto an independent support structure that was built around the water channel. A curved leading edge was used to prevent flow separation from affecting the boundary layer growth over the flat plate and scale array (Fransson, 2004; Hanson et al., 2012; Bhatia et al., 2020). The formation of a flow separation bubble behind the leading edge is a common problem with boundary layer experiments at or near zero-incidence (Smith et al., 2021; Fujiwara et al., 2020). The curved leading edge contains a radius of curvature of about 36.5 mm, an approximate arc length of 2 cm, and an estimated aspect ratio of 4:1. Due to the curvature, the definition of the leading-edge position is the point at which the leading-edge plate becomes flat. The sample mounting arm was constructed such that the height of the structured sample was 5 cm from the bottom of the channel, and the leading edge was located 55 cm from the entrance of the 90 cm test section. The smooth surface and structured sample have a combined total length of 26 cm and a width of 8 cm. Appendix A contains a more detailed analysis of the channel modifications, flow conditioning, and sample mounting arm iterations.

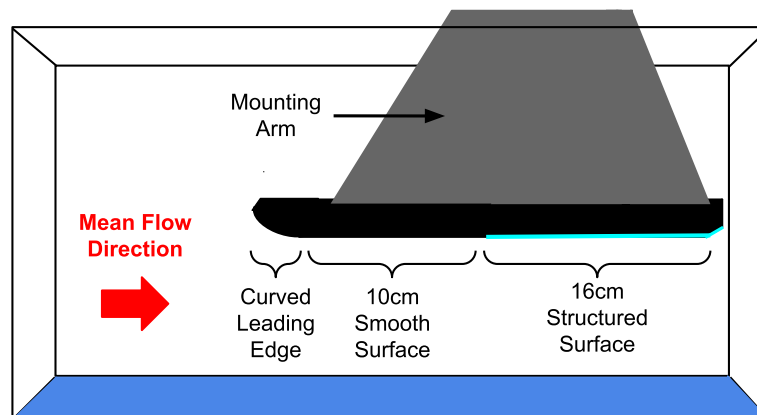


Figure 9: Schematic of the sample mounting arm.

2.3.2 Surface Design

As mentioned above, fish skin characterization techniques have enabled detailed analysis of the variations found between species and within different regions of the fish body (Wainwright & Lauder, 2016; Sudo et al., 2002; Ibañez et al., 2009). Due to the overlapping nature of the scales, only a portion at the back of the fish scale is exposed to the oncoming fluid, and it is the size and shape of this exposed area that is important from

a hydrodynamics perspective. Fish scales have been classified into the following four categories based on their shape and general scale features: Placoid, Ganoid, Ctenoid, and Cycloid (see Figure 10).

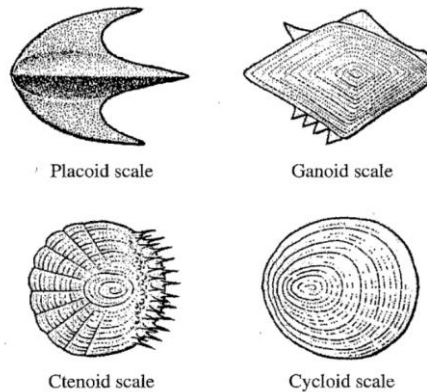


Figure 10: Different scale shapes (Sudo et al., 2002).

While the placoid scale is commonly found in sharks and has been shown to reduce drag in turbulent flow (Bechert et al., 2000), the other three scale geometries are more common in bony fish (Friedman, 2012), and limited work has been reported to understand their role from hydrodynamics perspective. Variations in scale shape between species and regions of the fish raise questions about the importance of scale geometry on hydrodynamic performance (Wainwright & Lauder, 2016). However, before one can understand how scale shape affects the hydrodynamic performance, there needs to be a deep understanding of the role and purpose of the traditional (circular) fish scale. Given that there is a lack of detailed experimental investigation and characterization of the near wall flow over fish scale arrays, this study will target a single (circular) scale geometry to develop the foundational knowledge which can be helpful in analyzing other scale geometries as well.

A common practice in hydrodynamic and aerodynamic research is scaling experimental models up or down, using the scaling laws (White, pp. 285–325, 2016), to characterize experimental phenomena that happen on an observable scale. For the present study, all length scales were scaled up by a factor of eight such that geometric similarity was maintained. To ensure similar flow conditions between the scale model and the actual

flow conditions, dynamic similarity would need to be maintained (White, p. 317, 2016). To maintain dynamic similarity, the non-dimensional values for the Reynolds number based on boundary layer thickness (equation 2.2) (White, p. 25, 2016) and the boundary layer thickness to scale height ratio (equation 2.3) were kept within the same order of magnitude. These scaling parameters were also used in Muthuramalingam et al. (2019 and 2020).

$$Re_{BL} = \frac{U_{\infty} \delta_{BL}}{\nu} \quad (2.2)$$

$$\theta_{ratio} = \frac{\delta_{BL}}{l_{sh}} \quad (2.3)$$

As mentioned in Wainwright and Lauder (2017), the undulatory fish swimming motion makes the characterization of the boundary layer over fish skin a particularly challenging task. Early theories by Lighthill (1971) suggest that undulatory motion causes alternating thin boundary layers with higher shear stress compared to a rigid plate boundary layer. More recently, Anderson et al. (2001) studied the boundary layer at several locations over two fish species with different undulatory motions and found that when swimming in still water, the boundary layer always suggested a laminar profile with no separation. Additionally, Yanase and Saarenrinne (2016) examined the unsteady boundary layer of a swimming rainbow trout and found that flow over the pectoral and pelvic regions¹ was most similar to laminar flow, while flow separation was delayed until the vortex shedding occurred in the posterior (rear) region of the fish. While there is still much to learn about the boundary layers over swimming fish, these studies highlight that the boundary layer generated over small and medium sized fish is best represented by a laminar boundary layer.

As mentioned earlier, a circular scale geometry was selected and was modeled after the Bluegill sunfish dimensions given in Wainwright and Lauder (2016). The swimming speed of the Bluegill sunfish and other similar fish is important for determining the non-dimensional parameters for scaling. Flammang and Lauder (2008) found that the speed of

¹ Regions located midway between head and tail on the mid-side and under-side, respectively.

a Bluegill Sunfish is dependent on the swimming mode where 0.5, 1.2, and 2.0 length per second corresponds to slow pectoral fin swimming, regular rhythmic undulations, and rapid body undulations, respectively. With a mean length of 0.17 m, the corresponding velocities for the Bluegill sunfish are all below 0.4 m/s (Flammang & Lauder, 2008). Other small fish which have a similar circular scale geometries such as the juvenile sea bass and grass carp larvae can reach speeds up to 0.7 m/s (Claireaux et al., 2006) and 0.6 m/s (George et al., 2018), respectively. Muthuramalingam et al. (2019) and Anderson (2005) also highlighted that although the fish shape approximates an airfoil, the laminar boundary layer thickness provides a good estimation for the order of magnitude of the boundary layer thickness over the fish body. Thus, following a similar process to Muthuramalingam et al. (2019) while assuming the critical swimming speeds to be between 0.4 - 0.8 m/s, and a length scale in the first 50% of the fish length (2 cm - 8 cm), the corresponding order of the boundary layer thickness was found to be 1 mm.

Using a geometry scaling factor of eight, the overall scale array contains 9 scales along the length and 4 scales across the width (8 cm wide by 16 cm long). To ensure the Reynolds number based on boundary layer thickness, and boundary layer thickness to scale height ratio were maintained within the same order of magnitude, the leading-edge length and fluid velocity were modified. Table 2 shows a summary of the original and scaled parameters used for the experiments.

Table 2: Scale Geometry Parameters

Parameter	Original	Scaled (8x)
Scale radius	1.75 mm	14 mm
Scale height	0.1 mm	0.8 mm
Streamwise offset	2 mm	16 mm
Spanwise offset	2.5 mm	20 mm
Free-stream velocity	~ 0.4 - 0.8 m/s	0.12 m/s
Leading edge length	~ 0.02 - 0.08 m	0.1 m
Re_{BL}	~ 500	550
θ_{ratio}	~ 10	5.6

The scale array used for testing was 3D printed using an industrial Stereo-Lithography (SLA) 3D printer with a layer height of 0.025 mm and in-plane tolerance of 0.02 mm. The scale array was printed with a 5 mm thick base and was mounted to the overhead mounting arm with adhesive such that there were minimal disturbances between the flat plate and the entrance of the scale array. Figure 11 shows the 3D model of the scale geometry and a photograph of the 3D printed scale array used for testing.

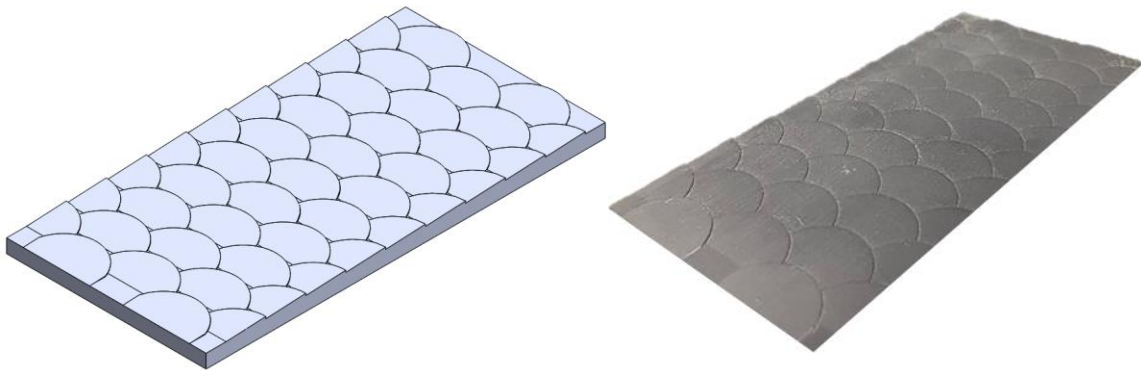


Figure 11: (Left) CAD model of scale array and (Right) photograph of the 3D printed scale array used for testing.

2.3.3 PIV Technique

The planar PIV technique was used to measure the two-dimensional velocity fields over the sample surface within the test section of the water channel. PIV measurements were conducted in separate experimental runs and in several horizontal and vertical measurement planes relative to the scale geometry. Figure 12 shows the PIV setup i.e., the configuration of the camera, laser head, and optics which allowed for PIV measurements in multiple horizontal and vertical planes.

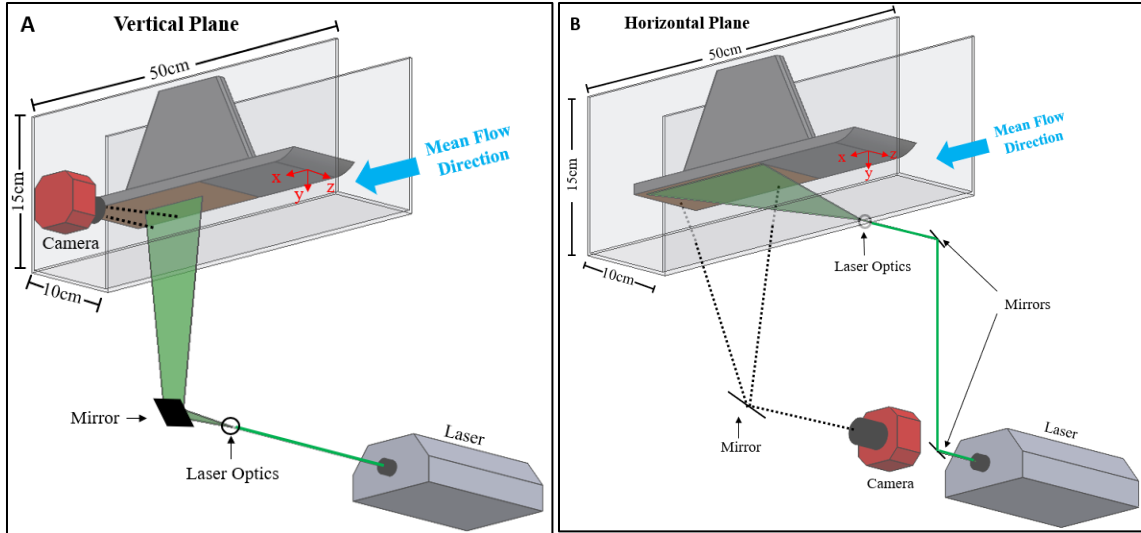


Figure 12: PIV Laser and camera setup for (A) vertical plane and (B) horizontal plane measurements.

The reference coordinate system is located at the center of the leading edge with the positive x -axis in the downstream direction over the plate, the positive y -axis away from the plate, and the positive z -axis towards the right wall of the channel (Figure 12). To capture the wall normal variations in the boundary layer, measurements were conducted on three vertical streamwise planes corresponding to the centerline ($z = 0$ cm), midline ($z = 0.7$ cm) and overlapping ($z = 1$ cm) planes (see green lines in Figure 13), measuring the u - and v -velocity components in the x - y plane. To characterize the flow behavior in the near wall region, measurements were conducted on eight horizontal planes corresponding to heights of $y = 1.3, 1.6, 2.0, 2.5, 3.0, 3.5, 4.0,$ and 5.0 mm, measuring the u - and w -velocity components in the x - z plane (see green lines in Figure 14). Considering the limitations on the camera field of view, measurements in both the horizontal and vertical planes were conducted in different sections relative to the distance from the leading edge such that the flow in the entire surface region could be characterized. The coloured dashed boxes in Figure 13 and Figure 14 show the different measurement regions in the horizontal and vertical planes, respectively. An overlap between the measurement regions in a given plane was considered to enable the patching of the velocity fields in each measurement region to construct the velocity field corresponding to the entire region.

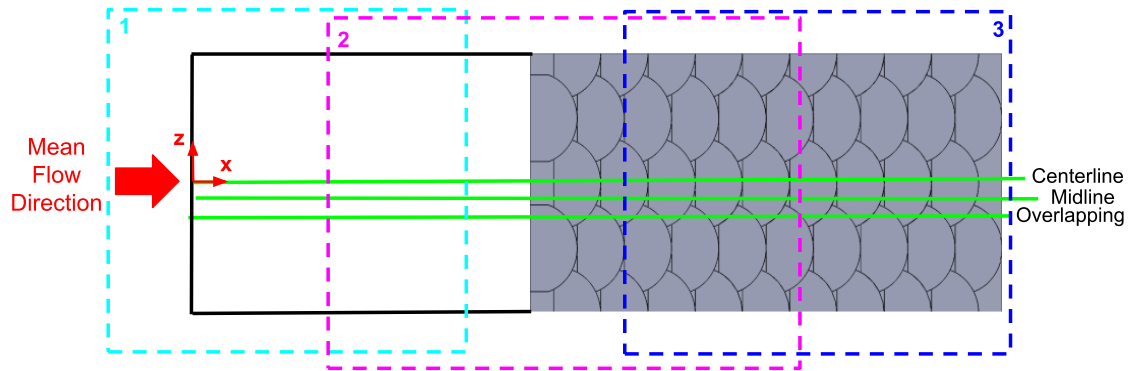


Figure 13: Locations of measurement planes. Green lines represent the spanwise locations of vertical planes: Centerline ($z = 0$ cm), Overlapping ($z = 1$ cm), and Midline ($z = 0.7$ cm). The coloured dashed boxes represent the overlapping fields of view in the horizontal plane measurements: 1 – Leading Edge, 2 – Scales Upstream, 3 – Scales Downstream.

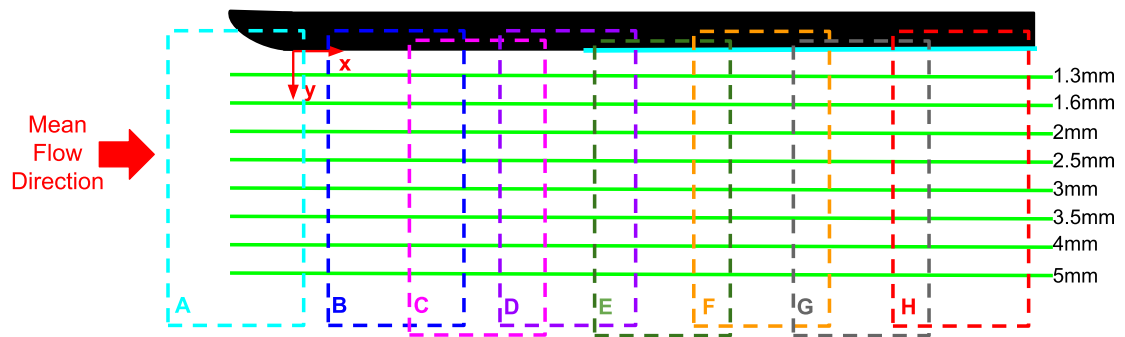


Figure 14: Locations of measurement planes. Green lines represent the vertical locations of horizontal planes varying from 1.3 mm to 5 mm from the surface. The coloured dashed boxes represent the overlapping fields of view in the vertical plane measurements: A – Leading Edge, B – Leading Edge 5 cm, C – Leading Edge 7.5 cm, D – Leading Edge 10 cm, E – Scales #1, F – Scales #2, G – Scales #3, H – Scales #4.

Given measurements in the horizontal plane were taken at different wall normal locations within the boundary layer, aligning and leveling the laser sheet presented one of the largest experimental challenges. A second camera was used along with an alignment sheet to measure the location of the laser sheet relative to the surface at all four corners.

Adjustments were made to the optics to ensure the laser sheet and surface were parallel, and that the laser sheet was at the desired wall normal location. However, given the laser sheet has a finite thickness (approximately 1 mm) and the laser optics cause the thickness of the sheet to vary, it was very difficult to get the measurement plane perfectly aligned. These challenges introduced some asymmetry into the horizontal plane results which should be kept in mind throughout the analysis.

A dual-cavity 120 mJ Nd:YAG laser (120XT 532 nm, SoloPIV) was used for PIV measurements and produced laser illumination at 15 Hz per cavity. A 48-Megapixel camera (Flare, IO industries) with a resolution of 7920×6004 pixels was used to acquire images via an image acquisition system (DVR2 Express CORE, IO Industries). Two camera lenses, 60 mm f/8 and 70-300 mm f/11 (Sigma Corp.) were each used in the vertical and horizontal planes, respectively. A spherical lens with focal length of 747.5 mm was used along with a cylindrical lens with focal length of 9.69 mm to convert the laser beam into a ~ 1 mm thick light sheet. The timing of the laser pulses was controlled using a four-channel pulse generator (555-4C, Berkeley Nucleonics) that was synchronized with the 48-Megapixel camera. The measurements in different horizontal and vertical planes were achieved by adjusting the location of the mirrors and the laser optics manually. The water in the channel was seeded using silver coated hollow glass spheres (Conduct-o-fil, Potters Industries)² through direct mixing in the water reservoir. Water was allowed to circulate for a minimum of two minutes before placing the structured surface in the water channel, and another two minutes before starting PIV image recording to ensure a uniform flow and steady state boundary layer formed over the flat plate and structured surface.

A minimum of 4,000 images (2,000 image pairs) were captured for each experiment at a rate of 15Hz using the frame-straddling technique. The laser pulses were timed using the delay generator such that the time between each image in a given pair ranged between 0.2 ms in the vertical streamwise plane, and 1 ms in the horizontal planes. The recorded PIV

² Mean diameter of 13 μm and density of 16 g/cc.

images were exported to an external hard drive for processing using a desktop computer and MATLAB. Prior to PIV processing, image enhancement operations such as image distortion correction, background subtraction, and contrast adjustment were completed to enhance the raw PIV images and reduce the signal to noise ratio. The use of a 70-300 mm macro zoom lens on the 200 mm lens setting resulted in a pincushion image distortion³ in the raw PIV images for the horizontal plane measurements. Thus, a single parameter 3rd order polynomial model was used to correct for radially symmetric distortions in MATLAB (Jaap de Vries, 2012). This simplified polynomial model is based off the famous Brown-Conrady distortion model proposed in 1966 (Clarke & Fryer, 1998), and as Zhang (1998) suggests, it assumes that distortion is a function of radial components dominated by the first term. The standard model was selected over the alternative division model because it works best with small levels of distortion (Wang et al., 2009). Correction was done by adjusting the distortion factor until grid calibration images were returned to normal for each experiment. Background subtraction was completed by calculating the mean or minimum images of the entire dataset and subtracting them from the individual images. The minimum background was subtracted for all vertical tests, and the mean was only used for horizontal heights of 1.3 mm and 1.6 mm as there was a stronger background influence. Finally, contrast adjustment enabled modification of the image histogram such that the entire image range was utilized.

Image pairs were processed using a standard PIV cross-correlation code developed by Marxen (1998) to obtain instantaneous velocity fields. The MATLAB implementation of the code uses a Fast Fourier Transform (FFT) cross-correlation with 50% overlap. It makes use of square interrogation windows between 32×32 pixels and 64×64 pixels, and corresponding search windows between 64×64 pixels and 128×128 pixels. To estimate pixel shifts with a sub-pixel resolution, a 2×3 Gaussian sub-pixel estimator (Marxen, 1998) is used, as it is more commonly implemented (Thielicke & Stamhuis, 2014; Thielicke, 2014; Liberzon et al., 2021) than other sub-pixel estimators such as

³ Where magnification increases with distance from the central axis (Encyclopedia Britannica, 1998).

those from Lourenco and Krothapalli (1995), Roesgen (2003), and Nobach and Honkanen (2005). Finally, a local median filter was used to identify and correct outliers in the velocity vector fields, and an Adaptive Gaussian Window (AGW) scheme was implemented to interpolate the velocity vectors onto a regular grid.

For all horizontal plane measurements an interrogation window size of 64×64 pixels was used with a spatial resolution of 0.605 mm/vector. In the vertical plane, full field measurements utilized a 48×48 pixel interrogation window with a spatial resolution of 0.125 mm/vector. To capture the near wall flow dynamics, a smaller image size was captured (7920×1500 pixels) and processed using a 64×64 pixel interrogation window and spatial resolution of 0.16 mm/vector. Within this near wall dataset, images were also cropped to the region directly behind the scale height and processed using a 32×32 pixel interrogation window with spatial resolution of 0.08 mm/vector. The cropped dataset would enable detailed characterization of the flow directly behind the scale heights, while the near wall dataset would allow analysis along the entire length of the scale in the near wall region.

The uncertainty associated with the digital PIV velocity computation was estimated based on the errors associated with particle size, AGW interpolation, image dynamic range, and out-of-plane motion. The uncertainty estimation in the velocity was based on the approach developed by Cowen and Monismith (1997). Appendix B contains the detailed analysis of the PIV uncertainty calculations and a qualitative discussion of the uncertainty associated with the velocity gradients and the seed density. The total maximum resultant velocity error due to the PIV measurement process was calculated for all experiments to be ± 0.617 cm/s or $\pm 5.05\%$ of the free-stream velocity at 0.12 m/s. This represents the velocity error in the instantaneous velocity due to the PIV measurement process. The uncertainty associated with the repeatability of the velocity measurements within the channel will be discussed in the channel flow results section.

2.3.4 Channel Flow Results

Before analyzing the flow over the structured surface, it was important to characterize the mean and turbulent characteristics of the channel flow without the surface to ensure that

the free-stream flow expected in the vicinity of the structured surface is uniform. These channel velocity measurements were taken at 55 cm from the entrance of the test section, which is the location of the leading edge of the surface. The PIV measurements were taken in the mid-vertical plane at $z = 0$ cm, and in the horizontal plane at a height of 5 cm from the bottom of the channel, which is the position where the structured surface is to be located. Note, although these measurements were taken relative to the location of the leading edge, the mounting arm and surface were not placed in the channel during these measurements.

To ensure the repeatability of the velocity measurements within the channel, a series of measurements were conducted over the course of one day to capture the flow consistency due to shutting down and restarting the pump that supplied water to the channel. Given that each measurement was conducted in a separate trial, the repeatability error of the channel would be a good estimate for the error in mean results. Six measurements were conducted in both the horizontal and vertical planes independently, and the spatial average value of the mean velocity and turbulence intensity in the region near the sample were used to calculate a 95% confidence interval. Table 3 shows the average values and associated 95% confidence intervals for the velocity and turbulence intensity values.

Table 3: Repeatability mean and 95% confidence intervals for channel velocity measurements.

Parameter	Mean Value	95% Confidence Interval
Horizontal Mean Velocity (m/s)	0.120	± 0.003
Vertical Mean Velocity (m/s)	0.118	± 0.005
Horizontal Turbulence Intensity (%)	3.23	± 1.07
Vertical Turbulence Intensity (%)	4.47	± 0.67

The mean streamwise velocity and turbulent intensity profiles in vertical and horizontal planes are presented in Figure 15 and Figure 16, respectively. As the figures show, the mean velocity and turbulence intensity behaviors are uniform in the regions near the virtual location of the surface. The velocity in the vertical and horizontal planes matches within the uncertainty identified above and shows a mean streamwise velocity of about

0.12 m/s. The turbulent intensity profiles show similar trends. Across the width of the sample and at the height near the sample surface, the turbulent intensity is nearly uniform. The magnitude of the turbulent intensity is found to vary between the horizontal and vertical planes; however, the values are within the uncertainty range identified above. It is important to note that in the horizontal plane, the boundary layers formed on the channel walls are found to influence the flow near the edges of the plate. As such, only the center region from $z \approx -2.6$ cm to $z \approx 2.6$ cm will be used for the horizontal plane analysis as this region is not affected by the boundary layer from the channel wall. The corresponding area over the scales is shown in Figure 16C.

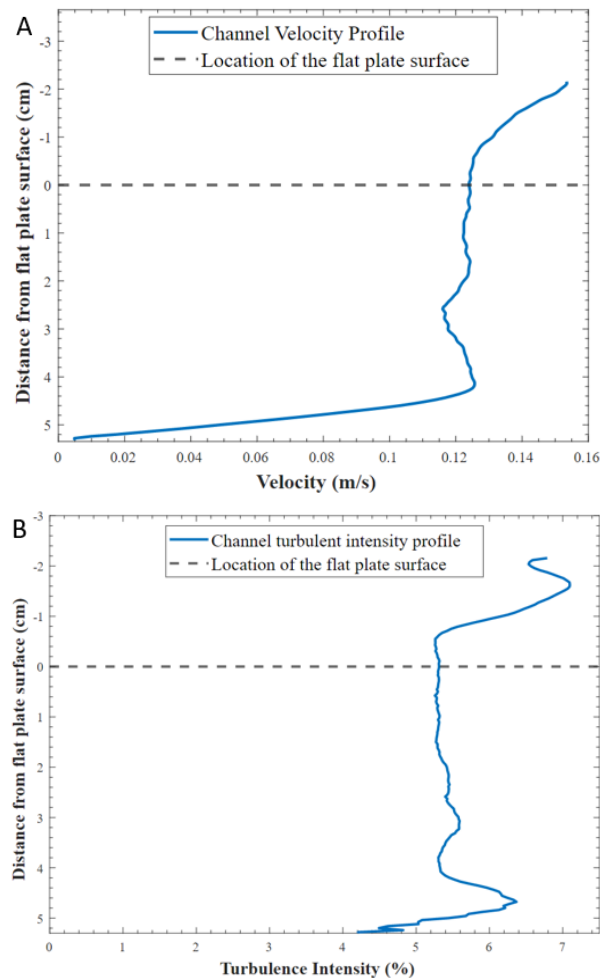


Figure 15: Profiles of the (A) mean streamwise velocity and (B) turbulent intensity, in the mid-vertical plane (at $z = 0$ cm) in the channel (in the absence of the surface).

The virtual location of the surface is marked with the dashed line.

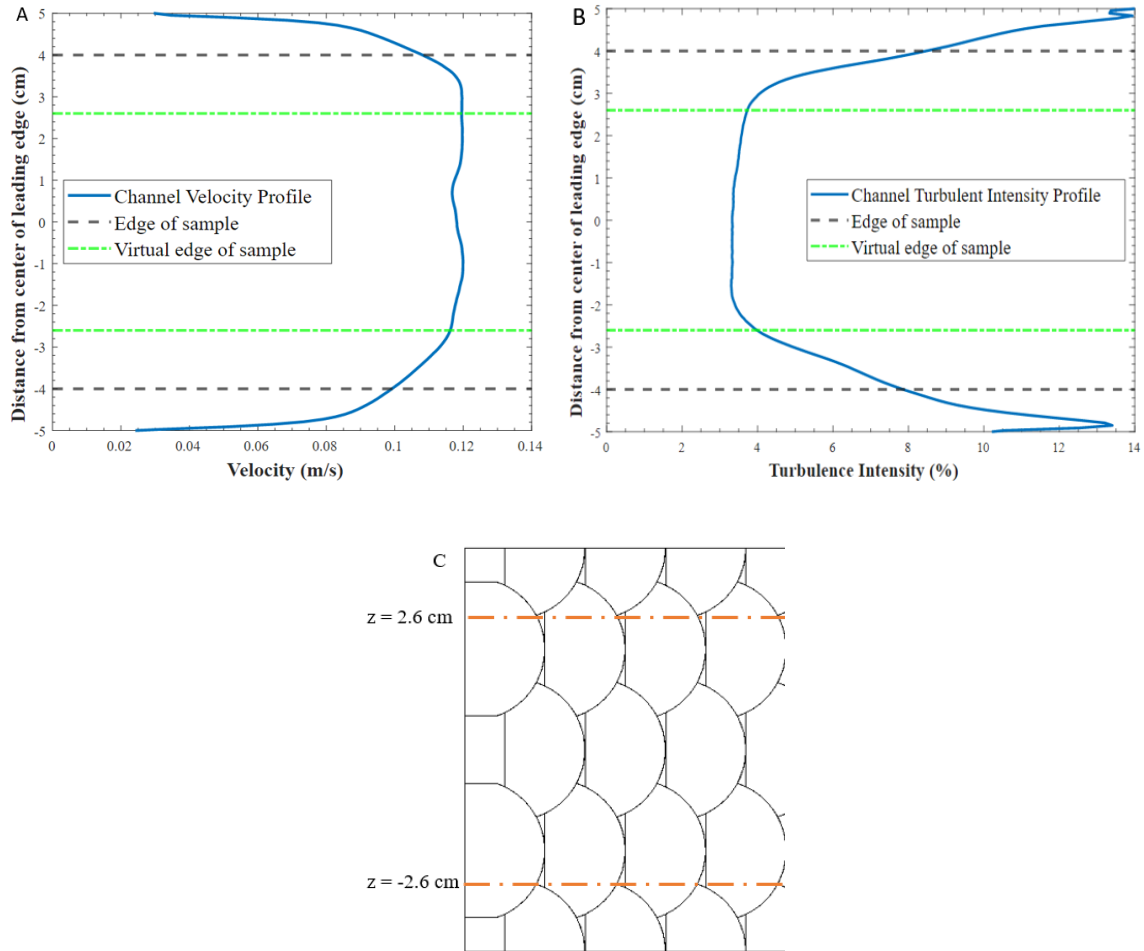


Figure 16: Profiles of the (A) mean streamwise velocity and (B) turbulent intensity, in the horizontal plane at the height of 5 cm from the channel base in the absence of the surface, which corresponds to the virtual location of the surface ($y = 0$ cm). The virtual locations of the surface edges are marked with dashed black lines. (C) The plan view of the structured surface schematic. The dash-dotted lines in (A, B and C) correspond to the region over the surface not impacted by the boundary layers on the channel walls ($z = -2.6$ cm to $z = 2.6$ cm).

In addition to the turbulent intensity, the channel Reynolds number was calculated using the hydraulic diameter (equation 2.4 from White, p. 372, 2016), which was found to be about 19,500 and lies within the turbulent regime for channel flow. This is reinforced by the turbulent intensity profiles throughout the channel indicating a moderate amount of turbulence. However, it is important to note that although the channel flow is turbulent,

the characteristics of the boundary layer that forms over the scale array are dependent on the length scale of the plate and hence, the boundary layer developing over the surface is not necessarily turbulent.

$$D_h = \frac{4 \cdot A_c}{P_w} \quad (2.4)$$

2.4 Results and Discussion

The results presented in this section are broken down into three parts; the first part describes the flow over the upstream region of the structured (fish scales) surface, which comprised of the curved leading surface and the smooth flat surface. The second part describes the flow over the structured surface, where the results in the vertical planes are presented first followed by the results in the horizontal planes. The third part describes exploratory results on the impact of Reynolds number on the flow over the structured surface. As mentioned previously, work by Muthuramalingam et al. (2019) and (2020) showed qualitative evidence of spanwise variations in the streamwise velocity over the scale array. However, their numerical simulations showed the velocity results in only one position over the scale array. A very qualitative assessment of the spanwise velocity component in the overlapping region, and recirculation behind the scale heights were also mentioned with little discussion. As such, the following analysis will provide a detailed investigation of each of these aspects, as well as others that could lead to the formation of these velocity streaks.

2.4.1 Flat Plate Upstream Flow Characterization

Before examining the flow over the scale array, it is important to characterize the flow behaviour over the curved leading edge and smooth flat surface to understand the flow conditions upstream of the scale array. This is important because it will provide a base comparison for the analysis over the scale array. The wall normal streamwise velocity profiles over the flat surface in the mid-vertical plane ($z = 0 \text{ cm}$) at 5 cm, 7.5 cm, and 10 cm downstream of the reference leading edge (see Figure 14 for the coordinates) are presented in Figure 17. The theoretical mean velocity profiles based on the Blasius solution are also presented for reference. The non-dimensional profiles were calculated

by dividing the velocity by the free-stream velocity identified far away from the surface. The height above the surface was normalized by the boundary layer thickness (δ_{99}) found by identifying the height at which 99% of the free-stream velocity is recovered (White, p. 450, 2016). Finally, the root mean squared (RMS) error is calculated using equation 2.5 and was used as a measure of accuracy.

$$RMS\ Error\ (\%) = \sqrt{\frac{\sum_{i=1}^n (u_i - u_{Blasius,i})^2}{n}} \times 100\% \quad (2.5)$$

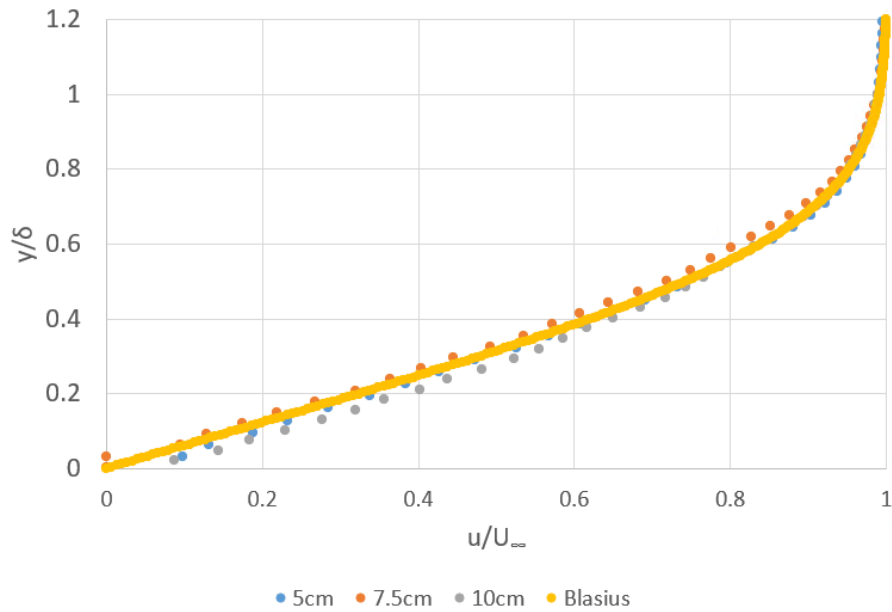


Figure 17: Non-dimensional streamwise velocity profiles at 5 cm, 7.5 cm, and 10 cm from the leading edge ($z = 0$ cm) compared to Blasius solution.

As the results show, the non-dimensional profiles at all three locations show a good agreement with the Blasius solution. Although there is some variation in the profiles throughout the boundary layer, the largest RMS error was found to be 3.14% in the 10 cm from the leading-edge profile. Additionally, the variations between the profiles do not appear to be related to the distance from the leading edge and instead appear random around the Blasius solution. This indicates that a robust laminar boundary layer was formed over the smooth surface upstream of the scale surface closely matching the theoretical Blasius solution. Figure 18 shows the wall normal mean streamwise velocity profiles at 10 cm from the leading edge in three spanwise locations ($z = 0$ cm, $z =$

0.7 cm, and $z = 1$ cm). The results show similar velocity behaviour consistent with the theoretical laminar boundary layer profile.

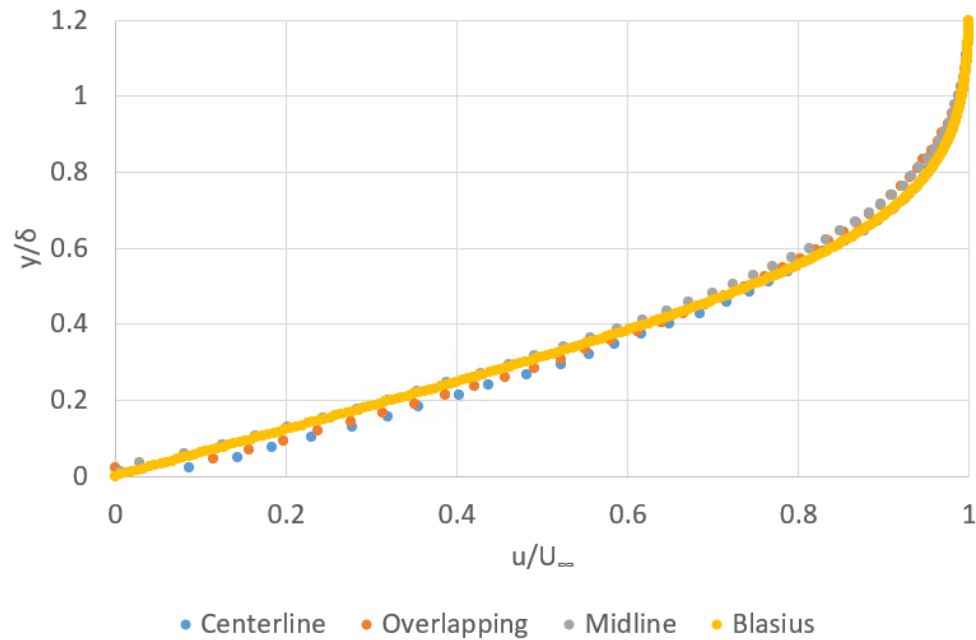


Figure 18: Non-dimensional streamwise velocity profiles 10 cm from the leading edge at $z = 0$ cm, $z = 0.7$ cm, and $z = 1$ cm, corresponding to the centerline, midline, and overlapping planes respectively.

As highlighted above, the non-dimensional velocity profile upstream of the scale array in the three critical scale regions shows a strong resemblance to the Blasius solution. The largest RMS error to the Blasius solution was found to be 3.14% associated with the velocity profile in the centerline region ($z = 0$ cm). Note that these spanwise locations correspond to specific geometrical aspects on the scales where wall normal velocity fields were measured. Hence, the results in Figure 18 confirmed that the flow approaching the scales was a well-established classical laminar boundary layer flow. Thus, when discussing the boundary layer profiles over the scale array, comparison to the Blasius solution will show how the scale array has modified the incoming laminar boundary layer flow.

Given the surface mounting apparatus caused a blockage ratio of about 13% in the channel, and the fact that the boundary layer was growing in a bounded fluid domain, a

flow acceleration was observed over the scale array. Although the experimental setup causes a flow acceleration over the surface, this acceleration is not expected to affect the laminar boundary layer because the local Reynolds number varies from 14,350 to 42,200 from the entrance to the end of the scale array when accounting for the velocity acceleration. Thus, given the agreement between the streamwise velocity profiles and the Blasius solution, as well as the verification that the local Reynolds number remains well below the threshold of 500,000 for transition to turbulence (White, p. 462, 2016), a laminar boundary layer is expected to form over the length of the scale array. Additionally, the Blasius solution should be used as the basis of comparison for wall normal streamwise velocity profiles further downstream.

Finally, given the channel flow was found to be turbulent, there exists the risk that the boundary layer flow is impacted by the free-stream turbulence present in the channel. Fransson and Shahinfar (2020) provide a good review of how free-stream turbulence impacts the boundary layer, and more specifically the transition from laminar to turbulent flow. Most notably, the presence of free-stream turbulence changes the mechanism for disturbance growth from exponentially growing Tollmien-Schlichting waves described by modal stability theory, to algebraically growing unsteady streamwise velocity streaks described by non-modal stability theory (Fransson & Shahinfar, 2020). The investigation of the instantaneous velocity along with streamwise and spanwise RMS velocity fluctuations, revealed that there are no apparent unsteady streaks that are formed over the leading edge. Figure 19 shows the colormaps of the streamwise and spanwise RMS velocity fluctuations indicating that the velocity fluctuations are homogeneous across the plate, leading to the growth of a uniform boundary layer.

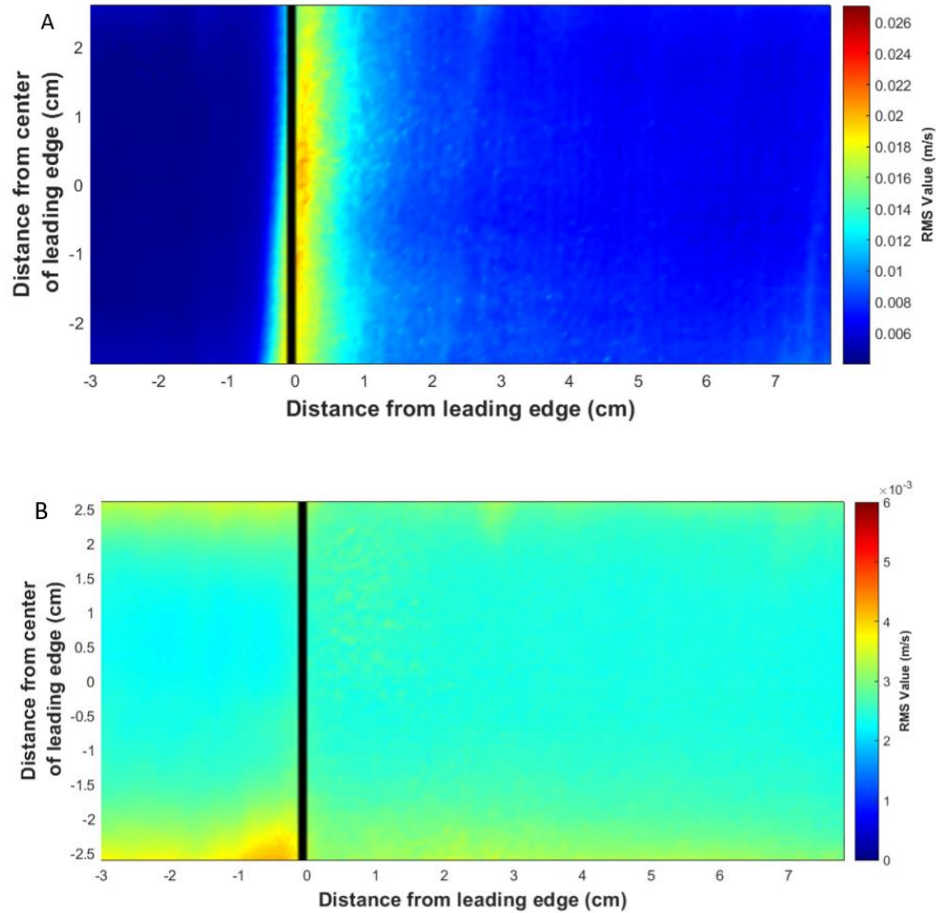


Figure 19: (A) Streamwise and (B) spanwise RMS velocity colourmaps over the leading edge at a wall normal distance of 1.3 mm. Flow is from left to right.

Additionally, Fransson and Shahinfar (2020) show that under different conditions of free-stream turbulence the location of laminar to turbulent flow transition can be moved upstream or downstream. Based on their experimental results, they plotted the Reynolds number based on transition location for different levels of free-stream turbulence. They showed that for free-stream turbulence values up to 5%, the Reynolds number based on transition location remains above 100,000. Given that the local Reynolds number at the end of the scale array was 42,200, this further validates that even in the presence of free-stream turbulence the boundary layer is expected to remain laminar over the length of the scale array.

2.4.2 Vertical Plane Results

To discuss the results over the scale array, a new coordinate system will be defined from the leading edge of the scale array. Each coordinate direction has an appropriate length scale and associated non-dimensional parameter. In the x -direction, the characteristic length is scale length ($l_{sl} = 16$ mm), in the z -direction, it is the physical maximum scale width ($l_{sw} = 26.65$ mm), and in the y -direction, both the boundary layer thickness (δ_{99}) and the maximum scale height ($l_{sh} = 0.8$ mm) are used to define a non-dimensional coordinate. These characteristic lengths are shown in Figure 20.

Given the scale geometry results in a variation in absolute height over the scale length, the height of the surface (y_0) which varies along the length of the scale, was used to normalize the distance from the surface boundary (see Figure 20). This normalized distance was then non-dimensionalized using the maximum scale height (l_{sh}) and the boundary layer thickness (δ_{99}) in equations 2.6 and 2.7. When considering the non-dimensional distance along a single scale (ϕ), the absolute x -position over a single scale was normalized using the absolute x -position at the upstream end of the scale (x_0) (see Figure 20), and non-dimensionalized using the scale length (l_{sl}) in equation 2.8. When discussing the non-dimensional distance (ϕ_t) over the scale array, the absolute x -position is non-dimensionalized using the scale length (l_{sl}) in equation 2.9. Finally, the spanwise location across the scale array is non-dimensionalized using the scale width (l_{sw}) in equation 2.10. For context, the centerline plane ($z = 0$ cm) is located at a $\xi = 0$, the midline plane ($z = 0.7$ cm) is located at $\xi = 0.26$, and the overlapping plane ($z = 1$ cm) is located at $\xi = 0.375$.

$$\lambda_1 = \frac{y - y_0}{l_{sh}} \quad (2.6)$$

$$\lambda_2 = \frac{y - y_0}{\delta_{99}} \quad (2.7)$$

$$\phi = \frac{x - x_0}{l_{sl}} \quad (2.8)$$

$$\phi_t = \frac{x}{l_{sl}} \quad (2.9)$$

$$\xi = \frac{z}{l_{sw}} \quad (2.10)$$

Additionally, a naming convention for the scales is assigned using a double subscript notation to reference each scale in the array. The first subscript corresponds to the scale row in the spanwise direction (-1, 0, or 1), and the second subscript describes the streamwise scale number (1-9). It is also noted that adjacent scale rows have a spanwise offset of $\xi = 0.75$ and streamwise offset of $\phi_t = 0.5$. Figure 20 shows the double subscript notation for all scales and the new coordinate system that is defined for the analysis.

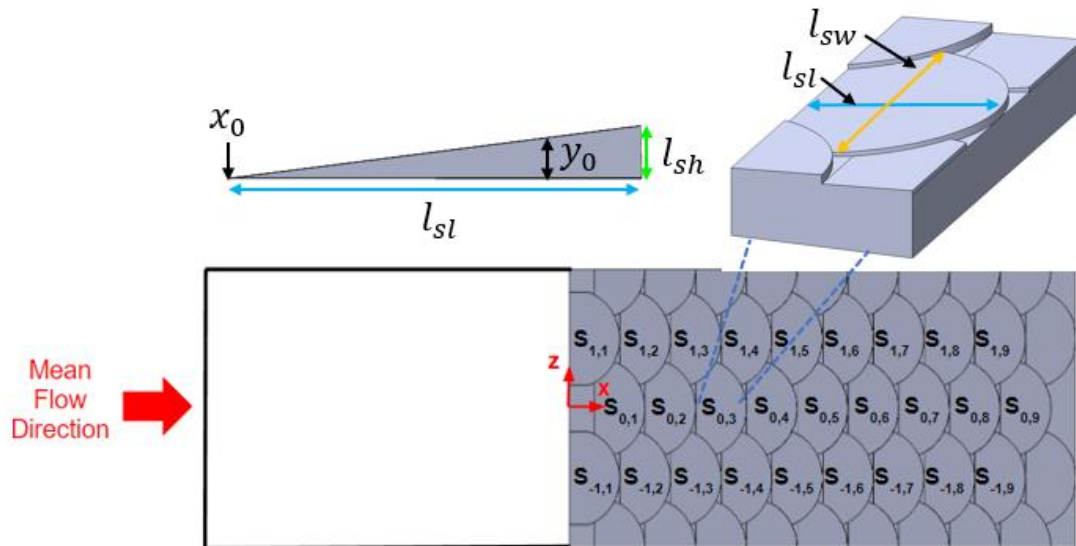


Figure 20: Coordinate system over the scale array. The blue arrow shows the scale length ($l_{sl} = 16$ mm), the orange arrow shows the scale width ($l_{sw} = 26.65$ mm), and the scale height is shown by the green arrow ($l_{sh} = 0.8$ mm). The varying height of the surface (y_0) along with the upstream position of the scale (x_0) are also shown. Scales are identified using double subscript notation where the first subscript corresponds to the spanwise row (-1,0,1), and the second subscript corresponds to the streamwise scale number (1-9).

Results in the vertical plane are presented at three different spanwise locations corresponding to the centerline ($\xi = 0$), midline ($\xi = 0.26$), and the overlapping ($\xi = 0.375$) regions. The vertical plane results in the centerline plane ($\xi = 0$) are presented

first, where a detailed analysis describes the variations over a single scale followed by a discussion on how these results vary in the streamwise direction. After analyzing the profiles along the centerline plane, the results in the midline and overlapping planes will be compared to the centerline plane to understand the three-dimensional flow behavior over a single scale.

2.4.2.1 Centerline Region (Mid-scale plane)

The centerline plane is particularly interesting because it marks the symmetrical line along the scale width and contains the largest wall normal variations in the surface pattern. Given the scale heights appear as abrupt disruptions in an otherwise smooth surface, the rapid changes in height are expected to cause some disruptions to the near wall flow. Figure 21 shows the colormap of the mean streamwise velocity in the centerline plane over scales $S_{0,4}$ and $S_{0,5}$. It is observed that the scale patterns do not cause any visible periodic variations in the overall boundary layer thickness, which indicates that the influence of the scale heights is likely confined to the near wall region within the boundary layer.

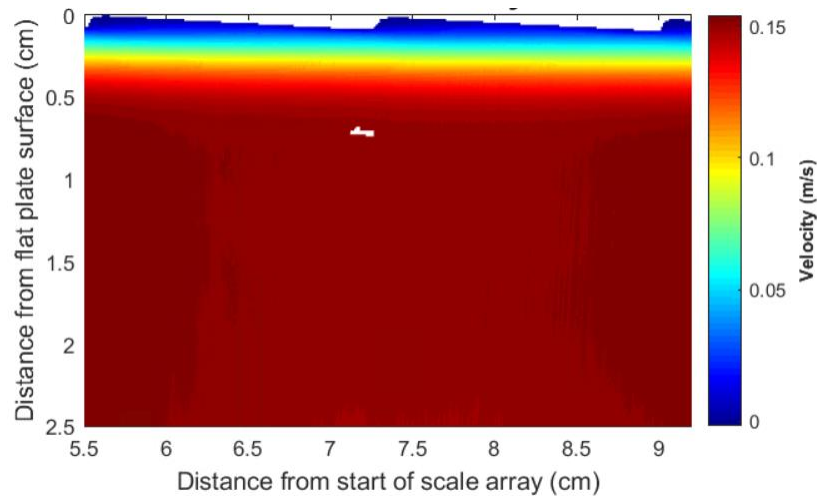


Figure 21: Colormap of the streamwise mean velocity in the mid-vertical plane ($\xi = 0$) over $S_{0,4}$ and $S_{0,5}$. Flow is from left to right.

As discussed earlier, the flow approaching the scale array has an established laminar boundary layer and it is expected that the laminar boundary layer will continue to grow

over the scale array. To investigate the behavior of the boundary layer as it grows over the scale array, the non-dimensional wall normal streamwise velocity profiles over the length of a single scale ($S_{0.5}$) are presented in Figure 22 along with the theoretical laminar boundary layer profile from the Blasius solution.

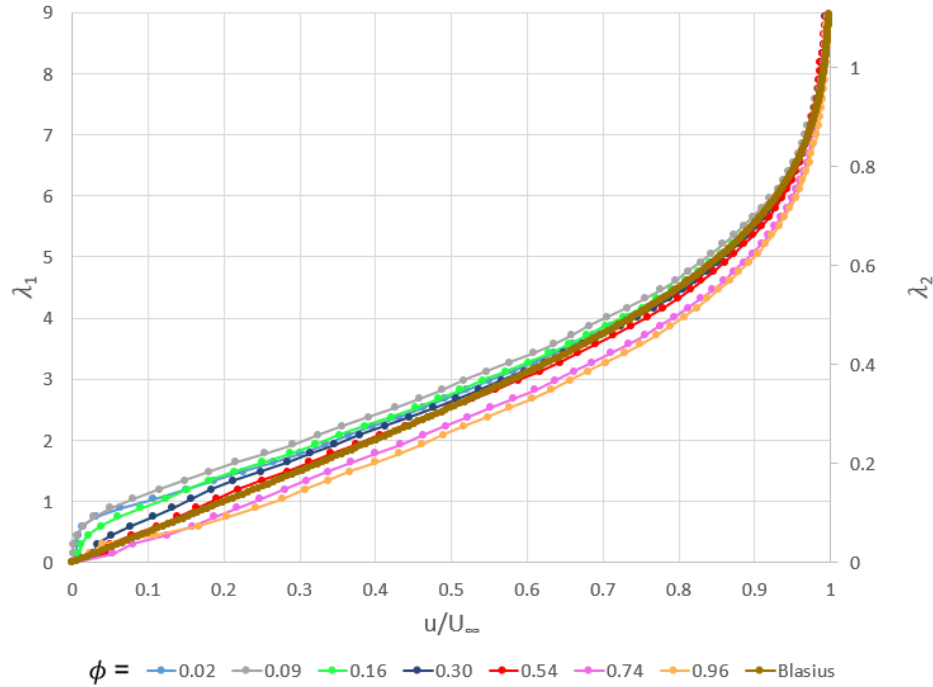


Figure 22: Non-dimensional wall normal mean streamwise velocity profiles for values of ϕ along the length of scale $S_{0.5}$. The velocity profile from the Blasius solution is also plotted for reference.

The result shows that the mean streamwise velocity profiles varied along the scale length and deviated from the theoretical Blasius solution in the near surface region. Over the first half of the scale length ($\phi < 0.5$), the velocity profiles are shifted upwards relative to the Blasius solution, whereas, in the latter half of the scale ($\phi > 0.5$), they are shifted downwards. As the scale height increases along the length of the scale, the flow was found to result in a downward shifted profile in response to the variation in the scale height. These deviations from the Blasius solution appear to diminish with increasing distance away from the surface. The upward shifted profiles converge at a height of about $\lambda_1 \approx 4 - 5$ ($\lambda_2 = 0.6$), while the downward shifted profiles did not converge until $\lambda_1 =$

7 ($\lambda_2 = 0.9$). A similar analysis was completed over scales $S_{0,3}$, $S_{0,7}$, and $S_{0,9}$, which showed that similar trends are found at different scales along the streamwise direction.

A particularly interesting feature of the profiles in the upstream end of the scale ($\phi < 0.5$) is the vertical shift within a height of $\lambda_1 \approx 1 - 2$ from the surface. To further explore this differentiation within the boundary layer, Figure 23 shows the near wall streamwise velocity profiles up to a height of about $\lambda_1 = 1.5$ along the length of scale $S_{0,5}$.

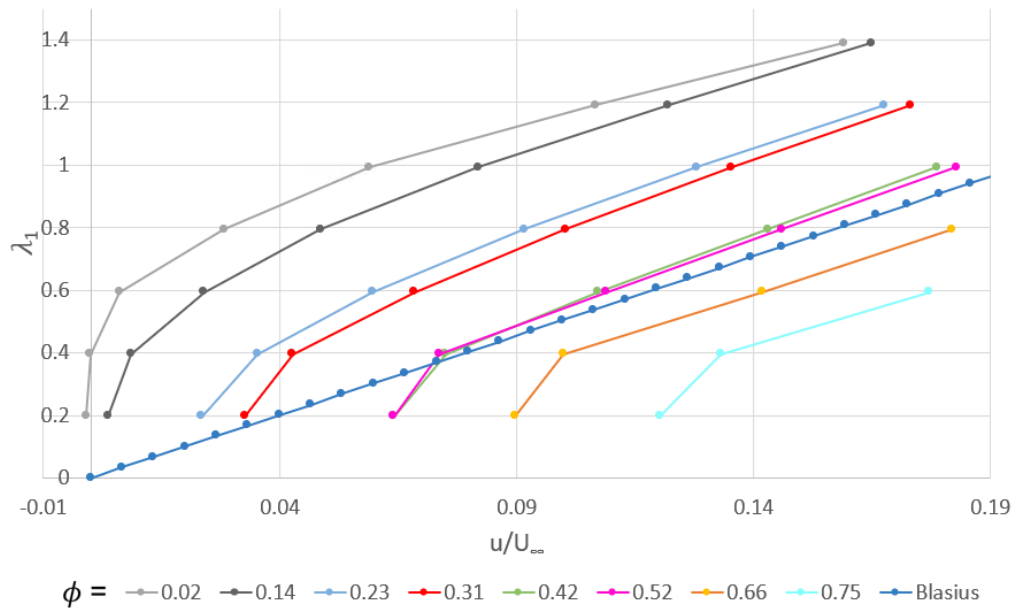


Figure 23: Non-dimensional wall normal mean streamwise velocity profiles over scale length ($S_{0,5}$) for various values of ϕ . The mean velocity profile from the Blasius solution is also plotted for reference.

The near wall velocity profiles along the length of scale $S_{0,5}$ show evidence of a potential flow separation region for small values of ϕ . This flow separation region results in velocity profiles shifted upwards from the Blasius solution due to the negative velocity close to the surface and slow recovery of the velocity over a height of about $\lambda_1 = 1$. The velocity profiles also show an increasing velocity trend over the length of the scale. At $\phi = 0.42$, the velocity profiles closely match the Blasius solution, and at greater values of ϕ , the velocity profiles are shifted downward. Given the scale height causes an area

reduction along the length of the scale, it is expected that the velocity will accelerate as ϕ increases. To further investigate the extent of the flow separation, a small region near the upstream end of the scale (small values of ϕ) was further analyzed. The mean streamwise velocity profiles in this region are shown in Figure 24 with a higher spatial resolution i.e., velocity profiles over shorter increments in the streamwise direction.

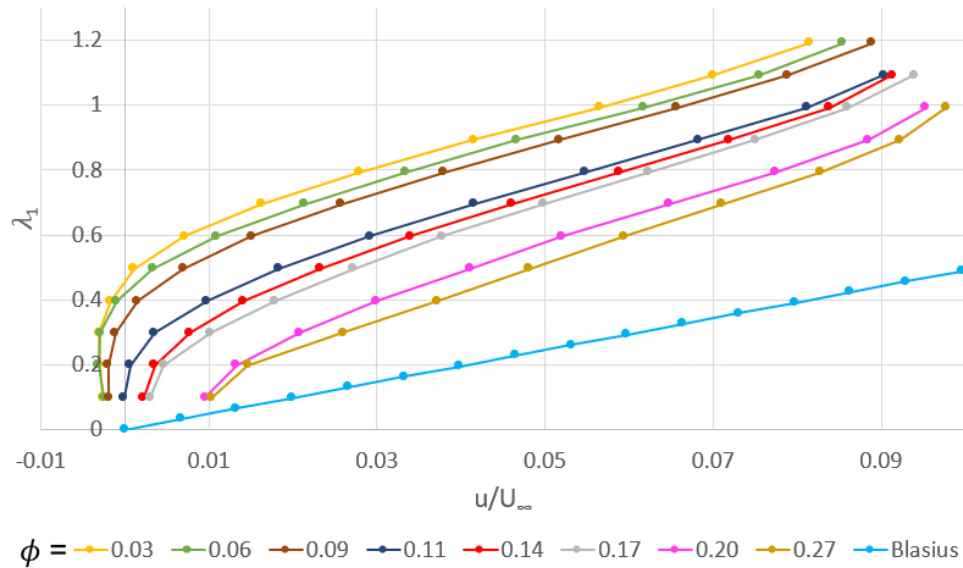


Figure 24: Non-dimensional wall normal mean streamwise velocity profiles in the separation region of scale $S_{0.5}$ at various values of ϕ . The mean velocity profile from the Blasius solution is also plotted for reference.

From Figure 24, it is evident a flow recirculation region exists which results in separated velocity profiles for small values of ϕ . The recirculation region causes a negative flow within a height of $\lambda_1 = 0.5$ and exists up to about $\phi = 0.11$. To visualize the flow in this region, Figure 25 shows the mean velocity vector field. The apparent location of the flow reattachment is also highlighted with a marked circle.

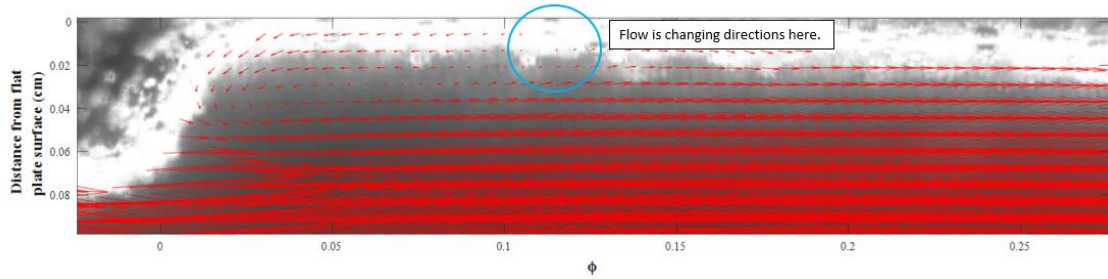


Figure 25: Mean velocity vector plot showing the flow recirculation over $S_{0.5}$. Flow is from left to right.

To get a better insight into the size of the recirculation region, the reattachment length was calculated for all scales in the streamwise direction along the centerline plane ($S_{0.1}$ - $S_{0.9}$). The reattachment length was determined using the PIV velocity data, by measuring the distance from the scale bottom to the position of the first velocity vector at the surface in which the u -component of velocity was positive. The scale length (l_{sl}) was used to non-dimensionalize the reattachment length as this would indicate the value of ϕ at which reattachment occurs. Figure 26 shows this non-dimensional reattachment length for all scales along the centerline plane.

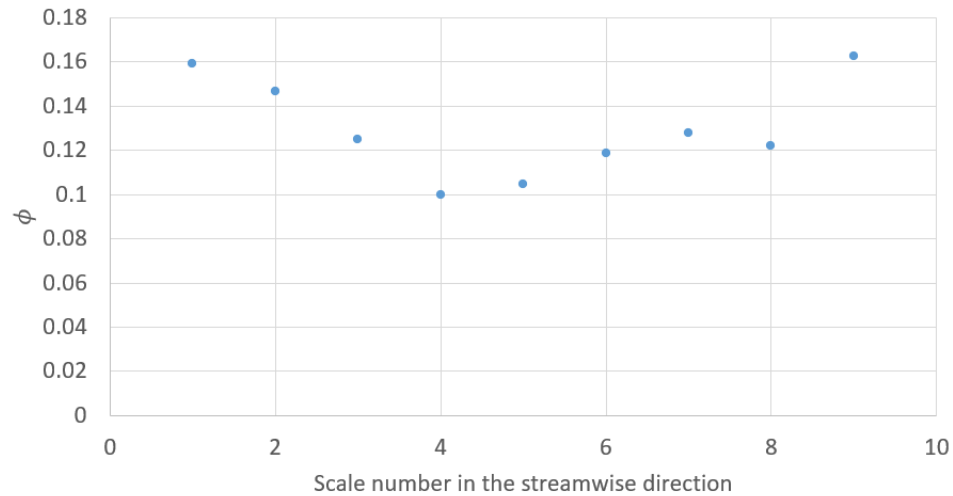


Figure 26: Non-dimensional reattachment length (ϕ) for scales along centerline plane.

From Figure 26, it can be observed that the reattachment length varies over the length of the scale array. The results show an apparent decrease in the reattachment length from the first scale to almost the middle of array, then an increasing trend in the reattachment length over the latter half of the scale (except for scale 8). This indicates that although similar wall normal streamwise velocity profiles are found over the scales in the streamwise direction, the position of these profiles over the length of the scale, and thus the reattachment length varies. While there does appear to be some variation over the length of the scale array, the average reattachment length and associated statistical 95% confidence interval can be computed for the purposes of characterizing the extent of this flow feature. Table 4 shows the reattachment length (absolute value and non-dimensional values in terms of the scale length and scale height) and associated 95% confidence intervals for the expected size of the recirculation region.

Table 4: Average reattachment lengths and confidence intervals

Parameter	Average Value and 95% Confidence Interval
Reattachment Zone Length (mm)	2.08 \pm 0.70
Non-dimensional reattachment length ($length/l_{sl}$)	0.13 \pm 0.05
Non-dimensional reattachment length ($length/l_{sh}$)	2.60 \pm 0.90

These average results highlight that the recirculation region extends to about $\phi = 0.13$ or 2.6 scale heights downstream. Despite the recirculation region being confined to $\phi < 0.13$, Figure 23 shows the velocity profiles up to $\phi = 0.4$ are shifted upward compared to the Blasius solution. Thus, flow recirculation is found to cause shifted velocity profiles over a streamwise distance more than twice the length of the recirculation region itself. Discussing the reattachment length in terms of the number of scale heights is arguably a more reasonable measure of the reattachment length because it is the abrupt change in the surface pattern (or height of the scale) that causes the flow to be separated. Thus, with reattachment occurring at 2.6 scale heights downstream, it is evident that the effect of the scale height causes flow separation over a streamwise distance twice as large as the size of the feature itself.

The reattachment length results are similar to those obtained by Muthuramalingam et al. (2019) where they numerically estimated the reattachment length to be about 2.5 times the scale height. Further, Muthuramalingam et al. (2019) compared their results to the flow over a horizontal backwards facing step in Goldstein et al. (1970). They found their results to be similar if the Reynolds number based on the step height was around 100. For the current experiments, the Reynolds number based on scale height is calculated to be about 98 confirming the similarity with the results of Goldstein et al. (1970). Additionally, Williams and Baker (1997) compare the reattachment length results over a backwards facing step in low Reynolds number flows for several numerical and experimental studies. They show that a reattachment length between 2.5 and 3 is expected for a Reynolds number based on step height of 100. This aligns closely with the reattachment length obtained in the current study, further validating the accuracy of these experimental results. This also highlights that while fish scale arrays may have a unique 3D topography and are positioned on an incline, the physics of the flow over the scale centerline and in the recirculation region, is similar to the flow over a backwards facing step.

To understand the impact of the shifted velocity profiles relative to the Blasius solution, the displacement thickness, momentum thickness, and shape factor at different values of ϕ over scale $S_{0.5}$ are compared in Table 5. The displacement thickness measures the mass flow deficit in the boundary layer and is defined using equation 2.11 (White, p. 455, 2016). The momentum thickness is a measure of the momentum deficit in the boundary layer and is defined using equation 2.12 (White, p. 453, 2016). Finally, the shape factor is the ratio of displacement thickness to momentum thickness and is shown in equation 2.13 (White, p. 461, 2016). The shape factor is used to describe the velocity deficit in the boundary layer where higher values of shape factor correspond to a greater velocity deficit and also a stronger adverse pressure gradient (White, p. 471, 2016). Table 5 summarizes the results for these parameters calculated using the trapezoidal method of numerical integration at different values of ϕ over scale $S_{0.5}$ and for the Blasius solution.

$$\delta^* = \int_0^{\delta} \left(1 - \frac{u}{u_{\infty}}\right) dy \quad (2.11)$$

$$\theta = \int_0^{\delta} \frac{u}{U_{\infty}} \left(1 - \frac{u}{U_{\infty}}\right) dy \quad (2.12)$$

$$H = \frac{\delta^*}{\theta} \quad (2.13)$$

Table 5: Displacement thickness, momentum thickness, and shape factor over scale $S_{0,5}$

Values of ϕ along the scale length	Displacement Thickness (10^{-3}) m	Momentum Thickness (10^{-4}) m	Shape Factor
0.02	2.42	7.82	3.09
0.06	2.54	7.85	3.23
0.12	2.56	7.98	3.20
0.16	2.43	7.97	3.05
0.23	2.45	8.17	3.00
0.30	2.33	8.18	2.85
0.45	2.24	8.44	2.65
0.54	2.24	8.35	2.68
0.66	2.14	8.25	2.59
0.74	2.03	8.17	2.49
0.88	1.94	8.07	2.40
0.96	1.96	7.94	2.47
Blasius	2.25	8.64	2.61

The variation in the displacement thickness is found to be the main driver of the change in the shape factor. A large displacement thickness is observed at small values of ϕ , and decreases as ϕ increases along the length of the scale. Comparing the magnitude of the displacement thickness to that of the Blasius solution, it is observed that for $\phi < 0.45$ the displacement thickness is greater than the Blasius solution, whereas for $\phi > 0.55$ the displacement thickness is less than the Blasius solution. The decreasing mass flow deficit along the length of the scale indicates a recovery of mass flow over the length of the scale and is a result of the deficit created in the flow recirculation region.

Further, the momentum thickness shows an increasing then decreasing trend with a maximum momentum thickness at $\phi \approx 0.45$. The increasing momentum thickness appears to be linked to the recovering velocity profiles from the recirculation region, whereas a decreasing trend appears linked to the continued acceleration of the velocity over the latter portion of the scale. When comparing the momentum thickness values to the Blasius solution, all values along the length of the scale appear to be below that of the Blasius solution. This indicates that the profiles at all values of ϕ have a lower momentum deficit and lower associated shear than the Blasius solution.

While both the displacement thickness and momentum thickness are used to calculate the shape factor, the trends in the variation of the shape factor over the length of the scale closely follow that of the displacement thickness. There is an initial increase in the shape factor within the recirculation region indicating the presence of a stronger adverse pressure gradient. The shape factor then quickly falls beyond the reattachment length as the flow reattaches and accelerates over the length of the scale. Throughout most of the scale length a decreasing trend in the value of the shape factor is observed. When comparing the value of the shape factor to the Blasius solution, the shape factor is only smaller for $\phi > 0.66$. Additionally, the higher shape factors (closer to 3.2) for $\phi < 0.12$ indicates the presence of a strong adverse pressure gradient and greater likelihood of flow separation. This aligns with the presence of the flow recirculation zone mentioned previously.

While the current analysis was focused on the values over a single scale ($S_{0,5}$), similar results are found over scales $S_{0,3}$, $S_{0,7}$, and $S_{0,9}$ highlighting that these patterns along the scale centerline are repeatable and periodic. Looking beyond the streamwise velocity component, the wall normal velocity component also shows an interesting periodic behaviour (see Figure 27).

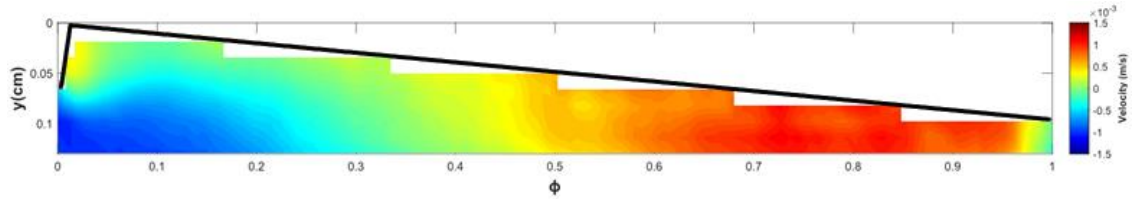


Figure 27: Colourmap of the mean wall normal velocity in the near wall region of scale $S_{0,5}$ over the centerline plane ($\xi = 0$). Flow is from left to right.

The colourmap plot in Figure 27 shows a clear link between the wall normal velocity and the scale heights. Near the upstream end of the scale (small values of ϕ) the fluid moves to fill the region behind the scale height creating a negative wall normal velocity. This negative velocity then flips positive as the flow moves along the scale length. For values of ϕ between 0.3 and 0.5, the wall normal velocity is negligible. This is also the region where the streamwise velocity profiles most closely match the Blasius solution and there is a peak in the momentum thickness. This suggests that the wall normal velocity may play a role in the decreased momentum thickness compared to the Blasius solution. Over the latter half of the scale, a positive wall normal velocity is observed as the flow accelerates towards the next scale. Finally, a small region very close to the upstream end of the scale (small values of ϕ) shows a positive velocity linked to the flow recirculation in that region.

The results in this section provide an in-depth understanding of the flow in the centerline plane ($\xi = 0$) or mid-scale location. Next, the analysis will look at how the flow behavior varies in the spanwise direction focusing on the midline plane. The following sections will begin to dissect the impact of the 3D scale geometry and will draw comparisons to the centerline results.

2.4.2.2 Midline Region

Due to the 3D nature of the scale geometry and the limitations of planar PIV, the entire near wall region in both the midline and overlapping planes could not be captured. In both cases, a portion of the scale closer to the camera obstructed the viewing of the flow in some regions near the wall. In the case of the midline plane (see Figure 28A), the

lower half of the region within the scale height was blocked by the scale closer to the camera. Despite these challenges, most of the domain remained unaffected, and data near the blocked regions could be used to infer patterns and compare the results to the centerline plane. Figure 28B shows an example of the blocked region over scale $S_{0.5}$ which occurs for ϕ between 0 and 0.3.

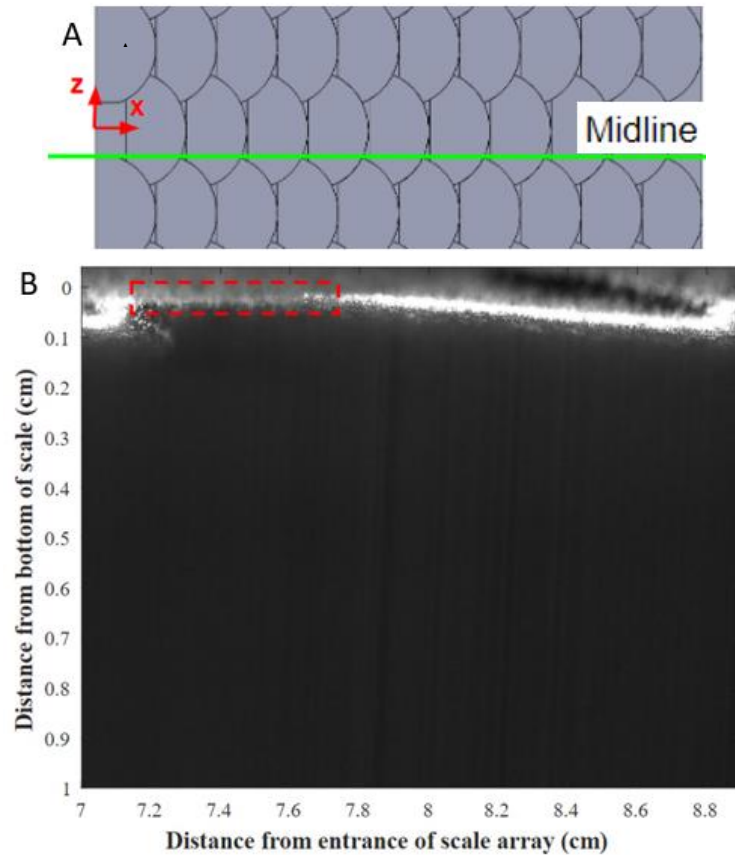


Figure 28: (A) Location of midline region over scale array; (B) Image showing blocked area along the midline plane ($\xi = 0.26$) over scale $S_{0.5}$.

To begin the analysis over the midline region, the mean wall normal velocity distribution in the near wall region will be examined to understand how the wall normal velocity pattern changes relative to that over the scale centerline plane. Figure 29 shows the colormap of the mean wall-normal velocity in the near wall region over scale $S_{0.5}$.

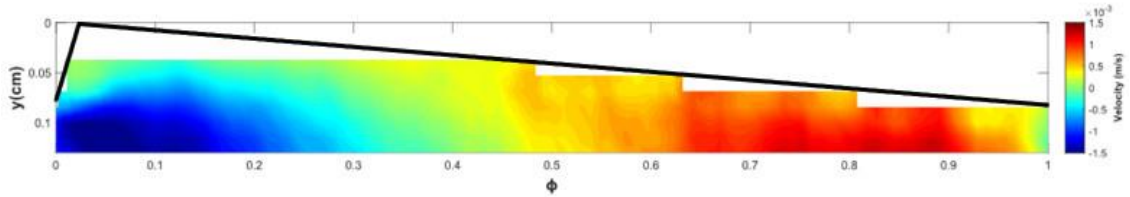


Figure 29: Mean wall normal velocity colormap in the near wall region over scale $S_{0,5}$ along the midline plane ($\xi = 0.26$). Flow is from left to right.

The colourmap shows a strong similarity to that of the velocity pattern along the centerline plane. There appears a similar negative wall normal velocity for small values of ϕ indicating flow entering the region behind the scale height and suggesting the formation of the flow recirculation region. This negative velocity turns positive at greater values of ϕ and has a similar region of negligible wall normal velocity ($\phi = 0.3 - 0.5$) as the centerline plane. The magnitude of the wall normal velocity is slightly stronger in the midline plane as compared to the scale centerline. These results show that although some of the near wall region is blocked by another scale, the patterns in the wall normal velocity show a strong indication that the flow in this region is similar to the flow in the centerline plane. Due to the strong similarity in the flow between these two regions, the wall normal streamwise velocity profiles over the length of a single scale ($S_{0,5}$) are compared along the midline plane ($\xi = 0.26$).

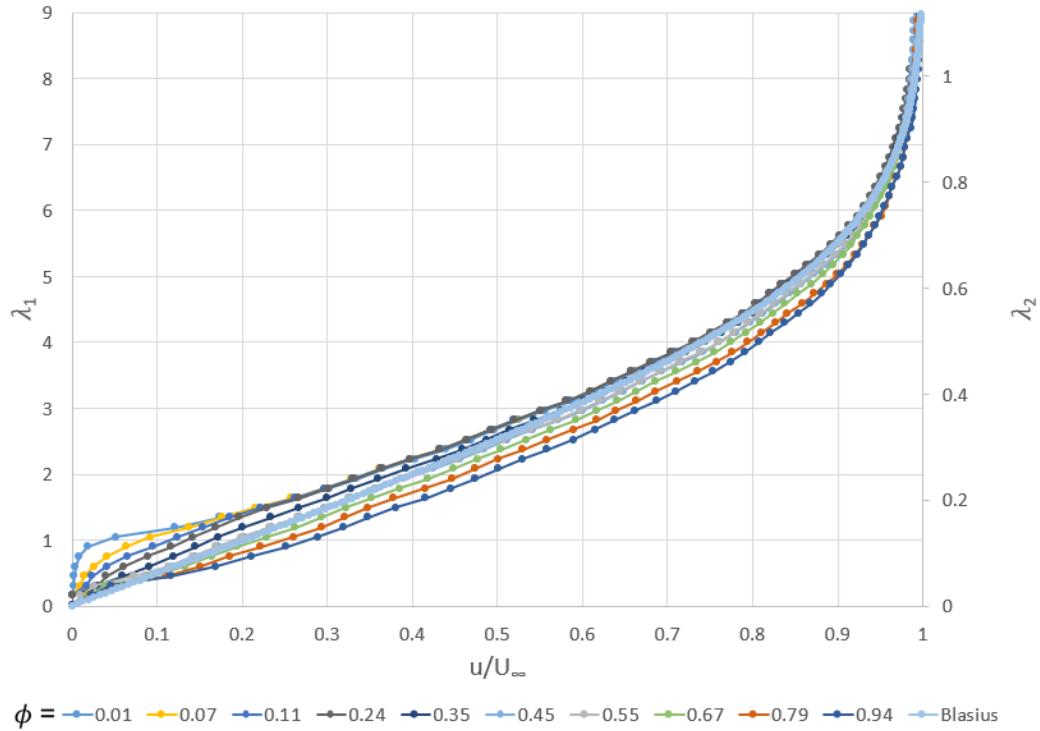


Figure 30: Non-dimensional wall normal mean streamwise velocity profiles for various values of ϕ over the length of scale $S_{0.5}$ along the midline plane ($\xi = 0.26$). The Blasius velocity profile is also plotted for comparison.

The wall normal streamwise velocity profiles along the midline plane show strong similarity to those along the centerline plane. The velocity profiles up to about $\phi = 0.35$ are shifted upward compared to the Blasius solution. In contrast to the profiles along the centerline, the upward shift converges back to the Blasius solution around a wall normal distance of $\lambda_1 = 2 - 3$ (or $\lambda_2 \approx 0.3$) instead of $\lambda_1 = 4 - 5$ that was observed along the centerline. This velocity recovery lower in the boundary layer shows that the streamwise velocity within the boundary layer has some dependence on the spanwise location. Since the local scale height varies in the spanwise direction as a result of the 3D scale topography, it is likely the recovery lower in the boundary layer is related to the change in local scale height.

Similar to the centerline plane, streamwise velocity profiles for $\phi > 0.67$ show a downward shift compared to the Blasius solution. This downward shift persists until about a height of $\lambda_1 = 7$ (or $\lambda_2 = 0.9$), similar to the trends observed in the centerline

plane. To further explore the flow behaviour in the near wall region, the streamwise velocity profiles for different values of ϕ were plotted in the near wall region up to a height of about $\lambda_1 = 2$ (see Figure 31).

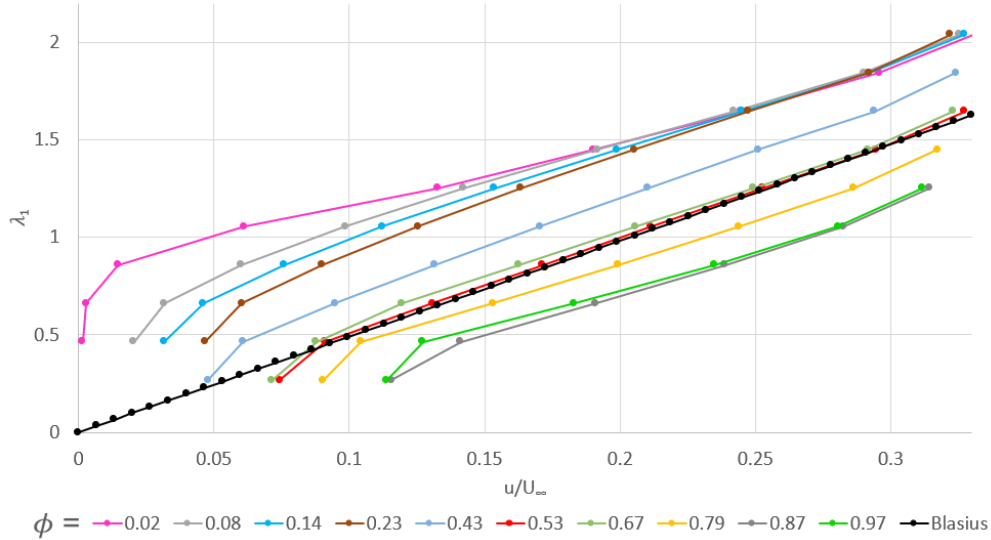


Figure 31: Near wall non-dimensional mean streamwise velocity profiles for various values of ϕ over the length of scale $S_{0,5}$ along the midline plane ($\xi = 0.26$). The Blasius velocity profile is also plotted for comparison.

The near wall region shows that the velocity profiles remain shifted upwards compared to the Blasius solution until about $\phi = 0.43$, where they begin to match closely the Blasius solution until $\phi = 0.67$, after which they are shifted downwards. The boundaries of the region where the profiles closely match the Blasius solution appear similar to those found in the centerline plane. This shows that moving in the spanwise direction to the midline plane results in a similar streamwise region of upward shifted velocity profiles that recover to the Blasius solution at smaller wall normal locations.

Despite values of $\lambda_1 < 0.5$ being blocked for small values of ϕ , the velocity profiles in this region show evidence of a low velocity region that extends up to a height of about $\lambda_1 = 1$. While no conclusions about the existence of a flow recirculation zone can be made, the similarities in the flow patterns between the midline and centerline region suggest flow recirculation may be present in this region as well. Finally, similar patterns

in the mean wall normal streamwise velocity profiles were observed over scales $S_{0,3}$, $S_{0,7}$, and $S_{0,9}$ in the streamwise direction suggesting these behaviours are periodic along the scales in the streamwise direction. Next, the results along the overlapping plane will be analyzed to understand how the flow behaviour in this region differs from both the centerline and midline planes.

2.4.2.3 Overlapping Region

As mentioned in the midline section above, the 3D nature of the scale geometry and experimental limitations resulted in a blockage of the camera viewing area over the scale array for the wall normal measurements in both the midline and overlapping planes. Changes in the surface topography in the overlapping region (see Figure 32A) result in scale heights facing towards and away from the camera. It is the scale heights facing away from the camera that are blocked in the measurements along the overlapping plane. Despite this blocked area, much of the domain remained unaffected and data near the blocked regions could be used to infer patterns and compare the results to the centerline and midline planes. Figure 32B shows that the blocked region over scale $S_{0,5}$ occurs for ϕ between 0.55 and 0.85.

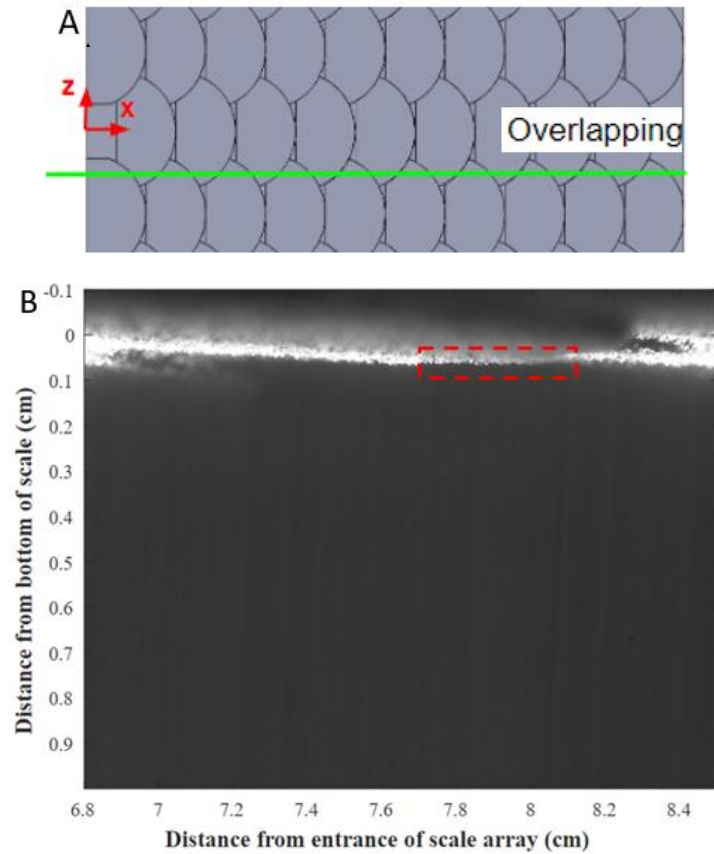


Figure 32: (A) Location of overlapping region over scale array; (B) Image showing blocked area along overlapping plane ($\xi = 0.375$) for scale $S_{0.5}$.

First, the wall normal velocity colourmap in the near wall region will be analyzed to understand how the wall normal velocity pattern changes moving into the overlapping region (see Figure 33).

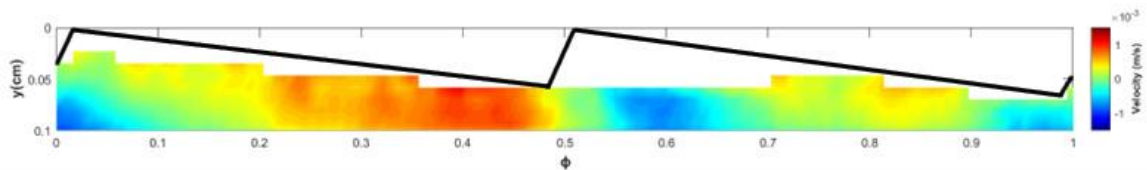


Figure 33: Mean wall normal velocity colourmap in the near wall region over scale $S_{0.5}$ in the overlapping region. Flow is from left to right.

The patterns in the wall normal velocity colourmap show similarities to the midline and centerline regions except with two negative, and two positive velocity regions over the

length of a scale as opposed to one. This is unique to the overlapping region as the edges of scales from the two adjacent rows converge to create twice the number of surface variations (or scale heights) as along the midline or centerline planes. While a greater wall normal component is observed for $\phi < 0.5$, this is likely because the blocked region of the scale occurs between $\phi = 0.55$ to 0.85 resulting in some of the near wall region not being captured over the latter half of the scale. To further explore the streamwise flow behaviour in the overlapping region, the wall normal streamwise velocity profiles are plotted for values of ϕ along the length of a single scale (see Figure 34).

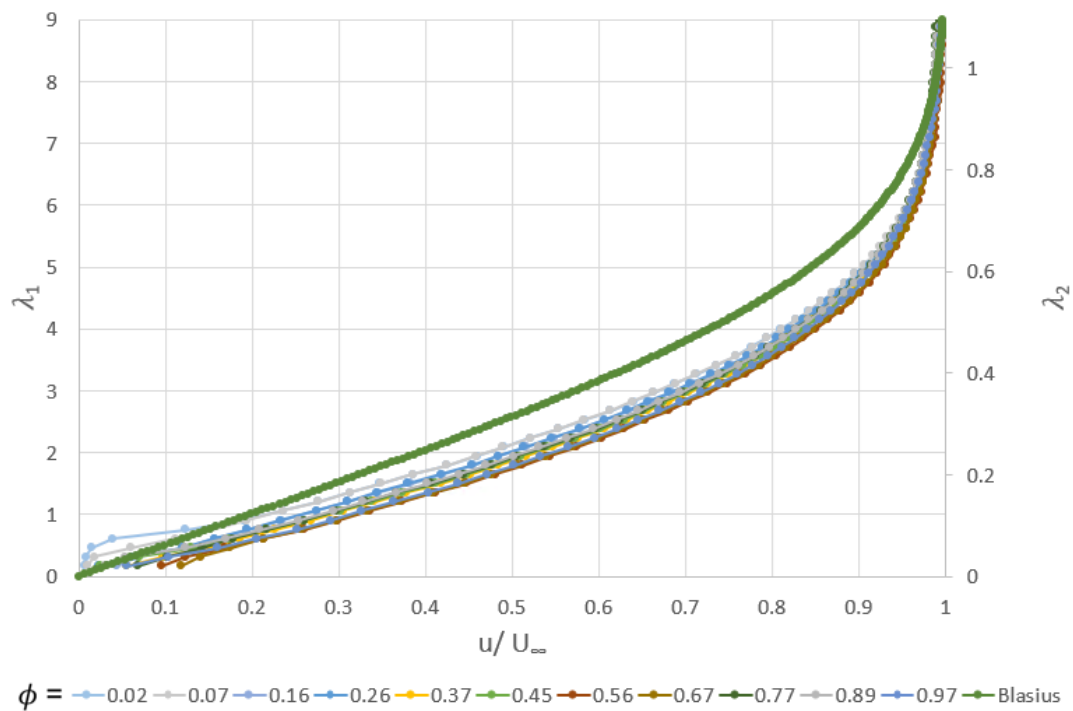


Figure 34: Non-dimensional wall normal streamwise velocity profiles along the overlapping plane over scale $S_{0,5}$ for various values of ϕ .

These profiles show strong differences in the streamwise flow behaviour compared to both the midline and centerline planes. For all values of ϕ considered, the velocity profiles show a downward shift from the Blasius solution throughout most of the boundary layer. This indicates a higher velocity magnitude is present throughout the boundary layer in the overlapping region relative to the classical laminar boundary layer over a flat surface. Comparing these results to the midline and centerline planes also

highlights that a variation in the streamwise velocity is expected in the spanwise direction across the array. The persistent downward shift in the velocity profiles is unique to the overlapping region and likely linked to the unique overlapping scale features in this region.

Additionally, while some variations are noted for small values of ϕ , all profiles converge below the Blasius solution within a height of $\lambda_1 = 1$. The higher velocity magnitudes closer to the surface in the overlapping region show that the effects of the surface variations are confined to a wall normal distance of $\lambda_1 < 1$. Similar to what was observed in the midline plane, the continued decrease in the local scale height in the overlapping region is likely to play a role in the increased velocities lower in the boundary.

To explore the impact of the downward shift of the velocity profiles over the length of a single scale in the overlapping region, the displacement thickness, momentum thickness, and shape factor are calculated using equations 2.11, 2.12, and 2.13, and the trapezoidal numerical integration scheme. While the overlapping region presented experimental challenges resulting in a blocked region between $\phi = 0.55$ and $\phi = 0.85$, calculation of these parameters can only be done accurately for values of $\phi < 0.5$. However, given the periodic behaviour observed in the mean wall normal velocity colourmap, it is hypothesized that these parameters may also undergo a similar periodic repetition in the region between $\phi = 0.5$ and $\phi = 1$. As such, Table 6 shows the displacement thickness, momentum thickness, and shape factor for values of $\phi < 0.5$ over scale $S_{0.5}$ in the overlapping region.

Table 6: Displacement thickness, momentum thickness, and shape factor for different values of ϕ over scale $S_{0.5}$ in the overlapping plane.

Values of ϕ along the scale length	Displacement Thickness (10^{-3}) m	Momentum Thickness (10^{-4}) m	Shape Factor
0.02	2.00	7.41	2.69
0.04	1.99	7.52	2.65
0.07	1.98	7.64	2.60
0.10	1.99	7.69	2.59
0.16	1.87	7.70	2.43
0.19	1.87	7.68	2.43
0.24	1.89	7.80	2.42
0.30	1.78	7.82	2.28
0.37	1.79	7.74	2.31
0.45	1.80	7.54	2.39
0.50	1.70	7.62	2.23
Blasius	2.29	8.77	2.61

The displacement thickness shows a decreasing trend for $\phi < 0.5$, which is similar to the displacement thickness over the centerline. However, the magnitude of the displacement thickness in the overlapping region is, at its largest, about 22% lower than along the centerline. Similarly, the momentum thickness in the overlapping region shows an increasing then decreasing trend with the maximum occurring at $\phi \approx 0.25 - 0.3$. This trend is similar to the momentum thickness along the scale centerline, however, the streamwise values of ϕ are half that of the centerline because there are twice the number of surface features along the overlapping plane. Similarly, the magnitude of the momentum thickness is, at its largest, about 7% lower than along the centerline plane. Finally, comparing the shape factor to that along the centerline, it is noted that both show a decreasing trend as ϕ increases, however, the shape factor is once again, at its largest, about 16% lower in the overlapping region than along the centerline. Comparison of these results to the centerline plane reveals that the trends in all three parameters remain similar, however, a lower magnitude is produced in the overlapping region.

The results for these parameters in the overlapping region can also be compared to the Blasius solution, showing that the displacement and momentum thickness obtained for all values of ϕ remain well below that of the Blasius solution. This implies that there is less mass flow and momentum deficit throughout the boundary layer compared to the Blasius solution. Further, the shape factor results reveal that for values of ϕ between 0.1 and 0.5 the shape factor is found to be smaller than that of the Blasius solution. Thus, the flow in this region is likely to result in a lower velocity deficit, a favourable pressure gradient, and a greater resistance to flow separation. Due to experimental challenges, the results are only shown for ϕ up to 0.5, however, given the overlapping nature of the features in this region and the presence of twice as many scale heights, it is expected that the patterns between $\phi = 0$ and 0.5 will be repeated between $\phi = 0.5$ and 1.

Similar trends in the wall normal streamwise velocity profiles, displacement thickness, momentum thickness, and shape factor were found over scales $S_{0.3}$, $S_{0.7}$, and $S_{0.9}$ in the overlapping region. This analysis showed that the overlapping plane and centerline plane contain flow behaviours which are distinct in the wall normal direction. The differences in the boundary layer profiles reveal that the streamwise velocity throughout the boundary layer is dependent on the spanwise location across the array. This spanwise dependency will be the focus of the following sections which will analyze the results along various horizontal (x - z) planes, at distinct wall normal locations.

2.4.3 Horizontal Plane Results

The coordinate system defined from the upstream edge of the scale array (see Figure 20) as well as the previously defined non-dimensional parameters (see equations 2.6, 2.7, 2.8, 2.9, and 2.10) will be used in the analysis of the results in horizontal plane as well. Measurements in the horizontal plane were completed at wall normal distances of 1.3 mm, 1.6 mm, 2 mm, 2.5 mm, 3 mm, 3.5 mm, 4 mm, and 5 mm measured from the flat plate surface. Due to the finite length and width of the scale array, horizontal results will be considered from $\xi = -1$ to 1 and $\phi_t = 1.5$ to 9, as this corresponds to the region over the array which is not influenced by the start, end, and sides of the scale array. The horizontal plane results have been analyzed in combination with the patterns observed in the wall normal planes and are used to provide a comprehensive 3D perspective of how

the scale topography modifies the flow behaviour in the near wall boundary layer. The horizontal plane analysis is focused on the streamwise velocity, the spanwise velocity, and the wall-normal vorticity, as the patterns identified in these variables were found to be uniquely linked to the underlying scale topography.

2.4.3.1 Streamwise Velocity

The colormap of the mean streamwise velocity over the scale array at a wall distance of $\lambda_1 = 2.5$ is shown in Figure 35. The results show a strong spanwise variation in the streamwise velocity. It is also found that these variations are aligned with the spanwise topographic changes in the scales, where higher velocities align with the overlapping regions of the scales and lower velocities align with the scale centerlines. These velocity variations or so-called “velocity streaks” have been mentioned in Muthuramalingam et al. (2019) who demonstrated qualitatively that these streaks exist over 3D biomimetic fish scale arrays. The present study provides the first experimental evidence of the presence of these velocity streaks over biomimetic fish scale arrays and provides a detailed analysis of their characteristic flow behaviour.

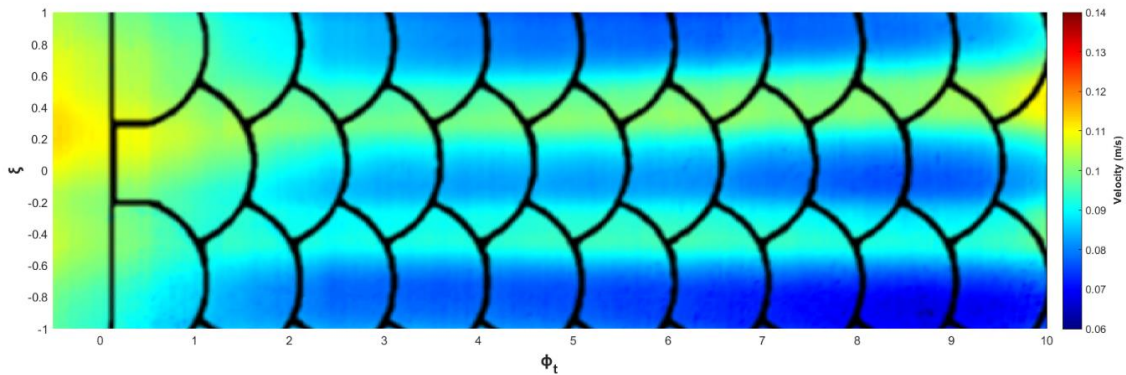


Figure 35: Colormap of the mean streamwise velocity at wall normal distance of $\lambda_1 = 2.5$. Flow is from left to right.

As the mean streamwise velocity colormap shows, the streamwise velocity streaks are formed after the flow enters the scale array and highlights some streamwise development over the length of the scale array. There does not appear to be any periodic variations in

the streamwise direction related to the scale heights. However, the magnitude of the low-velocity streaks appears to decrease in the streamwise direction.

As mentioned earlier in the vertical plane results, the wall normal streamwise velocity profiles over the scale centerline ($\xi = 0$) closely matched the Blasius solution, whereas those in the overlapping region ($\xi = \pm 0.375$) showed a strong downward shift from the Blasius profile. Given that the scales protrude from the surface with the largest surface variations located at $\xi = 0$ and $\xi = \pm 0.75$, it is the reaction of the fluid to these surface variations that causes the formation of the low velocity streaks. In addition to this, given the scale height is found to vary across the width of a single scale, the fluid taking the path of least resistance is pushed into the overlapping regions on either side of the scale centerline. Thus, the height variations across the width of the scale generate a path of least resistance which forces the fluid into the overlapping regions, contributing to a higher velocity in these regions. As a result, the unique surface variations lead to the formation of high-velocity streaks in the overlapping regions and low-velocity streaks along the scale centerline.

To explore the impact of the velocity streaks throughout the boundary layer, the non-dimensional streamwise velocity variation (ψ) is plotted across the scale array at a streamwise location of $\phi_t = 4.5$ for each wall normal location. The non-dimensional streamwise velocity variation (ψ) is defined as the maximum velocity at each height (between $\xi = 1$ and -1) minus the actual velocity divided by the free-stream velocity (see equation 2.14). This represents the range of velocity fluctuations as a fraction of the free-stream velocity. Normalizing the profiles to the largest velocity magnitude at each height allows for the velocity variations to be compared between heights. Figure 36 shows the non-dimensional streamwise velocity variation (ψ) at all wall normal heights (λ_1) across the array at a streamwise position of $\phi_t = 4.5$.

$$\psi = \frac{u_{max,y} - u}{U_\infty} \quad (2.14)$$

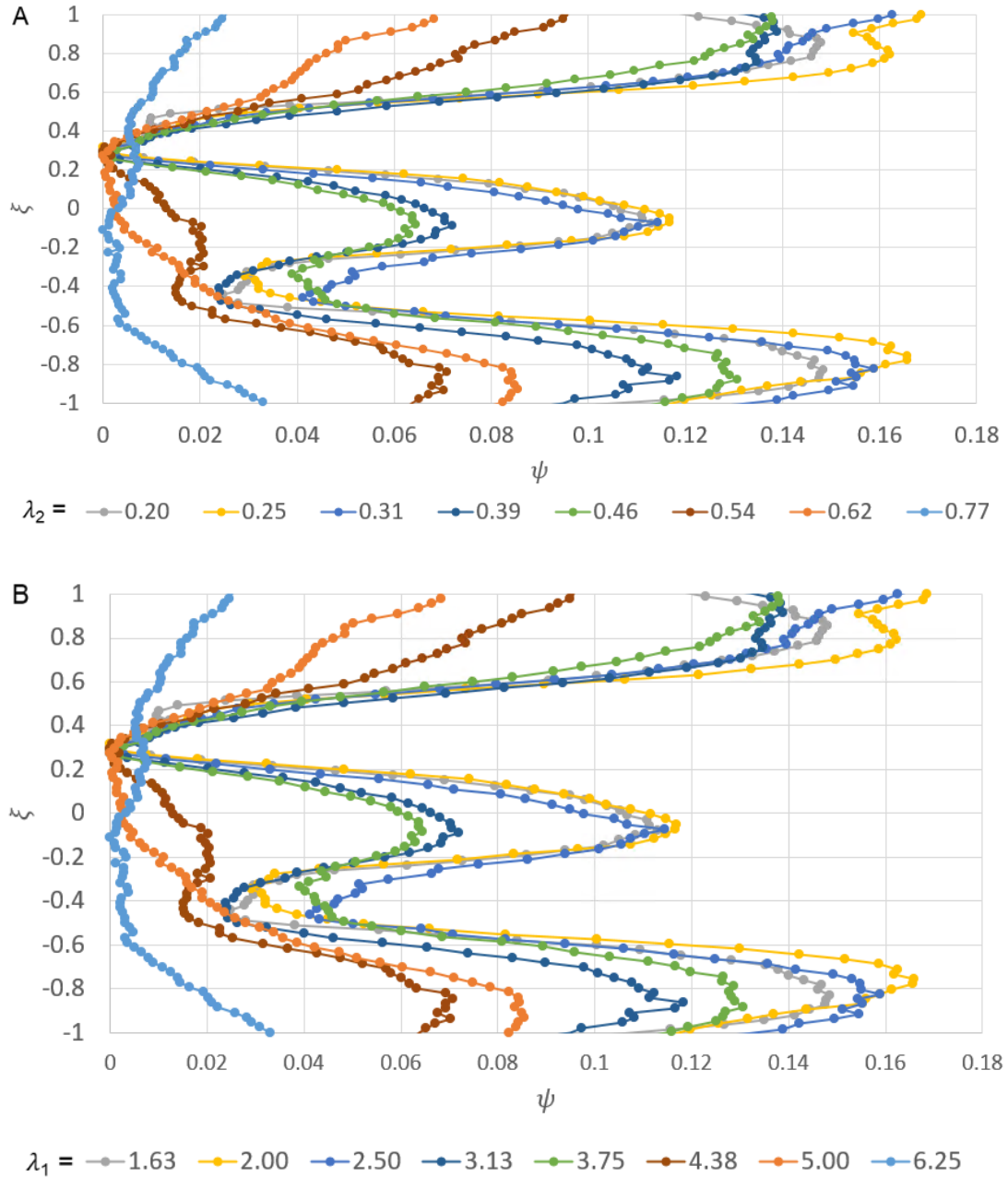


Figure 36: Non-dimensional mean streamwise velocity variation at different non-dimensional wall normal distances at a streamwise location of $\phi_t = 4.5$. (A) wall normal positions are plotted as a fraction of the boundary layer thickness (λ_2); (B) wall normal positions are plotted as the number of scale heights from the wall (λ_1).

It is observed from Figure 36 that the streamwise velocity variations are not identical in the three adjacent scale rows. The reason behind this is that adjacent scale rows contain a

streamwise offset of $\phi_t = 0.5$, as described previously. The scale rows corresponding to $\xi = \pm 0.75$ contain an additional scale at the upstream edge of the scale array as a result of the streamwise offset. The additional development length over the scales at $\xi = \pm 0.75$ results in a greater velocity variation in these regions. As such, the velocity variation over the scales at $\xi = 0$ is found to be smaller than those at $\xi = \pm 0.75$, for all measured heights.

Figure 36 also highlights that the strongest variations in the streamwise velocity are found closer to the surface at $\lambda_1 = 1.63, 2.0$, and 2.5 . There appears to be some asymptotic behaviour near the surface that results in similar velocity variations over a range of heights. This behaviour follows the trends found in the vertical plane results which showed that for $\lambda_1 = 1 - 2$ the velocity profiles in the overlapping plane exhibited a rapid convergence to the Blasius solution, whereas those along the centerline plane showed the largest upward shift. Thus, the combination of the upward shifted profiles along the scale centerline and rapidly converging profiles in the overlapping region results in similar velocity variations at multiple heights close to the surface.

Above the critical height of $\lambda_1 = 2.5$ (or $\lambda_2 = 0.31$), with increasing distance from the surface, a systematic decrease in the velocity streaks is observed. This follows the results found in the vertical plane which showed a relatively consistent downward shift in the wall normal streamwise velocity profiles in the overlapping plane above $\lambda_1 = 2.5$ (or $\lambda_2 = 0.31$). Thus, the decrease in the velocity variation is driven by the behaviour in the centerline region which shows the upward shifted profiles converging to the Blasius solution between $\lambda_1 = 2.5$ (or $\lambda_2 = 0.31$) and $\lambda_1 = 5$ (or $\lambda_2 = 0.61$). As the upward shift in the velocity profiles is induced by the variations in the surface topography, it is expected that these variations will become weaker with increasing height due to the viscous dissipation throughout the boundary layer.

The velocity variation over the scales at $\xi = 0$ was less than 2% of the free-stream velocity at a height of $\lambda_1 = 4.38$ (or $\lambda_2 = 0.54$). At and above this height, the velocity variations over the scales at $\xi = 0$ appear to vanish. Furthermore, at the height of $\lambda_1 = 6.25$ (or $\lambda_2 = 0.77$), the variation across all spanwise scales almost disappeared and the

flow approached a relatively uniform profile. Relating the behaviour at greater wall normal distances to the vertical plane results, it is found that the return of the wall normal streamwise velocity profiles in the overlapping plane to the Blasius solution leads to the decay in the velocity variation across the scale array. These results are similar to those found in Muthuramalingam et al. (2019) who showed numerically that above a height of $\lambda_2 = 0.75$ the velocity variation across the array was below 2%.

As mentioned earlier, the streamwise velocity streaks show some development of the velocity streaks in the streamwise direction. To further understand the impact of the streaks in the streamwise direction, the non-dimensional streamwise velocity variation (ψ) was plotted for four streamwise locations corresponding to $\phi_t = 2.5, 4.5, 6.5,$ and 8.5 at a wall normal height of $\lambda_1 = 2.5$ (see Figure 37).

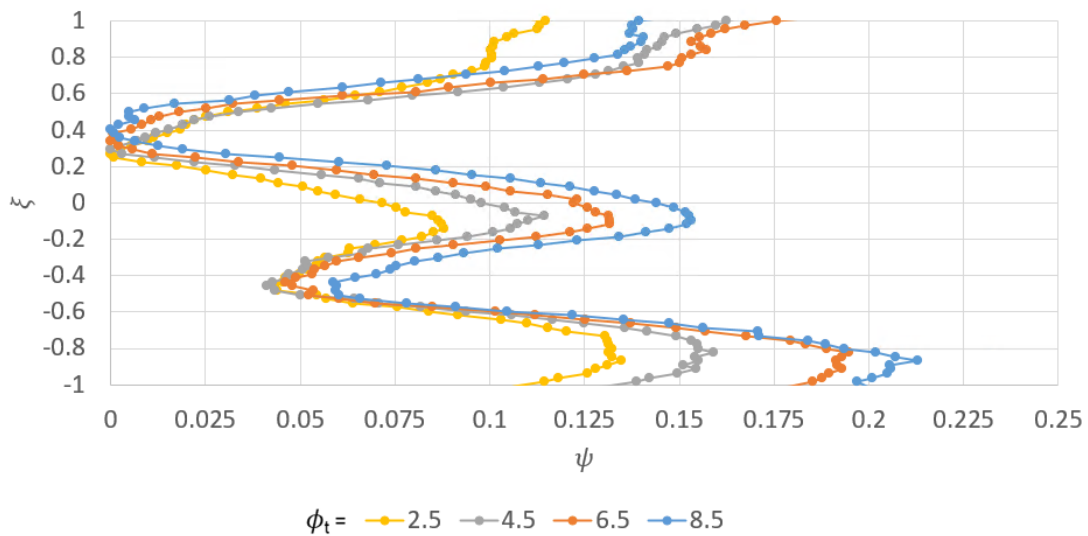


Figure 37: Non-dimensional streamwise velocity variation (ψ) at a wall normal position of $\lambda_1 = 2.5$ for streamwise locations of $\phi_t = 2.5, 4.5, 6.5,$ and 8.5 .

From Figure 37, it is observed that there is an increase in the magnitude of the velocity variation in the downstream direction. One explanation for this behaviour is that the boundary layer thickness increases in the downstream direction resulting in the fixed height measurements to be at a lower λ_2 . However, the analysis above found that below the critical height of $\lambda_1 = 2.5$, the velocity variation was similar at multiple heights. Thus, given that all wall normal locations resulted in a similar streamwise increase in the

velocity variation, the same asymptotic behaviour below a height of $\lambda_1 = 2.5$ is also observed at locations farther downstream ($\phi_t = 6.5$ and 8.5). Therefore, the increase in the velocity variation is concluded to be a result of the streamwise development of the velocity streaks and may be related to the boundary layer thickness, although this remains unclear. Further work is needed exploring the development length of the velocity streaks and examining the critical limits of the formation of these velocity streaks.

While Figure 36 shows the range of the velocity fluctuations, the amplitude of the velocity streaks is defined as half of the range according to equation 2.15 (Siconolfi et al., 2015). The streak amplitude between $\xi = -1$ and 1 was averaged for ϕ_t between 1.5 and 9 and plotted for all heights (λ_1) (see Figure 38) to summarize the behaviour of the streamwise velocity streaks in the wall normal direction. The 95% confidence interval calculated using two times the standard deviation of all streamwise streak amplitudes is shown as error bars.

$$A_{st} = \frac{(u_{max} - u_{min})}{2U_\infty} \quad (2.15)$$

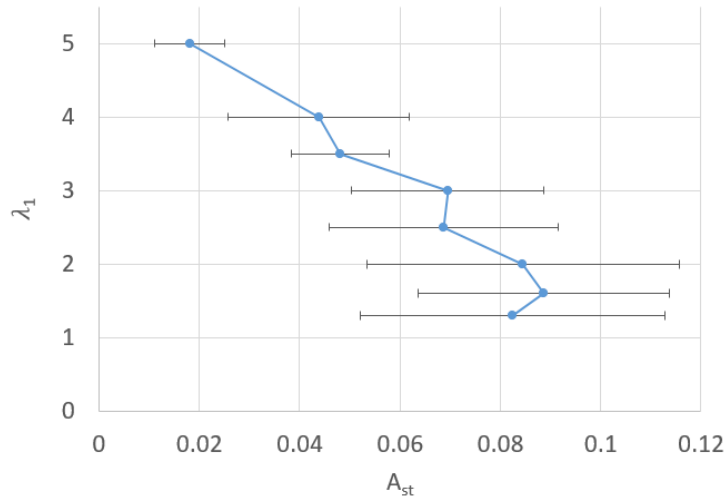


Figure 38: Average streamwise streak amplitude between $\xi = -1$ and 1 for the length of the array ($\phi_t = 1.5 - 9$).

The streak amplitude at each height shows the dissipation of the streamwise velocity streaks in the wall normal direction. Similar to the previous discussion, an asymptotic

behaviour is observed close to the surface below a height of $\lambda_1 = 2.5$ where a similar streak amplitude is found at multiple wall normal distance. Above this height, there is a consistent decrease in the streak amplitude as you move away from the surface until the streaks disappear below an amplitude of 2%. The dissipation in the wall normal direction is said to be linked to the viscous effects in the boundary layer.

The analysis of the streamwise streak amplitude is also critical when considering the transition to turbulence. The formation of unsteady streamwise streaks over a flat plate is part of the natural transition to turbulence, and Andersson et al. (2001) identified that a critical streak amplitude of 26% of the free-stream velocity leads to the onset of secondary instabilities and the breakdown to turbulence. While the generation of velocity streaks over the scale array is caused by the unique underlying surface topography, it can be argued that the same critical streak amplitude does not exist for flow over fish scales. Although the average streak amplitude in the presence of developing streaks is likely to underestimate the maximum streak amplitudes, variations at all heights were found not to exceed 10% of the free-stream velocity. Thus, although the streak generation mechanism is different over biomimetic fish scale arrays, the average streak amplitude achieved over the scale array remains below the previously identified critical threshold for decay to turbulence.

Muthuramalingam et al. (2020) found that the streamwise velocity streaks continued to have a stabilizing effect far downstream from the scale array attenuating Tollmien-Schlichting waves and delaying the transition to turbulence. While they studied the behaviour far downstream of the scale array, the current results suggest that the stability of the streak generation mechanism over the scale array and the underlying scale topography may contribute to a higher threshold at which the velocity streaks generated by fish scale arrays lead to the breakdown to turbulence, resulting in a greater delay in the transition to turbulence. Further investigation into the limitations of the streak amplitudes for breakdown to turbulence over fish scale arrays is needed.

Next, the spanwise velocity patterns over the array will be explored to further understand how the surface geometry impacts the flow behaviour across the scale array.

2.4.3.2 Spanwise Velocity

While the flow over the scale array is predominantly in the streamwise direction, there exists some spanwise velocity patterns that appear to be linked to the underlying geometry. Figure 39 shows the colormap of the average spanwise velocity over the scale array at a wall normal distance of $\lambda_1 = 2.5$.

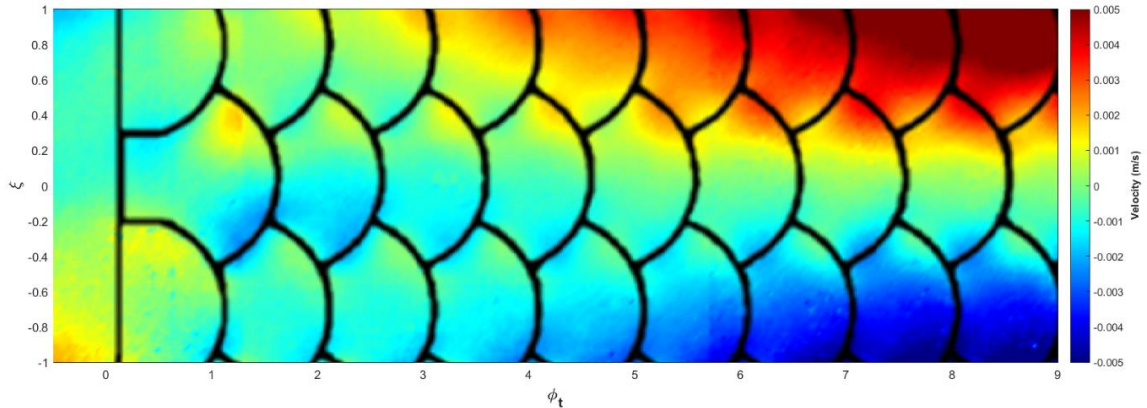


Figure 39: Colormap of the mean spanwise velocity at wall normal distance of $\lambda_1 = 2.5$. Flow is from left to right.

One of the challenges with a finite scale array is that the bounds of the array cause unexpected flow behaviour over the edges of the sample. In this case, the finite streamwise length and spanwise width cause a diverging spanwise velocity signature in the latter half of the scale array that is not related to the physical aspects of the scale features. As shown in Figure 39, beyond $\phi_t = 3$ there exists a strong negative spanwise velocity for values of negative ξ , and a strong positive spanwise velocity for values of positive ξ . This bias on either side of center of the scale array is caused by the finite bounds of the array and represents a diverging outflow towards the edges of the array as the flow approaches the end of the scale array.

This strong spanwise bias covers the underlying alternating spanwise velocity observed within the overlapping regions of the scale array (see Figure 39). Before removing this bias, the definition of the overlapping region is required. Figure 40 shows the bounds of the overlapping region ($\xi = \pm 0.26$ and ± 0.5) and the center of the overlapping region

(or overlapping plane at $\xi = \pm 0.375$) over the scale array. The spanwise velocity fluctuations of interest are observed in the overlapping region (between the blue dashed lines).

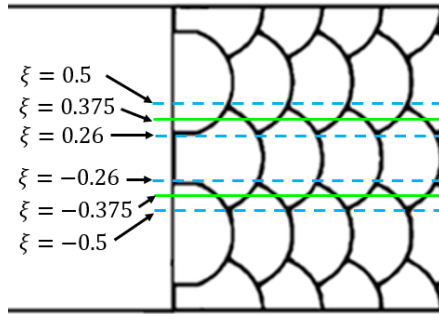


Figure 40: Schematic showing bounds of overlapping region (blue dashed lines) and center of overlapping region (or overlapping plane – green lines).

The bias found over the scale array is complex as it varies in both the streamwise and spanwise directions. To remove the bias and extract the underlying spanwise velocity fluctuations, the background flow field was obtained by applying a median filter to the original spanwise velocity field at each height to remove the localized fluctuations. This background flow field was then subtracted from the original field to isolate the fluctuations and obtain the unbiased spanwise velocity field. Given a median filter was used to remove the localized spanwise fluctuations observed in the overlapping regions ($\xi = \pm 0.375$), the size of the filter was selected such that the magnitude of these fluctuations was not impacted. To ensure these velocities were not impacted, the average peak amplitude for all fluctuations between $\phi_t = 1.5$ and 9 along spanwise locations of $\xi = \pm 0.375$ were calculated as a bulk parameter to track for different filter sizes. The non-dimensional spanwise velocity amplitude is defined in equation 2.16.

$$\omega = \frac{w}{U_\infty} \quad (2.16)$$

Various square median filters were tested ranging from 10 – 120 vectors in size at three wall normal location ($\lambda_2 = 1.63, 2.5, \text{ and } 5$). Figure 41 shows the convergence of the average peak spanwise velocity amplitude for different filter sizes.

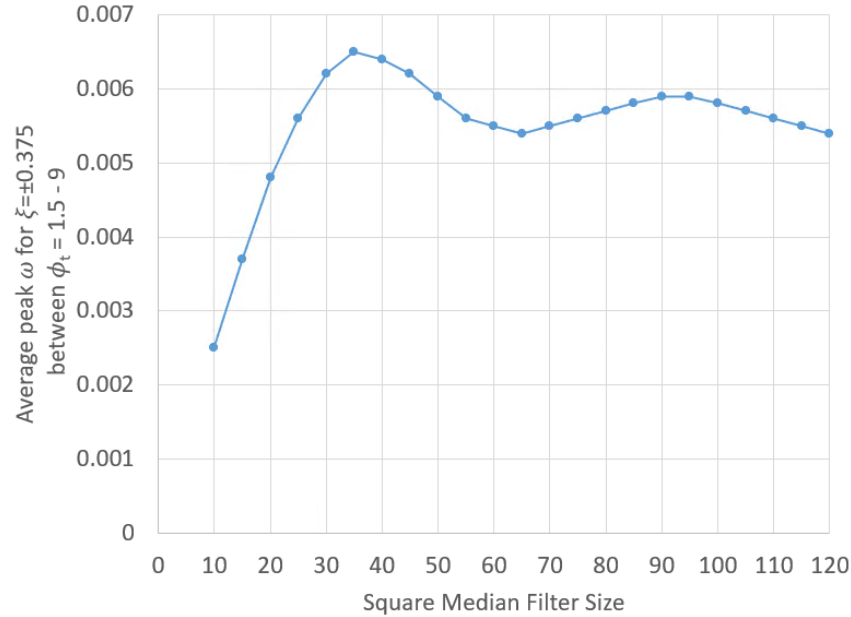


Figure 41: Convergence plot for square median filter size showing the average peak ω for $\xi = \pm 0.375$ at $\lambda_1 = 2.5$ between $\phi_t = 1.5$ to 9.

Given the convergence of the average peak amplitude above a filter size of 50 x 50 vectors, a square filter size of 55 x 55 vectors was selected as it produced a similar average peak amplitude to larger filter sizes but preserved the size of the resultant velocity field. Figure 42 shows the calculated background velocity colourmap using the median filter for $\lambda_1 = 2.5$ and Figure 43 shows the resultant unbiased spanwise velocity colourmap after subtraction for a wall normal location of $\lambda_1 = 2.5$.

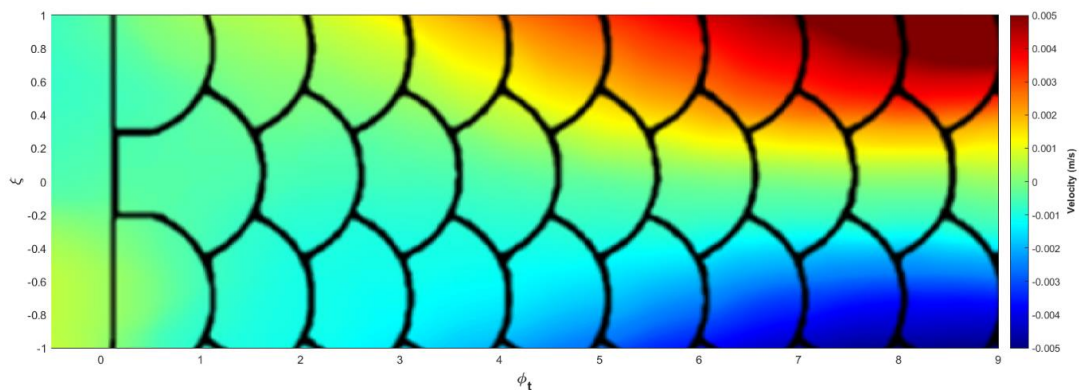


Figure 42: Filtered spanwise velocity field revealing the background spanwise velocity trends at a wall normal location of $\lambda_1 = 2.5$. Flow is from left to right.

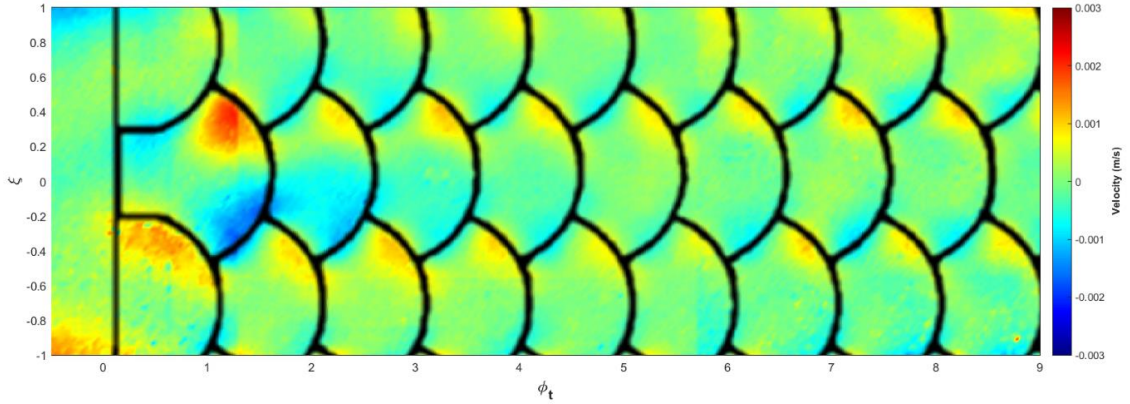


Figure 43: Resultant unbiased spanwise velocity field for a wall normal location of $\lambda_1 = 2.5$. Flow is from left to right.

The patterns in Figure 43 of the unbiased spanwise velocity field show a clear alternating spanwise velocity within the overlapping region of the scales. The velocity appears linked with the streamwise scales, alternating in relation to the scale heights in the overlapping region. This flow behaviour is similar to that mentioned in Muthuramalingam et al. (2019), where they only qualitatively assessed the wandering motion in the overlapping region. To understand how the spanwise velocity relates to streamwise scale heights, the magnitude of the spanwise velocity in the near surface region ($\lambda_1 = 2.5$) was plotted along the scale array ($1.5 < \phi_t < 9$) at spanwise locations of $\xi = \pm 0.375$ (see Figure 44). The spanwise position of $\xi = \pm 0.375$ is shown by the green lines in Figure 40.

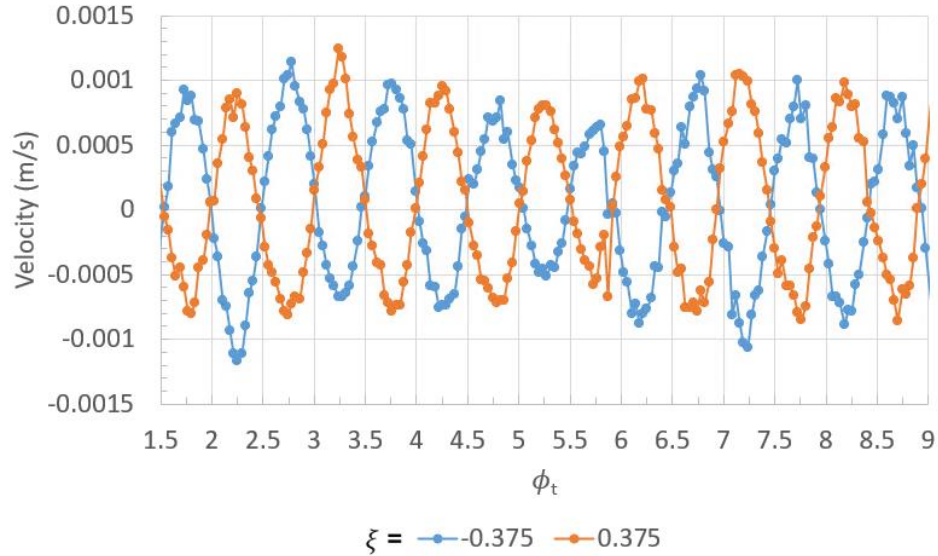


Figure 44: Spanwise velocity component along a streamwise line in the overlapping region ($\xi = -0.375$) at a wall normal distance of $\lambda_1 = 2.5$.

As Figure 44 shows, the spanwise velocity component is found to be related to the scale position in the streamwise direction. Peaks in the spanwise velocity occur at increments of $\phi_t = 0.5$ along the scale array. This relates to the streamwise offset of adjacent scale rows mentioned previously. Due to the overlapping nature of the scales from adjacent scale rows in the overlapping region, two scale heights are presented facing opposite spanwise directions for every increment of $\phi_t = 1$ in the overlapping region. This results in both a positive and negative spanwise velocity peak for each streamwise increment of $\phi_t = 1$. The spanwise velocity pattern is found to be mirrored between $\xi = -0.375$ (blue line in Figure 44) and $\xi = 0.375$ (orange line in Figure 44) as the scales overlap facing opposite spanwise directions on either side of the scale centerline. This results in velocity peaks at the same streamwise locations but with opposing magnitudes. To get a better perception of the alternating flow patterns that are generated in the overlapping regions, the wandering flow behaviour is shown schematically in Figure 45.

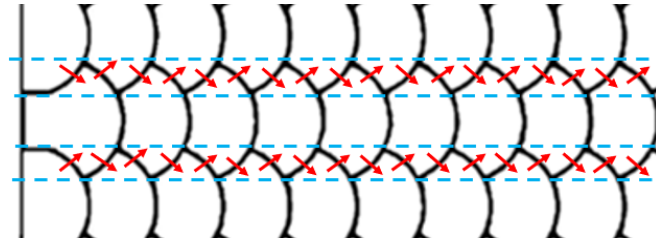


Figure 45: Schematic showing spanwise velocity patterns in the overlapping region.

This alternating flow behaviour is only observed in the overlapping region of the scales and appears confined by the edges of the overlapping scales shown by the blue dashed lines in Figure 45. The bounds of the overlapping region correspond to $\xi = \pm 0.26$ and ± 0.5 as is shown in Figure 40. Given the spanwise velocity is found to be confined to the overlapping region (see Figure 43), this reinforces the link between the alternating flow behaviour and the surface pattern.

To understand the wall normal extent of these spanwise variations, Figure 46 shows the non-dimensional spanwise velocity variation (ω) at all measured wall normal locations (λ_1) along a streamwise line in the overlapping region ($\xi = 0.375$).

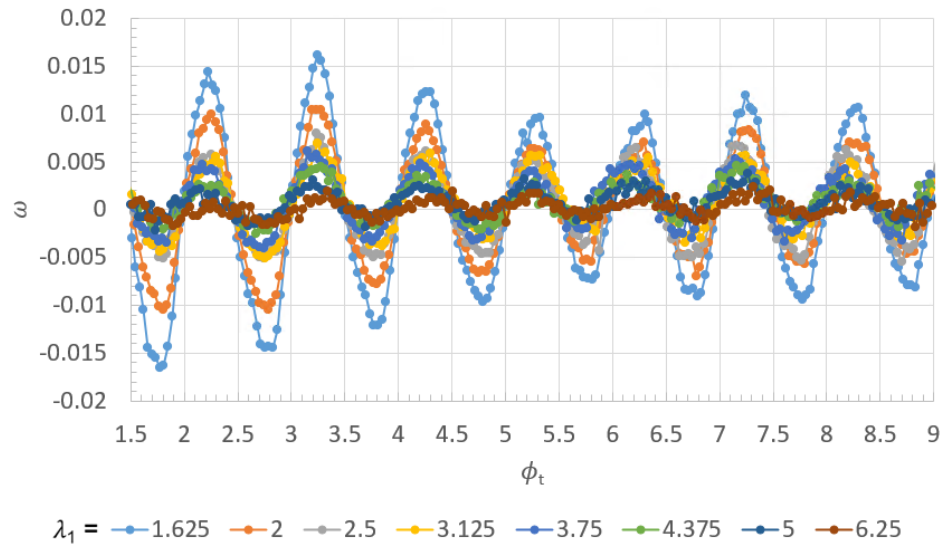


Figure 46: Non-dimensional spanwise velocity variation (ω) at all measured wall normal locations (λ_1) along a streamwise direction in the overlapping plane ($\xi = 0.375$).

Similar to the behaviour of the streamwise streaks, the amplitude of the spanwise velocity variations (ω) in overlapping region is found to decrease as λ_1 increases. The strongest variations are found closer to the surface where the scale pattern has the most influence on the flow behaviour. The wall normal dissipation of these flow patterns is said to be related to the viscous effects within the boundary layer. The peak amplitudes of the spanwise velocity shows minimal variations in the streamwise direction beyond $\phi_t = 4$. This indicates the consistency of these patterns in the streamwise direction and suggests a shorter development length is associated with the spanwise velocity. The largest amplitude of the spanwise variations is about 1.5% of the free-stream velocity indicating that the spanwise velocity variations are very small compared to the streamwise velocity.

To summarize the effects in the wall normal direction, the average peak spanwise velocity amplitude (ω) for all peaks between $\phi_t = 1.5$ and 9 at $\xi = \pm 0.375$ was computed for each wall normal height. Figure 47 shows the average peak spanwise velocity amplitude at each height (λ_1) and the error bars represent the associated 95% confidence intervals.

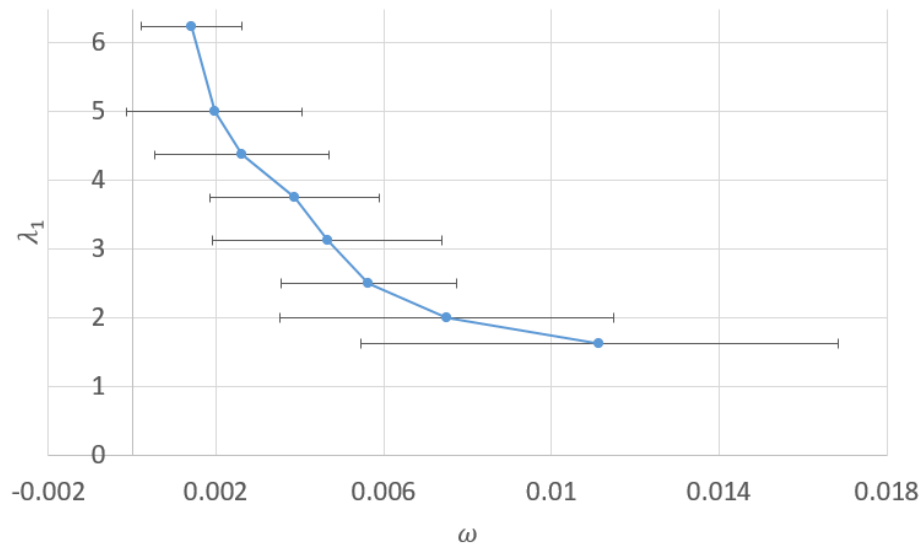


Figure 47: Average peak spanwise velocity amplitude (ω) for all peaks between $\phi_t = 1.5$ and 9 at spanwise locations of $\xi = \pm 0.375$ for each wall normal height (λ_1). The 95% confidence interval is plotted as error bars.

The pattern in the peak spanwise velocity amplitude shows a decreasing trend in the wall normal direction, as was highlighted previously. Interestingly, the amplitude of the spanwise fluctuations shows a much quicker dissipation in the wall normal direction than the streamwise velocity streaks (Figure 38). Additionally, where the streamwise amplitude showed a plateau close to the surface, the spanwise velocity amplitudes in the overlapping region show a plateau at larger wall normal distances. Given the predominantly streamwise flow that is present over the scale array and the smaller scale heights that are present in the overlapping region, it follows that the spanwise velocity variations dissipate quicker in the wall normal direction.

The alternating spanwise velocity component found in the overlapping region is similar to that which is created in transverse wall motion, or other active methods of drag reduction. The spanwise oscillations in these types of flows induce what is called a “Stokes Layer,” or an oscillating boundary layer (Agostini et al., 2014). The introduction of a Stokes layer via transverse wall motions has been proven to reduce friction drag in turbulent flows through the interaction with the near wall turbulence generation mechanisms (Leschziner, 2020). Although these findings are in the turbulent flow regime, research has also found that spanwise wall motion (and the associated Stokes layer) has the ability to modulate the streak intensity of unsteady boundary layer streaks formed over a flat plate in laminar flows (Ricco, 2011). Given that the overlapping nature of the scales creates localized spanwise motion via a passive mechanism, it is hypothesized that the localization of this behaviour plays an important role in delaying the transition to turbulence. The ability for transverse wall motion or spanwise wall forcing to attenuate instabilities (Agostini et al., 2014), suggests that these localized spanwise variations contribute to the suppression of instabilities in the boundary layer and may contribute to delaying the transition to turbulence.

The final section of the horizontal plane analysis will focus on the wall normal vorticity which is generated by the velocity gradients in the horizontal plane.

2.4.3.3 Wall Normal Vorticity

While the streamwise and spanwise velocity components reveal interesting flow behaviours across the scale array, the gradients associated with these velocities reveal an intriguing pattern in the wall-normal vorticity. The wall-normal vorticity is defined as the difference between the $\frac{\partial u}{\partial z}$ and $\frac{\partial w}{\partial x}$ velocity gradients, resulting in positive wall normal vorticity in the anticlockwise direction and vice versa. Figure 48 shows the colormap of the wall normal vorticity for the flow over the scale array at a wall normal height of $\lambda_1 = 2.5$.

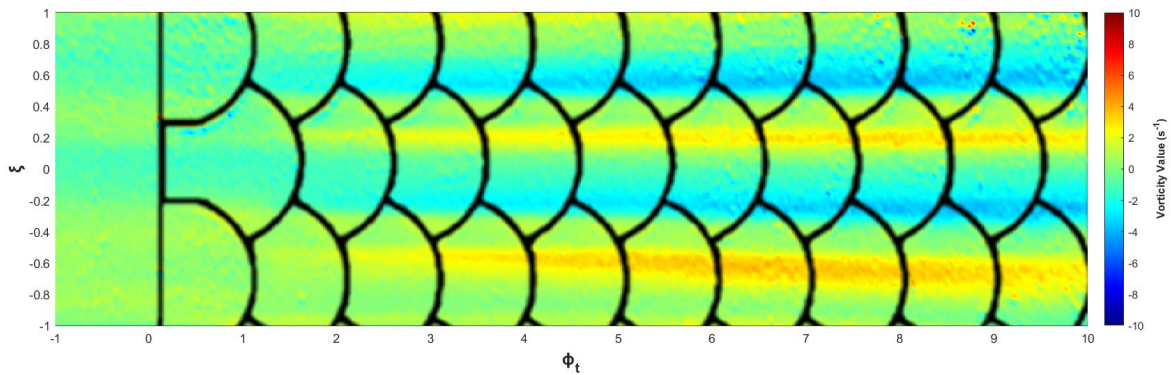


Figure 48: Colourmap of the mean wall-normal vorticity at wall normal distance of $\lambda_1 = 2.5$. Flow is from left to right.

The vorticity colourmap plot shows that there is some streamwise development of the vorticity streaks over the scale array. These streaks are observed adjacent to the overlapping region along the midline plane ($\xi = 0.26$). They appear to develop over some streamwise length of the scale array, and show a counter rotating pattern pushing fluid towards the overlapping region on either side of the scale centerline.

The patterns in vorticity arise due to the variations in the underlying surface patterns. The patterns in vorticity show the counter rotation of the fluid along the scale centerline towards the overlapping region, which relates to the changing scale height across the width of the scale. Given that the scales protrude from the surface with the largest surface variations located at $\xi = 0$ and $\xi = \pm 0.75$, fluid takes the path of least resistance moving towards the overlapping regions on either side of the scale centerline. This results

in strong velocity gradients and a vorticity pattern showing the rotation of the fluid from the centerline to the overlapping region.

Given that the flow is predominantly in the streamwise direction, and there is significant spanwise variation in the streamwise velocity within the boundary layer (Figure 35), these vorticity streaks are largely driven by the streamwise velocity gradient $\frac{\partial u}{\partial z}$. Although there exists some spanwise velocity in the overlapping region, this velocity component is approximately two orders of magnitude smaller than the streamwise component and therefore does not exhibit any significant contribution to the wall normal vorticity. As such, the vorticity patterns indicate a flow transfer from the scale centerline region into the overlapping region on either side of the scale. To explore how these vorticity patterns vary in the wall normal direction, the vorticity profiles across the array at the streamwise position of $\phi_t = 4.5$ were compared for all measured wall normal locations (see Figure 49).

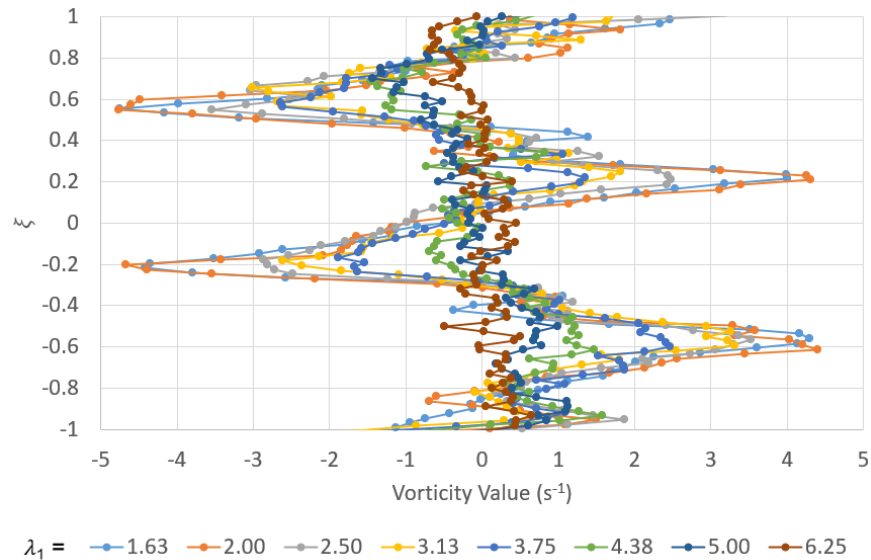


Figure 49: Wall-normal vorticity profiles across the array at a streamwise position of $\phi_t = 4.5$ for different wall normal distances (λ_1).

Figure 49 shows that the vorticity magnitudes are stronger in the near surface region and decrease as the distance from the surface increases. This trend matches the trend in the streamwise velocity streaks and confirms that this flow behaviour is related to the scale

topography. As the viscous dissipation effects take over in the wall normal direction, the magnitude of the streamwise velocity variations and associated velocity gradients decrease. Thus, resulting in a decrease in the vorticity as well.

It is also noted that the vorticity streaks appear to be bounded by the edges of the scale overlap defined previously in Figure 40 ($\xi = 0.26$ and 0.5). From Figure 49, it is observed that the spanwise locations of the vorticity peaks corresponds to values of $\xi = 0.2$ and 0.56 , which are located close to the corresponding scale overlap thresholds ($\xi = 0.26$ and 0.5). Thus, the midline region is found to serve as the connecting link between the flow characteristics along the scale centerline, and those in the overlapping region.

As mentioned earlier, the vorticity colormap plot shows some streamwise dependence of vorticity over the scale array, where the magnitude of wall normal vorticity increases in the downstream direction. This behaviour is linked to the streamwise dependence of the velocity streaks highlighted in Figure 37. As the velocity variation increases in the downstream direction, there must also be an increase in the velocity gradients leading to higher vorticity magnitudes. The vorticity peaks at a given wall normal distance in Figure 49 contain similar absolute magnitudes. The reason for this is that the symmetric design of the scale array ensures that flow is forced into the overlapping regions equally on either side of the scale centerline. To explore the streamwise dependence of these vorticity peaks, the average of the four absolute peak vorticity values (between $\xi = -1$ and 1) is plotted at four streamwise locations ($\phi_t = 2.5, 4.5, 6.5,$ and 8.5) and all wall normal heights in Figure 50. The associated 95% confidence intervals based on two times the standard deviation is included as error bars.

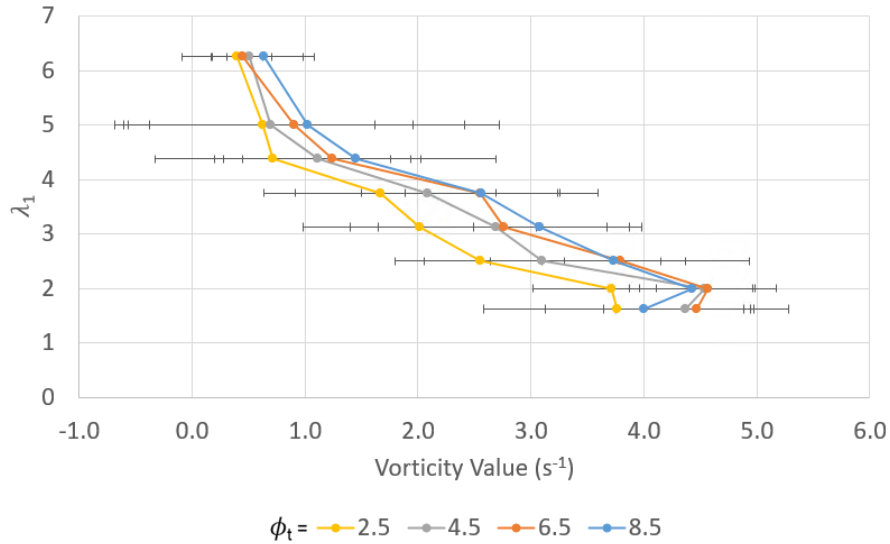


Figure 50: Average peak wall-normal vorticity (for ξ between -1 and 1) plotted at four streamwise locations ($\phi_t = 2.5, 4.5, 6.5, \text{ and } 8.5$) and all wall normal heights (λ_1).

It is observed from Figure 50 that at all streamwise locations the peak vorticity decreases with increasing distance away from the wall. However, the uncertainty bounds on the average peak values of vorticity in Figure 50 are too large to make any conclusive remarks about the peak magnitude dependence in the streamwise direction. The following discussion section will outline the key characteristics in the flow that lead to formation of such unique 3D flow over the scale array.

2.4.4 Discussion of 3D Flow Behaviour

While the flow behaviour over the fish scale arrays is inherently three-dimensional, breaking down the behaviour into different regions allows for a fundamental understanding of the flow patterns. Beginning with the flow along the scale centerline, the largest surface variations are found along this plane. As a result, a recirculation zone behind the scale height is found in the centerline region. This recirculation zone extends about 2.6 scale heights downstream (or about 13% of the scale length) and contributes to the upward shift in the mean wall normal velocity profiles compared to the Blasius solution (Figure 24). The streamwise flow which undergoes separation along the centerline ($\xi = 0$) is shown to have a continued impact throughout the boundary layer up

to a height of $\lambda_1 = 4 - 5$. It is noted that this corresponds to the height at which the streamwise velocity variations in the horizontal plane disappear (Figure 36). Thus, the recirculation zone and the vertical shift of the velocity profiles along the scale centerline is one mechanism which is causing the streamwise velocity variation over the scale array.

Shifting in the spanwise direction to the midline plane ($\xi = 0.26$) results in similar deviations in the mean streamwise velocity profiles compared to the Blasius solution (Figure 30). However, there appears to be a faster recovery to the Blasius profile ($\lambda_1 = 2 - 3$) compared to the centerline plane. Given the variation in scale height across the width of the scale, it is likely the smaller local scale height that results in a recovery to the Blasius solution at lower wall normal distances in the midline plane compared to the scale centerline. Although experimental challenges prevented measurement of flow recirculation in this region, the fact that the velocity profiles exhibit similar behaviours to that in the centerline plane, with recovery to the Blasius solution closer to the wall, it is speculated that the size of the recirculation zone in the midline plane is smaller than that in the centerline plane. The streamwise velocity profiles in the midline plane indicate a larger downward shift for profiles at greater values of ϕ relative to the centerline plane. These higher velocities are driven by the height variations across the width of the scale and the wall normal vorticity causing rotation of the fluid from the scale centerline to the overlapping regions on either side of the scale centerline.

Moving to the overlapping region revealed that the surface patterns had minimal impact on the mean wall normal streamwise velocity profiles (Figure 34) above a height of $\lambda_1 = 0.75$. As such, the wall normal streamwise velocity profiles showed a significant downward shift compared to the Blasius solution. This indicated a higher velocity was maintained throughout the near wall region of the boundary layer in the overlapping plane. Given the curvature of the scale geometry results in a difference in scale height across its width, valleys are formed in the overlapping region which contain a greater streamwise velocity as a result of the divergence of fluid from the centerline regions.

This divergence of the fluid from the scale centerline is observed in the wall normal vorticity colourmap (Figure 48). The larger surface variations along the scale centerline

result in a greater resistance to motion and fluid particles tend to move towards the overlapping regions on either side of the scale centerline. This vorticity pattern also relates to the formation of streamwise velocity streaks over the scale array (Figure 35). With low-velocity streaks aligned with the scale centerlines and high-velocity streaks aligned with the overlapping regions, the wall normal vorticity characterizes the streamwise velocity gradient associated with these velocity variations. Thus, the 3D variations in scale height are found to be a major contributor to both the streamwise velocity variations and wall normal vorticity streaks observed across the scale array.

The unique surface patterns are also found to contribute to the formation of a unique spanwise velocity pattern in the overlapping region. An alternating spanwise velocity pattern (Figure 44) is found to be related to the streamwise position along the array in the overlapping region ($\xi = \pm 0.375$). Peaks and valleys in the spanwise velocity component are found to be related to the streamwise location of the overlapping scale heights. As the scales in the adjacent rows merge, they form an alternating pattern of scale heights facing opposite spanwise directions. The spanwise velocity pattern shows that the flow in this region diverges off each of the overlapping scales as it moves in the streamwise direction (Figure 43). This creates an alternating spanwise velocity that is intrinsically linked to the underlying surface patterns (Figure 45). The spanwise velocity fluctuations are mirrored on either side of the scale centerline ($\xi = 0$) as the scales overlap facing opposite spanwise directions on either side of the scale centerline (Figure 44).

The spanwise velocity is speculated to have an impact on the recirculation region behind the scale heights. Given the overlapping scales meet the scale centerline region in the midline plane, the presence of a recirculation zone here would be impacted by the spanwise velocity. The spanwise velocity is likely to reduce the length of the recirculation zone and contribute to the movement of fluid along the edge of the scale toward the scale tip ($\xi = 0$). While it is difficult to experimentally demonstrate this from the current data, it is speculated that a 3D rolling vortex of this nature exists and facilitates the movement of fluid through the recirculation zone from the overlapping region to the scale centerline.

The alternating patterns in the spanwise velocity above the scale array and the wall normal vorticity streaks both appear bounded by the edge of the scale overlapping region ($\xi = \pm 0.26$ and ± 0.5). The interaction of these two flow behaviours is likely to result in the perpetuation of the spanwise velocity oscillations in the overlapping region. As the spanwise velocity approaches the edge of the scale overlap, it encounters a quickly accelerating streamwise velocity component with spanwise rotation back into the overlapping region. It is this interaction between the wall-normal vorticity and the spanwise velocity that continues the oscillatory flow patterns in the overlapping region.

All flow behaviours are found to diminish with increasing distance from the surface. This is said to be linked to the fluid viscosity whose contribution weakens these flow behaviours in the laminar boundary layer. In the near wall region, the streamwise velocity variations show an asymptotic behaviour below $\lambda_1 = 2.5$ (or $\lambda_2 = 0.31$). In this region, the streamwise velocity variations appear similar at multiple heights indicating a limit to the extent of the variations. These asymptotic trends are not observed in the spanwise velocity fluctuations, nor in the wall-normal vorticity streaks which show stronger trends incrementally closer to the surface.

Away from the surface, the wall normal extent of the streamwise variations is found to be considerable up to about $\lambda_1 = 4.38 - 5$ (or $\lambda_2 = 0.54 - 0.62$), after which the velocity variations quickly disappear. A similar trend is found in the wall-normal vorticity profiles as these are strongly linked to the streamwise velocity gradients. In contrast, the spanwise velocity variations in the overlapping region ($\xi = 0.375$) show a very weak signature above a wall normal distance of $\lambda_1 = 5.00$ (or $\lambda_2 = 0.62$). Overall these patterns highlight that while the flow is predominantly in the streamwise direction, the spanwise velocity fluctuations diminish more quickly (Figure 47) in the wall normal direction than the streamwise velocity streaks (Figure 38) and wall normal vorticity streaks (Figure 50). However, all flow behaviours are found to be contained well within the boundary layer.

The following section will discuss the impact of these unique flow structures on the potential friction drag generated over the scale array.

2.4.5 Drag Reduction Mechanisms

Now that a fundamental understanding of the 3D flow behaviour over the scale array has been developed, this section will discuss how these flow patterns impact surface drag. The above analysis has identified a few key flow behaviours that have the potential to play a role in the reduction of drag over fish scale arrays.

Looking first at the flow recirculation region, a small amount of fluid is found to be recirculated at small velocities relative to the streamwise flow in the region behind the scale heights. The vortex formed in this recirculation region converts the traditional sliding friction over a flat plate into a rolling friction at the boundary of the fluid vortex interface. A similar phenomenon was simulated in the flow over Barchan Dunes (Song et al., 2017) and fish scale pits (Hou et al., 2021), where it is hypothesized to be the dominant mechanism driving the drag reduction. While these geometries modeled the surface structures as pits below a flat surface, a similar phenomenon is observed in the current experimental results where the surface features protrude above the flat surface. The presence of such a vortex enables small negative flow velocities close to the wall decreasing the wall shear stress and associated skin friction in the region near the scale heights. This contributes to the lower shear-induced drag due to the interaction at the wall and enables the high-speed flow to instead interact with the upper fluid boundary of the recirculation vortex. This generates a lower overall surface drag because not only is the upper surface of the vortex already moving in the direction of the flow, but the fluid-fluid shear that is generated at this interface has less of an impact on the surface drag.

While Muthuramalingam et al. (2019) did not explore the impact of rolling friction, they discussed qualitatively, from simulation results, how the skin friction coefficient varied in relation to the scale heights. They compared the total simulated drag forces to the skin friction coefficient from laminar theory to determine if any drag reduction was present. In the current experimental analysis, given the wall normal streamwise velocity profiles vary in both the streamwise and spanwise directions, quantification of the skin friction coefficient is an experimentally challenging task. However, some insight can be gained from the evaluation of the momentum thickness.

While the momentum thickness is a measure of the momentum deficit within the boundary layer, it can be hypothesized that a lower momentum deficit relative to a flat plate may be related to a reduction in friction drag. Given a boundary layer is formed due to the interactions between a solid surface and the viscous flow, the presence of a boundary layer results in a momentum deficit. While a smooth plate is traditionally regarded as having the least resistance to flow, a smaller momentum deficit than the Blasius solution (representing the flat plate boundary layer) is likely the result of surface interactions which generate less drag. As highlighted in Table 5 and Table 6, the momentum thickness calculated for all positions along the scale length in both the centerline and overlapping region remained below that of a classical laminar boundary layer over a flat plate. This indicates potential for the biomimetic fish scale arrays to generate a friction drag reduction compared to the Blasius profile.

Another mechanism which is suggested to contribute to the drag reduction over the scale arrays is the delay in transition to turbulence. The delay in transition to turbulence is argued to decrease the friction drag because a turbulent boundary layer has a higher associated skin friction coefficient than that of a laminar boundary layer. Thus, the additional laminar region resulting due to a delay in transition to turbulence has a lower skin friction contribution decreasing the overall skin friction drag. Most notably is the work of Muthuramalingam et al. (2020) who assessed the downstream effects of a biomimetic fish scale array on the transition to turbulence experimentally. Their analysis suggests that biomimetic fish scale arrays can suppress the growth of Tollmien-Schlichting waves by reducing the time dependent velocity fluctuations far downstream of the scale array. A visualization technique and velocity measurements were used to determine the extent of the transition delay, which was then used to predict a 27% reduction in drag based on the laminar and turbulent boundary layer theory. While this work focused on the downstream effects of the scale array, only speculation about the mechanisms driving these observed behaviours is provided. The current research focuses on the detailed analysis over the scale array to determine the driving mechanisms.

Muthuramalingam et al. (2020) speculates the formation of streamwise velocity streaks as the mechanism resulting in delayed transition. They suggest that the formation of

streamwise velocity streaks leads to a spanwise average velocity profile with a smaller shape factor than the Blasius solution, contributing to the stabilization of the boundary layer. The current study quantifies the shape factor in the centerline and overlapping regions, showing a smaller shape factor compared to the Blasius solution is achieved throughout the overlapping region and for values of $\phi > 0.66$ on each scale in the centerline region. While the smaller shape factor results in a favourable pressure gradient and a greater resistance to flow separation, it is believed that the behaviour of the streamwise velocity streaks themselves contribute to the boundary layer stabilization.

Fransson et al. (2005) and Schlatter et al. (2010), show that introducing finite amplitude streaks within the boundary layer can result in the attenuation and in some cases complete suppression of Tollmien-Schlichting waves, which are often an instability that leads to turbulence. Additionally, Shahinfar et al. (2014) introduced streamwise streaks by miniature vortex generators and found that these streaks not only suppress Tollmien-Schlichting waves, but other instabilities such as single and pair oblique waves within the boundary layer. Thus, it has been shown that the presence of finite amplitude streamwise velocity streaks have particular benefits in suppressing flow instabilities. The mechanism driving this stabilization behaviour is suggested by Cossu and Brandt (2004) to be related to the kinetic energy associated with the spanwise shear. However, while the streamwise streaks have been proven effective, velocity streaks also play a fundamental role in the transition to turbulence (Cossu & Brandt, 2004), therefore it is important that the amplitude of the induced velocity streaks do not exceed some critical threshold that could lead to the breakdown of the streaks themselves into turbulence.

Previously, Andersson et al. (2001) simulated using DNS the natural formation of unsteady streamwise velocity streaks over a flat plate and found a critical streak amplitude of 26% of the free-stream velocity led to the amplification of streamwise travelling waves causing their breakdown to turbulence. Meanwhile, experimental work by Fransson et al. (2005) showed that using cylindrical roughness elements to generate streamwise velocity streaks led to turbulence breakdown above a critical streak amplitude of 12% of the free-stream velocity, as the vortex shedding behaviour over the roughness elements became unstable. Additionally, Fransson and Talamelli (2012) showed

experimentally that using mini-vortex generators the critical amplitude can be increased above 30% of the free-stream velocity. These findings suggest that the critical amplitude leading to the breakdown to turbulence is linked to the streak generation mechanism. Thus, while fish scale arrays present a unique method to generate streamwise velocity streaks, exploration into the critical streak amplitude leading to turbulent breakdown is still needed.

While traditional methods of inducing streamwise velocity streaks include the use of a single array of elements in the streamwise direction, the velocity streaks are found to decay rapidly in the streamwise direction (Fransson & Talamelli, 2012). Fransson and Talamelli (2012) also showed that by introducing a second array of vortex generators in the downstream direction the velocity streaks could be reintroduced resulting in a further delay in transition to turbulence. Thus, given the streak generation mechanism over fish scale arrays contains continued forcing in the streamwise direction, it is suggested that this will contribute to further delay in transition to turbulence compared to the alternative methods discussed here.

In the case of biomimetic fish scale arrays, it is argued that the critical streak amplitude leading to the breakdown to turbulence may be greater than the critical amplitudes found for mini-vortex generators and cylindrical roughness elements. The reason for this is that fish scale arrays present a passive method of streamwise streak generation, where the unique scale patterns have the benefit of continued forcing in the streamwise direction. This is likely to result in a stable streak behaviour that can support streamwise streak amplitudes much higher than those found using other methods. Further exploration into the transition process happening over the scale array is needed to understand the continued role this mechanism plays in the transition to turbulence.

Finally, another unique flow behaviour which is suggested to contribute to the drag reduction of flow over fish scale arrays is the spanwise velocity fluctuations found in the overlapping region. It is suggested that these fluctuations contribute as a mechanism delaying the transition to turbulence. The spanwise alternating patterns in the overlapping region draw close similarity to the flow behaviour found over surfaces undergoing

transverse wall motion. Transverse wall motion introduces a Stokes layer within the near wall region as a result of the oscillating boundary (Leschziner, 2020). This flow behaviour has been shown to influence the transition to turbulence through the ability to disrupt the growth of instabilities preceding the breakdown to turbulence (Agostini et al., 2014). Ricco (2011) also studied the impact of spanwise wall forcing in laminar flows and found that it had the ability to modify the amplitude of streamwise velocity streaks. Thus, given the ability for the overlapping features to create a steady localized spanwise oscillation, it is hypothesized that these oscillations not only suppress instabilities within the boundary layer leading to the delay in transition, but may also contribute to amplification of the streamwise velocity streaks.

In this section, the different mechanisms leading to drag reduction over fish scale arrays were explored. Mechanisms such as the flow recirculation region converting sliding friction into rolling friction, and the comparison of momentum thickness to the Blasius solution were discussed in terms of their impact on the friction drag directly. The streamwise velocity streaks and spanwise velocity variations were discussed in the context of suppressing boundary layer instabilities and delaying the transition to turbulence. Ultimately, it is the combination of different mechanisms which results in the ability for the fish scale arrays to not only reduce friction drag but also suppress instabilities and delay the transition to turbulence.

2.5 Impact of Reynolds Number

The detailed results and analyses presented in the preceding sections are based on the flow over the scale array at a free-stream velocity of 0.12 m/s and θ_{ratio} of 5.6. This section will summarize the exploratory results regarding the impact of the free-stream velocity on the flow structures in the near wall boundary layer over the biomimetic fish scale array. The same experimental setup and scale array as described earlier were used. Measurements were conducted at a fixed height from the wall of 2 mm and captured a region across the scale array up to $\phi_t = 6$ (or $S_{0,6}$). The free-stream velocity varied between 0.028 m/s and 0.182 m/s resulting in a boundary layer to scale height ratio (θ_{ratio}) between 4.6 and 12. The non-dimensional parameters Re_{BL} and θ_{ratio} are

calculated using equations 2.2 and 2.3 and shown in Table 7 along with the free-stream velocities for each flow condition.

Table 7: Free-stream velocity and non-dimensional values for experiments at all flow conditions.

Parameter	Speed 1	Speed 2	Speed 3	Speed 4	Speed 5	Speed 6	Speed 7
U_∞ (m/s)	0.028	0.036	0.066	0.083	0.12	0.14	0.18
Re_{BL}	265	300	400	450	550	600	670
θ_{ratio}	11.8	10.4	7.7	6.9	5.7	5.2	4.6

Figure 51 shows the colormaps of the non-dimensional mean streamwise velocity component over the scale array at all measured flow conditions. The streamwise and spanwise positions are non-dimensionalized using equations 2.9 and 2.10, respectively.

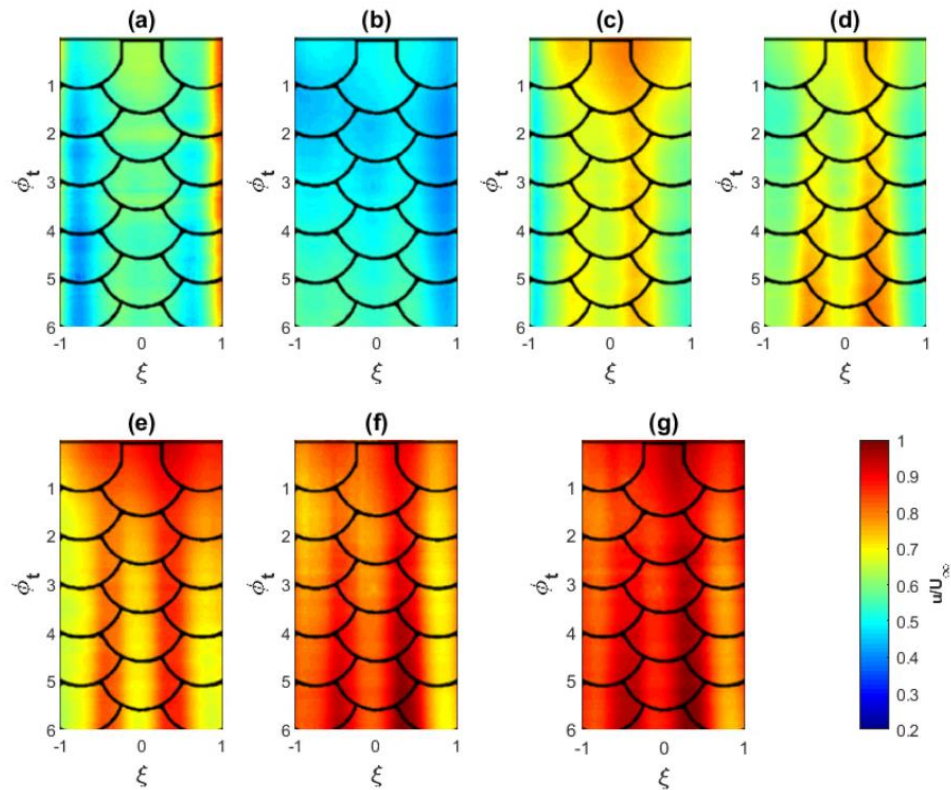


Figure 51: Colormap of the non-dimensional mean streamwise velocity over the scale array at free-stream velocities of (a) 0.028 m/s (b) 0.036 m/s (c) 0.066 m/s (d) 0.083 m/s (e) 0.12 m/s (f) 0.14 m/s (g) 0.18 m/s. Flow is from top to bottom.

The mean streamwise velocity colourmaps show the presence of streamwise velocity streaks at all flow conditions. Although streamwise velocity streaks appear in all cases, the strength of these streaks appears to depend on the free-stream velocity magnitude. To quantitatively explore the strength of these velocity streaks, the streamwise velocity variation (ψ) is plotted in Figure 52 at a streamwise location of $\phi_t = 4.5$ for all flow conditions.

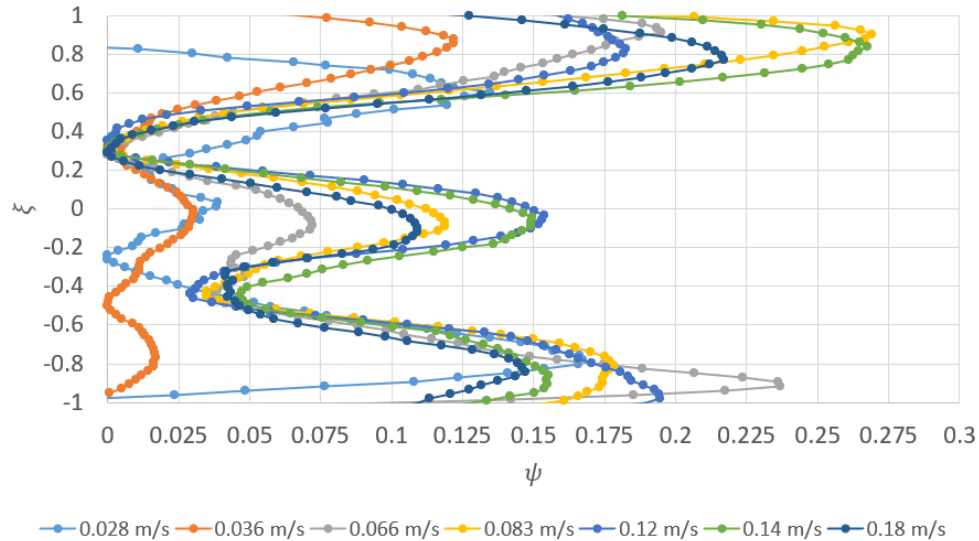


Figure 52: Non-dimensional streamwise velocity variation (ψ) at a wall normal distance of $\lambda_1 = 2.5$ and streamwise position $\phi_t = 4.5$, for varying flow conditions.

The results show that the magnitude of the streamwise velocity variations decreases as the free-stream velocity decreases. Thus, the range of velocity variations across the array follow the trend of the free-stream velocity. It is important to note that the boundary layer thickness increases with decreasing free-stream velocity. Hence, a fixed height would result in a non-dimensional location relative to the boundary layer thickness (λ_2) closer to the surface for smaller free-stream velocities. Thus, one could also plot the streamwise velocity variation across the array for various wall normal location (λ_2) to understand the relationship between the streamwise velocity variation and the boundary layer thickness.

Given the exploratory nature of these experiments, only horizontal plane measurements were completed at one height, which did not give any information regarding the boundary

layer thickness. However, given the close agreement to the classical theoretical laminar boundary layer upstream (see Figure 17), a theoretical estimation of the boundary layer thickness based on the free-stream velocity and distance from the leading edge can be done using equation 2.16 (White, p. 459, 2016). This boundary layer thickness can then be used to estimate λ_2 for each flow condition. The streamwise velocity variation (ψ) was then plotted for varying values of λ_2 (see Figure 53).

$$\delta = \frac{5x}{\sqrt{\frac{x * U_{\infty}}{\nu}}} \quad (2.16)$$

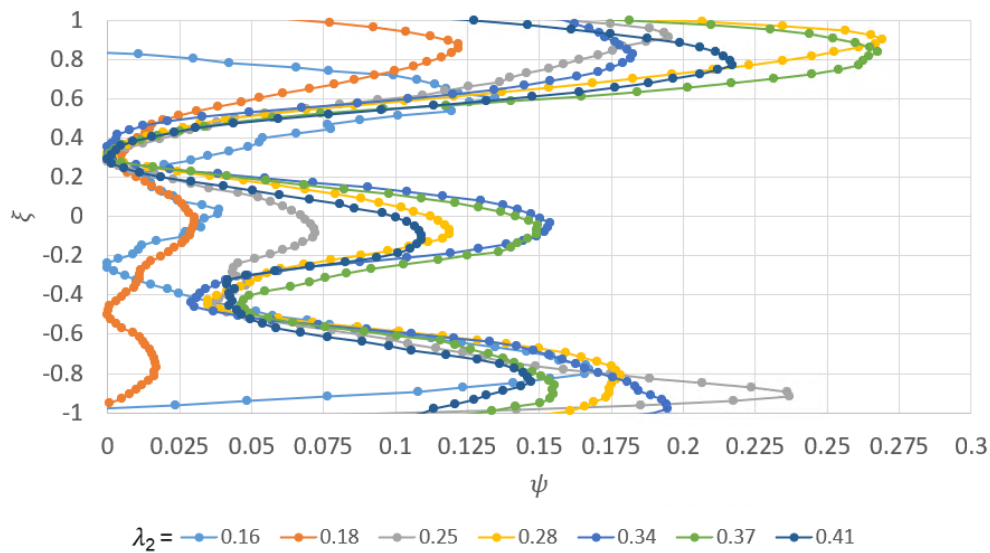


Figure 53: Non-dimensional streamwise velocity variation (ψ) at a streamwise position of $\phi_t = 4.5$ for different wall normal distances (λ_2) based on varying free-stream velocity conditions.

Given that different free-stream velocities result in different boundary layer thicknesses, Figure 53 shows that decreasing the non-dimensional distance from the wall (λ_2) results in a decrease in the magnitude of the velocity variation. The earlier results in Figure 36 show that at a given free-stream velocity the magnitude of velocity streaks increases with a decrease in λ_2 . Thus, the results here act in opposition to this and show that if the free-stream velocity is changed resulting in a decrease in λ_2 , the magnitude of the velocity streaks is found to decrease. This highlights that the behaviour of the streamwise velocity

variations under varying flow conditions appears related to the free-stream velocity rather than the boundary layer thickness.

Similarly, the non-dimensional unbiased spanwise velocity component over the scale array at all measured flow conditions is presented in Figure 54. It was mentioned previously that the finite nature of the scale array produced a bias in the spanwise velocity component that appears as a flow divergence for large values of ϕ_t . The same median filter was used to identify the spanwise velocity bias over the scale array and isolate the spanwise velocity variations.

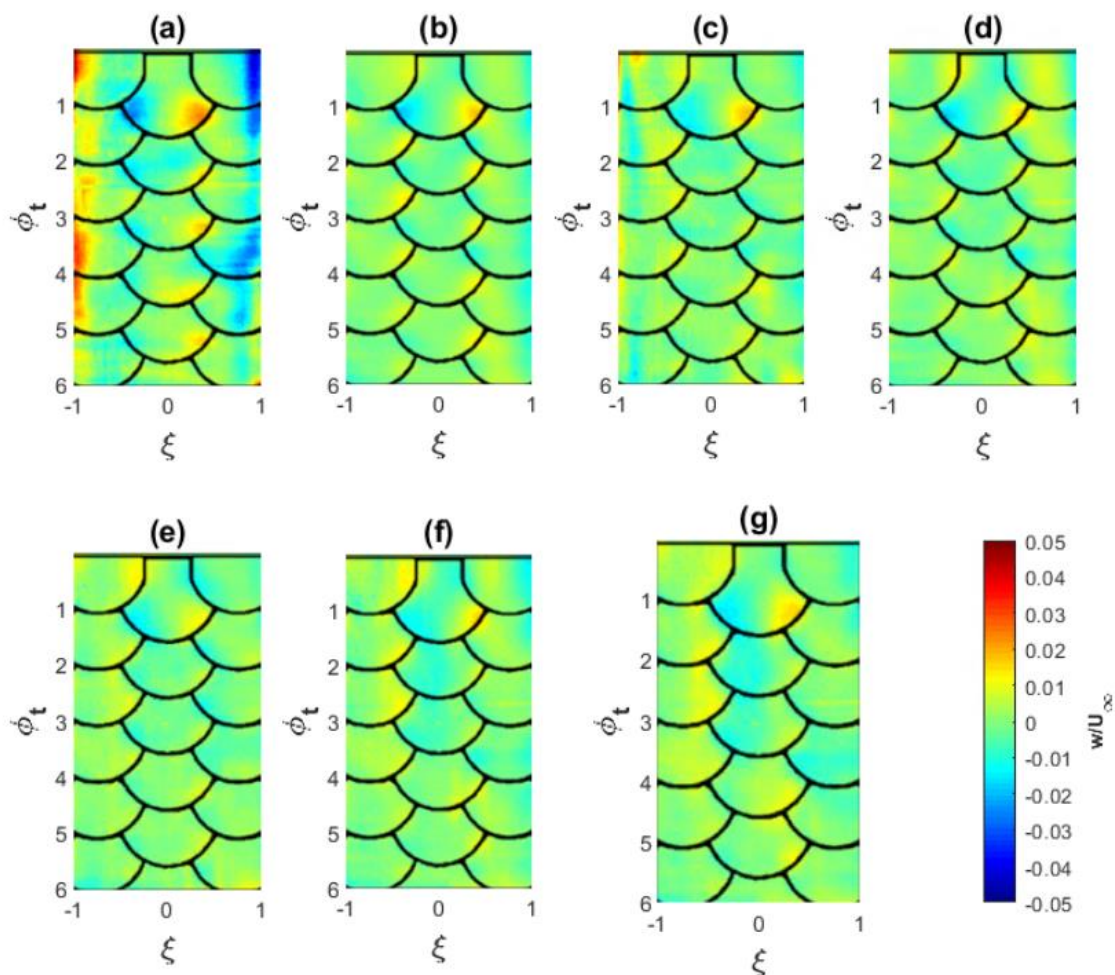


Figure 54: Colormap of the non-dimensional normalized mean spanwise velocity for all measured speeds over the scale array (a) 0.028 m/s (b) 0.036 m/s (c) 0.066 m/s (d) 0.083 m/s (e) 0.12 m/s (f) 0.14 m/s (g) 0.18 m/s. Flow is from top to bottom.

The colourmap plots show that all free-stream velocity conditions appear to exhibit an alternating spanwise velocity component in the overlapping region. Given the magnitude of the spanwise velocity is normalized using the free-stream velocity, similar variations are found across all flow conditions. To further explore the quantitative extent of these spanwise velocity fluctuations, the non-dimensional spanwise velocity (ω) is plotted for a spanwise location of $\xi = 0.375$ at a wall normal distance of $\lambda_1 = 2.5$ for all flow conditions (Figure 55).

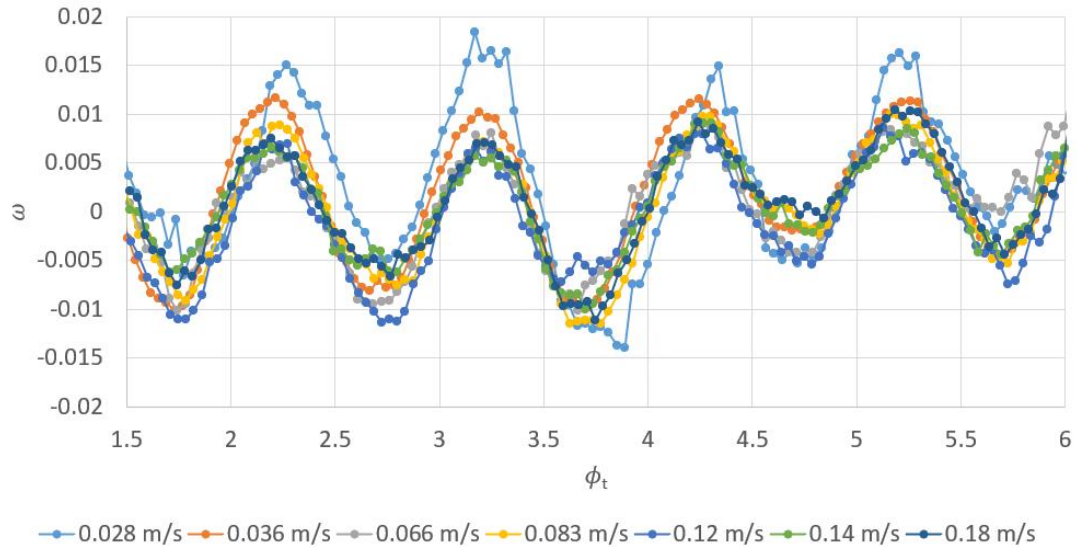


Figure 55: Non-dimensional spanwise velocity (ω) at a wall normal location of $\lambda_1 = 2.5$ and spanwise position $\xi = 0.375$ for all flow conditions.

The non-dimensional spanwise velocity in the overlapping region shows that at the same wall normal position the amplitude of the velocity fluctuations remains almost the same percentage of the free-stream velocity for all flow conditions, except the smallest velocity (0.028 m/s). Although the magnitudes of the spanwise velocity will vary depending on the free-stream conditions, the behaviour relative to the free-stream velocity does not change. Given the measurements were conducted at a fixed wall normal location, the alternating patterns are found to be independent of the boundary layer thickness and instead clearly linked to the underlying surface geometry and the free-stream velocity.

Given the induced flow behaviours are analogous to flow instabilities, the viscous effects of the boundary layer tend to have a dissipative effect. This was observed in the results for a single free-stream velocity which showed that increasing distance from the wall resulted in decreases in the observed flow behaviour. As such, smaller free-stream velocities are shown to exhibit smaller variations, limiting the strength and wall normal extent of the observed flow behaviours. Further work is needed to explore the factors driving the relationship between the streamwise velocity variations and changes in the flow conditions. Also, a deeper understanding of the practical limits and optimal flow conditions for the observed behaviours is required.

2.6 Conclusion

An experimental water channel was designed and built for the purpose of conducting PIV measurements over structured surfaces. The facility was tested and validated to ensure a consistent channel velocity profile and minimal turbulence intensity were present in the region of the structured surface. A biomimetic fish scale array with eight times geometry scaling was manufactured and tested inside the facility. PIV results were obtained along multiple planes horizontal and vertical to capture the flow behaviours within the near wall boundary layer. Three vertical planes were considered along the scale centerline, midline and overlapping region. Multiple horizontal planes captured the dynamics across the scale array. The lack of experimental analysis exploring the flow features in the near wall region over biomimetic fish scale arrays was the main motivation for this analysis. Given the potential for these features to reduce drag, understanding the physical mechanisms governing their flow behaviour will help inform the design of engineered surfaces for the purposes of reducing drag.

The velocity results over the leading edge proved a steady laminar boundary layer was formed in the region upstream of the scale array. Additionally, the velocity results over the scale array allowed for detailed analysis of the 3D flow behaviour and deeper understanding of the unique flow structures. The variations in the underlying surface topography were found to be the main drivers of the unique flow structures. In the spanwise direction over a single scale it is the local change in peak scale height which causes the divergence of flow from the scale centerline to the overlapping regions. The

larger surface variations along the scale centerline cause a greater resistance to streamwise motion. This resistance to motion manifests itself as low velocity streaks originating along the centerline plane. The gradual change in height as you move in the spanwise direction across the scale results in a wall normal vorticity pattern characteristic of the rotation of fluid towards the overlapping regions. With less resistance to streamwise motion the fluid is forced towards the overlapping region while keeping its momentum. This results in high-velocity streaks found in the overlapping region. This describes the formation of the streamwise velocity streaks and wall normal vorticity that are characteristic of the underlying changes in surface topography.

While the streamwise velocity streaks are likely to contribute to the stabilization of the boundary layer and delaying the transition to turbulence, two other unique flow behaviours were observed in the near wall boundary layer. First, the flow recirculation region behind the scale centerline was found to have a reattachment length similar to that of a horizontal backwards facing step. The recirculation zone results in a region of upward shifted wall normal streamwise velocity profiles that contribute to a lower wall shear stress within the boundary layer. The conversion of sliding friction to rolling friction is also hypothesized to contribute to drag reduction over the fish scale arrays. The second unique flow behaviour identified was the alternating spanwise velocity found in the overlapping region. This alternating spanwise velocity is found to be related to the streamwise overlapping of scales from adjacent scale rows. This flow behaviour is also hypothesized to contribute to the suppression of instabilities and delaying the transition to turbulence. Given all flow behaviours are found to dissipate with increasing wall normal distance, this highlights the impact of the viscous dissipation effects within the boundary layer and the link between the observed flow patterns and underlying scale topography.

Finally, preliminary work investigating the relationship between the free-stream flow conditions and the observed flow patterns revealed that the streamwise velocity variations follow the trends in the free-stream velocity, where smaller velocity variations are found at smaller free-stream velocities. In contrast, the spanwise velocity fluctuations are found to exhibit the same non-dimensional velocity amplitude regardless of the free-stream conditions. Thus, the alternating spanwise velocity remains the same percentage of the

free-stream velocity, and only the magnitude of the spanwise component is impacted by the free-stream conditions. The behaviours in the streamwise velocity streaks appear to be related to the free-stream velocity, whereas the alternating spanwise velocity variations appear to have a similar behaviour at multiple flow conditions.

Future work is required to strengthen our understanding of the impact of free-stream velocity on the observed flow behaviours. This would enable a more robust understanding of the practical limits and optimal conditions under which these fundamental mechanisms are generated. The next chapter will focus on the development of a numerical model for simulating the flow over these scale arrays and explore the impact of scale shape on the observed flow behaviours.

Bibliography

- Abbas, A., Bugada, G., Ferrer, E., Fu, S., Periaux, J., Pons-Prats, J., Valero, E., & Zheng, Y. (2017). Drag reduction via turbulent Boundary Layer Flow Control. *Science China Technological Sciences*, 60(9), 1281–1290. <https://doi.org/10.1007/s11431-016-9013-6>
- Agostini, L., Toubert, E., & Leschziner, M. A. (2014). Spanwise oscillatory wall motion in channel flow: Drag-reduction mechanisms inferred from DNS-predicted phase-wise property variations at $Re = 1000$. *Journal of Fluid Mechanics*, 743, 606–635. <https://doi.org/10.1017/jfm.2014.40>
- Anderson, E. J. (2005). Advances in the visualization and analysis of boundary layer flow in swimming fish (Phd thesis). Woods hole oceanographic institution, United States.
- Anderson, E. J., McGillis, W. R., & Grosenbaugh, M. A. (2001). The boundary layer of swimming fish. *Journal of Experimental Biology*, 204(1), 81–102. <https://doi.org/10.1242/jeb.204.1.81>
- Andersson, P., Brandt, L., Bottaro, A., & Henningson, D. S. (2001). On the breakdown of boundary layer streaks. *Journal of Fluid Mechanics*, 428, 29–60. <https://doi.org/10.1017/s0022112000002421>
- Bai, H. L., Zhou, Y., Zhang, W. G., Xu, S. J., Wang, Y., & Antonia, R. A. (2014). Active control of a turbulent boundary layer based on local surface perturbation. *Journal of Fluid Mechanics*, 750, 316–354. <https://doi.org/10.1017/jfm.2014.261>
- Bechert, D. W., Bruse, M., & Hage, W. (2000). Experiments with three-dimensional riblets as an idealized model of shark skin. *Experiments in Fluids*, 28(5), 403–412. <https://doi.org/10.1007/s003480050400>
- Bechert, D. W., Bruse, M., Hage, W., Van Der Hoeven, J. G., & Hoppe, G. (1997). Experiments on drag-reducing surfaces and their optimization with an adjustable geometry. *Journal of Fluid Mechanics*, 338, 59–87. <https://doi.org/10.1017/s0022112096004673>
- Bell, J. H., & Mehta, R. D. (1988). (tech.). *Contraction Design for Small Low-Speed Wind Tunnels*. National Aeronautics and Space Administration.
- Bhatia, D. D., Yang, G., Li, G., & Wang, J. (2020). Selection and impact of leading edge on boundary layer transition. <https://doi.org/10.21203/rs.3.rs-29913/v1>
- Bhushan, B., Jung, Y. C., & Koch, K. (2009). Self-cleaning efficiency of artificial superhydrophobic surfaces. *Langmuir*, 25(5), 3240–3248. <https://doi.org/10.1021/la803860d>
- Bixler, G. D., & Bhushan, B. (2013). Fluid drag reduction with shark-skin riblet inspired microstructured surfaces. *Advanced Functional Materials*, 23(36), 4507–4528. <https://doi.org/10.1002/adfm.201203683>
- Burdak, V. D. (1986). Morphologie fonctionnelle du tegument ecailleux des poissons. *Cybiurn*, 10, 1-128.

- Claireaux, G., Couturier, C., & Groison, A.-L. (2006). Effect of temperature on maximum swimming speed and cost of transport in Juvenile European Sea bass (*dicentrarchus labrax*). *Journal of Experimental Biology*, 209(17), 3420–3428. <https://doi.org/10.1242/jeb.02346>
- Clarke, T. A., & Fryer, J. G. (1998). The development of camera calibration methods and Models. *The Photogrammetric Record*, 16(91), 51–66. <https://doi.org/10.1111/0031-868x.00113>
- Cossu, C., & Brandt, L. (2004). On Tollmien–Schlichting-like waves in streaky boundary layers. *European Journal of Mechanics - B/Fluids*, 23(6), 815–833. <https://doi.org/10.1016/j.euromechflu.2004.05.001>
- Cowen, E. A., Monismith, S. G., Cowen, E. A., & Monismith, S. G. (1997). A hybrid digital particle tracking velocimetry technique. *Experiments in Fluids*, 22(3), 199–211. <https://doi.org/10.1007/s003480050038>
- Dean, B., & Bhushan, B. (2010). Shark-skin surfaces for fluid-drag reduction in turbulent flow: A Review. *Philosophical Transactions of the Royal Society A: Mathematical, Physical and Engineering Sciences*, 368(1929), 4775–4806. <https://doi.org/10.1098/rsta.2010.0201>
- Dou, Z., Wang, J., & Chen, D. (2012). Bionic research on fish scales for drag reduction. *Journal of Bionic Engineering*, 9(4), 457–464. [https://doi.org/10.1016/s1672-6529\(11\)60140-6](https://doi.org/10.1016/s1672-6529(11)60140-6)
- Encyclopedia Britannica. (1998, July 20). *Aberration*. Encyclopedia Britannica. Retrieved January 18, 2023, from <https://www.britannica.com/technology/aberration#ref249089>
- Fish, F. E., & Lauder, G. V. (2006). Passive and active flow control by swimming fishes and mammals. *Annual Review of Fluid Mechanics*, 38(1), 193–224. <https://doi.org/10.1146/annurev.fluid.38.050304.092201>
- Fish, F. E., Weber, P. W., Murray, M. M., & Howle, L. E. (2011). The tubercles on humpback whales' flippers: Application of bio-inspired technology. *Integrative and Comparative Biology*, 51(1), 203–213. <https://doi.org/10.1093/icb/icr016>
- Flammang, B. E., & Lauder, G. V. (2008). Speed-dependent intrinsic caudal fin muscle recruitment during steady swimming in bluegill sunfish, *Lepomis Macrochirus*. *Journal of Experimental Biology*, 211(4), 587–598. <https://doi.org/10.1242/jeb.012096>
- Fransson, J. H. (2004). Leading edge design process using a commercial flow solver. *Experiments in Fluids*, 37(6), 929–932. <https://doi.org/10.1007/s00348-004-0858-3>
- Fransson, J. H., Brandt, L., Talamelli, A., & Cossu, C. (2005). Experimental study of the stabilization of Tollmien–Schlichting waves by finite amplitude streaks. *Physics of Fluids*, 17(5), 054110. <https://doi.org/10.1063/1.1897377>

- Fransson, J. H., & Shahinfar, S. (2020). On the effect of free-stream turbulence on boundary-layer transition. *Journal of Fluid Mechanics*, 899. <https://doi.org/10.1017/jfm.2020.444>
- Fransson, J. H., & Talamelli, A. (2012). On the generation of steady streamwise streaks in flat-plate boundary layers. *Journal of Fluid Mechanics*, 698, 211–234. <https://doi.org/10.1017/jfm.2012.80>
- Friedman. (2012). Ray-finned fishes from the type Maastrichtian. *Scripta Geol.*, (8)
- Fujiwara, K., Sriram, R., & Kontis, K. (2020). Experimental investigations on the sharp leading-edge separation over a flat plate at zero incidence using particle image velocimetry. *Experiments in Fluids*, 61(9). <https://doi.org/10.1007/s00348-020-03039-w>
- George, A. E., Garcia, T., Stahlschmidt, B. H., & Chapman, D. C. (2018). Ontogenetic changes in swimming speed of silver carp, Bighead carp, and grass carp larvae: Implications for larval dispersal. *PeerJ*, 6. <https://doi.org/10.7717/peerj.5869>
- Goldstein, R. J., Eriksen, V. L., Olson, R. M., & Eckert, E. R. (1970). Laminar separation, reattachment, and transition of the flow over a downstream-facing step. *Journal of Basic Engineering*, 92(4), 732–739. <https://doi.org/10.1115/1.3425124>
- Government of Canada. (2022, July 28). *Energy Production*. Provincial and Territorial Energy Profiles – Canada. Retrieved January 30, 2023, from <https://www.cer-rec.gc.ca/en/data-analysis/energy-markets/provincial-territorial-energy-profiles/provincial-territorial-energy-profiles-canada.html>
- Government of Canada. (2022, December 6). *Energy Supply and demand, 2021*. The Daily. Retrieved January 30, 2023, from <https://www150.statcan.gc.ca/n1/daily-quotidien/221206/dq221206e-eng.htm>
- Hamner, W. M. (1979). [Review of *Nekton.*, by Y. G. Aleyev]. *Limnology and Oceanography*, 24(6), 1173–1175. <http://www.jstor.org/stable/2835593>
- Hanson, R. E., Buckley, H. P., & Lavoie, P. (2012). Aerodynamic optimization of the flat-plate leading edge for experimental studies of Laminar and transitional boundary layers. *Experiments in Fluids*, 53(4), 863–871. <https://doi.org/10.1007/s00348-012-1324-2>
- Heidarian, A., Ghassemi, H., & Liu, P. (2018). Numerical Analysis of the effects of riblets on drag reduction of a flat plate. *Journal of Applied Fluid Mechanics*, 11(3), 679–688. <https://doi.org/10.29252/jafm.11.03.28344>
- Hou, J.-M., Shi, G.-F., Li, L., Li, Hong-da., & Xia, Mingqiang. (2021). Analysis of the influence of pit unit arrangement on the drag reduction performance of fish-scale pits. *Journal of Physics: Conference Series*, 1885(2), 022029. <https://doi.org/10.1088/1742-6596/1885/2/022029>
- Ibañez, A. L., Cowx, I. G., & O'Higgins, P. (2009). Variation in elasmoid fish scale patterns is informative with regard to taxon and swimming mode. *Zoological*

- Journal of the Linnean Society*, 155(4), 834–844. <https://doi.org/10.1111/j.1096-3642.2008.00465.x>
- Jaap de Vries (2012). barrel and pincushion lens distortion correction (<https://www.mathworks.com/matlabcentral/fileexchange/37980-barrel-and-pincushion-lens-distortion-correction>), MATLAB Central File Exchange. Retrieved January 19, 2023.
- Koeltzsch, K., Dinkelacker, A., & Grundmann, R. (2002). Flow over convergent and divergent wall riblets. *Experiments in Fluids*, 33(2), 346–350. <https://doi.org/10.1007/s00348-002-0446-3>
- Lakshman, R., & Basak, R. (2018). Analysis of transformed fifth order polynomial curve for the contraction of wind tunnel by using OpenFoam. *IOP Conference Series: Materials Science and Engineering*, 377, 012048. <https://doi.org/10.1088/1757-899x/377/1/012048>
- Leschziner, M. A. (2020). Friction-drag reduction by transverse wall motion – A Review. *Journal of Mechanics*, 36(5), 649–663. <https://doi.org/10.1017/jmech.2020.31>
- Liberzon, A., Käufer, T., Bauer, A., Vennemann, P., & Zimmer, E. (2021). OpenPIV/openpiv-python.
- Lighthill, M. J. (1971). Large-amplitude elongated-body theory of fish locomotion. *Proceedings of the Royal Society of London. Series B. Biological Sciences*, 179(1055), 125–138. <https://doi.org/10.1098/rspb.1971.0085>
- Lourenco, L., & Krothapalli, A. (1995). On the accuracy of velocity and vorticity measurements with PIV. *Experiments in Fluids*, 18(6), 421–428. <https://doi.org/10.1007/bf00208464>
- Malik, M., Liao, W., Li, F., & Choudhari, M. (2015). Discrete-roughness-element-enhanced swept-wing natural laminar flow at high Reynolds Numbers. *AIAA Journal*, 53(8), 2321–2334. <https://doi.org/10.2514/1.j053637>
- Marxen, M. (1998). *Particle Image Velocimetry in Strömungen Mit Starken Geschwindigkeitsgradienten* (Diploma Thesis).
- Muthuramalingam, M., Puckert, D. K., Rist, U., & Bruecker, C. (2020). Transition delay using biomimetic fish scale arrays. *Scientific Reports*, 10(1). <https://doi.org/10.1038/s41598-020-71434-8>
- Muthuramalingam, M., Villemin, L. S., & Bruecker, C. (2019). Streak formation in flow over biomimetic fish scale arrays. *Journal of Experimental Biology*. <https://doi.org/10.1242/jeb.205963>
- Nakanishi, R., Mamori, H., & Fukagata, K. (2012). Relaminarization of turbulent channel flow using traveling wave-like wall deformation. *International Journal of Heat and Fluid Flow*, 35, 152–159. <https://doi.org/10.1016/j.ijheatfluidflow.2012.01.007>
- Nobach, H., & Honkanen, M. (2005). Two-dimensional gaussian regression for sub-pixel displacement estimation in particle image velocimetry or particle position

- estimation in particle tracking velocimetry. *Experiments in Fluids*, 38(4), 511–515. <https://doi.org/10.1007/s00348-005-0942-3>
- Ou, J., Perot, B., & Rothstein, J. P. (2004). Laminar drag reduction in microchannels using ultrahydrophobic surfaces. *Physics of Fluids*, 16(12), 4635–4643. <https://doi.org/10.1063/1.1812011>
- Parfitt, A. R., & Vincent, J. F. (2005). Drag reduction in a swimming Humboldt penguin, *Spheniscus humboldti*, when the boundary layer is turbulent. *Journal of Bionic Engineering*, 2(2), 57–62. <https://doi.org/10.1007/bf03399481>
- Ricco, P. (2011). Laminar streaks with spanwise wall forcing. *Physics of Fluids*, 23(6), 064103. <https://doi.org/10.1063/1.3593469>
- Roesgen, T. (2003). Optimal subpixel interpolation in particle image velocimetry. *Experiments in Fluids*, 35(3), 252–256. <https://doi.org/10.1007/s00348-003-0627-8>
- Sagong, W., Kim, C., Choi, S., Jeon, W.-P., & Choi, H. (2008). Does the sailfish skin reduce the skin friction like the shark skin? *Physics of Fluids*, 20(10), 101510. <https://doi.org/10.1063/1.3005861>
- Schlatter, P., Deusebio, E., de Lange, R., & Brandt, L. (2010). Numerical Study of the stabilisation of boundary-layer disturbances by finite amplitude streaks. *International Journal of Flow Control*, 2(4), 259–288. <https://doi.org/10.1260/1756-8250.2.4.259>
- Schlichting (Deceased), H., & Gersten, K. (2018). Fundamentals of Boundary-Layer Theory. In *Boundary-layer theory* (9th ed., pp. 29–50). Springer Berlin.
- Shahinfar, S., Sattarzadeh, S. S., & Fransson, J. H. M. (2014). Passive boundary layer control of oblique disturbances by finite-amplitude streaks. *Journal of Fluid Mechanics*, 749, 1–36. <https://doi.org/10.1017/jfm.2014.211>
- Siconolfi, L., Camarri, S., & Fransson, J. H. (2014). Boundary layer stabilization using free-stream vortices. *Journal of Fluid Mechanics*, 764. <https://doi.org/10.1017/jfm.2014.731>
- Sindagi, S., & Vijayakumar, R. (2020). Succinct review of MBDR/BDR technique in reducing ship's drag. *Ships and Offshore Structures*, 16(9), 968–979. <https://doi.org/10.1080/17445302.2020.1790296>
- Smith, J. A., Pisetta, G., & Viola, I. M. (2021). The scales of the leading-edge separation bubble. *Physics of Fluids*, 33(4), 045101. <https://doi.org/10.1063/5.0045204>
- Song, X.-wen, Zhang, M.-xiao, & Lin, P.-zhe. (2017). Skin friction reduction characteristics of nonsmooth surfaces inspired by the shapes of Barchan Dunes. *Mathematical Problems in Engineering*, 2017, 1–12. <https://doi.org/10.1155/2017/6212605>
- Sudo, S., Tsuyuki, K., Ito, Y., & Ikohagi, T. (2002). A study on the surface shape of fish scales. *JSME International Journal Series C*, 45(4), 1100–1105. <https://doi.org/10.1299/jsmec.45.1100>

- Thielicke, W. (2014). *The Flapping Flight of Birds - Analysis and Application* (Phd thesis).
- Thielicke, W., & Stamhuis, E. J. (2014). PIVlab – towards user-friendly, affordable and accurate digital particle image velocimetry in Matlab. *Journal of Open Research Software*, 2. <https://doi.org/10.5334/jors.bl>
- United States Department of Transportation. (2022, Sept. 8). *U.S. energy consumption by the transportation sector*. Bureau of Transportation Statistics. Retrieved February 1, 2023, from <https://www.bts.gov/content/us-energy-consumption-transportation-sector>
- U.S. Energy Information Administration. (2022, June 28). *Energy use for transportation*. Use of energy for transportation in depth. Retrieved February 1, 2023, from <https://www.eia.gov/energyexplained/use-of-energy/transportation-in-depth.php>
- Wainwright, D. K., Karan, E. A., & Collar, D. C. (2022). Evolutionary patterns of scale morphology in damselfishes (Pomacentridae). *Biological Journal of the Linnean Society*, 135(1), 138–158. <https://doi.org/10.1093/biolinnean/blab140>
- Wainwright, D. K., & Lauder, G. V. (2016). Three-dimensional analysis of scale morphology in bluegill sunfish, *Lepomis macrochirus*. *Zoology*, 119(3), 182–195. <https://doi.org/10.1016/j.zool.2016.02.006>
- Wainwright, D. K., & Lauder, G. V. (2017). Mucus matters: The slippery and complex surfaces of fish. *Biologically-Inspired Systems*, 223–246. https://doi.org/10.1007/978-3-319-74144-4_10
- Walters, V. (1963). The trachipterid integument and an hypothesis on its hydrodynamic function. *Copeia*, 1963(2), 260. <https://doi.org/10.2307/1441341>
- Wang, A., Qiu, T., & Shao, L. (2009). A simple method of radial distortion correction with centre of distortion estimation. *Journal of Mathematical Imaging and Vision*, 35(3), 165–172. <https://doi.org/10.1007/s10851-009-0162-1>
- White, F. M. (2016). Dimensional Analysis and Similarity. In *Fluid mechanics* (8th ed., pp. 285–325). McGraw-Hill.
- White, F. M. (2016). Dimensional Analysis and Similarity. In *Fluid mechanics* (8th ed., p. 317). McGraw-Hill.
- White, F. M. (2016). Flow Past Immersed Bodies. In *Fluid mechanics* (8th ed., p. 450). McGraw-Hill.
- White, F. M. (2016). Flow Past Immersed Bodies. In *Fluid mechanics* (8th ed., p. 453). McGraw-Hill.
- White, F. M. (2016). Flow Past Immersed Bodies. In *Fluid mechanics* (8th ed., p. 455). McGraw-Hill.
- White, F. M. (2016). Flow Past Immersed Bodies. In *Fluid mechanics* (8th ed., p. 459). McGraw-Hill.
- White, F. M. (2016). Flow Past Immersed Bodies. In *Fluid mechanics* (8th ed., p. 461). McGraw-Hill.

- White, F. M. (2016). Flow Past Immersed Bodies. In *Fluid mechanics* (8th ed., p. 462). McGraw-Hill.
- White, F. M. (2016). Flow Past Immersed Bodies. In *Fluid mechanics* (8th ed., p. 471). McGraw-Hill.
- White, F. M. (2016). Viscosity and Other Properties. In *Fluid mechanics* (8th ed., p. 25). McGraw-Hill.
- White, F. M. (2016). Viscous Flow in Ducts. In *Fluid mechanics* (8th ed., p. 372). McGraw-Hill.
- Williams, P. T., & Baker, A. J. (1997). Numerical simulations of laminar flow over a 3D backward-facing step. *International Journal for Numerical Methods in Fluids*, 24(11), 1159–1183. [https://doi.org/10.1002/\(sici\)1097-0363\(19970615\)24:11<1159::aid-flid534>3.0.co;2-r](https://doi.org/10.1002/(sici)1097-0363(19970615)24:11<1159::aid-flid534>3.0.co;2-r)
- Wood, R. M. (2004). Impact of advanced aerodynamic technology on Transportation Energy Consumption. *SAE Technical Paper Series*. <https://doi.org/10.4271/2004-01-1306>
- Wu, L. Y., Jiao, Z. B., Song, Y. Q., Ren, W. T., Niu, S. C., & Han, Z. W. (2017). Water-trapping and drag-reduction effects of fish ctenopharyngodon idellus scales and their simulations. *Science China Technological Sciences*, 60(7), 1111–1117. <https://doi.org/10.1007/s11431-016-0630-x>
- Yanase, K., & Saarenrinne, P. (2016). Boundary Layer Control by a fish: Unsteady laminar boundary layers of rainbow trout swimming in turbulent flows. *Biology Open*, 5(12), 1853–1863. <https://doi.org/10.1242/bio.020008>
- Yang, X., Wang, J., Jiang, B., Li, Z., & Xiao, Q. (2021). Numerical study of effect of sawtooth riblets on low-Reynolds-number airfoil flow characteristic and aerodynamic performance. *Processes*, 9(12), 2102. <https://doi.org/10.3390/pr9122102>
- Yu, C., Liu, M., Zhang, C., Yan, H., Zhang, M., Wu, Q., Liu, M., & Jiang, L. (2020). Bio-inspired drag reduction: From nature organisms to artificial functional surfaces. *Giant*, 2, 100017. <https://doi.org/10.1016/j.giant.2020.100017>
- Zhang, L., Shan, X., & Xie, T. (2020). Active control for wall drag reduction: Methods, mechanisms and performance. *IEEE Access*, 8, 7039–7057. <https://doi.org/10.1109/access.2020.2963843>
- Zhang, Z. (1998). (tech.). *A Flexible New Technique for Camera Calibration* (pp. 7–8). Redmond, Washington: Microsoft.

Chapter 3

3 Numerical Investigation into the Influence of Scale Shape on the Hydrodynamic Performance of Biomimetic Fish Scale Arrays

3.1 Introduction

While global warming and climate change have brought the issues of energy consumption and greenhouse gas emissions to the forefront, advances in technology are required to help the world meet emissions reduction targets. In 2020, the transportation sector alone accounts for about 27% (Government of the United States, 2022) and 24% (Government of Canada, *Greenhouse Gas Emissions by Economic Sector*, 2022) of greenhouse gas (GHG) emissions, and 28% (U.S. Energy Information Administration, 2022) and 23% (Government of Canada, *Energy Production*, 2022) of energy consumption in the United States (US) and Canada, respectively. Despite advances in technology, energy consumption in the transportation sector has remained stagnant around 28% in the US since 2000 (United States Department of Transportation, 2022), while Canada saw a 5% increase in consumption in 2021 (Government of Canada, *Energy Supply and Demand*, 2022). Thus, not only is transportation a major sector due to the fraction of total energy consumption and emissions, the non-declining consumption trends by this sector highlights that any effort to reduce the energy consumption would have a significant impact on emissions mitigation.

Although several factors such as size of vehicle, and type of engine affect vehicle performance, Wood (2004) estimated that 16% of the energy consumed in the US is used to overcome aerodynamic drag in the transportation sector. While aerodynamic drag is composed of both pressure and friction drag, the friction drag's contributions are significant across all transportation modes (up to 80% of a ships total drag (Sindagi & Vijayakumar, 2020), about 50% of an aircraft's drag (Abbas et al., 2017, Malik et al., 2015), and 20% of vehicular total drag (Wood, 2004)). As such, drag reduction methods targeting the reduction of friction drag in the transportation sector could potentially have a significant impact on the reduction of energy consumption and consequently emissions.

Friction drag reduction research has largely focused on the development of both active and passive methods (Abbas et al., 2017; Zhang, 2020; Fish & Lauder, 2006). Although several active methods of drag reduction such as plasma- and jet-actuators (Abbas et al., 2017), wall motion (Leschziner, 2020), wall-deformation (Nakanishi et al., 2012), and micro-vibrations (Bai et al., 2014) have shown promising results, in all cases control technology and energy input are required. In contrast, passive methods interact naturally with the fluid requiring little to no additional control, often making them a desirable solution in drag reduction applications.

Many drag reduction methods have been inspired by nature in what are known as biomimetic applications. Some examples include the hydrophobic behavior of lotus leaves whose superhydrophobic microchannel structure has been found to entrap air and introduce fluid slip at the wall boundary (Ou et al., 2004 from Yu et al. 2020), the tubercles on the leading edge of Humpback whale flippers which delay separation over the fin (Fish et al., 2011), and the microstructures of shark skin inspired riblets which reduce drag in turbulent flow (Dean & Bhushan, 2010). These methods of drag reduction have shown varying degrees of success with the development of hydrophobic surfaces achieving up to 30% drag reduction in high Reynolds number flows (Xu, et al., 2020), and a sawtooth shark-skin inspired riblet achieving about 11% drag reduction in turbulent flow (Heidarian et al., 2018).

Inspiration is not only found in biology as Song et al. (2017) investigated the drag reduction performance of a non-smooth surface inspired by the shape of the Barchan dunes and found a 33.6% drag reduction at 30 m/s. They propose the drag reduction mechanism as the translation of sliding friction into rolling friction in the regions of recirculation behind the non-smooth features. A similar phenomenon is also observed in Li et al. (2019) while studying the effect of transverse grooves under turbulent flow conditions, in which they found a 40% drag reduction with an optimal riblet geometry at 1.5 m/s. Developing a deep understanding of how these surfaces modify the near wall flow is a key to understanding the mechanisms by which they reduce drag. A structured surface that has received little attention from a fluid dynamics perspective is the surface of fish scales.

Fish scales have been of interest to biologists and ecologists for some time as the importance of scale size and shape has been studied from an evolutionary perspective (Kuusipalo, 1998; Sudo et al., 2002; Ibañez et al., 2009; Wainwright et al., 2022). As mentioned in Wainwright and Lauder (2017), much of the early work considering the hydrodynamic function of fish scales was hypothetical (Walters, 1963; Hamner, 1979; Burdak, 1986) with little quantitative proof. More recently, studies have focused on the influence of individual scales. In 2008, Sagong et al. studied the effect of V-shape protrusions from the skin of sailfish experimentally in a turbulent flow and found that although the skin friction was reduced in some cases, the total drag was found to be larger than that of a smooth surface. In 2012, Dou et al. explored bionic microscale cave features introduced using spray-paint and found that drag reduction increased with flow speed and about a 10% drag reduction was measured experimentally at 13.1 m/s. They explored numerically the mechanism by which these features entrap air near the surface modifying the boundary conditions in this region. However, the fish scale replication technique did not accurately model the unique features of fish scale arrays. Further, in 2017, Wu et al. investigated crescent-like structures modeled after grass carp fish scales experimentally and found that they produced a hydrophilic surface able to achieve 2.8% drag reduction at 0.66 m/s. While some of these authors have shown promising results in terms of drag reduction, they all treated the fish scale as an isolated feature without considering the 3D aspect of the entire fish scale array.

Muthuramalingam et al. in 2019 advanced the hydrodynamic analysis of fish scales by studying the effect of these 3D overlapping features on the near wall flow. They found numerically that the overlapping scale arrays produced periodic streamwise low- and high-speed velocity streaks in the boundary layer with a maximum velocity difference of about 9%. The alternating streaks were aligned with the scale geometry and produced a net drag reduction when the scale height was small relative to the boundary layer thickness. These numerical results were only qualitatively validated using flow visualization techniques and explored the flow behaviours in a small region above the scale array. The experimental results presented in Chapter 2 helped fill this need by improving our understanding of the physical mechanism governing the flow over biomimetic fish scale arrays.

Further, Muthuramalingam et al. (2020) studied experimentally the influence of fish scale arrays on the laminar to turbulent transition location and found that they tend to suppress the growth of Tollmien-Schlichting (TS) waves, which are characteristic of the transition to a turbulent boundary layer. These authors found a delay in the transition location downstream by 55% and hypothesized that this would lead to a theoretical drag reduction of about 27% based on the associated skin friction coefficients. Additionally in 2021, Mosghani et al. numerically studied Ctenoid-shaped microstructures placed on an underwater horizontal pole and found that the model reduced the total drag force about 20% for Reynolds numbers between $3.2(10^6)$ and $1.3(10^7)$. Further, Hou et al. (2021) studied different arrangements of fish scale pits numerically and argued that the “vortex cushion effect” which translates sliding friction to rolling friction is the leading mechanism causing a drag reduction rate up to 6%. As these studies highlight, there is significant evidence that biomimetic fish scale arrays reduce drag; however, each study has considered a uniquely modeled geometry. With no geometry standardization, it is difficult to classify and compare the drag reduction results obtained. Thus, the focus of the present study is to evaluate the influence of scale geometry on the near wall flow patterns and associated surface drag.

3.2 Objectives and Scope

The objective of the current study is to investigate the influence of scale shape and fluid velocity on the near wall flow behaviour over 3D biomimetic fish scale arrays. This numerical analysis will provide deeper insight into how the near wall flow behaviour is modified with different scale shapes and the relative friction drag reduction of different geometries. The motivation for this work is driven by the need to develop a more general knowledge of how fish scale arrays can impact the drag to better inform the design of engineered functional surfaces targeting drag reduction.

3.3 Methodology

The following methodology section describes the scale design, numerical model, model validation, and grid independence.

3.3.1 Scale Design

As mentioned previously, fish scale size and shape has been studied from an evolutionary perspective finding that scale size and shape can vary significantly based on species, ecology, age, or region on the fish body (Kuusipalo, 1998; Sudo et al., 2002; Ibañez et al., 2009; Wainwright et al., 2022). Wainwright and Lauder (2016) provided a detailed analysis of the surface topography of the Bluegill sunfish and characterized the variations in size and shape of the scales based on the body region. They also hypothesized about how these variations in scale shape may play a role in the hydrodynamic performance of the scales. Further, in Wainwright and Lauder (2017), the discussion centered around the lack of existing knowledge about the functional importance of fish scales, let alone understanding how the scale size and shape may affect their performance. Given the recent work of Muthuramalingam et al. (2019 & 2020) as well as the detailed experimental analysis provided in the previous chapter, the next step is to explore how scale shape affects the performance of the scale arrays.

Fish scales can generally be classified into the following four categories based on their shape and individual features (Sudo et al., 2002):

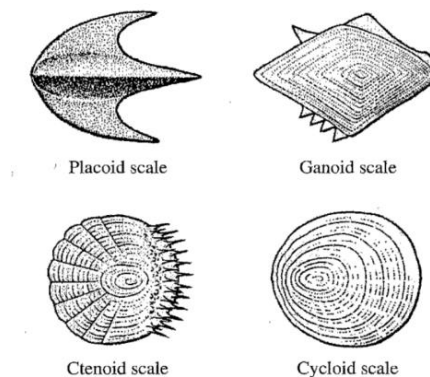


Figure 56: Different scale shapes (Sudo et al., 2002).

Placoid scales are commonly found in sharks and have been shown to reduce drag in turbulent flows (Bechert et al., 2000). However, little work has been done to investigate the hydrodynamic significance of the other three scale geometries commonly found in bony fish. Combining the above classifications with the detailed characterization of the

Bluegill sunfish (Wainwright and Lauder, 2016), three simplified scale geometries were identified: circular, diamond, and flat back (Table 8).

The typical or “circular” scale geometry replicates the shape of a cycloid scale with the focus⁴ located on the upstream side of the scale. This shape also matches the shape of the scales found in the tail region of the Bluegill sunfish. The second scale geometry replicates the ganoid scale type and has a “diamond” shape with straight sides and a pointed tip. Although the ganoid scales are not present on the Bluegill sunfish, the scales found in the opercle region of the Bluegill sunfish look similar to a diamond shaped scale. Lastly, the ctenoid scale is most similar to a “flat-back” scale where the focus is located on the downstream side of the scale making it shorter and wider. The flat-back scale replicates the scales found in the central region of the Bluegill sunfish. It is important to note that the three geometries identified by no means encompass all possible geometries, nor may they all appropriately reflect the scale topographies of the Bluegill sunfish. The purpose of these generalizations is to modify one feature of the scale (scale shape), and have it reflect the shape of general scale classifications and those found on the Bluegill sunfish.

To validate the simulation results against the experimental results presented in Chapter 2, an eight times scaling factor was applied to all geometries. This resulted in an 8 cm wide \times 16 cm long scale array consisting of 4 scales across the width and 9 scales along the length. To maintain similar flow conditions between the scale model and the actual flow, dynamic similarity would need to be maintained (White, p. 317, 2016) by keeping the non-dimensional values of Reynolds number based on boundary layer thickness (equation 3.1) and the boundary layer to scale height ratio (equation 3.2) within the same order of magnitude. Note, the boundary layer thickness (δ_{99}) is computed by identifying the height at which 99% of the free-stream velocity has been recovered (White, p. 450, 2016).

⁴ Center of the scale where growth circuli begin, and where the scale attaches to the fish body (Wainwright and Lauder, 2017).

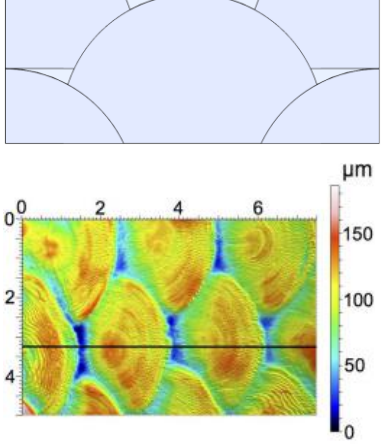
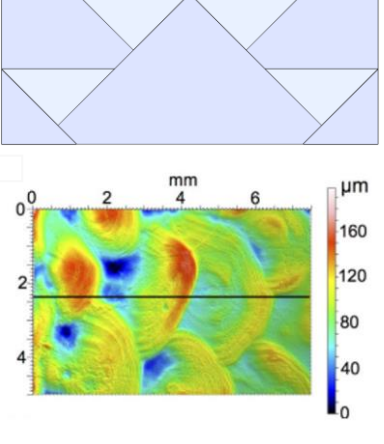
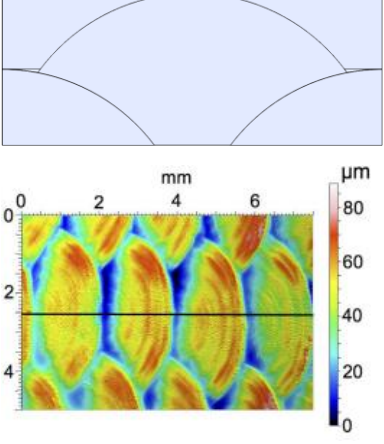
$$Re_{BL} = \frac{U_{\infty} \delta_{99}}{\nu} \quad (3.1)$$

$$\theta_{ratio} = \frac{\delta_{99}}{l_{sh}} \quad (3.2)$$

As mentioned in Wainwright and Lauder (2017), there is little understanding of the boundary layer over the swimming fish surface. Anderson et al. (2001) and Yanase and Saarenrinne (2016) examined the boundary layer experimentally over two species of fish and found that the boundary layer remained in the laminar and transitional regimes, while flow separation and vortex shedding was delayed until the posterior (rear) region of the fish. While there is still much to learn about the boundary layer flow over the fish surface, these studies highlight that a laminar boundary layer is the most appropriate approximation to the real boundary layer over small and medium sized fish. However, the free-stream velocity and distance from the leading edge would still be needed to calculate the order of the Reynolds number and boundary layer thickness.

Based on the analysis provided in Chapter 2, using critical swimming speeds between 0.4 - 0.8 m/s and a length scale in the first 50% of the fish length (2 cm - 8 cm), the corresponding order of magnitude of the Reynolds number based on boundary layer thickness and boundary layer thickness were found to be ~500 and ~1 mm, respectively. Table 8 shows the 3D CAD models of each fish scale geometry, their associated scales from the Bluegill sunfish, the key scaled parameters, and non-dimensional quantities used for their design and simulation.

Table 8: Different scale geometries and their key parameters (Wainwright & Lauder, 2016)

Circular	Diamond	Flat Back
 <p style="text-align: center;">Tail Region</p>	 <p style="text-align: center;">Opercle Region</p>	 <p style="text-align: center;">Central Region</p>
<p><u>Original</u> Height (mm): 0.1 Streamwise Offset (mm): 2 Spanwise Offset (mm): 2.5 Radius (mm): 1.75 Re_{BL}: ~500 θ_{ratio}: ~10</p> <p><u>Scaled (8x)</u> Height (mm): 0.8 Streamwise Offset (mm): 16 Spanwise Offset (mm): 20 Radius (mm): 14 Re_{BL}: 550 θ_{ratio}: 5.6</p>	<p><u>Original</u> Height (mm): 0.1 Streamwise Offset (mm): 2 Spanwise Offset (mm): 2.5 Diamond Angle: 90 Degrees Re_{BL}: ~500 θ_{ratio}: ~10</p> <p><u>Scaled (8x)</u> Height (mm): 0.8 Streamwise Offset (mm): 16 Spanwise Offset (mm): 20 Diamond Angle: 90 Degrees Re_{BL}: 550 θ_{ratio}: 5.6</p>	<p><u>Original</u> Height (mm): 0.1 Streamwise Offset (mm): 2 Spanwise Offset (mm): 2.5 Radius (mm): 2.5 Re_{BL}: ~500 θ_{ratio}: ~10</p> <p><u>Scaled (8x)</u> Height (mm): 0.8 Streamwise Offset (mm): 16 Spanwise Offset (mm): 20 Radius (mm): 20 Re_{BL}: 550 θ_{ratio}: 5.6</p>

After modeling the scale geometry in Solidworks, a fluid domain was created in Solidworks by modeling the water above the scale array using an 8 cm wide \times 31 cm long \times 1.5 cm high box. The scale geometry was assembled coincident to the sides and bottom of the fluid domain such that only the scales protruded into the domain. The

scales were fixed 1 cm from the back of the domain and 14 cm from the entrance. The cavity feature was used to remove the scale positions from the fluid domain, and two lines were split onto the surface in front of the scales to enable meshing over the leading edge. Figure 57 shows the fluid simulation domain used for mesh independence.

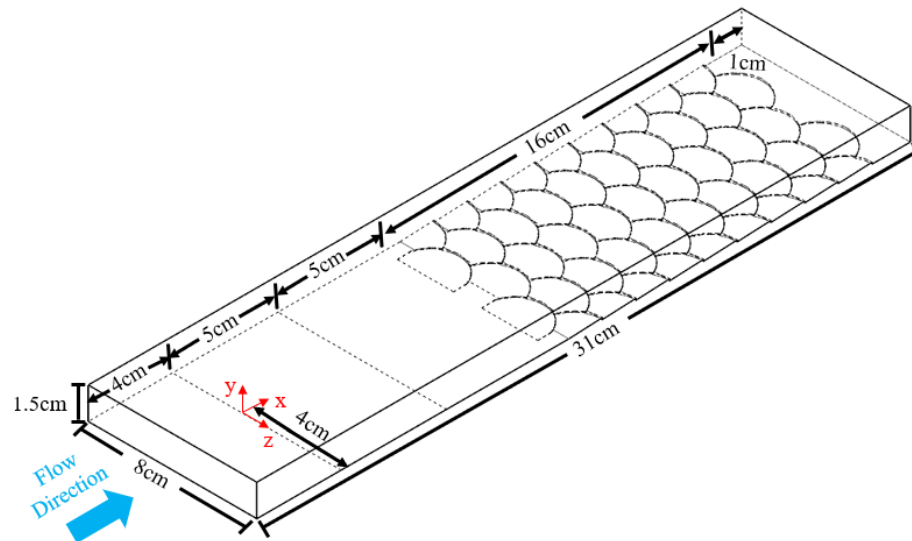


Figure 57: Circular geometry fluid domain for mesh independence.

3.3.2 Numerical Models

The ANSYS meshing software was used to create a 3D tetrahedral mesh. Three separate bodies of influence (BOI) were used to create a progressively finer mesh close to the surface. All bodies of influence extended 1 cm in front of the leading edge to the back of the scale array through the entire width of the domain. The BOI closest to the surface was 3 mm tall, on top of that there was another 3 mm tall BOI, and the last BOI was 4 mm for a total height of 10 mm. The element size within each of these BOI's and in the outer fluid domain were specified throughout the mesh refinement process. Additionally, a refinement setting was added to the leading-edge segments, the scale faces, and the flat end. Finally, the element size on the scale heights was also specified throughout the mesh refinement process. Table 9 shows the sizes for each parameter throughout the mesh refinement process including the total number of elements.

Table 9: Mesh refinement parameters

Mesh Size	Bulk Mesh (mm)	BOI Upper (mm)	BOI Middle (mm)	BOI Lower (mm)	Scale Heights Sizing (mm)	Total Elements (Millions)
1.6M	2.6	2.4	2.2	2.1	0.8	1.6M
2.3M	2.4	2.2	2.0	1.9	0.6	2.3M
3.7M	2.2	2.0	1.8	1.7	0.4	3.7M
5.5M	2.1	1.9	1.7	1.6	0.3	5.5M
5.8M	2.0	1.8	1.5	1.3	0.3	5.8M
6.6M	2.0	1.8	1.5	1.0	0.3	6.6M
7.2M	1.75	1.5	1.25	0.9	0.3	7.2M
8.4M	1.5	1.25	1.0	0.8	0.3	8.4M
11.8M	1.5	1.25	1.0	0.8	0.2	11.8M
13M	1.5	1.2	0.9	0.7	0.2	13M

The ANSYS Fluent simulation software was used with the laminar model to solve the steady state incompressible Navier-Stokes equations for all fluid velocities within the flow domain. Although other studies (Sagong et al., 2008; Dou et al. 2012; Wu et al., 2017; Mosghani et al., 2021; Hou et al., 2021) used a turbulent model (k-epsilon, k-omega, SST, etc.) to solve problems of boundary layer flow over similar structured surfaces, the previous discussion about the flow over actual fish skin revealed that the profiles are best represented by a laminar boundary layer. Additionally, Muthuramalingam et al. (2019 & 2020) studied fish scale surfaces under laminar flow concluding that the scales play a role in the delay in transition from laminar to turbulent flow. Thus, a laminar flow simulation will most accurately represent the flow conditions over the fish scale arrays. The equations that are solved in the simulation include the conservation of mass and momentum equations as shown in Equations 3.3 and 3.4, respectively (Ansys, *Theory Guide* pp. 2-3, 2013). These represent the full form of the equations which are simplified to equation 3.5 and 3.6 using the steady state and incompressible fluid assumptions.

$$\frac{\partial \rho}{\partial t} + \nabla \cdot (\rho \vec{v}) = 0 \quad (3.3)$$

$$\frac{\partial}{\partial t}(\rho \vec{v}) + \nabla \cdot (\rho \vec{v} \vec{v}) = -\nabla p + \rho \vec{g} + \vec{F} + \nabla \cdot \mu \left[(\nabla \vec{v} + \nabla \vec{v}^T) - \frac{2}{3} \nabla \cdot \vec{v} I \right] \quad (3.4)$$

$$\nabla \cdot \vec{v} = 0 \quad (3.5)$$

$$\rho \vec{v} \cdot \nabla(\vec{v}) = -\nabla p + \rho \vec{g} + \mu \nabla^2 \vec{v} \quad (3.6)$$

where μ is the molecular viscosity, p is the static pressure, ρ is the density.

The boundary conditions applied to the domain include a uniform velocity inlet condition (0.12 m/s), a zero-gauge pressure outlet condition, a symmetry condition applied between the left and right sides of the domain, a no-slip condition applied to the leading edge and all scale faces, and a free shear condition applied to the upper surface of the domain and the 4 cm portion in front of the leading edge. The fluid was specified to be water with a density of $998.2 \frac{kg}{m^3}$ and a viscosity of $0.001003 \frac{kg}{ms}$. For all simulations, residuals were considered converged when the residual plots reached a plateau, and the magnitude of the residuals were below at least 10^{-3} . In all cases, the momentum equations residuals converged below 10^{-5} and the residuals for the continuity equation converged below 10^{-4} , except in a few cases where the continuity equation converged below 10^{-3} . The “coupled” pressure-velocity coupling scheme was used to solve the momentum and pressure-based continuity equations together as it provided advantages in single-phase steady state flow over other segregated solution schemes (Ansys, *Theory Guide* pp. 651-652, 2013). The “least squares cell-based” spatial gradient discretization scheme was used which assumed the solution to vary linearly between cell centers (Ansys, *Theory Guide* p. 643, 2013). The “second order” spatial pressure discretization scheme was used to reconstruct the face pressure using a central differencing scheme (Ansys, *Theory Guide* p. 647, 2013). Finally, the “second order upwind” spatial momentum discretization scheme was used to evaluate the momentum results on the cell faces using a multidimensional linear reconstruction approach (Ansys, *Theory Guide* pp. 634-635, 2013 from Barth and Jespersen, 1989).

3.3.3 Grid Independence

The grid independence process required solving the same domain with successively smaller grid sizes until additional refinement did not produce more accurate results. Grid independence is an important step because it ensures the results obtained from the simulation are not dependent on the grid size, and it highlights the trade-off required between the computational intensity and additional solution accuracy. For the purposes of grid independence, only the circular geometry was considered. To validate different mesh sizes, the profiles of streamwise velocity in wall normal, streamwise, and spanwise directions at various locations were compared. Figure 58 depicts each validation location within the simulation domain.

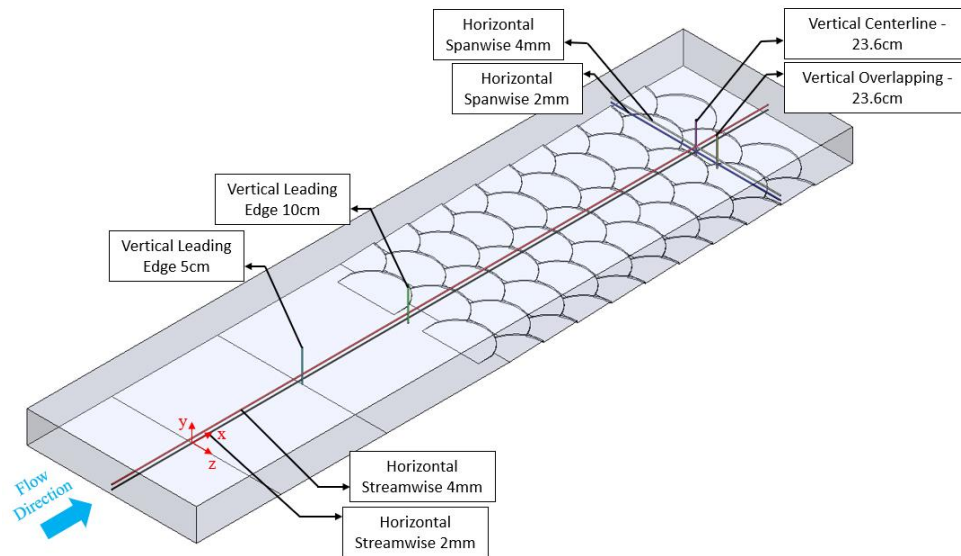


Figure 58: Horizontal Streamwise 2 mm – $y = 2$ mm and $z = 0$ cm; Horizontal Streamwise 4 mm – $y = 4$ mm and $z = 0$ cm; Vertical Leading Edge 5 cm – $x = 5$ cm and $z = 0$ cm; Vertical Leading Edge 10 cm – $x = 10$ cm and $z = 0$ cm; Vertical Centerline 23.6 cm – $x = 23.6$ cm and $z = 0$ cm; Vertical Overlapping 23.6 cm – $x = 23.6$ cm and $z = 1$ cm.

The grid sizes used for this mesh refinement study varied from 1.6 to 13 million cells where the individual specifications of the mesh sizing are outlined in Table 9. To create the non-dimensional profiles, the velocity was divided by the free-stream velocity

identified far outside the boundary layer, and the normalized height above the surface was divided by the boundary layer thickness (δ_{99}). Figure 59 shows the non-dimensional wall normal streamwise velocity profiles at the 10 cm leading edge location, and the streamwise velocity along the horizontal spanwise line located at $x = 23.6$ cm and $y = 2$ mm. All validation locations showed similar results, therefore only two locations are shown here.

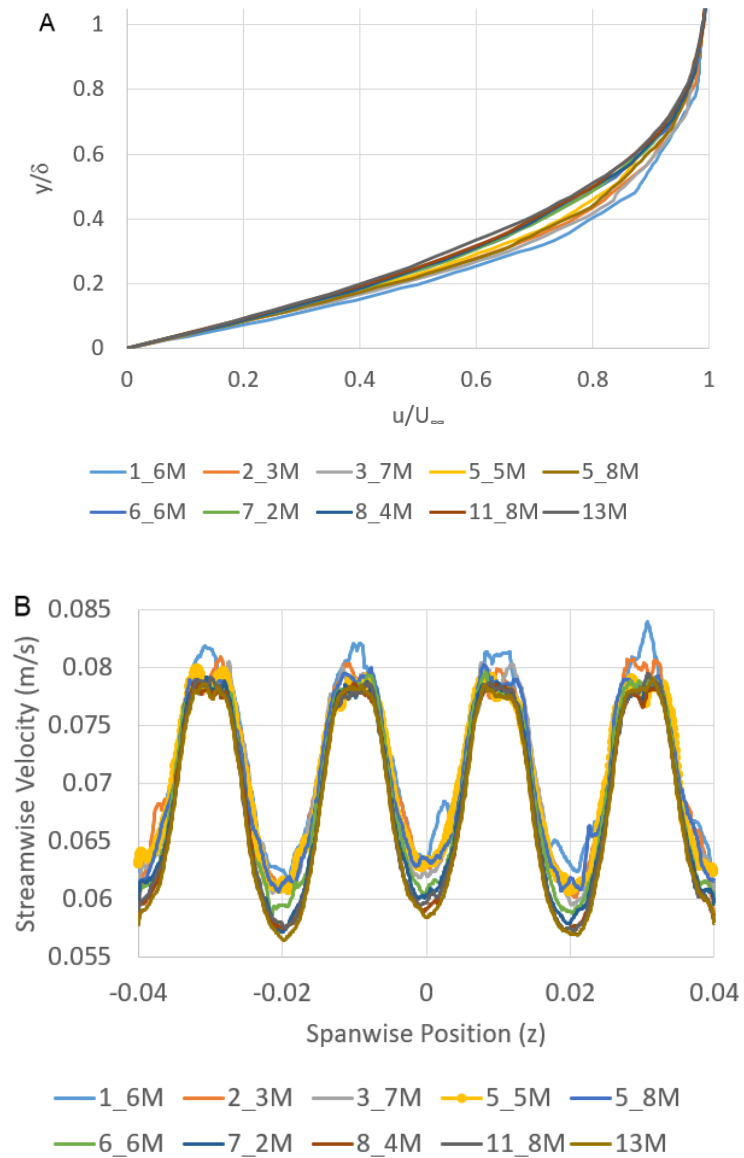
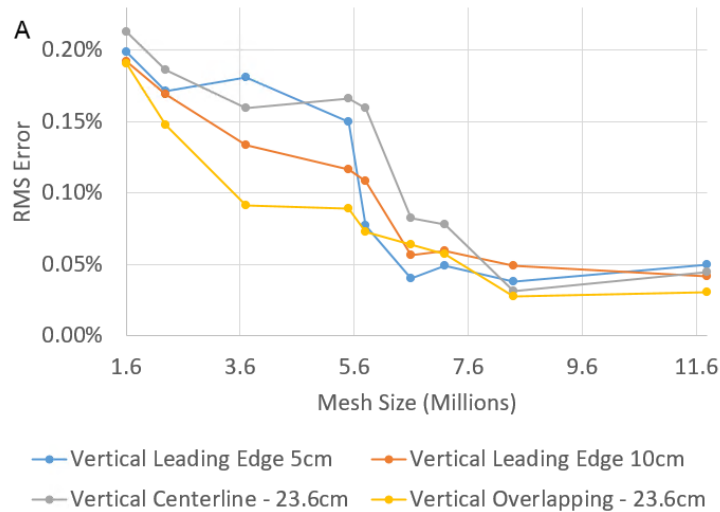


Figure 59: Streamwise velocity profiles for mesh independence study: A - Vertical Leading Edge 10 cm ($x = 10$ cm and $z = 0$ cm); B - Horizontal Spanwise 2 mm ($x = 23.6$ cm and $y = 2$ mm).

As Figure 59 shows, mesh refinement results in smoother velocity profiles. It is also observed that initial steps in the mesh refinement process, such as steps from the 1.6M to 2.3M cases, produced greater changes in the velocity profiles than later steps, such as between the 11.8M and 13M cases. The convergence throughout the mesh refinement process was evaluated by calculating the root mean squared (RMS) error between each mesh size and the finest mesh (13M case). The RMS error was calculated using equation 3.7 and would give a baseline comparison for the results produced in each case and allow for the observation of a convergence plateau when the results become independent of mesh size. Figure 60 shows the convergence process of the RMS error between each mesh and the 13M case for all vertical and horizontal streamwise velocity profiles at locations shown in Figure 58.

$$RMS\ Error\ (\%) = \sqrt{\frac{\sum_{i=1}^n (u_i - u_{13M,i})^2}{n}} \times 100\% \quad (3.7)$$



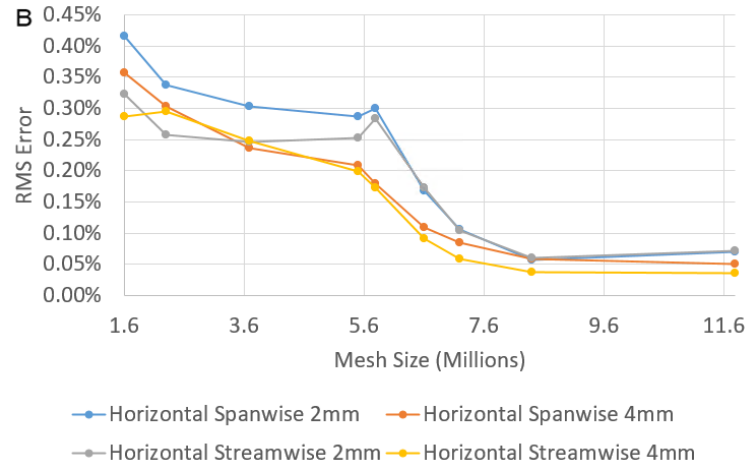


Figure 60: RMS error convergence graphs for all vertical (A) and horizontal (B) streamwise velocity profiles. RMS error was taken with respect to the finest mesh (13M) as the base case.

As the RMS error plots in Figure 60 show, the magnitude of the RMS error for all vertical and horizontal profiles is below 0.5%. This indicates that the overall error between the coarsest and finest mesh sizes is small. However, the trend of the RMS error shows a reduction in the RMS error with the mesh refinement until the mesh size is about 8.4M, where the RMS error is at or below 0.05% for all cases. A similar process was followed to track the maximum percent difference between each mesh size and the finest mesh (13M). The range of the maximum difference was between 10% and 30% for the 1.6M case and a plateau was found around 5% for mesh sizes above 8.4M. Thus, above a mesh size of 8.4M the velocity results are found to be independent of mesh size, and additional refinement would only increase the spatial resolution of the results and simulation time, not affecting the accuracy of the solution obtained.

When considering the trade-off between mesh size and simulation time, the goal is to choose a mesh size that minimizes simulation time while maintaining solution accuracy. Thus, mesh size closer to 8.4M would result in a shorter simulation time. However, the simulation time to reach a converged solution with the finest mesh (13M) was not more than 24 hours. Therefore, given that a converged solution would be reached in a reasonable amount of time, the meshing parameters corresponding to those in the 11.8M

case would be used in the final simulation meshing process. The additional spatial resolution would enable better characterization of the flow behaviour in the vicinity close to the scale and lead to better insight into the influence of the shape on the near-surface flow dynamics.

3.3.4 Model Validation

Given that the individual meshing parameters which produce a timely, yet accurate solution have been selected, a new domain with a shortened upstream distance was used along with the experimental velocity profile (from Chapter 2) 5 cm upstream from the scale array imposed at the inlet of the simulation domain. This domain was meshed using the same meshing parameters identified in the mesh refinement process. Figure 61 shows the new domain which is 22 cm long by 8 cm wide and 1.5 cm tall. The other boundary conditions remain as mentioned above. A new origin is defined at the center of the entrance of the scale array and will be used going forward throughout the model validation and analysis sections.

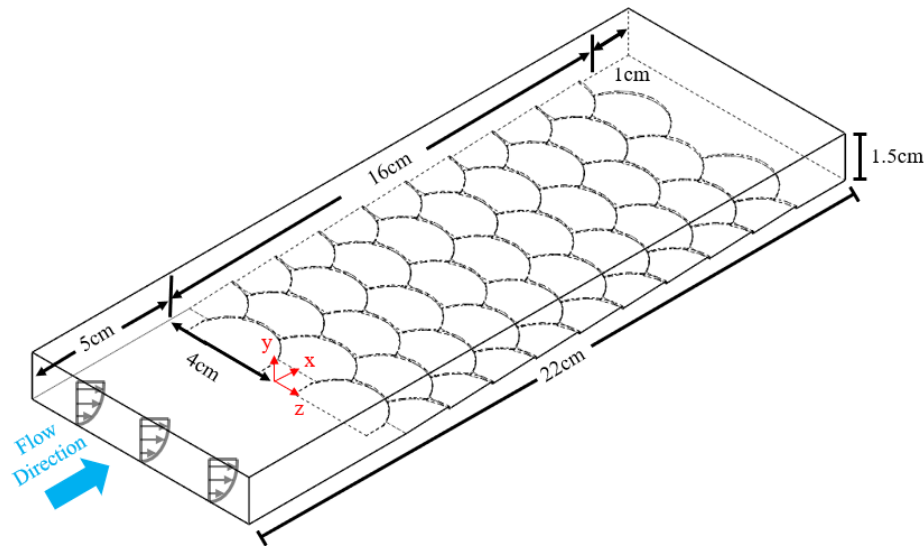


Figure 61: New model domain with experimental boundary layer inlet profile 5 cm upstream of the scale array.

In this model validation section, the results over the upstream portion are compared with the theoretical laminar boundary layer solution (Blasius solution), and the results over the

scale array are compared with previous studies and the experimental work presented in Chapter 2. In addition to the velocity profiles, the RMS error between the simulation results and the respective validation profile will be discussed to further validate the accuracy of the solution obtained. The eight validation locations considered correspond to those depicted in Figure 62.

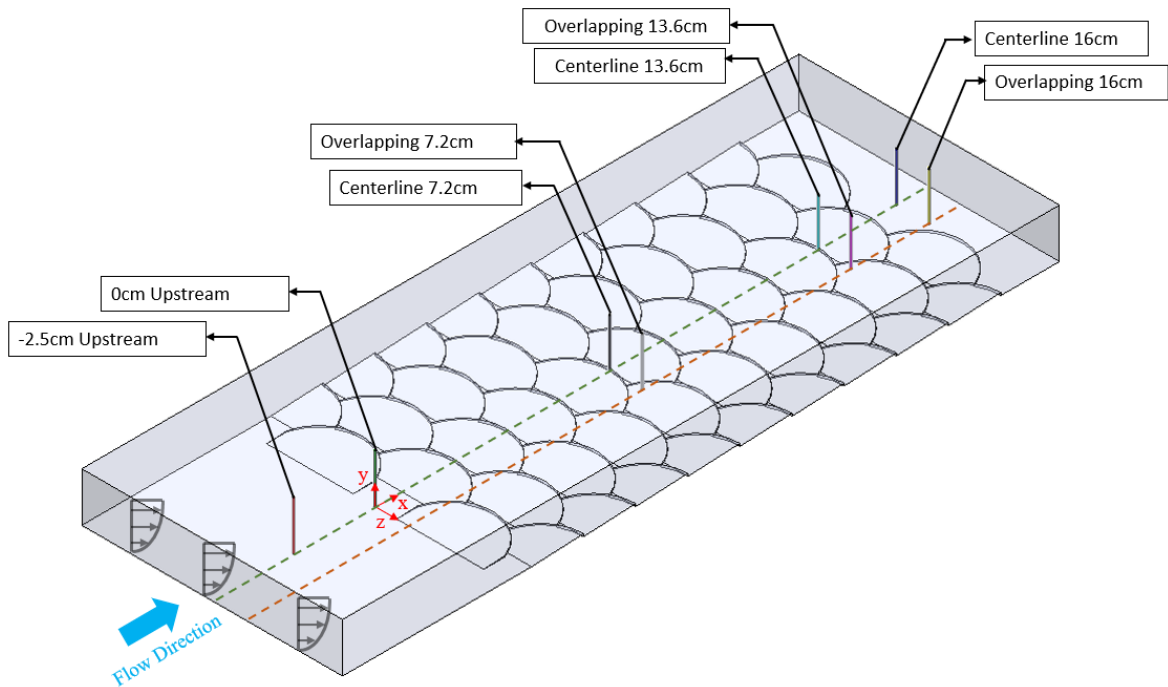


Figure 62: Model validation locations: -2.5 cm ($z = 0$ cm) Upstream, 0 cm ($z = 0$ cm) Upstream, Centerline 7.2 cm ($z = 0$ cm), Overlapping 7.2 cm ($z = 1$ cm), Centerline 13.6 cm ($z = 0$ cm), Overlapping 13.6 cm ($z = 1$ cm), Centerline 16 cm ($z = 0$ cm), and Overlapping 16 cm ($z = 1$ cm).

First, the non-dimensional wall normal streamwise velocity profiles at -2.5 cm and 0 cm upstream of the scale array are compared with the Blasius profile and experimental results (from Chapter 2) to validate that a laminar boundary layer has developed over the flat region upstream of the scale array (Figure 63).

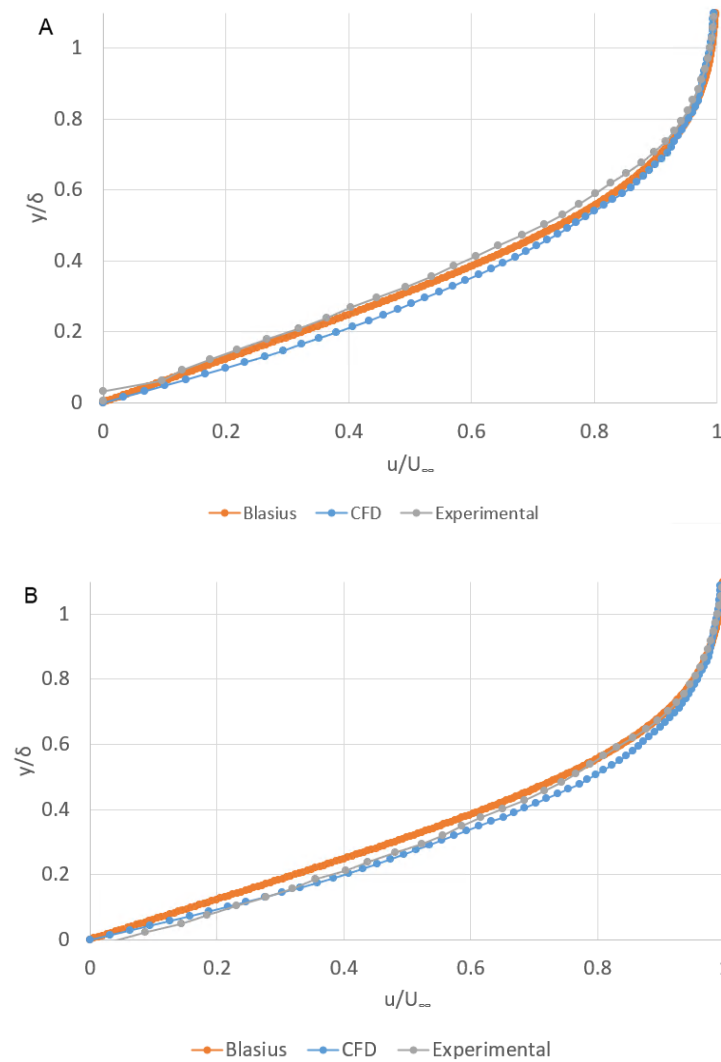
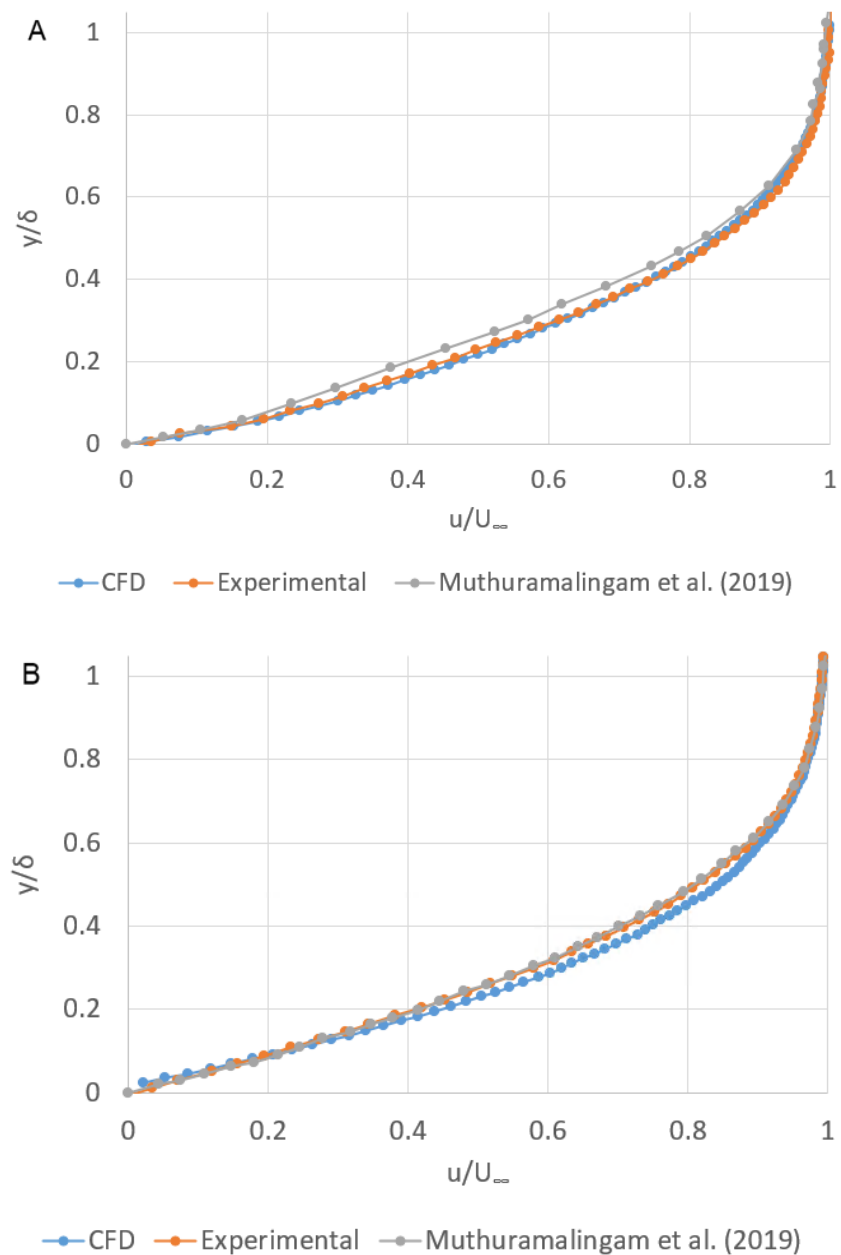


Figure 63: Validation of non-dimensional wall normal streamwise velocity profiles - 2.5 cm (A), and 0 cm (B) upstream of the scale array over the flat plate.

The comparison of the simulation results over the flat plate portion of the domain shows that the simulated solution is very similar to both the experimental results and the Blasius solution. The largest deviation from the experimental results was found in the -2.5 cm upstream case with an RMS error of 2.93%, whereas the deviation to the Blasius solution was largest in the 0 cm upstream case with an RMS error of 2.74%. While there exists about a 3% deviation between the simulation results and both the experimental data and theory, this indicates that there is a strong resemblance between the profiles and gives confidence that the incoming flow over the leading edge represents that of a classical laminar boundary layer.

Next, the non-dimensional wall normal streamwise velocity profiles over the scales at 7.2 cm and 13.6 cm from the entrance of the scale array in both the centerline and overlapping regions are compared to the numerical results from Muthuramalingam et al. (2019) and the experimental results presented in Chapter 2. The wall-normal distance or distance from the scale surface was calculated by subtracting the respective scale height from the absolute wall-normal position in each case. Figure 64 shows the comparison in the centerline and overlapping regions at 7.2 cm and 13.6 cm from the entrance of the scale array.



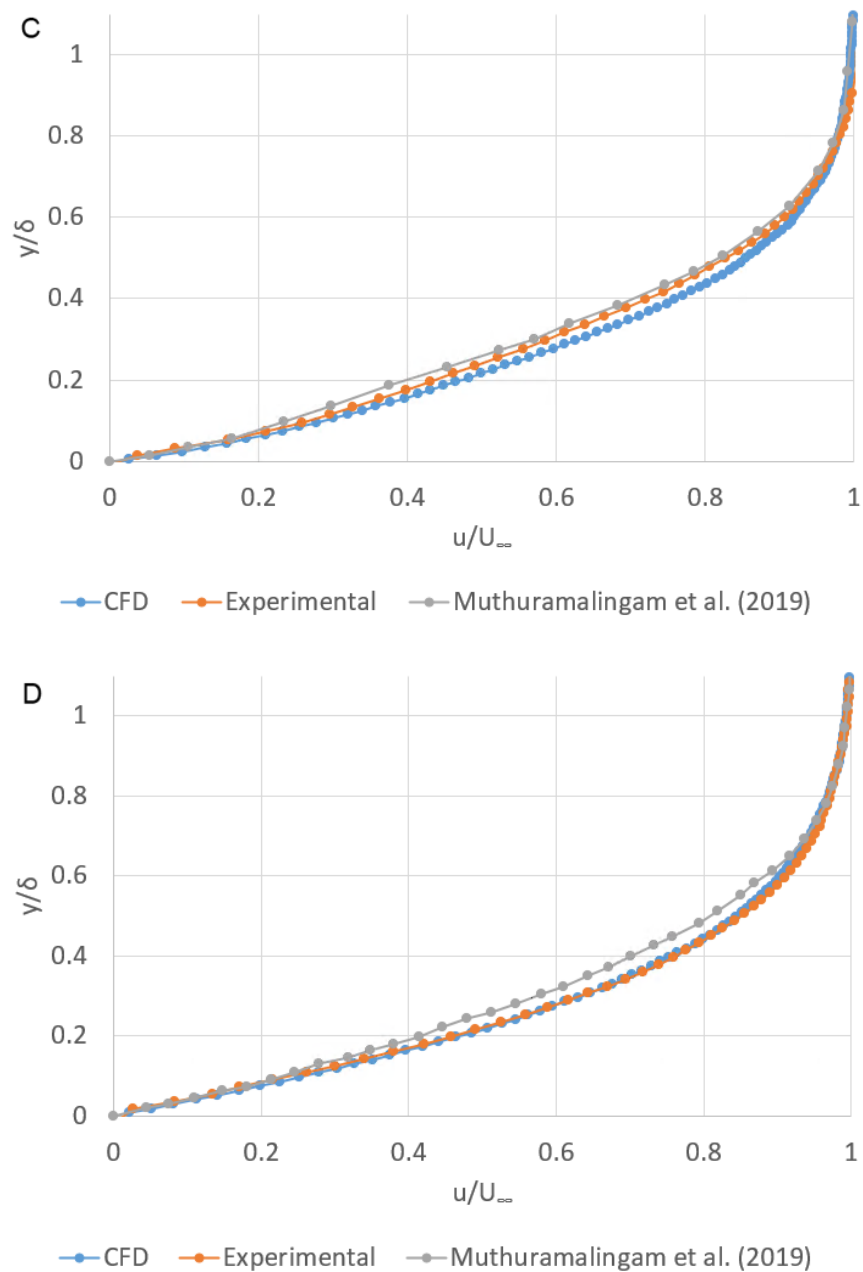


Figure 64: Nondimensional vertical velocity validation plots: A – Centerline 7.2 cm; B – Overlapping 7.2 cm; C – Centerline 13.6 cm; D – Overlapping 13.6 cm.

In all four locations, a strong agreement between the present simulation results and both the experimental (Chapter 2) and numerical results from Muthuramalingam et al. (2019) is found. The largest deviation between the current simulation results and both the experimental results (Chapter 2) and previous numerical results occurs over the centerline 13.6 cm profile and corresponds to an RMS error of 1.89% and 3.73%, respectively.

While a deviation of about 2-4% exists over the scale array, some error is expected as the discretization of the fluid domain is likely to introduce some non-zero errors. The fact that these errors are less than 4% over the scale array gives confidence that the simulation results are accurately capturing the flow behaviour over the scale array.

Finally, the non-dimensional wall normal velocity profiles after the scale array (16 cm from the entrance of the scale array) in both the centerline and overlapping regions were compared to the experimental and numerical results from Muthuramalingam et al. (2020). Figure 65 shows the comparison in the centerline and overlapping region behind the scale array (16 cm from the entrance of the scale array).

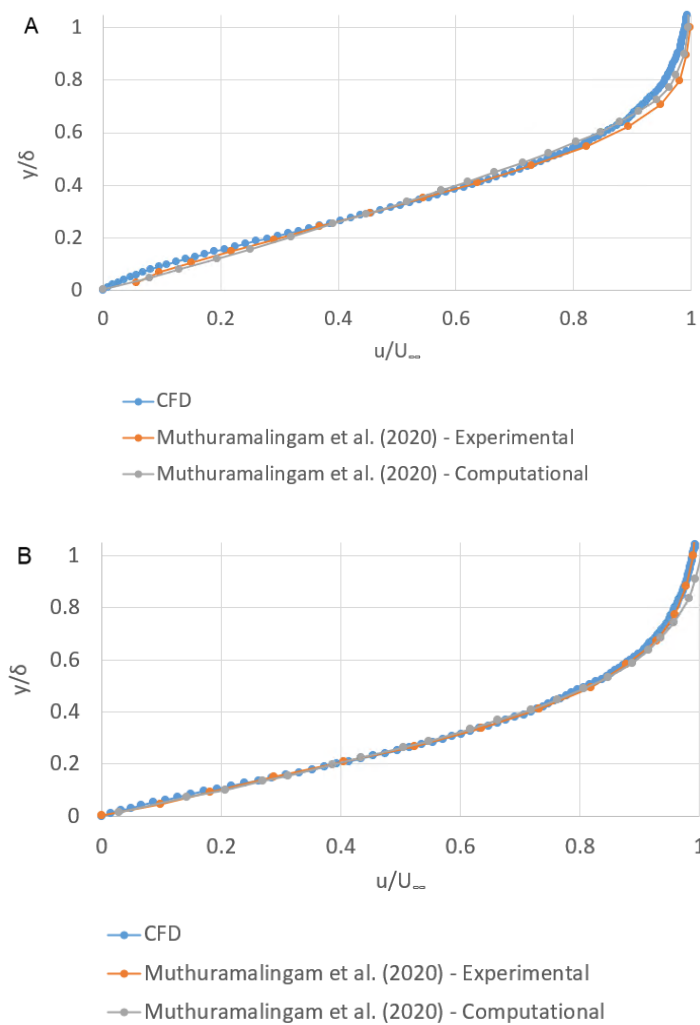


Figure 65: Centerline (A) and overlapping (B) vertical velocity profile validation 13 cm from the entrance of the scale array.

Once again, the comparison of velocity profiles in the region behind the scale array shows a strong agreement between the current simulation and the experimental and numerical results from Muthuramalingam et al. (2020). The largest deviation occurs along the centerline profile and results in an RMS error of 2.03% and 2.38% when compared to the experimental and numerical results, respectively. While a less than 2.4% deviation in the results does exist, the resemblance of the profiles and accuracy of the simulation solution is validated in the region behind the scale array.

Finally, it is also important that the simulation is able to model specific flow features over the scale array such as the recirculation behind the scale height, and the spanwise velocity components in the overlapping region. Through a qualitative assessment of the velocity vectors in both regions, a recirculation zone and spanwise wandering of the velocity were found behind the scale array and in the overlapping region, respectively. Evidence of these critical flow features which were found in the experimental results (Chapter 2) adds further credibility to the accuracy of the current simulation results. Thus, given the agreement between the velocity profiles and evidence of important flow features, the simulation results can be trusted as they are deemed to accurately model the flow behaviours throughout the domain.

3.3.5 Simulation Parameters

The simulations in this study were conducted by varying both the scale geometry and the oncoming flow conditions. The three geometries present in the analysis are those described in detail above. Additionally, three flow conditions were considered corresponding to an Re_{Bl} between 300 and 550 calculated using equation 3.1, and a θ_{ratio} between 5.6 and 11 calculated using equation 3.2. Table 10 shows the simulation parameters and associated non-dimensional scaling parameters for each simulation case.

Table 10: Simulation Parameters for all cases

Geometry	U_{∞} (m/s)	Re_{Bl}	θ_{ratio}
Circular	Experimental (0.12)	550	5.6
Circular	0.065	415	8.0
Circular	0.035	300	10.6
Diamond	Experimental (0.12)	550	5.6
Diamond	0.065	415	8.0
Diamond	0.035	300	10.6
Flat back	Experimental (0.12)	550	5.6
Flat back	0.065	415	8.0
Flat back	0.035	300	10.6

In the base case, the experimental velocity profile 5 cm upstream of the scale array was applied at the inlet. To vary the flow conditions at the inlet, the experimental profile was non-dimensionalized using its associated free-stream velocity and boundary layer thickness. This profile was then re-dimensionalized using the new free-stream velocity and boundary layer thickness identified to result in the desired θ_{ratio} at the entrance of the scale array. The new re-dimensionalized profile was then applied at the inlet of the domain. The goal was to select θ_{ratio} values close to those explored experimentally in Chapter 2.

3.4 Results and Discussion

Before discussing the results of the simulations, the coordinate system used throughout the analysis is defined at the center of the entrance of the scale array (see Figure 66). Each coordinate direction has an appropriate length scale used to non-dimensionalize its position. In the x -direction, the scale length ($l_{sl} = 16$ mm) is used, in the z -direction, the scale width ($l_{sw} = 26.65$ mm) is used, and in the y -direction, both the boundary layer thickness (δ_{99}) and the scale height ($l_{sh} = 0.8$ mm) are used to define a non-dimensional y -coordinate. These characteristic lengths are shown in Figure 66.

Given the scale geometry results in a variation in absolute height over the scale length, the height of the surface (y_0), which varies along the length of the scale, was used to

normalize the distance from the surface boundary (see Figure 66). This normalized distance was then non-dimensionalized using the maximum scale height (l_{sh}) and the boundary layer thickness (δ_{99}) in equations 3.8 and 3.9. When considering the non-dimensional distance along a single scale (ϕ), the absolute x -position over a single scale was normalized using the absolute x -position at the upstream end of the scale (x_0) (see Figure 66), and non-dimensionalized using the scale length (l_{sl}) in equation 3.10. When discussing the non-dimensional distance (ϕ_t) over the scale array, the absolute x -position is non-dimensionalized using the scale length (l_{sl}) in equation 3.11. Finally, the spanwise location across the scale array is non-dimensionalized using the scale width (l_{sw}) in equation 3.12.

$$\lambda_1 = \frac{y - y_0}{l_{sh}} \quad (3.8)$$

$$\lambda_2 = \frac{y - y_0}{\delta_{99}} \quad (3.9)$$

$$\phi = \frac{x - x_0}{l_{sl}} \quad (3.10)$$

$$\phi_t = \frac{x}{l_{sl}} \quad (3.11)$$

$$\xi = \frac{z}{l_{sw}} \quad (3.12)$$

A scale naming convention is introduced which assigns names to scales using a double subscript notation. The first subscript corresponds to the scale row in the spanwise direction (-1, 0, or 1), and the second subscript describes the streamwise scale number (1-9). It is also noted that adjacent scale rows have a spanwise offset of $\xi = 0.75$, and a streamwise offset of $\phi_t = 0.5$. Figure 66 shows the double subscript notation for all scales and the new coordinate system that is defined for the analysis.

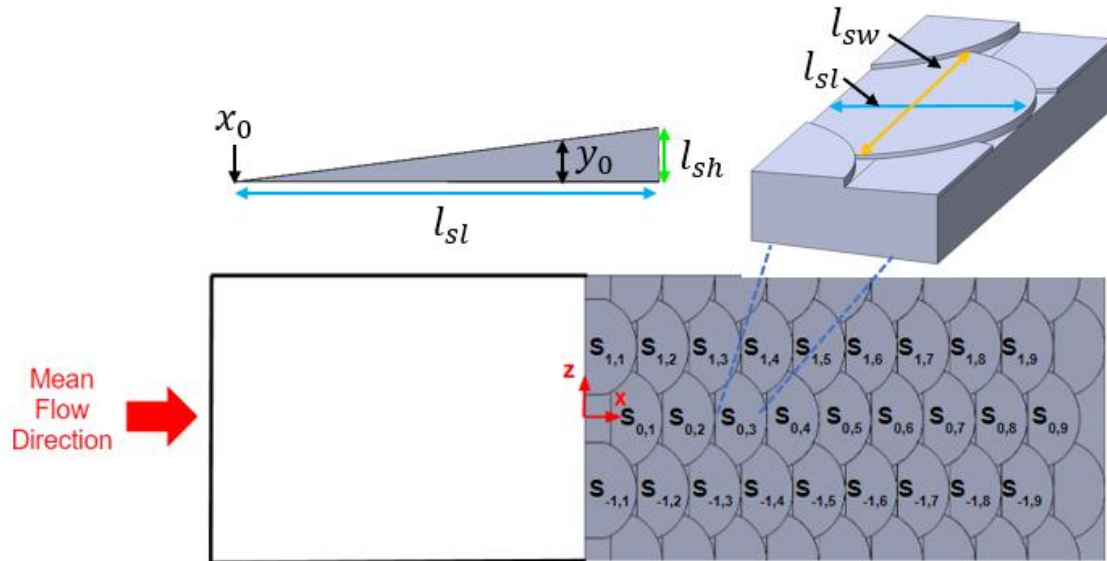


Figure 66: Coordinate system for discussion of results over scale array. The blue arrow shows the scale length ($l_{sl} = 16$ mm), the orange arrow shows the scale width ($l_{sw} = 26.65$ mm), and the scale height is shown by the green arrow ($l_{sh} = 0.8$ mm). The varying height of the surface (y_0) along with the upstream position of the scale (x_0) are also shown. Scales are identified using double subscript notation where the first subscript corresponds to the spanwise row (-1, 0, 1), and the second subscript corresponds to the streamwise scale number (1-9).

It should be noted that given the finite nature of the scale pattern and the change in the surface condition to a flat plate at the end of the array, the velocity magnitudes are often much larger over the final scale than the rest of the array. This is purely due to the transition effects to the flat plate rather than related to the physics over the scale array. As such, analysis over the scale array will be limited to $\phi_t = 9$ such that the flow over the last scale is ignored.

The results section is separated into sections exploring specific features of the flow and comparing them across geometries for the experimental inlet profile flow conditions only. These sections will explore how the geometry impacted the wall normal streamwise velocity profiles, the recirculation zone, the streamwise velocity, the spanwise velocity, and the wall normal vorticity. Following this is a discussion of the impact of scale shape

on the friction drag performance before summarizing the overall impact of scale shape on the flow behaviour. Finally, a section discussing how changing the flow conditions impacts the observed behaviours and scale performance will conclude the analysis.

3.4.1 Vertical Profiles

The wall normal streamwise velocity profiles provide valuable information about how the scale features are impacting the flow within the boundary layer. First, the wall normal streamwise velocity profiles for all three geometries are compared along the scale centerline ($\xi = 0$) at streamwise locations of $\phi_t = 4.5$ and 8.5 (see Figure 67).

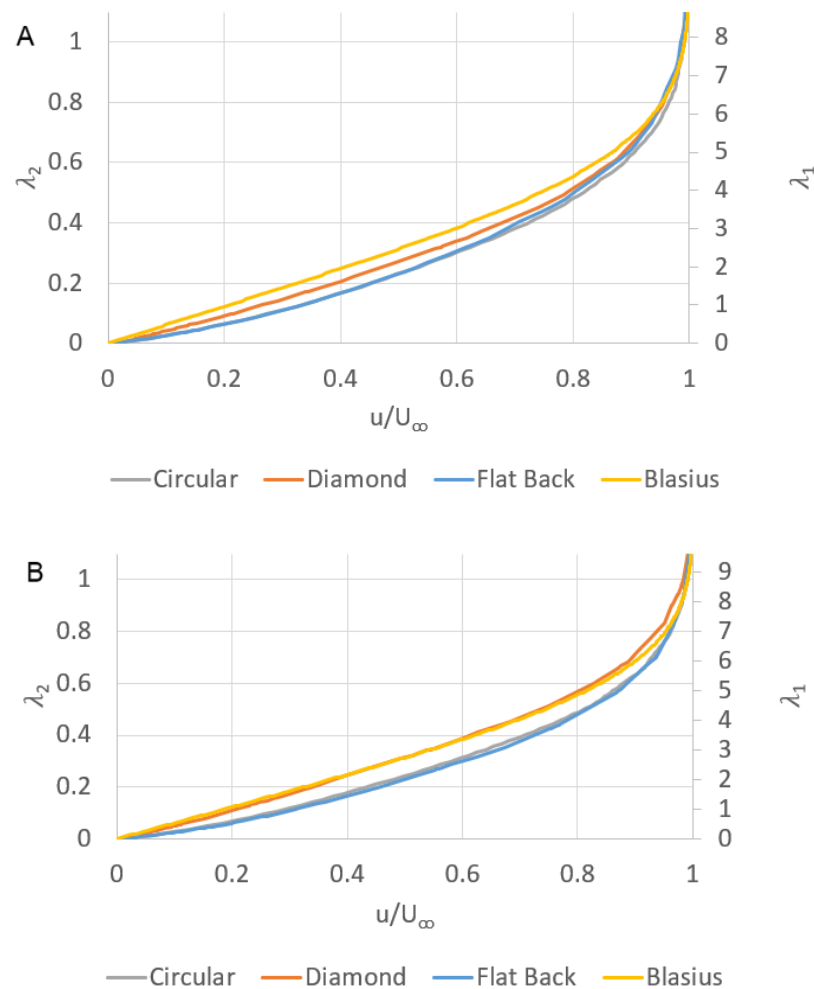


Figure 67: Non-dimensional wall normal streamwise velocity profiles at (A) $\phi_t = 4.5$ and (B) $\phi = 8.5$ along the scales centerline ($\xi = 0$) for all three geometries. The theoretical Blasius profile is also plotted as reference.

While the circular and flat back scales present a very similar geometrical shape, this is reflected in their wall normal streamwise velocity profiles along the scale centerline. Interestingly, the diamond scales have quite a different scale shape and show an upward shift compared to both the circular and flat back scales. Given that these profiles were obtained at the downstream end of the scale, they do not include any effects of the recirculation and thus all show a downward shift from the Blasius solution. The one exception to this is the wall normal profile for the diamond scale at a streamwise location of $\phi_t = 8.5$ which shows a close relation to the Blasius solution. The velocity profiles for both the flat back and circular scale patterns show little change in the streamwise direction, whereas the diamond shape shows an upward shift in the streamwise direction. This is likely related to the streamwise development of the velocity along the centerline.

Given the differences observed in the diamond scale profile, a deeper analysis into the wall normal streamwise velocity profiles along the length of a single scale are required. For this purpose, first the wall normal streamwise velocity profiles along the length of a scale, $S_{0,7}$ at $\xi = 0$ are analyzed for the flat back scale and circular scale are provided in Figure 68A and Figure 68B, respectively.

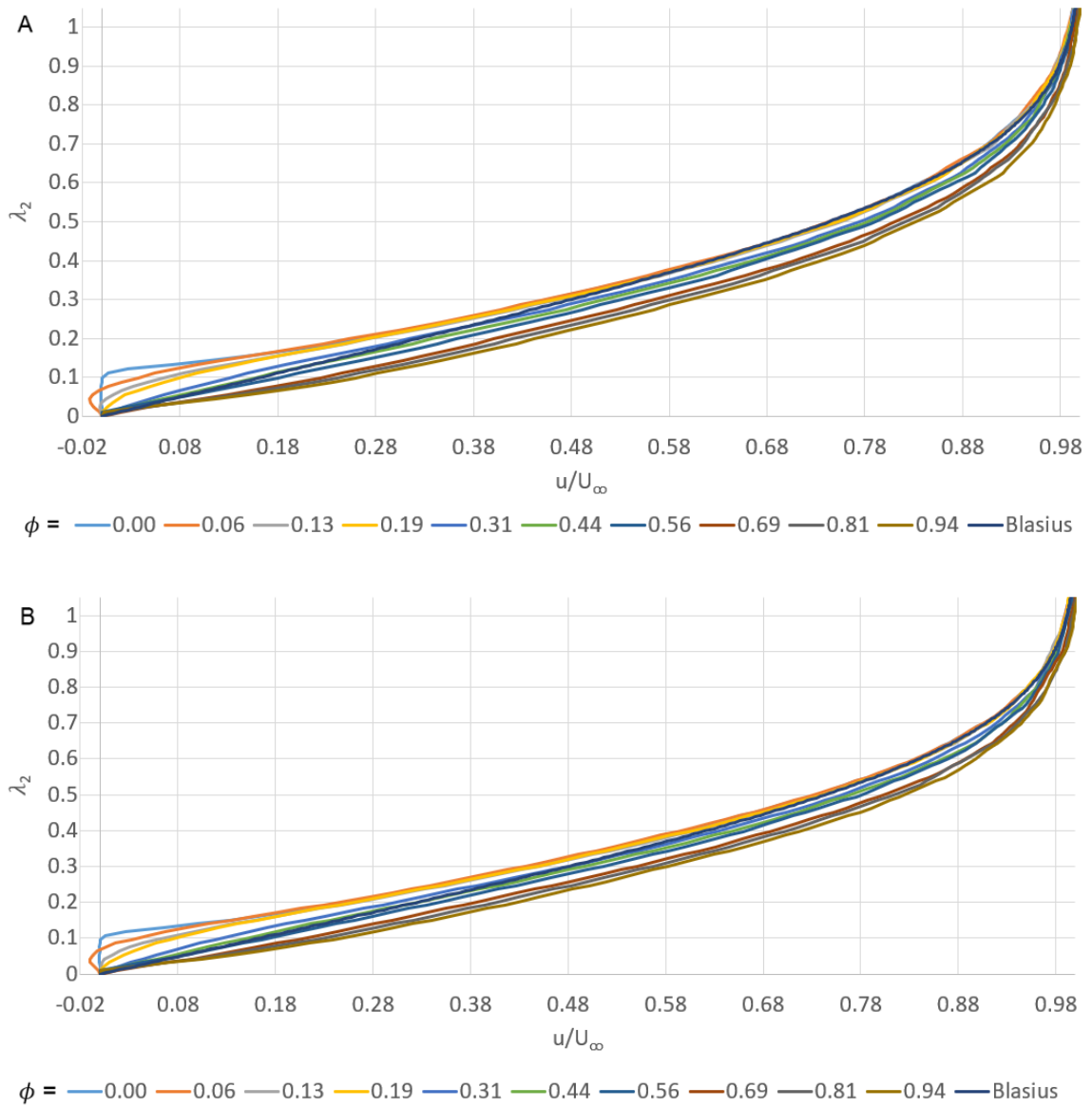


Figure 68: Non-dimensional wall normal streamwise velocity profile for different values of ϕ over a single scale $S_{0,7}$ at $\xi = 0$ for (A) flat back shaped scale and (B) Circular shaped scale.

From analysis of the wall normal streamwise velocity profiles along the centerline of a scale in the flat back array, strong similarities can be drawn to the circular scale. The profiles for the flat back array show that there exists a flow recirculation region near the scale height which causes an upward shift in the wall normal streamwise velocity profiles for small values of ϕ . The wall normal extent of the upward shift extends to about $\lambda_2 =$

0.3 within the boundary layer, indicating a quicker recovery to the Blasius profile compared to the circular scale, which extends too about $\lambda_2 = 0.4$.

In the streamwise direction along both the flat back and circular scale, the results show that the upward shift compared to the Blasius solution persists up to about $\phi = 0.3$ after which the velocity profiles closely match the Blasius profile. Moving farther along the scale, the profiles begin to show a downward shift relative to the Blasius profile after about $\phi = 0.56$. The downward shift is a result of the changing scale height that causes the fluid above the surface to accelerate. This downward shift persists throughout much of the boundary layer until it begins to converge back to the Blasius profile at $\lambda_2 = 0.8$. These trends are similar for both the flat back and circular shaped scales. The wall normal streamwise velocity profiles over scale $S_{0,7}$ along the centerline ($\xi = 0$) for the diamond scale shape are shown in Figure 69.

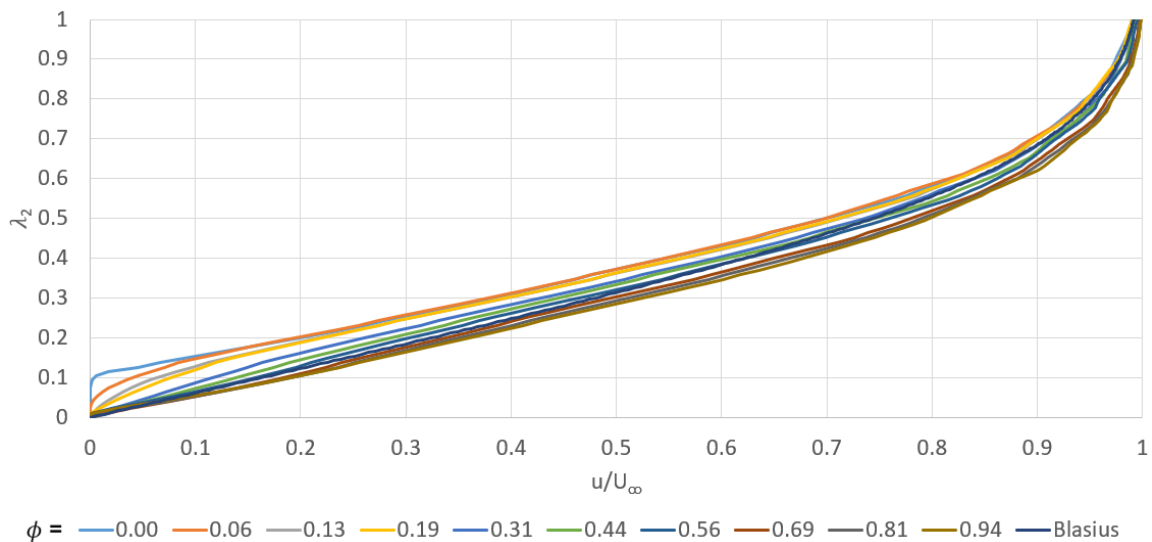


Figure 69: Non-dimensional wall normal streamwise velocity profiles for different values of ϕ over scale $S_{0,7}$ at $\xi = 0$ for the diamond scale.

The wall normal streamwise velocity profiles over the diamond shape scale are much closer to the Blasius solution over the length of the scale compared to the flat back and circular scale shapes. The profiles over a similar streamwise length ($\phi = 0.3$) experience an upward shift compared to the Blasius profile and extends up to a wall normal distance

of about $\lambda_2 = 0.6$. This indicates the presence of a flow recirculation region for small values of ϕ . The wall normal extent of these variations is larger than what was found over the circular and flat back scale geometry (see Figure 68).

While the diamond scale shape results in a greater wall normal extent of upward shifted velocity profiles, it also results in less of a downward shift for greater values of ϕ compared to the flat back and circular scales. The diamond scale does produce some downward shifted wall normal profiles as compared to the Blasius solution, but they do not occur until values of $\phi > 0.69$. Not only is this farther downstream than what was found over the flat back and circular scale shape, but the extent of the downward shifted profiles in the diamond scale does not become significant until a wall normal height of $\lambda_2 = 0.3$. With upward shifted profiles persisting higher in the boundary layer and a delayed deviation in the downward shifted profiles, the overall trend of the velocity profiles over the centerline of the diamond shaped scale are closer to the Blasius solution than those in either the circular or flat back scale shapes. This highlights that along the scale centerline of the diamond shaped scale, smaller velocities persist higher into the boundary layer with less flow acceleration over the length of the scale.

To understand the spanwise influence of different scale geometries, the velocity profiles in the overlapping region of the scale are compared. Figure 70 shows the non-dimensional wall normal streamwise velocity profiles in the overlapping region ($\xi = 0.375$) at a streamwise distance of $\phi_t = 4.5$ and 8.5 for all scale geometries.

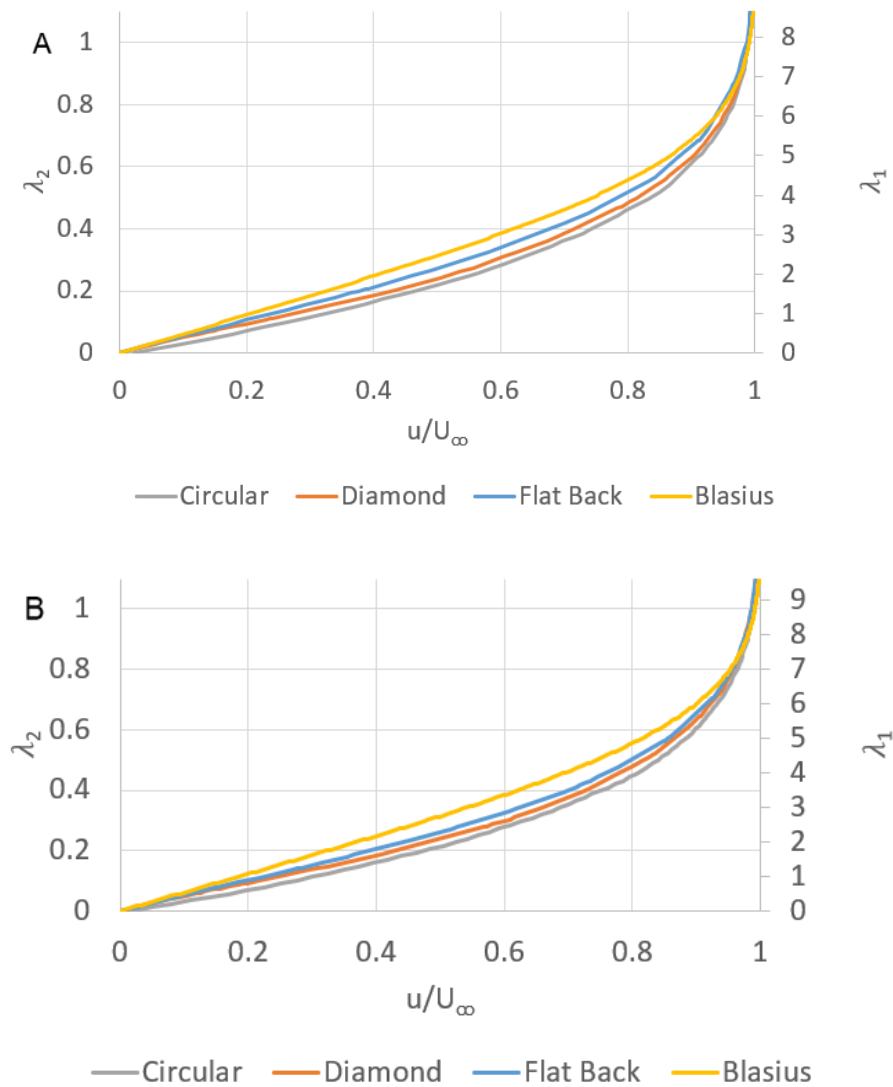


Figure 70: Non-dimensional wall normal streamwise velocity profiles at (A) $\phi_t = 4.5$ and (B) $\phi_t = 8.5$ in the scales overlapping region ($\xi = 0.375$) for all three scale geometries.

The results show downward shifted velocity profiles at both streamwise locations for all geometries in the overlapping region compared to the Blasius profile. It is also observed that the flat back scale has less of a downward shift in the velocity profile relative to the Blasius profile, compared to the other two geometries. The diamond and circular scales have a comparable downward shift which is greater than the flat back scale shape. For the diamond shaped scale, these trends are different from what was found along the scale centerline where the velocity profile over diamond scale matched more closely the

Blasius profile. Comparison of the velocity profiles over the centerline and overlapping regions (Figure 67 and Figure 70) indicates that the streamwise velocity over the diamond scale shape experiences the largest variation in the spanwise direction, while the flat back scale shape experiences the least spanwise variation.

While the vertical profiles have given some insight into the 3D nature of the flow behaviour across the different scale shapes, the following section will explore the extent of the flow recirculation zone for the different scale geometries.

3.4.2 Recirculation Zone

The wall normal profiles presented in the previous section show evidence of a potential recirculation zone behind the scale heights for all scale geometries. However, the streamwise and spanwise extent of these recirculation zones was unclear. To examine the spanwise extent of the recirculation, colourmap plots of the negative streamwise velocities in multiple vertical planes are used to illustrate the recirculation regions behind the scale heights. Figure 71 shows the negative streamwise velocity regions behind the scale height of scale $S_{0,5}$ for all scale shapes along vertical planes extending spanwise from the centerline to the overlapping region.

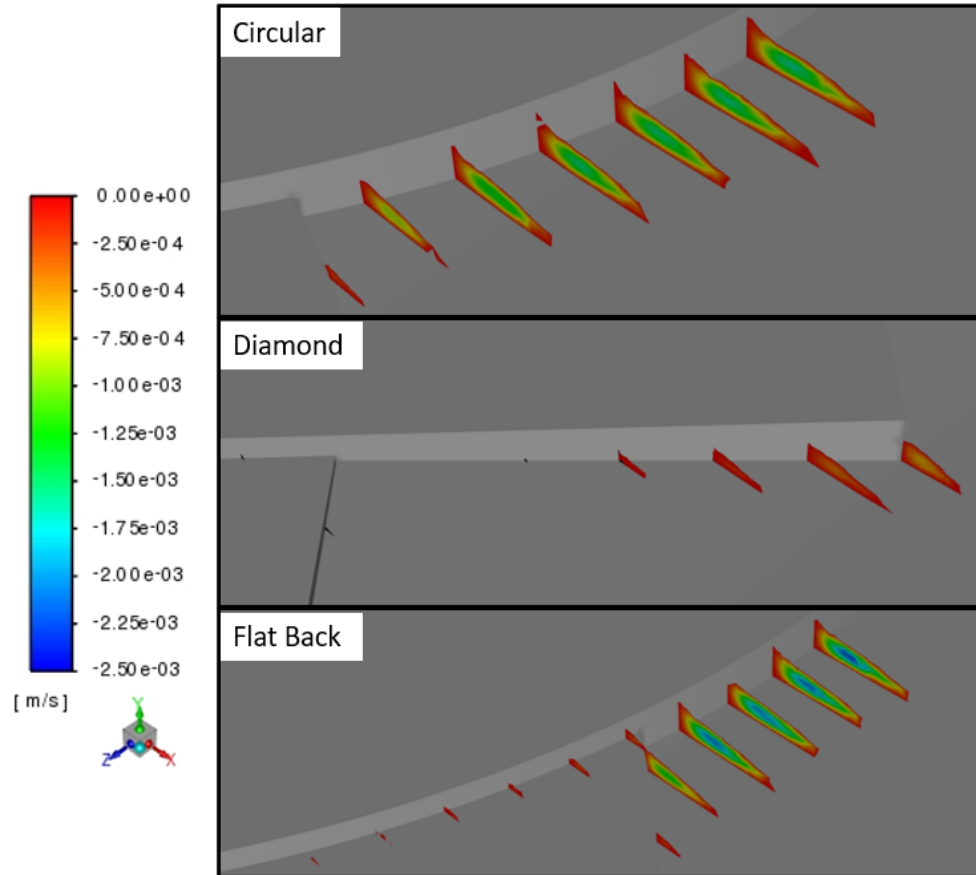


Figure 71: Colourmap plot showing regions of negative streamwise velocity over all scale geometries in 1 mm increments from the centerline plane ($\xi = 0$) to the overlapping plane ($\xi = 0.375$).

From Figure 71 it is observed that the extent and strength of the recirculation region across the scale have a strong dependency on scale shape. The circular and flat back geometries show relatively similar trends in the spanwise direction with the flat back scale containing a stronger negative velocity. In both the circular and flat back geometries, the extent of the negative velocity region in the spanwise direction extends through the midline plane to the edge of the overlapping scale. This shows that in both cases, flow recirculation is found at all spanwise locations across the centerline region of the scale until the edge of the adjacent overlapping scale. In both cases, the size of the negative velocity region is found to decrease slowly in the spanwise direction showing that the streamwise extent of the recirculation region changes gradually in the spanwise direction.

The diamond geometry shows a considerable difference in the size and strength of the negative streamwise velocity associated with the recirculation region. First, it is noted that the magnitudes of the negative velocities are much smaller than those found in both the circular and flat back geometries. This indicates that the size of the flow recirculation zone is smaller for the diamond scale geometry. Secondly, the spanwise extent of the negative streamwise velocity region is much smaller than the circular or flat back geometries. In the case of the diamond scale, a rapid decrease in the streamwise extent of the negative velocity is observed in the spanwise direction, which resulted in an almost complete elimination of the flow recirculation region about halfway to the edge of the overlapping scales. Given the smaller spanwise extent of the flow recirculation behind the diamond shaped scale, this is expected to have an impact on the size of the low-velocity streaks that are observed along the scale centerline.

While Figure 71 highlights the differences in the spanwise extent of the recirculation zone, it does not provide quantitative information about the streamwise extent of the recirculation zone for different scale geometries. To quantify this, the reattachment length for each scale along $\xi = 0$ was measured as the streamwise distance from the scale height where the streamwise velocity, immediately above the surface, switches from negative to positive. Given the first and last scales in the array provide different velocity patterns (related to the finite nature of the scale array), only scales $S_{0,2}$ to $S_{0,8}$ were considered for the calculation of the reattachment length. The average reattachment lengths for all scales of a given geometry and associated 95% confidence intervals (based on two times the standard deviation) are shown in Table 11 for all scale geometries.

Table 11: Reattachment length and associated 95% confidence interval for each geometry

Geometry	Reattachment Length (length/l_{sh})	95% Confidence Interval (\pm)
Circular	3.39	0.17
Diamond	1.68	0.13
Flat back	3.66	0.37

The reattachment length data shows that the scale shape does play an important role in the streamwise extent of the recirculation zone. It is noted that while the circular and flat back scales present a very similar geometry, the reattachment length is also similar. In the case of the flat back geometry, the reattachment length is found to be slightly larger than the circular geometry. However, given the uncertainty associated with these measurements, no distinction can be conclusively made. When comparing the reattachment length of the circular geometry to the value of 2.6 ± 0.9 , found experimentally in chapter 2, it is noted that the simulation predicts a larger reattachment length than the experimental results. However, given the difference is within the uncertainty range for both results and there exists some numerical uncertainty that is unaccounted for, the reattachment length results shown here can be trusted and will be used for comparison against the other scale geometries.

Looking at the reattachment length for the diamond scale geometry, it is noted that the reattachment length is equal to about half the reattachment length found in the circular and flat back geometry. Given the sharp point and straight edges associated with the diamond scale geometry, the region of negative streamwise velocity is small and weak resulting in a very short recirculation zone behind the scale height. However, the wall normal streamwise velocity profiles showed a significant upward shift in the velocity profiles over the length of the scale. This indicates that the presence of the scale height continues to have a strong influence on the flow behaviour above the scale array, despite having a smaller recirculation zone. These results show that the size of the recirculation zone varies between geometries but highlights that the flow behaviour in the wall normal direction along the scale centerline is not significantly influenced by the size of the corresponding recirculation zone.

Next, the flow patterns across the scale array are analyzed in the horizontal plane showing variations in the spanwise direction starting with the streamwise velocity component.

3.4.3 Streamwise Velocity

In Chapter 2, the generation of streamwise velocity streaks in the near wall boundary layer over a circular fish scale array were explored experimentally. To develop a broad understanding of the difference in the streamwise velocity patterns over different scale geometries, colourmap plots at a wall normal distance of $\lambda_1 = 2$ are shown in Figure 72 for all three geometries.

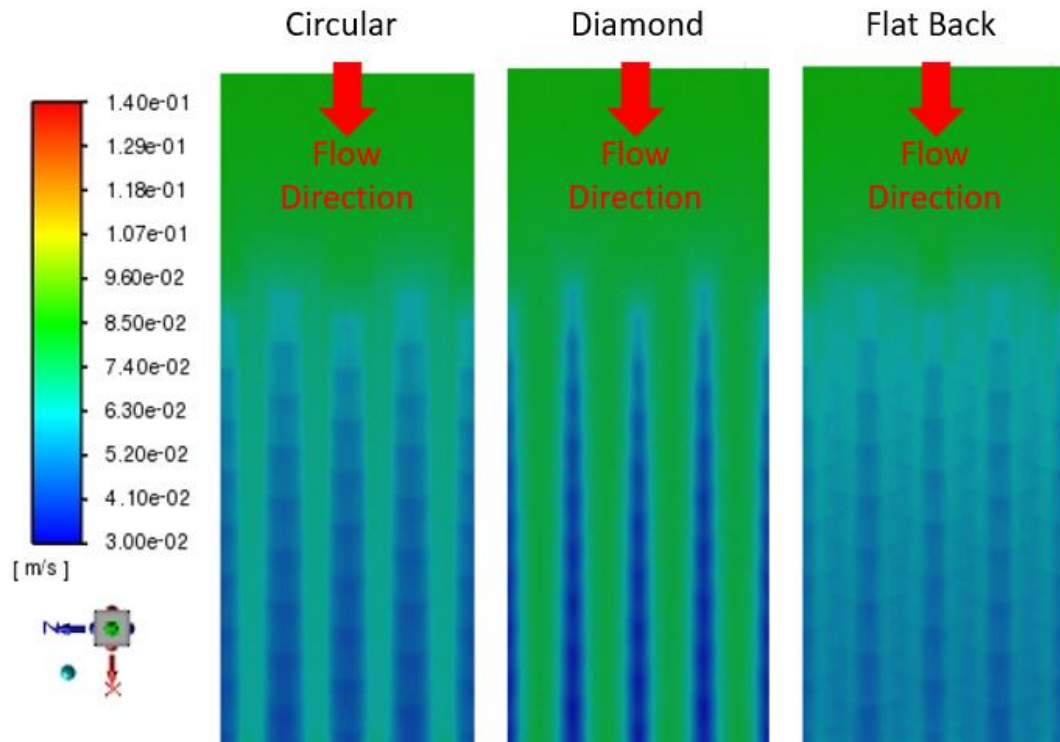


Figure 72: Colourmap of the streamwise velocity at a wall normal distance of $\lambda_1 = 2$ for all geometries. The flow is from top to bottom.

The colourmap plots show that the diamond shaped scale has the strongest streamwise velocity variations in the spanwise direction. It also shows that the diamond scale has a narrower low-velocity region compared to both the circular and flat back geometries. Given the vertical plane results revealed the recirculation zone associated with diamond scale was smaller in the spanwise direction compared to the circular scale, it is expected that the low velocity region will also be smaller. This behaviour is also consistent with the relative size of the overlapping region. When defined by the boundaries of the

overlapping scales, the width of the overlapping region is 6.6 mm in the circular geometry, 8 mm in the diamond geometry, and 12.5 mm in the flat back geometry (see Figure 73).

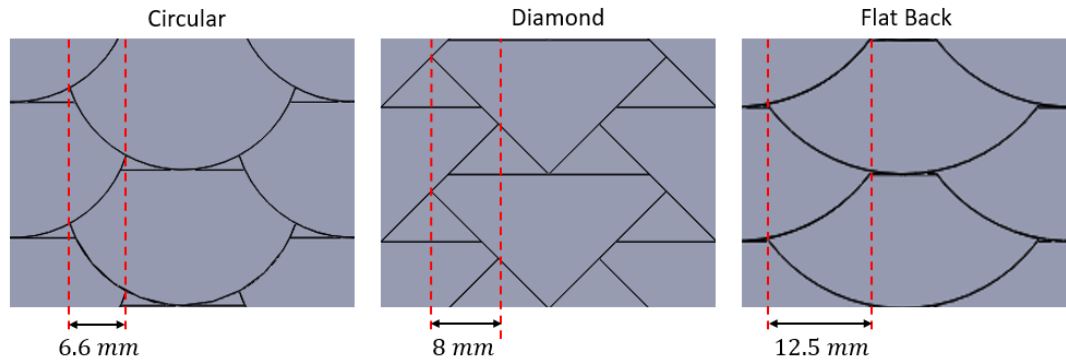


Figure 73: Size of overlapping region for each scale shape.

The flat back geometry has the largest width of the overlapping region compared to the other two geometries and has the lowest streamwise velocity variations. While smaller variations are observed in the flat back geometry, the size of the high-velocity region does appear larger than the circular geometry, in line with the larger overlapping region. Comparing the patterns of streamwise velocity in the circular and diamond scale arrays it is noted that the high-velocity streaks appear wider in the diamond array compared to the circular scale array. However, the high-velocity regions in the diamond and flat back geometries appear similar, suggesting it is inconclusive whether the size of the high-velocity region is related to the size of the overlapping region.

While the colourmaps show the magnitude of the velocity, it is useful to look at the range of the velocity variations. Thus, the streamwise velocity variation is defined as the difference between the max velocity at each height and the velocity at any given location in that plane, divided by the free-stream velocity (equation 3.13).

$$\psi = \frac{u_{max} - u}{U_{\infty}} \quad (3.13)$$

To explore the effect of these variations in the wall normal direction, the streamwise velocity variation (ψ) is plotted for all geometries at a streamwise location of $\phi_t = 4.5$ and wall normal heights of $\lambda_1 = 2.5$ and 5 in Figure 18.

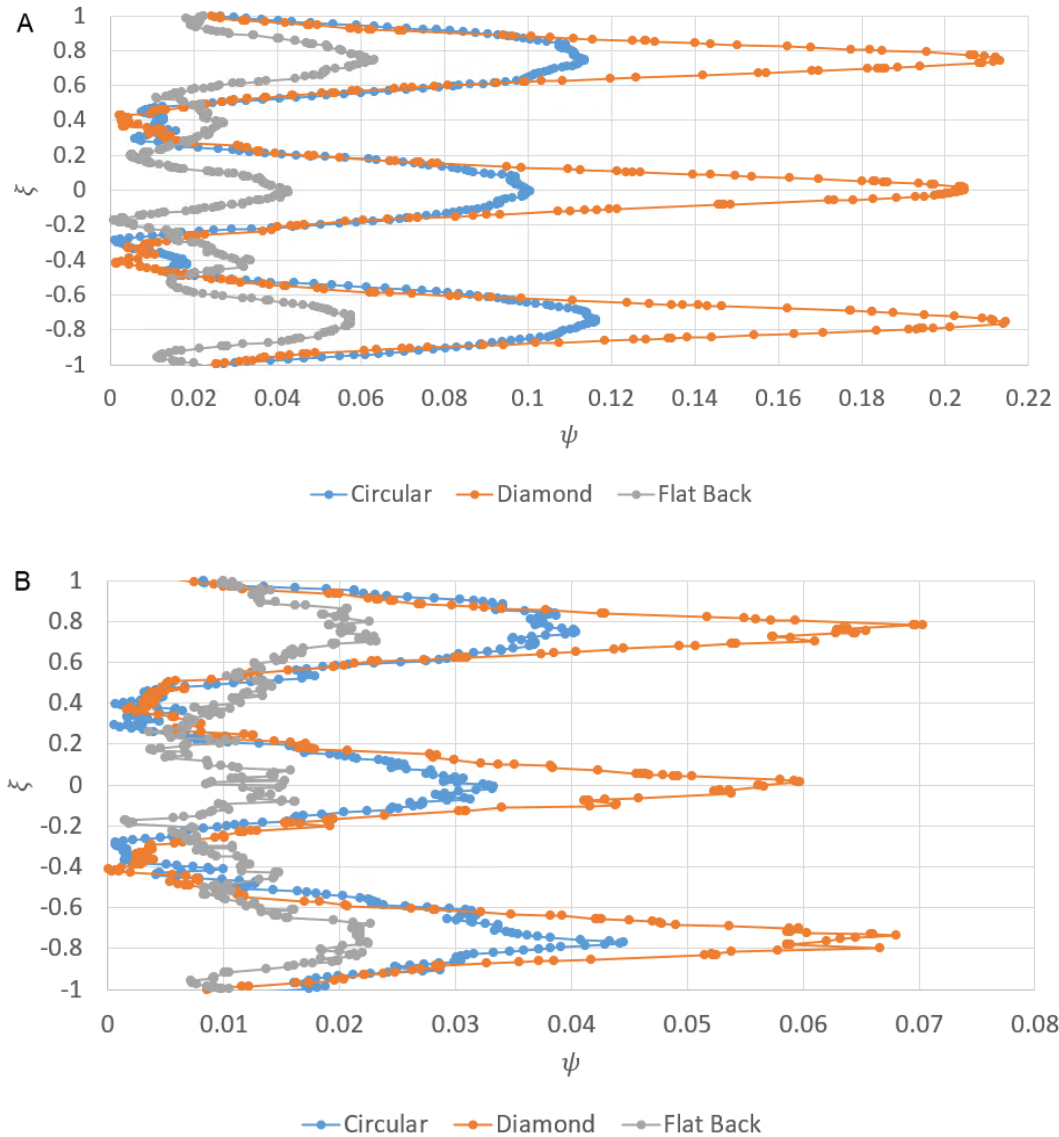


Figure 74: Streamwise velocity variation (ψ) for all geometries at a streamwise position of $\phi_t = 4.5$ and wall normal locations of (A) $\lambda_1 = 2.5$ and (B) $\lambda_1 = 5$.

Comparing the plots of velocity variation (ψ) between geometries, similar trends to those found in the colourmap plots (Figure 72) are observed. The largest velocity variations are found in the diamond scale shape, while the smallest variations are found in the flat back

scale. These differences are observed at all wall-normal locations (shown here only at $\lambda_1 = 2.5$ and 5 as representative profiles). Additionally, it is noted that the variations found over the centerline of the circular scale are about half of those found over the centerline of the diamond scale. Similarly, those found over the flat back scale are about half of those found over the circular scale. These trends and differences between geometries are found to persist with the distance away from the surface until the streaks dissipate within the boundary layer.

The strength and width of these velocity streaks is related to the changes in height across the width of the scale. With the max scale height occurring in the scale centerline, the scale shape results in different local scale heights moving towards the overlapping region. The diamond scale contains the largest variation in local scale height resulting in a greater streamwise velocity in the overlapping region and larger streamwise velocity variations. The flow along the scale centerline wants to take the path of least resistance, which as a result of the varying local scale height in the spanwise direction, is towards the overlapping region. The greater variations in height across the diamond scale array result in more fluid being pushed to the overlapping region and thus a higher velocity compared to the other scale geometries.

As was observed in the wall normal streamwise velocity profiles, a larger upward shift in the velocity along the scale centerline of the diamond scale array results in a low-velocity region extending farther into the boundary layer compared to the other scale geometries. Given the larger surface variations lead to more fluid being pushed to the overlapping regions, and the greater upward shift in the wall normal streamwise velocity profiles along the scale centerline led to a stronger low-velocity region, the overall effect over the diamond scale array is larger streamwise velocity streaks. Similarly, the smaller variations in local scale height across the flat back scale result in a smaller velocity variation observed across the scale array.

While the streaks show some streamwise development (Figure 72), it is found that the magnitude of the velocity variation (ψ) also changes in the streamwise direction. Figure 75 illustrates this behavior as the velocity variation (ψ) is plotted at a downstream

location of $\phi_t = 8.5$ at the same wall normal locations $\lambda_1 = 2.5$ and 5. As Figure 75 shows, the magnitude of the velocity variation (ψ) increased considerably as the flow progressed downstream. Given that these wall normal locations are a fixed distance from the wall and the boundary layer is found to grow in the downstream direction, these measurement locations are closer to the surface relative to the boundary layer thickness.

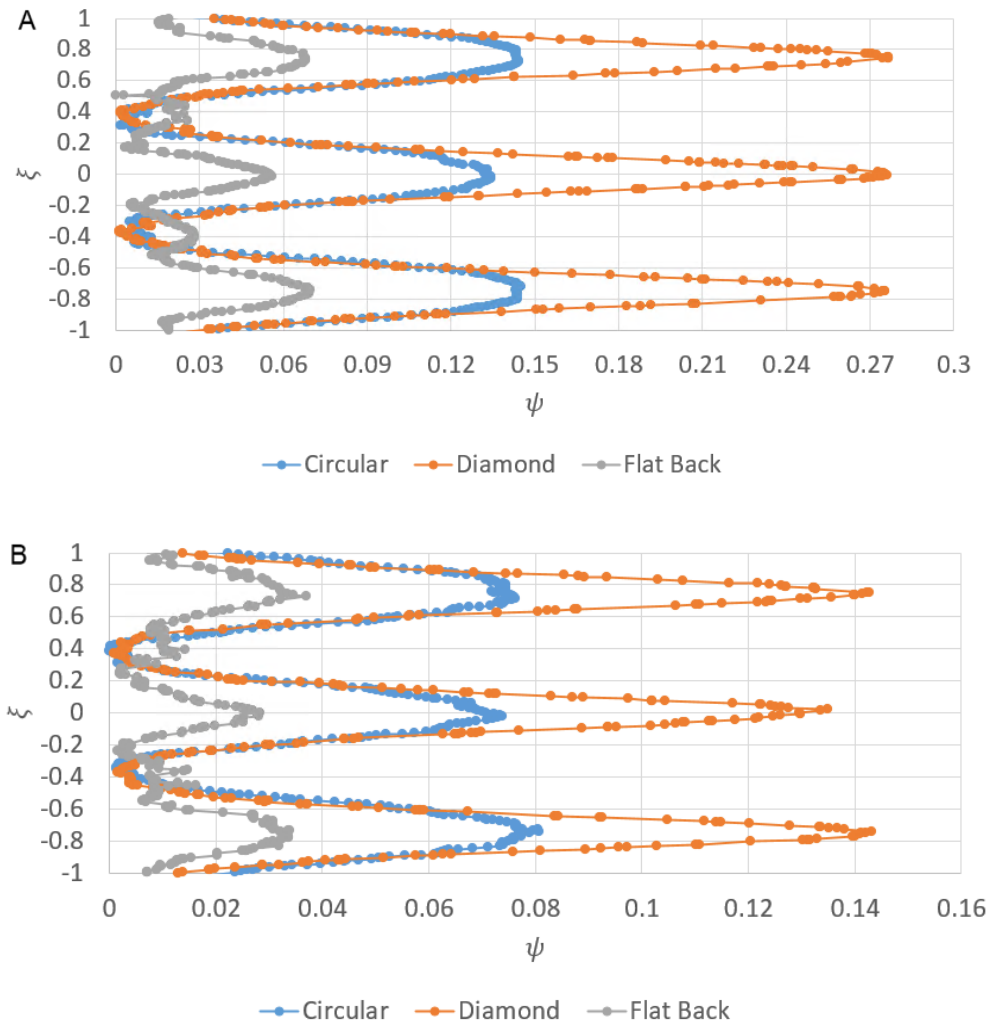


Figure 75: Streamwise velocity variation (ψ) for all geometries at a streamwise position of $\phi_t = 8.5$ for wall normal heights corresponding to (A) $\lambda_1 = 2.5$ and (B) $\lambda_1 = 5$.

Due to the increasing velocity variations in the streamwise direction, the wall normal extent of the streamwise variations is expected to grow with the boundary layer in the

streamwise direction for all geometries. This results in larger magnitudes of velocity variations closer to the surface and an increase in the streak strength in the downstream direction. Given the finite nature of the scale array, further work is required to fully understand the behaviour of the streamwise velocity streaks in the downstream direction to determine if there exists some development length after which the behaviour is unchanged.

Another interesting flow behaviour which is observed in the streamwise velocity variation plots (Figure 74 and Figure 75), is the secondary local maximum which is present in the overlapping region of the flat back geometry. While this flow behaviour is much stronger in the flat back geometry, it exists very briefly in the circular and diamond geometries in Figure 74. This secondary local maximum of the velocity variation shows that within the high-velocity region (i.e., overlapping region), there exists a smaller region of lower streamwise velocity. This behaviour may be linked to the size of the overlapping region as the flat back array has the largest overlapping region (12.5 mm).

Next, the following section will explore the spanwise velocity over the scale array and discuss how the scale shape influences the spanwise velocity component over the scale array.

3.4.4 Spanwise Velocity

While the analysis in Chapter 2 revealed an alternating pattern of spanwise velocity in the overlapping region, similar results are observed in the simulations. To understand the impact of scale shape on the spanwise velocity over the scale array, the colourmap plots of the spanwise velocity across the array at a wall normal location of $\lambda_1 = 2$ are shown in Figure 76 for all geometries.

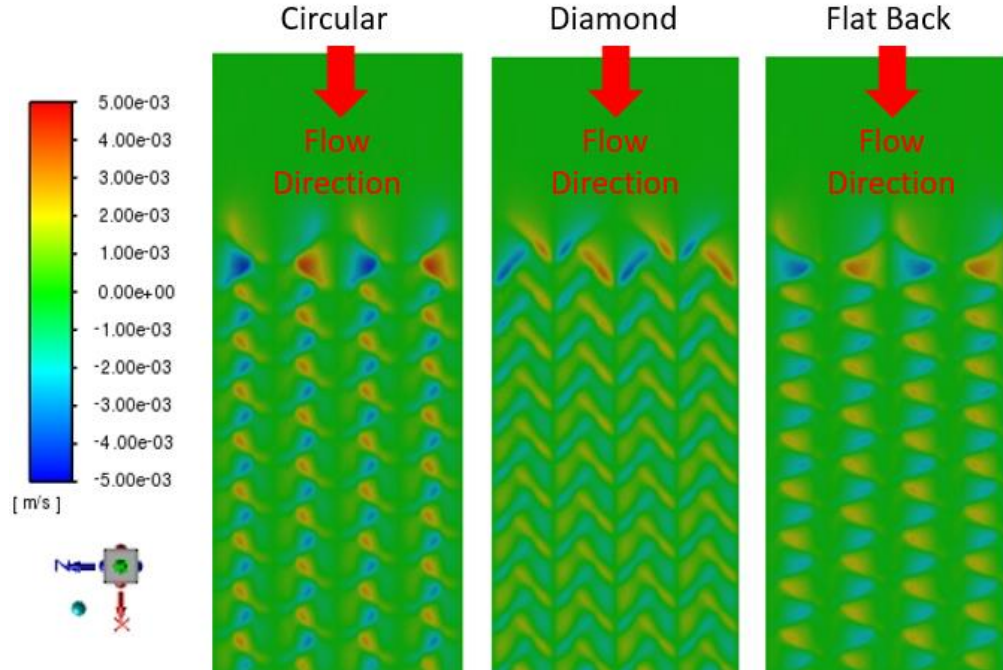


Figure 76: Colourmap of the spanwise velocity at a wall normal distance of $\lambda_1 = 2$ for all geometries. Flow is from top to bottom.

The colourmap plots show that the circular scale geometry has the strongest spanwise velocity magnitude while the diamond scale has the weakest. The diamond scale also shows a weaker elongated region of spanwise velocity along the edge of the scale compared to the circular and flat back geometry. While a similar elongation is weakly present in the circular geometry, it is likely that the size and strength of the elongation in the diamond scale is related to the scale shape.

To get a better understanding of the influence of scale geometry on the spanwise velocity behavior in the overlapping region, the spanwise velocity along the streamwise direction in the overlapping region ($\xi = 0.375$) is plotted for all geometries in Figure 77 at wall normal distances of $\lambda_1 = 2.5$ and 5. The spanwise velocity is expressed as ω (see equation 3.14), which is a non-dimensional representation of the spanwise velocity as a fraction of the free-stream velocity (U_∞).

$$\omega = \frac{w}{U_\infty} \quad (3.14)$$

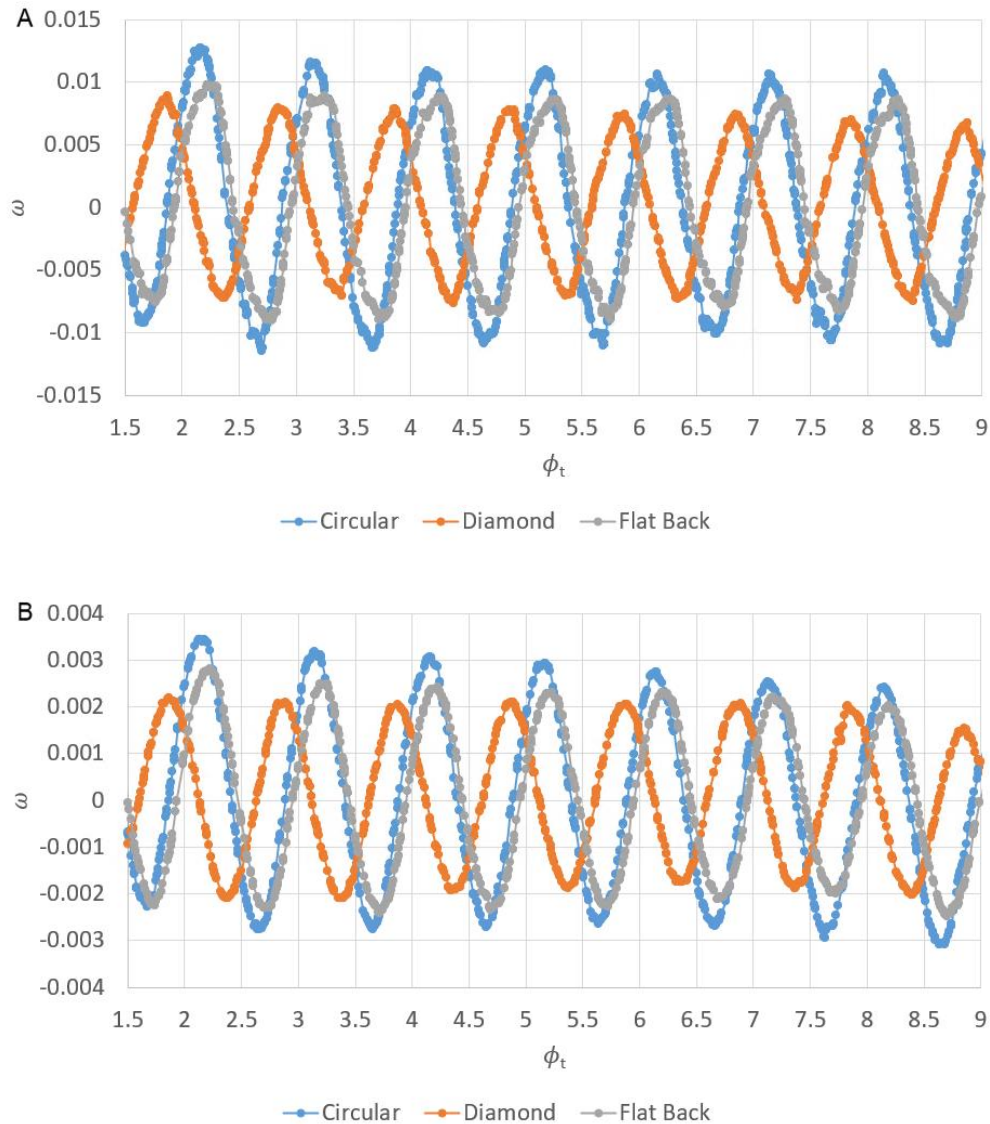


Figure 77: Non-dimensional spanwise velocity (ω) in the overlapping region ($\xi = 0.375$) at wall normal heights of (A) $\lambda_1 = 2.5$ and (B) $\lambda_1 = 5$ for all three geometries.

The plots show trends similar to what is observed in the colourmap plots. Overall, the variations in the velocity amplitudes are similar for all three geometries. From a relative perspective, the circular scale shape has the largest magnitudes, and the diamond scale shape has the smallest magnitudes. Comparison between the non-dimensional velocities at the two heights show that the velocity amplitudes decrease with an increase in the distance from the wall, as expected due to viscous dissipation. These trends are consistent

with the spanwise velocity variations observed experimentally in Chapter 2. Figure 77 also shows that despite the difference in amplitudes as the distance from the surface increases, the trends of the spanwise velocity remained similar between geometries. These trends persist as the wall normal distance is increased and only $\lambda_1 = 2.5$ and 5 are shown as a sample.

A small streamwise phase shift between the patterns of spanwise velocity is also observed in Figure 77. While the circular and flat back geometries contain peaks at a similar streamwise location, the peaks of the diamond scale appear shifted upstream. Given that the spacing between the scales in the streamwise direction remains consistent between geometries, the period of the spanwise oscillations also remains the same. However, it is the changes in the scale geometry which resulted in the phase shift of scale heights in the overlapping region. Thus, the difference in streamwise locations of the scale heights in the overlapping region, drives the phase shift observed in Figure 77. The straight edges of the diamond scale resulted in the scale heights shifting upstream, whereas the larger radius of the flat back scale resulted in scale heights shifting downstream. This peak shifting is fundamentally related to the changes in scale geometry and has little impact on the flow behaviour otherwise.

To further explore the influence of scale geometry on the spanwise velocity patterns in the vicinity close to the peak scale height, colourmap plots over single scale are explored above and below the peak scale height ($\lambda_1 = 1$). Figure 78A shows the spanwise velocity component for all geometries immediately above ($\lambda_1 = 1.25$) the peak scale height ($S_{0.5}$), and Figure 78B shows the spanwise velocity component for all geometries immediately below ($\lambda_1 = 0.625$) the peak scale height ($S_{0.5}$).

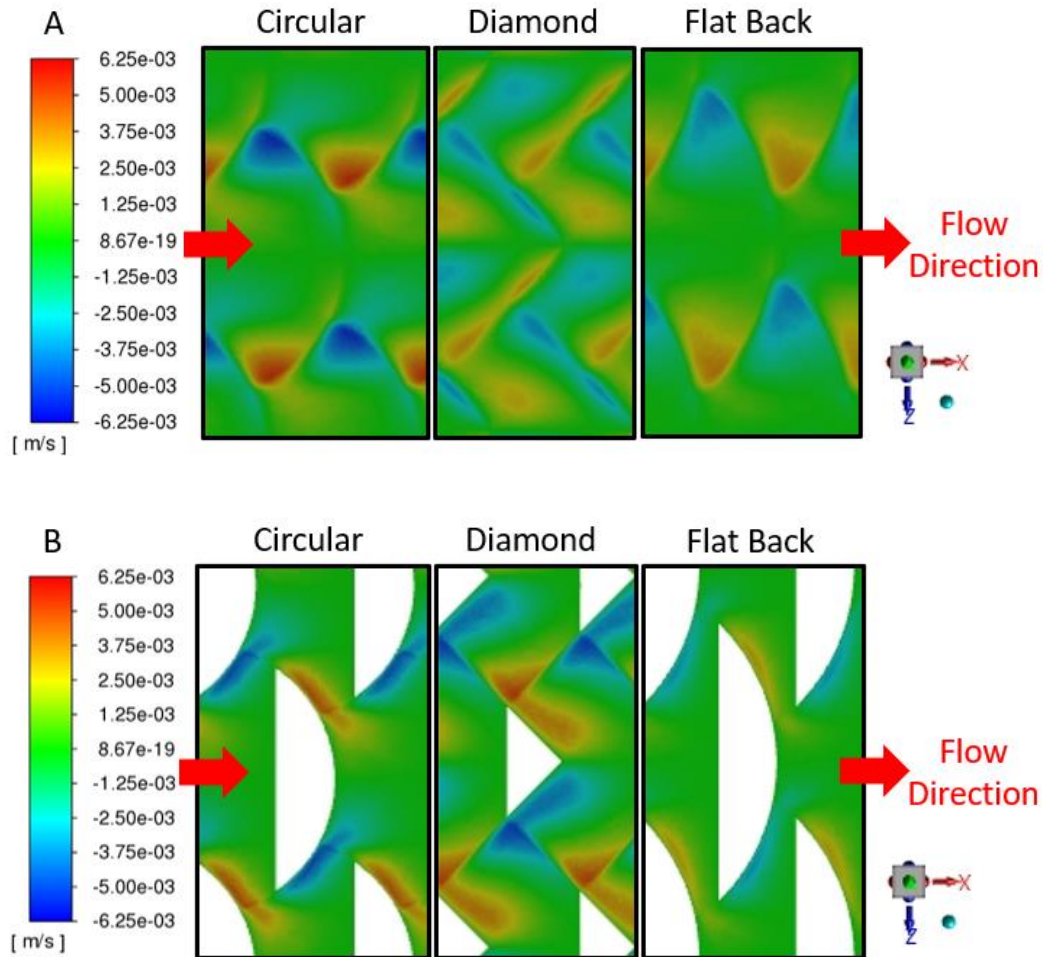


Figure 78: Colourmap of the spanwise velocity over scale $S_{0.5}$ at a wall normal distance of (A) $\lambda_1 = 1.25$ and (B) $\lambda_1 = 0.625$ for all geometries. Flow is from left to right.

The colourmap plots of the spanwise velocity above the scale peak height (Figure 78A) show the alternating velocity pattern in the overlapping region over all geometries. Looking first at the circular and flat back geometries, it is noted that the largest spanwise velocity is concentrated in the corners of the scale where they overlap with the adjacent scale row. While the overlapping region is larger in the flat back geometry, the magnitude of the spanwise velocity component is lower. While the larger scale radius creates less of a height difference across the scale width, it also increases the size of the overlapping region resulting in weaker variations of the spanwise velocity.

The colourmap of the diamond geometry above the scale peak height (Figure 78A) shows a different spanwise velocity pattern which is characterized by two elongated regions concentrated on the edges of the scale. A similar velocity magnitude is found across these regions highlighting the consistent spanwise motion along the entire edge of the diamond scale. While a weak elongation is found in the spanwise velocity of the circular geometry, the change in shape from circular to straight edges resulted in a more elongated but lower magnitude region of spanwise velocity.

In addition to the elongated spanwise region associated with the edge of the diamond scale, the diamond array contains a secondary region of spanwise velocity in the region downstream of the scale height. The secondary region is comprised of two components, on either side of the scale centerline, whose velocity is linked to the adjacent scale row. A similar pattern is only weakly observed in the colourmap of the circular scale shape. The connection between this secondary spanwise velocity region and the adjacent scale row suggests that the spanwise fluid motion is not confined to the overlapping region close to the surface and plays a role in modifying the flow in the centerline region.

Moving closer to the surface in the region below the peak scale height (Figure 78B), the extent of the spanwise velocity which extends from the adjacent scale rows into the centerline region is observed. The magnitudes of the spanwise velocities below the peak scale height appear lowest in the flat back scale and highest in the diamond scale. The patterns in the colourmaps of the circular and diamond scale geometries show a region of spanwise velocity extending from the overlapping region into the centerline region, below the peak scale height (Figure 78B). In the circular geometry, this spanwise velocity is quickly dissipated and likely has a weak impact on the flow recirculation in the centerline region. However, the spanwise velocity below the peak scale height in the diamond geometry is found to have a much greater magnitude and extend farther into the centerline region than in the circular geometry.

In all cases where the spanwise velocity persisted below the peak scale height towards the centerline region, the flow recirculation zone acted as a 3D rolling vortex moving fluid towards the scale tip. While stronger spanwise components below the scale height

persisted closer to the scale centerline in the diamond shaped array, the associated streamwise recirculation zone was found to be smaller in both the spanwise and streamwise directions. Thus, this spanwise motion in the region below the peak scale height weakened and, in some cases, prevented the formation of the recirculation zone until closer to the centerline plane ($\xi = 0$).

Next, the wall normal vorticity patterns across the scale array will explore how the streamwise and spanwise velocities interact above the scale array.

3.4.5 Wall Normal Vorticity

The wall normal vorticity represents the spanwise rotation of the fluid across the scale array. Figure 79 shows the colourmaps of the wall normal vorticity for all geometries in a horizontal plane located at a wall distance of $\lambda_1 = 2$.

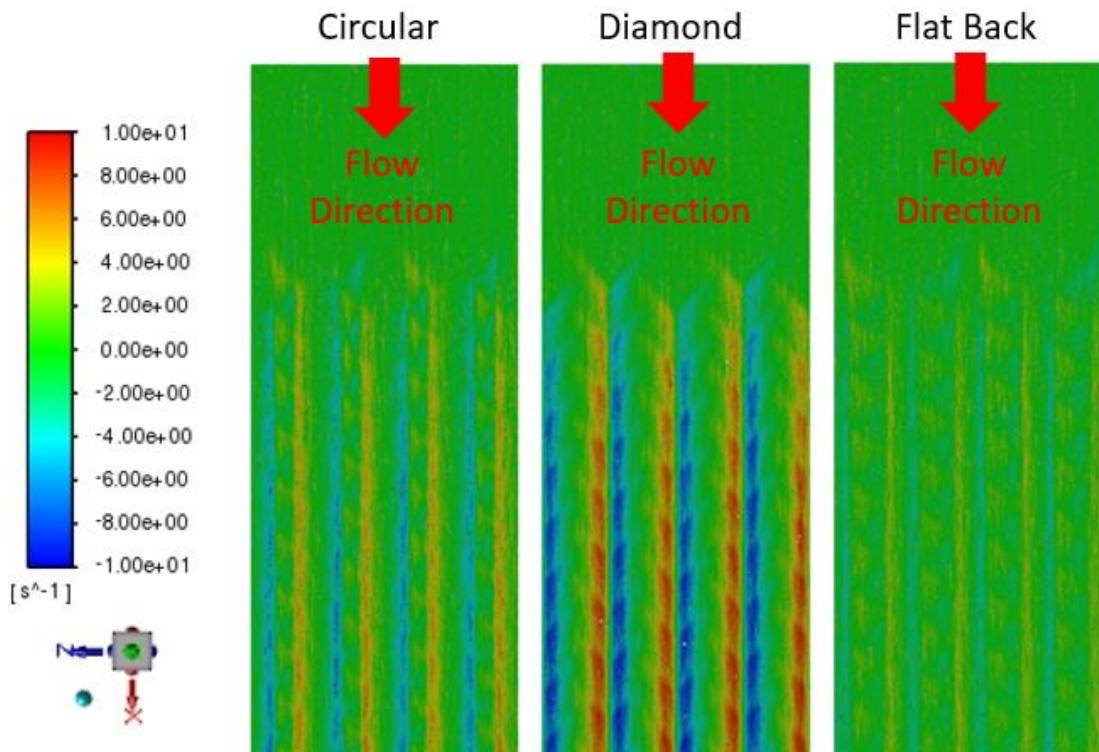


Figure 79: Colourmap of the wall normal vorticity at a wall normal distance of $\lambda_1 = 2$ for all geometries. Flow is from top to bottom. The positive values correspond to clockwise rotation, whereas negative values correspond to anticlockwise rotation.

The wall normal vorticity colourmaps in Figure 79 shows that all geometries result in a counter-rotation of the fluid from the centerline of the scales towards the overlapping region on either side of the scale centerline. Given that the peak scale height results in the largest surface variations along the scale centerline, the fluid experiences the greatest resistance to streamwise motion along the centerline. Moving towards the overlapping region, the changing scale shape results in a smaller local scale height leading to less resistance to streamwise motion. In a frame of reference moving with the fluid, peaks are found along the scale centerline and valleys along the overlapping region. It is this variation in height that drives the rotation of the fluid away from the scale centerline towards the overlapping region.

The colourmap plots show the strongest vorticity in the diamond array and the weakest vorticity is in the flat back array, which is expected considering the specific geometric features of these scales. The diamond array contains straight edges at 45-degrees, hence the variation in height experienced in the spanwise direction is greater than the flat back scale, which has a scale shape whose height remains relatively consistent across the scale width. The circular scale has a smaller radius and more height variation across its width than the flat back scale, thus the vorticity magnitude is larger than the flat back scale but not as large as the diamond scale.

All geometries show a consistent trend in the streamwise direction, indicating that the vorticity patterns have little streamwise development. To understand the variations in the wall normal direction, the wall normal vorticity in spanwise direction at the streamwise location of $\phi_t = 4.5$ is plotted for all geometries at wall normal distances of $\lambda_1 = 2.5$ and 5 (see Figure 80).

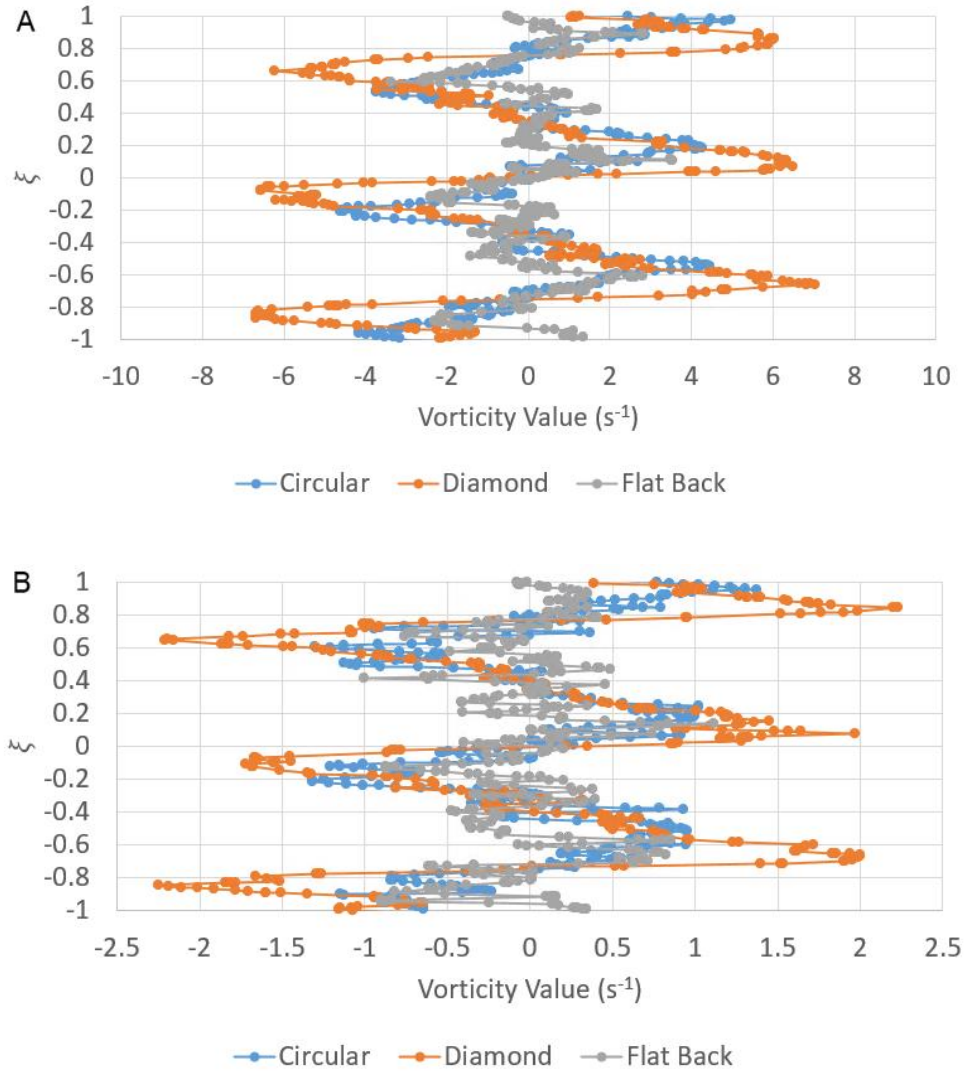


Figure 80: Spanwise profiles of the wall-normal vorticity for all geometries at a streamwise location of $\phi_t = 4.5$ and wall normal heights (A) $\lambda_1 = 2.5$ and (B) $\lambda_1 = 5$.

The vorticity profiles show that the magnitude of wall normal vorticity decreases with increasing distance from the wall. This is expected as the viscous effects begin to dissipate the induced wall normal vorticity. The plots show that the peak vorticity values over the diamond scale are found to occur at spanwise locations closer to the scale centerlines ($\xi = 0, \pm 0.75$) compared to the circular and flat back scale. Due to the straight edges of the diamond scale, the change in scale height across the width is continuous, whereas in the circular and flat back scales the height variation increases

moving closer to the overlapping region. Thus, the curvature at the tip of the scale in the circular and flat back geometries results in very little height variation in the centerline region causing the peak vorticity to occur closer to the overlapping region. This is not the case in the diamond scale which have a consistent variation in height along the edges of the scale, thus the peak vorticity is found closer to the scale centerlines ($\xi = 0, \pm 0.75$).

The wall normal vorticity streaks in all three geometries appear to remain bounded by the edges of the scale overlap (Figure 73) producing negligible vorticity in the overlapping region. Given the geometry of the scales in the overlapping region forms an overlapping pattern, the scale height from the perspective of the oncoming fluid is found to vary minimally across the width of the overlapping region. As such, while fluid is taking the path of least resistance towards the overlapping region relative to the scale centerline, however, within the overlapping region itself the height variations contribute to the alternating spanwise velocity rather than a wall normal vorticity.

The wall normal vorticity patterns are closely related to the large streamwise velocity gradient in the spanwise direction, $\frac{\partial u}{\partial z}$, that arises during the formation of streamwise velocity streaks. A stronger vorticity is present over the diamond scale array as the streamwise velocity variation found in Figure 74 and Figure 75 are larger. This behaviour is driven by the larger local height variations across the width of the diamond geometry compared to the circular and flat back geometries.

To summarize the key flow behaviours mentioned above, the rolling behaviour of the recirculation zone found along the scale centerline in the region behind the scale height is expected to influence the friction drag along the centerline region. Also, the impact of the shifted wall normal profiles along the scale centerline are likely to change the wall shear stress experienced by different scale geometries. In addition to these behaviours which are suggested to affect the skin friction directly, the streamwise velocity streaks and spanwise alternating velocity may contribute to friction drag reduction through delaying the transition to turbulence. These are the fundamental flow behaviours that have been explored in detail and the next section will discuss the overall impact of scale shape on surface drag and the role each of these flow behaviours plays.

3.4.6 Drag Analysis

The skin friction coefficient, which is the non-dimensional form of the wall shear stress is used to characterize the friction drag. The skin friction coefficient (C_f) is computed using equation 3.15 where the fluid density and free-stream velocity were used to normalize the wall shear stress. The colourmap of the skin friction coefficient magnitude at all locations across the surface of the scale array is presented for each geometry in Figure 81.

$$C_f = \frac{\tau_w}{\frac{1}{2}\rho U_\infty^2} \quad (3.15)$$

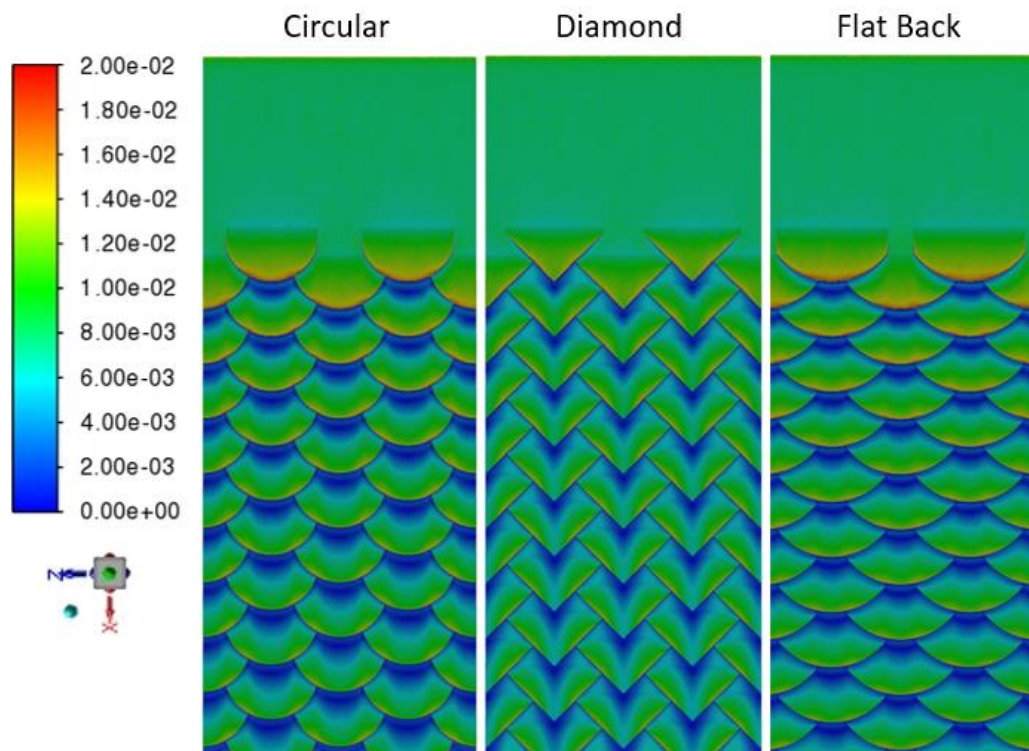


Figure 81: Colourmap of the skin friction coefficient along the surface for all geometries.

Figure 81 shows the colourmap plots of the skin friction coefficients along the surface for the three geometries considered. As the plot shows, the skin friction coefficient varied in both the streamwise and spanwise directions for all geometries. Given that the skin friction coefficient is based on the wall shear stress, which is a measure of the velocity gradient at the wall, higher values of the skin friction coefficient are characteristic of a

higher wall shear stress and steeper velocity gradient at the wall. In contrast, low values of skin friction indicate lower wall shear stress and smaller velocity gradient at the wall. The analysis of the non-dimensional wall normal streamwise velocity profiles (Figure 67, Figure 68 and Figure 70) showed variations along the length of the scale and in the spanwise direction, hence, the velocity gradients at all positions varied which manifest in the colourmap of the skin friction coefficient. The patterns appear periodic, with variations across a single scale repeating in the streamwise and spanwise directions.

In general, higher values of skin friction are observed near the downstream end of a single scale, as the inclination of the scale results in flow acceleration and greater wall normal streamwise velocity gradients in the downstream portion of the scale. Also, the higher velocity observed in the overlapping regions results in a greater wall shear stress and higher skin friction coefficients compared to the scale centerline. Finally, the recirculation region found on the upstream side of an individual scale is associated with smaller wall normal streamwise velocity gradients and hence, a smaller skin friction coefficient. While different regions across the scale array results in different skin friction coefficient magnitudes, the relative size of each region depends on the scale geometry.

Both the circular and flat back geometries show relatively similar skin friction coefficient colourmaps where the higher values of skin friction are concentrated over the entire downstream portion of the scale near the scale tip. In comparison, the diamond scale array shows higher values of skin friction concentrated on either side of the centerline plane ($\xi = 0$), over the downstream portion of the scale. This behaviour is due to the larger velocity variation observed in the diamond array (Figure 74) which yields a greater upward shift in the wall normal streamwise velocity profiles along the scale centerline (Figure 69). These upward shifted profiles have a streamwise velocity gradient which results in a lower wall shear stress and skin friction coefficient along the centerline plane of the diamond scale array.

The circular and flat back geometry contain similar recirculation regions (Figure 71). With the width of the centerline region being smaller in the flat back geometry, this yields a smaller region with a low skin friction coefficient on the upstream portion of the

scale. This decreased area with a small skin friction coefficient is likely to contribute to inferior friction drag performance for the flat back scale compared to the circular scale.

In contrast, a thinner more elongated region with a small skin friction coefficient is found along the centerline region of the diamond scale geometry. While the diamond scale array resulted in a smaller recirculation region overall (Figure 71), the scale geometry led to greater streamwise velocity variations and lower velocities along the scale centerline compared to the other geometries. It is the smaller streamwise velocities and upward shifted wall normal streamwise velocity profiles that contribute to the elongated region of small skin friction as discussed previously.

To understand how these patterns compare to the skin friction coefficient associated with the classical laminar boundary layer over a flat plate, an additional simulation with no surface features was completed to serve as the base case. Plots of the skin friction coefficients over a single scale ($S_{0,5}$) in the centerline ($\xi = 0$) and overlapping ($\xi = 0.375$) regions were obtained by using the wall shear stress in the x-direction over the scale array and equation 3.15 (Figure 82).

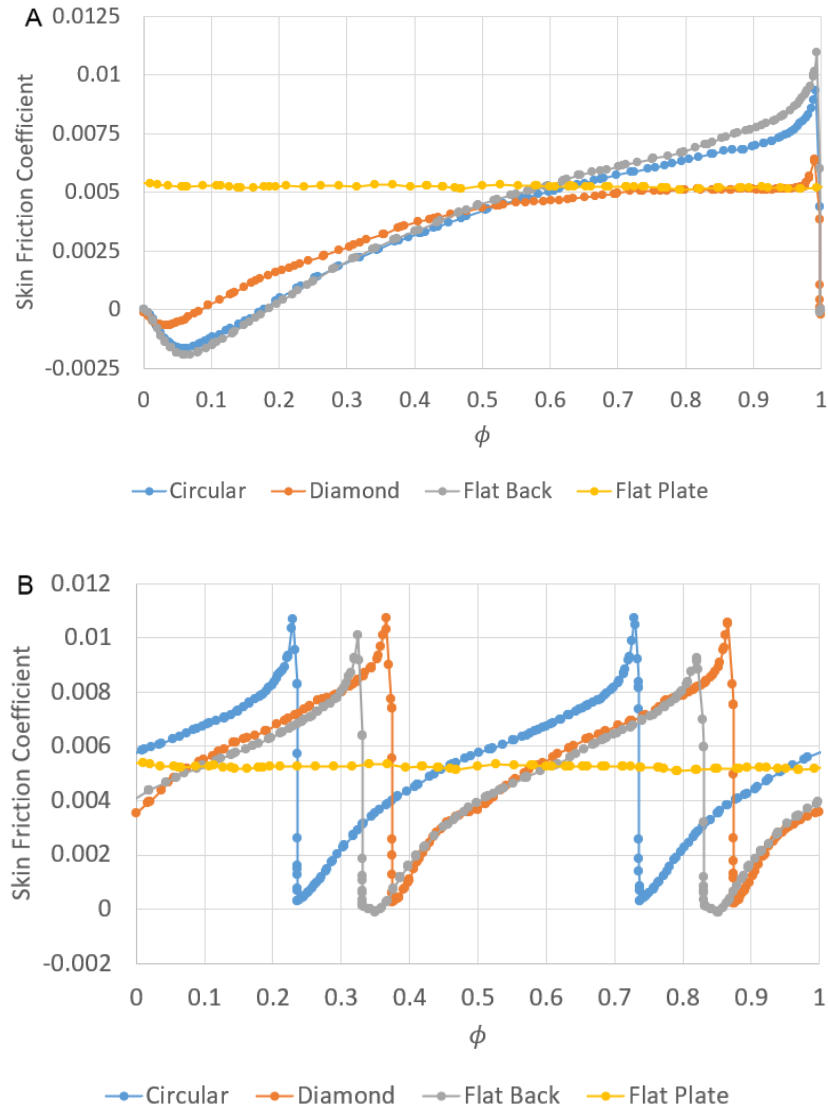


Figure 82: Skin friction coefficient along scale $S_{0.5}$ in the (A) centerline ($\xi = 0$) and (B) overlapping ($\xi = 0.375$) regions for all three scale geometries.

The plot of skin friction in the scale centerline shows that the skin friction coefficient is negative at the upstream end of the scale in the presence of the flow recirculation zone. There is a decrease and increase along the length of the recirculation region before the flow reattachment length. The negative skin friction coefficients in this region are associated with the negative streamwise velocities within the flow recirculation region. Beyond the flow reattachment length there is a gradual increase in the skin friction coefficient along the length of the scale. This increase is associated with the gradual

acceleration of the velocity over the scale which results in greater wall shear stress. Finally, at the downstream end of the scale a sharp drop in the skin friction coefficient is found in line with the sharp drop in the scale height. In general, along the scale centerline values of $\phi < 0.6$ result in skin friction coefficients lower than the flat plate theory, whereas, for $\phi > 0.6$ they are greater, except in the diamond scale shape.

When comparing across geometries in the scale centerline region, it is found that the circular and flat back scale follow a similar trend along the length of the scale with only a small difference in the peak values reach at the downstream end of the scale. The reason for this difference is the streamwise velocity variation is greater in the circular shape resulting in a lower velocity and velocity gradient along the scale centerline compared to the flat back geometry. The diamond scale shape contains a much different skin friction coefficient pattern resulting in lower overall skin frictions along the scale centerline.

The diamond scale shape contains a similar region with negative skin friction coefficients associated with the flow recirculation zone. The trends in the recirculation zone match the trends in the circular and flat back scale shape but are smaller in magnitude and streamwise extent due to the smaller recirculation zone found in the diamond scale array (Figure 71). The skin friction coefficient then increases along the length of the diamond shaped scale and reaches a plateau at about $\phi = 0.6$. The magnitude of the skin friction plateau is similar to the skin friction coefficient associated with the flat plate theory and contributes to an overall lower skin friction coefficient along the centerline of the diamond scale array. The reason for this skin friction plateau was discussed previously and relates to the upward shifted wall normal streamwise velocity profiles that result because of the formation of streamwise velocity streaks within the boundary layer.

The trend of the skin friction coefficient in the overlapping region is different from the centerline because two scale heights exist along the length of one scale. While flow recirculation is not present in the overlapping region, there does not exist a small region near the scale height of negative values of skin friction. In contrast, after the scale height, the skin friction coefficient begins gradually increasing along the length of the scale. Little difference is observed between geometries with similar peak values being reached

at the downstream end of the scales. The difference in peak magnitudes is related to the differences in the streamwise velocity variations between geometries. The patterns are found to repeat over scale heights in the streamwise direction.

A phase shift is observed in the skin friction coefficient along the overlapping region for the same reasons a phase shift was observed in the spanwise velocity component. The streamwise position of the overlapping scale changes with scale shape resulting in the observed phase shift. Given the phase shift is purely related to the scale geometry, it is otherwise observed that the skin friction coefficient between all geometries exhibits similar trends over the length of a scale in the overlapping region.

To quantify the variations between the centerline and overlapping regions, and differences observed between geometries, the average skin friction coefficient over scale $S_{0,5}$ was calculated for each geometry in the centerline ($\xi = 0$) and overlapping ($\xi = 0.375$) region by integrating numerically over the length of the scale and dividing by the length of integration (see Table 12).

Table 12: Average skin friction coefficient over a single scale ($S_{0,5}$) along centerline and overlapping regions.

Geometry	Centerline (10^{-3})	Overlapping (10^{-3})
Circular	3.60	5.09
Diamond	3.45	5.44
Flat back	3.84	4.61
Flat plate	5.14	5.14

The average skin friction over a single scale in both the centerline and overlapping regions highlights the trends discussed above. In general, all geometries result in a lower skin friction coefficient in the centerline region compared to the flat plate. With the diamond scale shape having the best performance, the flat back scale shape results in an average skin friction coefficient closest to the flat plate. In the overlapping region, all geometries except the diamond scale result in a decrease in skin friction coefficient compared to the flat plate. While the diamond scale shape results in the largest variation in skin friction coefficient between the centerline and overlapping region, the flat back

scale shape results in the smallest variation. These results have considered the variations over a single scale, Figure 83 and Table 13 expand these results to show the variations in the centerline and overlapping regions over the entire length of the scale array ($\phi_t = 1.5 - 9$).

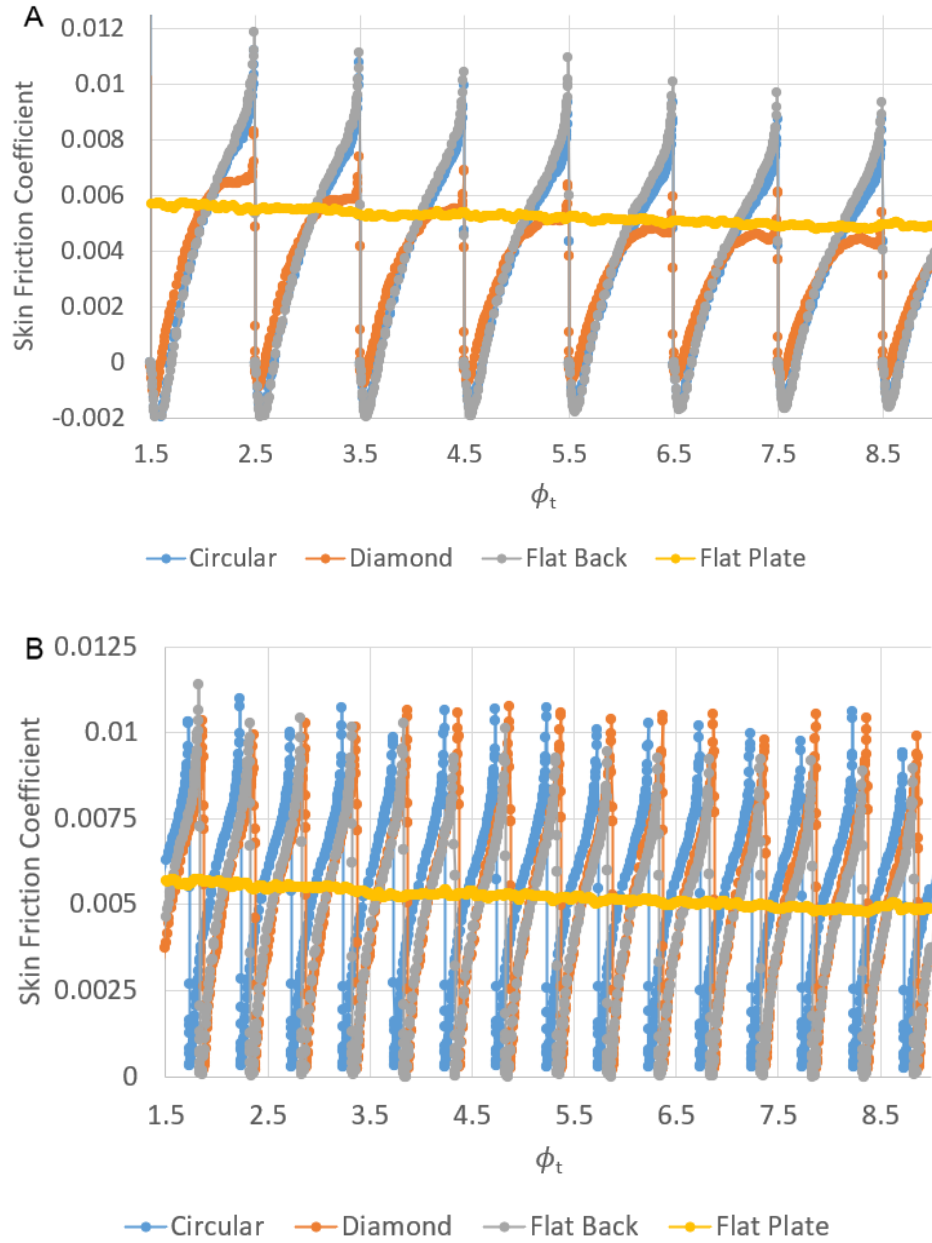


Figure 83: Skin friction coefficient along a streamwise line located at $\xi = 0$ (A) and $\xi = 0.375$ (B) over the surface. The skin friction coefficient for a classical flat plate laminar boundary layer is also presented for comparison.

Table 13: Average skin friction coefficient over scale arrays along centerline and overlapping regions.

Geometry	Centerline (10^{-3})	Overlapping (10^{-3})
Circular	3.48	5.24
Diamond	3.42	5.42
Flat back	3.67	4.69
Flat Plate	5.20	5.20

Figure 83 shows that there is some streamwise development of the skin friction coefficients over the scale arrays. Given the theoretical skin friction coefficient over a flat plate is proportional to the inverse of Reynolds number, it is expected that as the Reynolds number grows in the downstream direction, the skin friction coefficient will decrease. While the trends in the overlapping region show the peak skin friction over the scale arrays decreasing at a similar rate to the flat plate, the same behaviour is not observed in the centerline region. The peaks in the skin friction coefficient over the scale centerline appear to decrease faster than the flat plate. Thus, a relative decrease in the total skin friction coefficient over the scale arrays is found in the downstream direction.

The average skin friction coefficient along the scale centerline and overlapping regions show a similar trend to what was observed over a single scale (Table 13). The average skin friction coefficient for the circular and flat back geometries over the entire scale array contains a large decrease in the centerline and increase in the overlapping region compared to over a single scale. This results in a drag increase in the overlapping region for the circular scale geometry over the entire scale array. In contrast, the average skin friction coefficient for the diamond geometry is only slightly smaller over the entire scale array compared to a single scale. While the total skin friction along the centerline and overlapping region does not capture the spanwise variations of the skin friction coefficient, it gives some indication as to how the skin friction varies in critical regions over the scale array. It also suggests that the flow behaviour along the scale centerline is likely to be one of the main drivers reducing the friction drag over the scale arrays.

Given the 3D scale geometries create unique patterns in the skin friction coefficient which vary in both the streamwise and spanwise direction, the friction drag must be examined over the entire surface. Table 14 shows the magnitude of the friction drag coefficient (calculated using the free-stream velocity and planform area in equation 3.16) and the frictional drag force over the entire scale array.

$$C_{D,friction} = \frac{2F}{\rho U_{\infty}^2 A} \quad (3.16)$$

Table 14: Total friction drag for all geometries at the experimental flow condition.

Geometry	Friction Drag Coefficient (10^{-3})	Friction Drag (10^{-4} N)
Circular	4.72	6.79
Diamond	4.66	6.70
Flat back	4.80	6.90
Flat Plate	4.89	7.02

Based on the estimation of the total friction drag over the scale arrays, it is confirmed that all three scale geometries result in a reduction in friction drag compared to the flat plate case. Comparing the scale geometries, the diamond shape provides the largest reduction in the drag followed by the circular scale and the flat back scale. These results confirm the trends observed in the total skin friction coefficient along the scale centerline which showed the largest reductions for the diamond array followed by the circular scales. The results for the friction drag over the entire array fall in contrast to those found in the overlapping region, which showed a decrease for the flat back scale array and a drag increase for both the circular and diamond scale arrays. As such, it is evident that the drag associated with the flow behaviour in the centerline region drives the overall surface drag in comparison to the overlapping region. Thus, the following discussion will focus on the mechanisms governing the reduction in drag along the scale centerline.

One mechanism which is hypothesized to be driving this reduction in overall friction drag is the conversion of sliding friction to rolling friction along the scale centerline. The scale heights introduce surface variations which have been shown to cause flow recirculation in the near wall region behind the scale heights. The wall shear stress and skin friction in the

recirculation region is found to be negative contributing to a reduction in drag compared to the flat plate. The flow recirculation region has a secondary benefit of converting the sliding friction into rolling friction. With the fluid flowing over the scale height interacting with the upper boundary of the rolling vortex instead of the stationary surface, the contribution to the overall shear stress along this region is drastically reduced. A similar phenomenon was observed in Song et al. (2017) and Hou et al. (2021) where they studied flow over non-smooth surfaces modeled after the Barchan dunes and fish scale pits, respectively. While the features in these studies were modeled as pits in a flat surface as opposed to raised features, a similar rolling vortex contributed to the drag reduction in both cases.

While rolling friction is one mechanism driving the drag reduction, the formation of streamwise velocity streaks also contributes to the overall friction drag reduction. Given the scale shape results in different local scale heights across the width of a scale, fluid is forced towards the overlapping regions forming regions of high- and low-velocity over the scale array. The low-velocity regions located along the scale centerline contain upward shifted wall normal streamwise velocity profiles which have a lower wall shear stress compared to the flat plate profiles. It is the skin friction associated with the low-velocity streaks that leads to the overall drag reduction over the scale array.

This is clear when considering the outperformance of the diamond scale shape. While the diamond scale shape resulted in the smallest recirculation region, it contained the greatest friction drag reduction. Thus, while the rolling friction phenomenon contributes to the reduction in friction drag for the diamond array, it is not the driving mechanism. The diamond scale array produces the largest streamwise velocity streaks as a result of the changes in scale height across the width of the scale. These streamwise velocity variations contribute to a greater upward shift in the wall normal streamwise velocity profiles along the scale centerline, ultimately reducing the skin friction in this region.

While friction drag is one factor affecting the performance of these scale arrays, it is important to note that it does not account for drag reduction as a result of delay in transition to turbulence. Delaying the transition to turbulence results in drag reduction

because the skin friction associated with a laminar boundary layer is lower than that of a turbulent boundary layer. Thus, the additional distance in the laminar domain results in a reduction in drag compared to the drag which would have occurred given an earlier transition to turbulence. Muthuramalingam et al. (2020) showed that fish scale arrays can attenuate Tollmien-Schlichting waves within the boundary layer downstream of the scale array. This attenuation resulted in a delay in transition location by up to 55%, which correlated to a 27% theoretical reduction in drag. Thus, the ability for fish scale arrays to delay the transition to turbulence could reduce the surface drag above and beyond the friction drag reduction discussed above.

The mechanisms which could lead to the delay in transition to turbulence were discussed in Chapter 2. It has been shown previously that streamwise velocity streaks of finite amplitude can suppress a variety of instabilities within the boundary layer (Cossu & Brandt, 2004; Fransson et al., 2005; Schlatter et al., 2010; Shahinfar et al., 2014) leading to the delay in transition to turbulence. While this is one mechanism driving the delay in transition, it has also been shown that above a critical amplitude, the streaks themselves tend to breakdown to turbulence. The critical amplitude for streaks formed over a flat plate was identified by Andersson et al. (2001) to be 26%, while the critical amplitude for streamwise velocity streaks generated by cylindrical roughness elements was found by Fransson et al. (2005) to be 12%. While the mechanisms generating the streamwise velocity streaks over fish scale arrays are passive and continuous in the downstream direction, it is hypothesized that the streamwise velocity streaks generated over fish scale arrays are more robust and resistant to self-amplification. As such, larger streak amplitudes may be achieved resulting in a considerable delay in laminar to turbulent transition and a greater friction drag reduction.

In Chapter 2, the spanwise alternating velocity in the overlapping region was suggested as a secondary mechanism contributing to the delay in transition. The close similarities of this alternating flow to the Stokes layer found above transverse oscillating plates (Leschziner, 2020; Agostini et al., 2014; Ricco, 2011) suggests that the spanwise oscillations also play an important role in suppressing instabilities and delaying the transition to turbulence. The combination of the spanwise velocity fluctuations and

streamwise velocity streaks contributing to the suppression of instabilities is likely to greatly increase the ability for fish scale arrays to delay the transition to turbulence.

The above analysis provided evidence that fish scale arrays can reduce the friction drag in comparison to a smooth surface. The patterns of the skin friction coefficient across the different scale shapes revealed interesting trends linked to the underlying flow behaviour. While all geometries produced a reduction in skin friction, the diamond scale array performed better than the others. The regions of low skin friction coefficients were found to dictate the overall performance of the scale arrays. Regions of low skin friction are found to be related to the streamwise velocity streaks and the underlying variations in the scale heights. While analysis of the skin friction coefficients and friction drag described the performance of each scale geometry, this analysis did not include the impact of the delay in transition to turbulence. Next, discussion of the overall impact of the scale geometry on the observed flow behaviours and performance of the fish scale arrays will bring together all the findings outlined above.

3.4.7 Overall Impact of Scale Geometry

While differences are noted in the flow patterns between all three geometries, the behaviour of the circular and flat back scales are found to be similar for most regions examined. Given that the flat back scale has an increased scale radius compared to the circular scale, it has a wider overlapping region and smaller centerline region. This geometry has smaller height variations across the width of a scale resulting in less diversion of flow from the scale centerline to the overlapping region as is evident in the vorticity profile shown in Figure 79. The wall normal streamwise velocity profiles (Figure 67) showed an overall similar behaviour over the flat back and circular scales in the centerline region, however, the flat back scale resulted in a profile closer to the Blasius solution in the overlapping region (Figure 70). This upward shift is due to weaker streamwise velocity variations across the scales and highlighted the smaller streak amplitudes that are present in the flat back geometry (Figure 72). The resultant weaker flow behaviours observed in the flat back scale array led to a lower reduction in friction drag (Table 14) compared to the other geometries.

In contrast, the diamond scale generated the strongest wall normal vorticity (Figure 79) due to the height variations across the width of the scale. With more fluid being forced into the overlapping region on either side of the scale centerline, the strength of the streamwise velocity variations is strongest in the diamond scale array compared to the other geometries (Figure 72). The straight edges of the diamond scale result in a consistent change in height across the width of the scale which leads to peak vorticity values closer to the scale centerline (Figure 80) in the diamond array.

Given the diamond scale shape results in more fluid being forced to the overlapping region, the high-velocity streaks are found to be wider compared to the other geometries. The region of low-velocity fluid formed along the scale centerline contains upward shifted wall normal streamwise velocity profiles (Figure 69) which ultimately contribute to a larger decrease in the skin friction coefficient compared to the other scale geometries (Figure 82).

The recirculation zone is found to be similar between the circular and flat back geometries whereas the diamond scales have a much smaller recirculation zone. Not only is the streamwise extent of the recirculation zone smaller, but so is the spanwise width. While the circular and flat back geometries have recirculation zones that extend to the adjacent scale overlap (see Figure 71), the diamond array has a recirculation zone that extends less than half-way to the adjacent scale overlap. Given that the shape of the diamond scale is much different than the circular or flat back geometries, it is hypothesized that the spanwise velocity component below the peak scale height in the centerline region plays an important role in regulating the size of the recirculation zone.

The spanwise velocity below the peak scale height is largest in the diamond scale as the velocity from the adjacent scale rows cause spanwise fluid movement through to the scale centerline (see Figure 78). This spanwise fluid motion disrupts the streamwise recirculation region limiting its streamwise and spanwise extent. The spanwise motion below the peak scale height causes the recirculation zone to be a 3D rolling vortex transporting fluid to the tip of the scale. In cases such as the diamond scale array, where

the spanwise motion below the peak scale height is strong, the flow recirculation is reduced in size and even eliminated along a portion of the centerline region.

As discussed earlier, the flow behaviour along the scale centerline resulted in a lower average skin friction coefficient than the flat plate, whereas the flow behaviour along the overlapping region resulted in an increased average skin friction coefficient for the circular and flat back geometries. When considering the total friction drag across the entire scale array, the friction drag coefficient for all scale arrays resulted in an overall reduction compared to the flat plate. Comparing geometries, the diamond scale array resulted in the largest drag reduction, whereas the flat back array resulted in the smallest reduction. Variations along a single scale showed similar patterns between geometries in the overlapping region, but very different behaviours along the scale centerline. All geometries had negative skin friction coefficients in the flow recirculation region, however, the diamond scale array resulted in a plateau of the skin friction coefficient on the downstream portion of the scale. While the recirculation region plays a role in converting sliding friction to rolling friction and creating a small skin friction coefficient on the upstream side of the scale, it is the formation of the low-velocity streaks and upward shifted wall normal streamwise velocity profiles that leads to a plateau in the skin friction coefficient for the diamond scale shape.

Beyond the skin friction coefficient, the other flow behaviours associated with the scale geometry such as the streamwise velocity streaks, and spanwise velocity variations in the overlapping region are hypothesized to contribute to the suppression of instabilities and to contribute to additional drag reduction through the delay in transition to turbulence. Overall, the flow behaviours appear strongest over the diamond scale and weakest over the flat back scale. In terms of drag performance, the diamond array performed better than both the circular and flat back geometries as it results in a larger region of low shear stress over the centerline of the scales.

3.4.8 Impact of Reynolds Number

To investigate the impact of different flow conditions on the performance of these fish scale arrays, the free-stream velocity was varied resulting in Reynolds numbers, Re_{BL} , (equation 3.1) between 300 and 550 and a θ_{ratio} (equation 3.2) between 5.6 and 11.

Table 10 shows the simulation parameters and associated non-dimensional scaling parameters for each simulation case. Throughout the analysis the different flow conditions will be referred to by the θ_{ratio} parameter. This parameter represents the boundary layer thickness to scale height ratio at the entrance of the scale array. As such, a decrease in the free-stream velocity results in a greater boundary layer thickness, therefore the θ_{ratio} increases when the free-stream velocity is decreased. Given the observed flow behaviours are confined to the boundary layer, the analysis will explore how the flow behaviours induced by the scale array are impacted by an increasing boundary layer thickness (or increasing θ_{ratio}). The analysis will first focus on the circular geometry to understand how the flow behaviour varies with increasing θ_{ratio} . Then comparison with the other scale geometries would yield the overall impact of the flow conditions on the performance of these fish scale arrays.

First, the non-dimensional wall normal streamwise velocity profiles at the different flow conditions were explored along the scale centerline ($\xi = 0$) and overlapping ($\xi = 0.375$) regions (Figure 84) at a streamwise distance of $\phi_t = 8.5$ for the circular geometry.

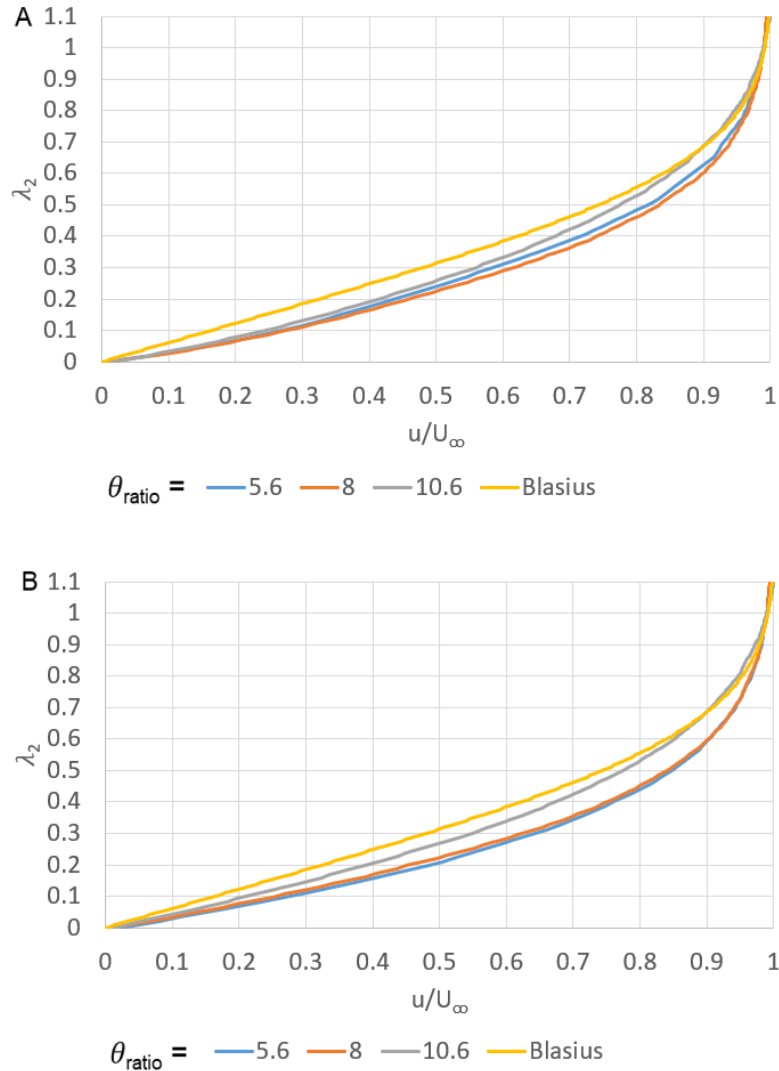


Figure 84: Non-dimensional wall normal streamwise velocity profiles for the circular geometry at a streamwise distance of $\phi_t = 8.5$ in the (A) centerline ($\xi = 0$) and (B) overlapping ($\xi = 0.375$) regions for the circular geometry. The classical laminar Blasius profile is plotted for reference.

From the plot it was found that the non-dimensional profiles along the centerline and overlapping region remain similar for a θ_{ratio} of 5.6 and 8. However, for a θ_{ratio} of 10.6, the wall normal streamwise velocity profile appears closer to the Blasius solution in both the centerline ($\xi = 0$) and overlapping ($\xi = 0.375$) regions. While there appears to be little variations between the centerline and overlapping profiles, the differences appear greatest closer to the surface. However, given there exists some variation in the wall

normal streamwise velocity profiles along the length of a single scale ($S_{0,7}$), Figure 85 shows the variations along the scale centerline ($\xi = 0$) for the circular geometry with a $\theta_{ratio} = 10.6$.

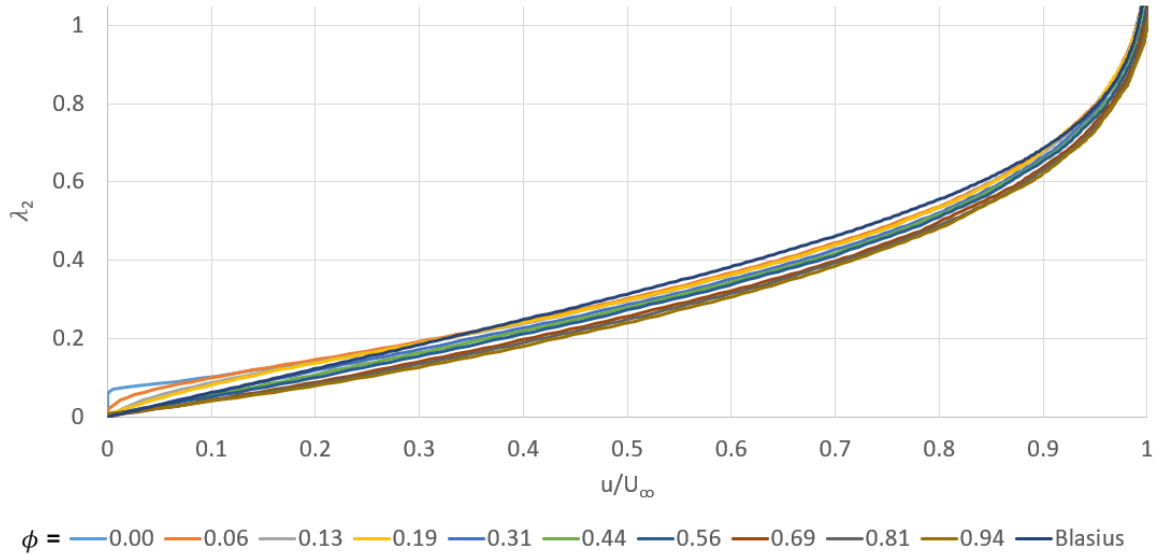


Figure 85: Non-dimensional wall normal streamwise velocity profiles in the centerline plane along the length of scale $S_{0,7}$ in the circular geometry at a $\theta_{ratio} = 10.6$. The classical laminar Blasius solution is plotted for reference.

Figure 85 shows that for small values of ϕ , an upward shift in the velocities compared to the Blasius profile only extends to $\lambda_2 = 0.2$. The results for the circular geometry presented for $\theta_{ratio} = 5.6$ in Figure 68, showed an upward shift in the velocity until a wall normal height of about $\lambda_2 = 0.4$. Thus, increasing the θ_{ratio} (or decreasing the free-stream velocity) is found to result in the observed variations in the streamwise velocity being confined closer to the surface.

To further explore the extent of the streamwise velocity variations across the scale array, the non-dimensional streamwise velocity variation (ψ), defined in equation 3.13, was plotted for all flow conditions at a streamwise location of $\phi_t = 8.5$. Three wall normal positions were considered corresponding to $\lambda_1 = 2.5, 5.0, \text{ and } 6.25$ (Figure 86).

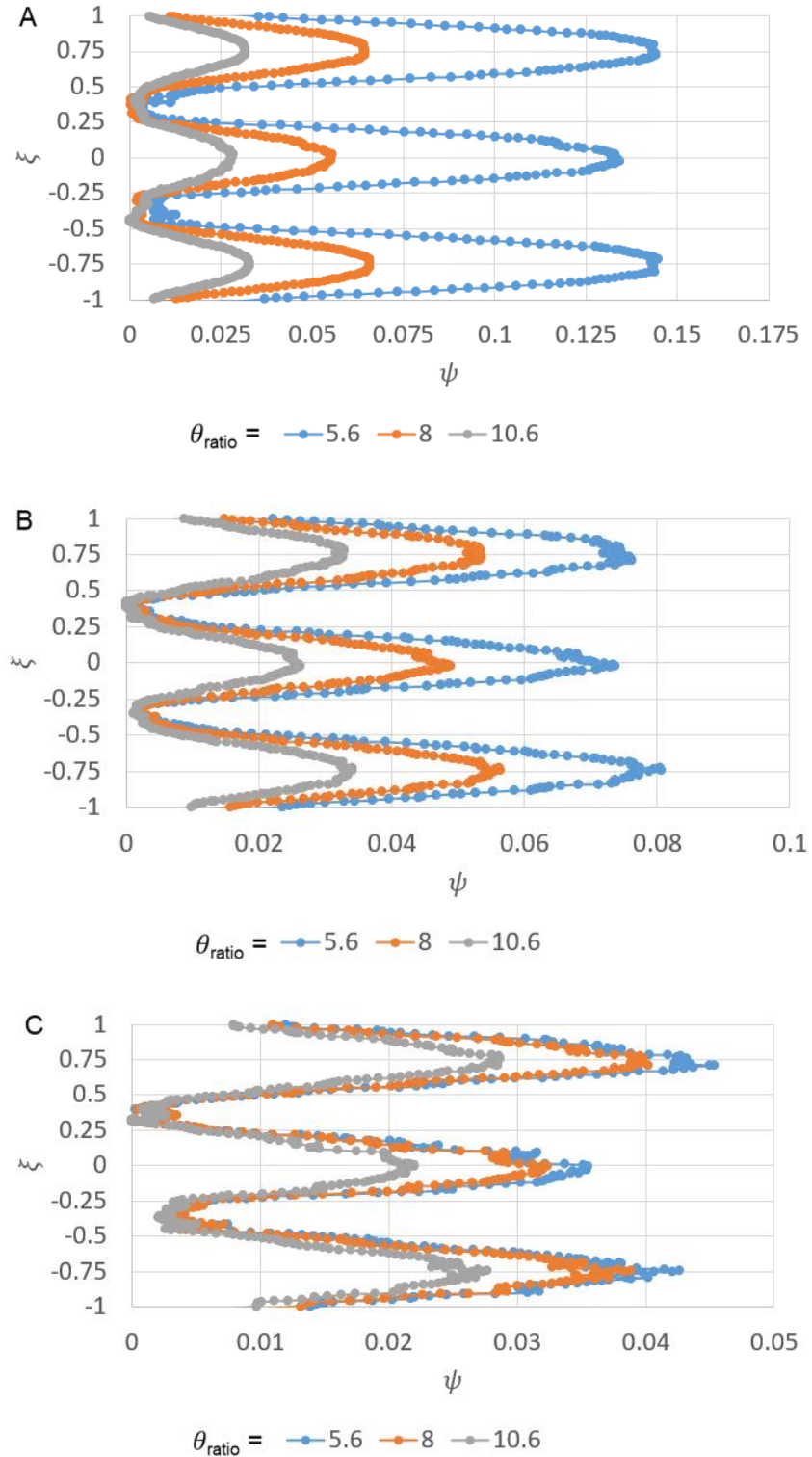


Figure 86: Non-dimensional streamwise velocity variation (ψ) for all flow conditions at a streamwise distance of $\phi_t = 8.5$ for three wall normal locations corresponding to (A) $\lambda_1 = 2.5$, (B) $\lambda_1 = 5.0$, and (C) $\lambda_1 = 6.25$ for the circular geometry.

The non-dimensional streamwise velocity variation profiles across the scale array highlight that at all three flow conditions, streamwise velocity streaks are formed. The magnitude of the velocity streaks is found to vary with the flow conditions, highlighting that an increase in θ_{ratio} results in a decrease in the magnitude of the velocity variation. Given an increase in θ_{ratio} is caused by an increase in the boundary layer thickness at smaller free-stream velocities, the behaviour of the streamwise velocity streaks appears related to the trends in the free-stream as opposed to the boundary layer thickness.

The differences in the magnitude of the streamwise velocity variations for different flow conditions are found to decrease as the distance from the surface increases. Increasing distance from the surface results in the magnitude of the streamwise velocity streaks for different flow conditions to collapse at a height of $\lambda_1 = 6.25$. Thus, decreasing θ_{ratio} (or increasing the free-stream velocity) is found to result in greater streamwise velocity variations in the region closest to the surface. While the analysis in Chapter 2 highlighted the behaviour of the streamwise velocity variation was related to the free-stream velocity, a similar result is highlighted here. The variations decrease in the region closest to the surface (for increasing θ_{ratio}) despite the boundary layer thickness increasing.

To further explore how the flow conditions impact the streamwise velocity streaks, the streamwise velocity variation (ψ) is plotted for $\theta_{ratio} = 10.6$ at multiple wall normal locations (λ_1) and a streamwise position of $\phi_t = 8.5$ (Figure 87).

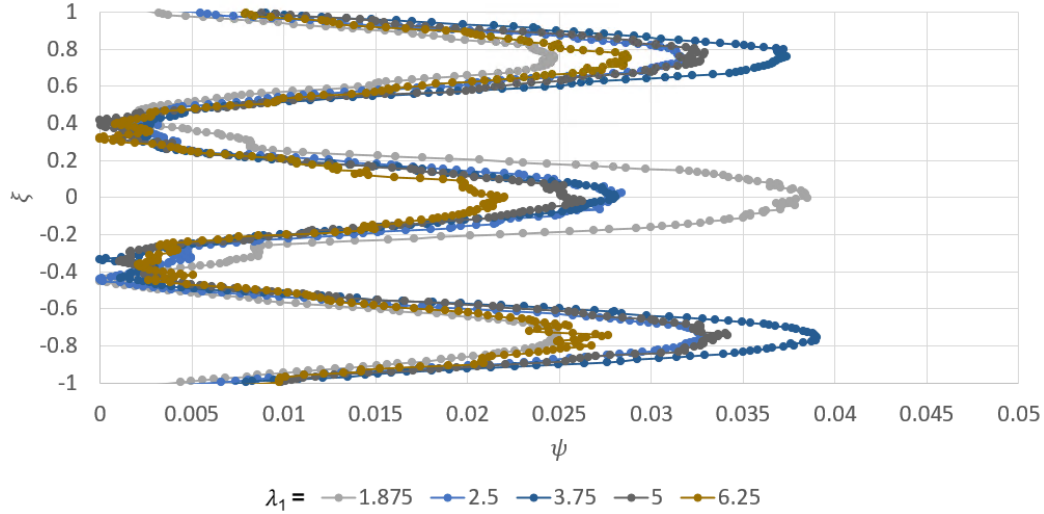


Figure 87: Non-dimensional streamwise velocity variation (ψ) at streamwise distance of $\phi_t = 8.5$ for $\theta_{ratio} = 10.6$ at several wall normal locations (λ_1) for the circular geometry.

The streamwise velocity variations through the boundary layer shows little variation for a $\theta_{ratio} = 10.6$. While close to the surface ($\lambda_1 = 1.875$) a greater magnitude of streamwise velocity variation is observed at $\xi = 0$, increasing distance away from the surface ($\lambda_1 = 2.5$) results in greater streamwise velocity variations at $\xi = \pm 0.75$. Beyond the height of $\lambda_1 = 2.5$ the changes in the streamwise velocity variations with increasing distance from the surface are small. As such, the flow behaviour over the scale array at $\theta_{ratio} = 10.6$ in general results in streamwise velocity streaks which experience little amplification close to the surface compared to the other free-stream conditions (Figure 86). The amplification of the streamwise velocity streaks is experienced close to the surface and increases only when the free-stream velocity is increased (or θ_{ratio} is decreased).

While the streamwise velocity streaks appear dependent on the free-stream velocity, it is also important to explore the impact of varying flow conditions on the spanwise velocity component in the overlapping region ($\xi = 0.375$). As such, the non-dimensional spanwise velocity (ω) defined in equation 3.14, was plotted in the streamwise direction at

a spanwise location of $\xi = 0.375$ and wall normal heights of $\lambda_1 = 2.5$ and 5.0 , for all flow conditions (see Figure 88).

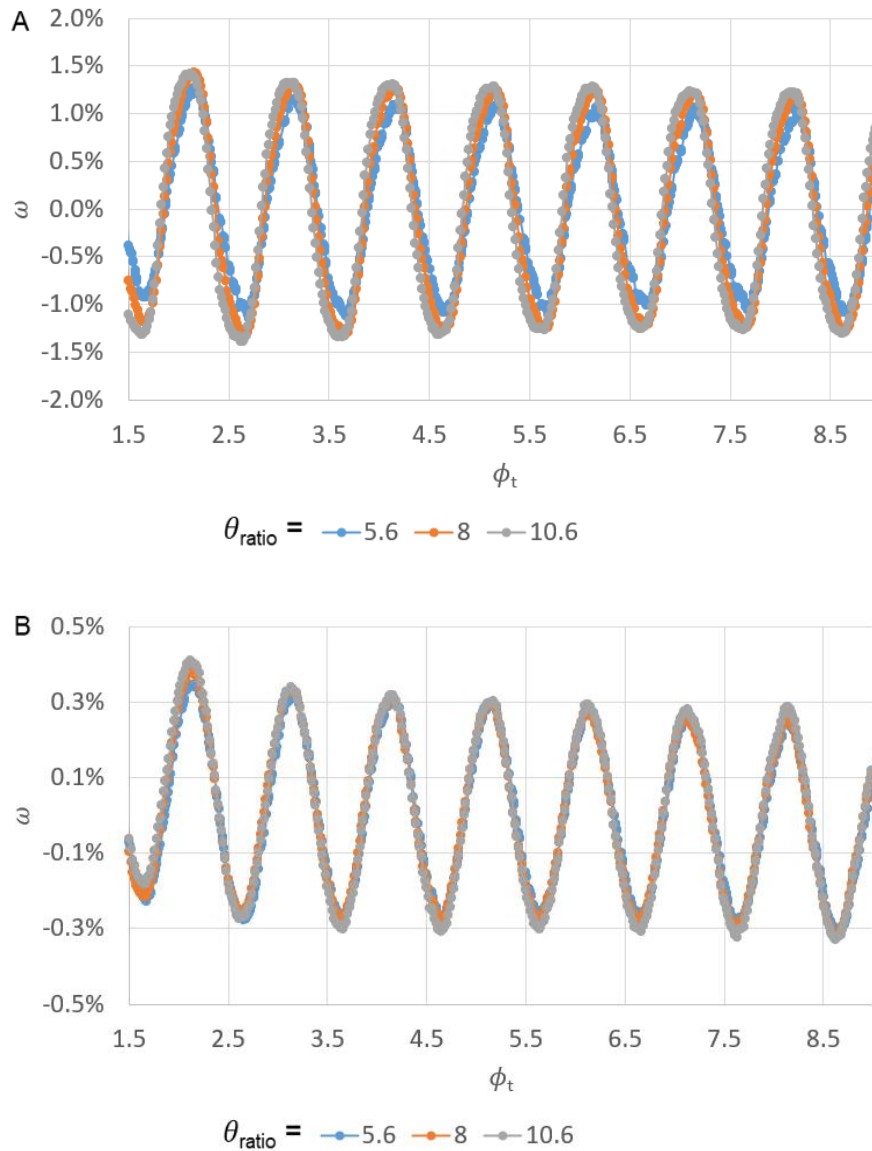


Figure 88: Non-dimensional spanwise velocity (ω) in the streamwise direction at a spanwise location of $\xi = 0.375$ and wall normal heights of (A) $\lambda_1 = 2.5$ and (B) $\lambda_1 = 5.0$, for all flow conditions over the circular geometry.

Figure 88 shows that for all flow conditions the non-dimensional spanwise velocities (ω) are the same at a given height. This pattern is observed at multiple wall normal heights and highlights that the flow patterns in the overlapping region are the same regardless of

the flow conditions. While different values of θ_{ratio} represent different boundary layer thicknesses, the spanwise velocity fluctuations in the overlapping region are found to be independent of the boundary layer thickness. Thus, it is concluded that the spanwise fluctuations remain the same percentage of the free-stream velocity regardless of the flow conditions. This reinforces that the spanwise fluctuations are characteristic of the surface topography and the flow conditions only impact the velocity magnitudes.

While the above analysis focused on the differences in the velocity patterns at different flow conditions for the circular geometry, it was found that similar variations existed in the flow behaviours for the diamond and flat back scales. The collapse of the non-dimensional spanwise velocity was found in the overlapping region of all geometries. Meanwhile, the trends in the streamwise velocity variation at different flow conditions were the same as the circular array for both the diamond and flat back scale. The only difference was the magnitude of the variations followed the trends in Figure 74 and Figure 80.

To understand how varying the flow conditions impacts each geometry, the reattachment length was calculated and summarized in Table 15 showing the average reattachment length and associated 95% confidence interval for each geometry and flow condition.

Table 15: Reattachment length and associated 95% confidence interval for each geometry and flow condition.

Geometry	$\theta_{ratio}= 5.6$	$\theta_{ratio}= 8.0$	$\theta_{ratio}= 10.6$
Circular	3.39 \pm 0.17	2.23 \pm 0.21	1.55 \pm 0.12
Diamond	1.68 \pm 0.13	0.94 \pm 0.13	0.66 \pm 0.12
Flat back	3.66 \pm 0.37	2.33 \pm 0.23	1.61 \pm 0.09

It is noted that across all geometries the reattachment length decreases for increasing values of θ_{ratio} . This decrease is associated with the decreasing free-stream velocity that results in an increase in θ_{ratio} . As the free-stream velocity decreases and the boundary layer thickness increases, the speed of the fluid close to the surface also decreases, resulting in a smaller reattachment zone behind the scale height. Between a θ_{ratio} of 5.6 and 8.0 the reattachment length is found to decrease by about 35% for the circular and

flat back geometries, and by about 45% for the diamond geometry. Additionally, between a θ_{ratio} of 8.0 and 10.6, the reattachment length for all geometries decreases by about 30%. The trends between geometries remain the same at each flow condition highlighting that the diamond scale has the shortest reattachment length, and the flat back scale has the largest.

Another important parameter used to characterize the performance of each scale array is the friction drag coefficient. The friction drag coefficient was calculated using the free-stream velocity and the planform area in equation 3.16 and is shown in Table 16 for all geometries and flow conditions.

Table 16: Friction drag coefficients for all geometries under different flow conditions.

Geometry	$\theta_{ratio} = 5.6 (10^{-3})$	$\theta_{ratio} = 8.0 (10^{-3})$	$\theta_{ratio} = 10.6 (10^{-3})$
Circular	4.72	7.20	10.6
Diamond	4.66	6.96	10.2
Flat back	4.80	7.33	10.8
Flat Plate	4.89	7.31	10.7

Table 16 highlights that increasing θ_{ratio} results in an increase in the friction drag coefficient. This increase in friction drag is expected as the free-stream velocity decreases resulting in the skin friction coefficient increasing. When comparing the friction drag to the flat plate, it was found that for all geometries except the flat back scale, the friction drag was reduced at all flow conditions. In the flat back geometry, only a slight reduction in the friction drag coefficient was observed for $\theta_{ratio} = 5.6$, while above $\theta_{ratio} = 5.6$ the friction drag shows a slight increase in comparison to the flat plate. It was also noted that as the θ_{ratio} increases, the amount of friction drag reduction for each geometry appears to decrease in comparison to the flat plate. To highlight this, Table 17 shows the percentage reduction in the friction drag coefficient compared to the flat plate for each geometry and all flow conditions.

Table 17: Percentage reduction in the friction drag coefficient compared to the flat plate.

Geometry	$\theta_{ratio} = 5.6$	$\theta_{ratio} = 8.0$	$\theta_{ratio} = 10.6$
Circular	3.32%	1.57%	0.81%
Diamond	4.55%	4.80%	4.73%
Flat back	1.71%	-0.24%	-0.61%

The percentage drag reduction highlights that the diamond scale array resulted in the greatest friction drag reduction across all three flow conditions. The diamond scale array shows a reduction in the friction drag coefficient above 4.5% for all flow conditions. In contrast, the friction drag reduction for the circular geometry shows a decreasing trend as θ_{ratio} increases. Similarly, the flat back geometry shows a decreasing trend which results in a slight drag increase for flow conditions above $\theta_{ratio} = 5.6$. The percentage friction drag reduction for the diamond scale array does not follow this decreasing trend and instead shows a similar reduction in the friction drag coefficient for all flow conditions.

As discussed in the previous section, the variations in height across the diamond scale result in a larger wall normal vorticity and greater velocity variations across the array. With more movement of fluid to the overlapping region, the low-velocity streaks formed along the scale centerlines contain smaller velocities and extend higher into the boundary layer compared to the other geometries. This low-velocity region was found to contribute to the decrease in skin friction along the centerline region of the scale, and lead to an overall reduction in friction drag across the scale array. Given the diamond scale array presented a greater streamwise velocity variation compared to the other geometries for a $\theta_{ratio} = 5.6$, this trend is found to persist as the θ_{ratio} increases (or free-stream velocity decreases). Thus, the greater streamwise velocity variation magnitude that persist in the diamond scale array at higher values of θ_{ratio} results in the continued better performance of the diamond scale array compared to the other geometries. The flow patterns produced over the diamond scale array are found to be more robust and provide greater drag reduction capabilities over a range of θ_{ratio} values.

3.5 Conclusion

A numerical model to simulate the flow over biomimetic fish scale arrays was developed and validated using the experimental results provided in Chapter 2 and the previous literature. Three scale geometries (circular, diamond, and flat back) were evaluated under three flow conditions corresponding to values of $\theta_{ratio} = 5.6$ to 10.6. This analysis serves as the first biomimetic fish scale study to explore the impact of scale geometry on the flow behaviours over the fish scale arrays and helps to develop the knowledge surrounding the optimization and practical application of biomimetic fish scale arrays.

Comparison across scale geometries revealed striking similarities between the circular and flat back geometry. In many cases the patterns observed in the flat back geometry were weaker compared to the circular geometry due to the increase in scale radius, smaller centerline region, and less height variation across the width of the scale. The flat back geometry had the worst drag reduction performance of the three scale geometries and at greater values of θ_{ratio} resulted in a drag increase in comparison to the flat plate. The inferior performance of the flat back geometry is related to the smaller surface variations found in the underlying scale topography.

The diamond geometry had the opposite impact and often resulted in stronger variations over the scale array compared to the circular geometry. A larger height variation across the width of the scales resulted in a stronger wall normal vorticity which enabled more fluid to be moved to the overlapping region. The increase in fluid velocity along the overlapping region created greater streamwise velocity variations across the scale array. The straight edges of the scale also enabled an elongated spanwise velocity along the edge of the scales. The spanwise velocity below the peak scale heights was found to be driven by the flow from the adjacent scale rows and extend through the centerline region impacting the flow recirculation over the diamond scale shape.

Ultimately, the low-velocity streaks that are formed along the scale centerline were found to contribute to smaller skin friction coefficients in the centerline region, and lead to an overall friction drag reduction over all scale arrays. Given the diamond array produced

the greatest streamwise velocity variations, this resulted in a greater reduction in skin friction drag compared to the circular and flat back geometries.

Variations in the free-stream velocity resulted in flow conditions with a θ_{ratio} between 5.6 and 10.6. By decreasing the free-stream velocity, the boundary layer thickness and the θ_{ratio} were increased. While the differences between geometries remained similar, increasing the θ_{ratio} resulted in a decrease in the magnitude of the streamwise velocity streaks close to the surface. While the streamwise velocity variations were found to converge in the wall normal direction, the increase in the θ_{ratio} was concluded to result in a decreased amplification of the streamwise velocity variations close to the surface. Additionally, the non-dimensional spanwise velocity was found to show the same behaviour at all values of θ_{ratio} for multiple wall normal locations. As such, the flow behaviour in the overlapping region was found to be directly related to the scale topography where the flow conditions only impact the magnitude of the velocity fluctuations. Lastly, the size of the recirculation zone was found to decrease as θ_{ratio} increased. This is a result of the smaller velocities present close to the surface reducing the streamwise extent of the flow recirculation.

Comparing the scale geometries at different flow conditions resulted in the diamond array having the largest drag reduction across all flow conditions. While the performance of the flat back and circular geometry decreased as θ_{ratio} increased, the performance of the diamond array remained relatively constant across all flow conditions. This was found to be a result of the increased streamwise velocity variations that are produced in the diamond scale array. With a greater variation in the streamwise velocity at similar wall normal locations, the streamwise velocity streaks are found to be more robust in the diamond array and contribute to a greater drag reduction over a larger range of θ_{ratio} values.

While this work serves as the first study exploring the impact of scale geometry on the hydrodynamic performance of biomimetic fish scale arrays, further work is needed to optimize the type of scale geometry that results in improved surface drag. While the diamond scale was found to perform better than the other scale geometries in terms of

drag performance, varying parameters such as the angle of the scale edges or size of the overlapping region will help in the optimization of a scale geometry for improved surface drag. Understanding how these biomimetic fish scale arrays modify the near wall flow and reduce drag is just the first step in the development of similar surfaces for improved drag performance. Exploration into the limitations and optimal operating conditions, as well as optimal geometries and spacing of these arrays is also required. Ultimately, the passive ability of these structured surfaces to reduce drag through multiple mechanisms presents a promising opportunity for their use in commercial applications.

Bibliography

- Abbas, A., Bugada, G., Ferrer, E., Fu, S., Periaux, J., Pons-Prats, J., Valero, E., & Zheng, Y. (2017). Drag reduction via turbulent Boundary Layer Flow Control. *Science China Technological Sciences*, 60(9), 1281–1290. <https://doi.org/10.1007/s11431-016-9013-6>
- Agostini, L., Toubert, E., & Leschziner, M. A. (2014). Spanwise oscillatory wall motion in channel flow: Drag-reduction mechanisms inferred from DNS-predicted phase-wise property variations at $Re_t = 1000$. *Journal of Fluid Mechanics*, 743, 606–635. <https://doi.org/10.1017/jfm.2014.40>
- Anderson, E. J., McGillis, W. R., & Grosenbaugh, M. A. (2001). The boundary layer of swimming fish. *Journal of Experimental Biology*, 204(1), 81–102. <https://doi.org/10.1242/jeb.204.1.81>
- Andersson, P., Brandt, L., Bottaro, A., & Henningson, D. S. (2001). On the breakdown of boundary layer streaks. *Journal of Fluid Mechanics*, 428, 29–60. <https://doi.org/10.1017/s0022112000002421>
- ANSYS Inc. (2013). Chapter 1.2. Continuity and Momentum Equations. In *ANSYS Fluent Theory Guide* (Vol. 15, pp. 2–3). ANSYS Inc.
- ANSYS Inc. (2013). Chapter 20.3.1. Spatial Discretization. In *ANSYS Fluent Theory Guide* (Vol. 15, pp. 634–635). ANSYS Inc.
- ANSYS Inc. (2013). Chapter 20.3.3.4. Least Squares Cell-Based Gradient Evaluation. In *ANSYS Fluent Theory Guide* (Vol. 15, p. 643). ANSYS Inc.
- ANSYS Inc. (2013). Chapter 20.4.2. Discretization of the Continuity Equation. In *ANSYS Fluent Theory Guide* (Vol. 15, p. 647). ANSYS Inc.
- ANSYS Inc. (2013). Chapter 20.4.3. Pressure-Velocity Coupling. In *ANSYS Fluent Theory Guide* (Vol. 15, pp. 651–652). ANSYS Inc.
- Bai, H. L., Zhou, Y., Zhang, W. G., Xu, S. J., Wang, Y., & Antonia, R. A. (2014). Active control of a turbulent boundary layer based on local surface perturbation. *Journal of Fluid Mechanics*, 750, 316–354. <https://doi.org/10.1017/jfm.2014.261>
- Barth, T., & Jespersen, D. (1989). The design and application of upwind schemes on unstructured meshes. *27th Aerospace Sciences Meeting*. <https://doi.org/10.2514/6.1989-366>
- Bechert, D. W., Bruse, M., & Hage, W. (2000). Experiments with three-dimensional riblets as an idealized model of shark skin. *Experiments in Fluids*, 28(5), 403–412. <https://doi.org/10.1007/s003480050400>
- Burdak, V. D. (1986). Morphologie fonctionnelle du tegument ecailleux des poissons. *Cybiurn*, 10, 1-128.
- Cossu, C., & Brandt, L. (2004). On Tollmien–Schlichting-like waves in streaky boundary layers. *European Journal of Mechanics - B/Fluids*, 23(6), 815–833. <https://doi.org/10.1016/j.euromechflu.2004.05.001>

- Dean, B., & Bhushan, B. (2010). Shark-skin surfaces for fluid-drag reduction in turbulent flow: A Review. *Philosophical Transactions of the Royal Society A: Mathematical, Physical and Engineering Sciences*, 368(1929), 4775–4806. <https://doi.org/10.1098/rsta.2010.0201>
- Dou, Z., Wang, J., & Chen, D. (2012). Bionic research on fish scales for drag reduction. *Journal of Bionic Engineering*, 9(4), 457–464. [https://doi.org/10.1016/s1672-6529\(11\)60140-6](https://doi.org/10.1016/s1672-6529(11)60140-6)
- Fish, F. E., & Lauder, G. V. (2006). Passive and active flow control by swimming fishes and mammals. *Annual Review of Fluid Mechanics*, 38(1), 193–224. <https://doi.org/10.1146/annurev.fluid.38.050304.092201>
- Fish, F. E., Weber, P. W., Murray, M. M., & Howle, L. E. (2011). The tubercles on humpback whales' flippers: Application of bio-inspired technology. *Integrative and Comparative Biology*, 51(1), 203–213. <https://doi.org/10.1093/icb/icr016>
- Fransson, J. H., Brandt, L., Talamelli, A., & Cossu, C. (2005). Experimental study of the stabilization of Tollmien–Schlichting waves by finite amplitude streaks. *Physics of Fluids*, 17(5), 054110. <https://doi.org/10.1063/1.1897377>
- Government of Canada. (2022, May 26). *Greenhouse Gas Emissions by Economic Sector*. Canada.ca. Retrieved February 1, 2023, from <https://www.canada.ca/en/environment-climate-change/services/environmental-indicators/greenhouse-gas-emissions.html>
- Government of Canada. (2022, July 28). *Energy Production*. Provincial and Territorial Energy Profiles – Canada. Retrieved January 30, 2023, from <https://www.cer-rec.gc.ca/en/data-analysis/energy-markets/provincial-territorial-energy-profiles/provincial-territorial-energy-profiles-canada.html>
- Government of Canada. (2022, December 6). *Energy Supply and demand, 2021*. The Daily. Retrieved January 30, 2023, from <https://www150.statcan.gc.ca/n1/daily-quotidien/221206/dq221206e-eng.htm>
- Government of the United States. (2022, July 14). *Fast Facts on Transportation Greenhouse Gas Emissions*. EPA. Retrieved February 1, 2023, from <https://www.epa.gov/greenvehicles/fast-facts-transportation-greenhouse-gas-emissions>
- Hamner, W. M. (1979). [Review of *Nekton.*, by Y. G. Aleyev]. *Limnology and Oceanography*, 24(6), 1173–1175. <http://www.jstor.org/stable/2835593>
- Heidarian, A., Ghassemi, H., & Liu, P. (2018). Numerical Analysis of the effects of riblets on drag reduction of a flat plate. *Journal of Applied Fluid Mechanics*, 11(3), 679–688.
- Hou, J.-M., Shi, G.-F., Li, L., Li, Hong-da., & Xia, Mingqiang. (2021). Analysis of the influence of pit unit arrangement on the drag reduction performance of fish-scale pits. *Journal of Physics: Conference Series*, 1885(2), 022029. <https://doi.org/10.1088/1742-6596/1885/2/022029>

- Ibañez, A. L., Cowx, I. G., & O'Higgins, P. (2009). Variation in elasmoid fish scale patterns is informative with regard to taxon and swimming mode. *Zoological Journal of the Linnean Society*, *155*(4), 834–844. <https://doi.org/10.1111/j.1096-3642.2008.00465.x>
- Kuusipalo, L. (1998). Scale morphology in malawian cichlids. *Journal of Fish Biology*, *52*(4), 771–781. <https://doi.org/10.1111/j.1095-8649.1998.tb00819.x>
- Leschziner, M. A. (2020). Friction-drag reduction by transverse wall motion – A Review. *Journal of Mechanics*, *36*(5), 649–663. <https://doi.org/10.1017/jmech.2020.31>
- Li, L., Zhu, J., Li, J., Song, H., Zeng, Z., Wang, G., Zhao, W., & Xue, Q. (2019). Effect of vortex frictional drag reduction on ordered microstructures. *Surface Topography: Metrology and Properties*, *7*(2), 025008. <https://doi.org/10.1088/2051-672x/ab1671>
- Malik, M., Liao, W., Li, F., & Choudhari, M. (2015). Discrete-roughness-element-enhanced swept-wing natural laminar flow at high Reynolds Numbers. *AIAA Journal*, *53*(8), 2321–2334. <https://doi.org/10.2514/1.j053637>
- Mosghani, M. M., Alidoostan, M. A., & Binesh, A. (2021). Numerical analysis of drag reduction of fish scales inspired ctenoid-shape microstructured surfaces. *Chemical Engineering Communications*, 1–16. <https://doi.org/10.1080/00986445.2021.1992398>
- Muthuramalingam, M., Puckert, D. K., Rist, U., & Bruecker, C. (2020). Transition delay using biomimetic fish scale arrays. *Scientific Reports*, *10*(1). <https://doi.org/10.1038/s41598-020-71434-8>
- Muthuramalingam, M., Villemin, L. S., & Bruecker, C. (2019). Streak formation in flow over biomimetic fish scale arrays. *Journal of Experimental Biology*. <https://doi.org/10.1242/jeb.205963>
- Nakanishi, R., Mamori, H., & Fukagata, K. (2012). Relaminarization of turbulent channel flow using traveling wave-like wall deformation. *International Journal of Heat and Fluid Flow*, *35*, 152–159. <https://doi.org/10.1016/j.ijheatfluidflow.2012.01.007>
- Ou, J., Perot, B., & Rothstein, J. P. (2004). Laminar drag reduction in microchannels using ultrahydrophobic surfaces. *Physics of Fluids*, *16*(12), 4635–4643. <https://doi.org/10.1063/1.1812011>
- Ricco, P. (2011). Laminar streaks with spanwise wall forcing. *Physics of Fluids*, *23*(6), 064103. <https://doi.org/10.1063/1.3593469>
- Sagong, W., Kim, C., Choi, S., Jeon, W.-P., & Choi, H. (2008). Does the sailfish skin reduce the skin friction like the shark skin? *Physics of Fluids*, *20*(10), 101510. <https://doi.org/10.1063/1.3005861>
- Schlatter, P., Deusebio, E., de Lange, R., & Brandt, L. (2010). Numerical Study of the stabilisation of boundary-layer disturbances by finite amplitude streaks. *International Journal of Flow Control*, *2*(4), 259–288. <https://doi.org/10.1260/1756-8250.2.4.259>

- Shahinfar, S., Sattarzadeh, S. S., & Fransson, J. H. M. (2014). Passive boundary layer control of oblique disturbances by finite-amplitude streaks. *Journal of Fluid Mechanics*, 749, 1–36. <https://doi.org/10.1017/jfm.2014.211>
- Sindagi, S., & Vijayakumar, R. (2020). Succinct review of MBDR/BDR technique in reducing ship's drag. *Ships and Offshore Structures*, 16(9), 968–979. <https://doi.org/10.1080/17445302.2020.1790296>
- Song, X., Zhang, M., & Lin, P. (2017). Skin friction reduction characteristics of nonsmooth surfaces inspired by the shapes of Barchan Dunes. *Mathematical Problems in Engineering*, 2017, 1–12. <https://doi.org/10.1155/2017/6212605>
- Sudo, S., Tsuyuki, K., Ito, Y., & Ikohagi, T. (2002). A Study on the Surface Shape of Fish Scales. *JSME International Journal Series C*, 45(4), 1100–1105. doi:10.1299/jsmec.45.1100
- U.S. Energy Information Administration. (2022, June 28). *Energy use for transportation*. Use of energy for transportation in depth. Retrieved February 1, 2023, from <https://www.eia.gov/energyexplained/use-of-energy/transportation-in-depth.php>
- United States Department of Transportation. (2022, Sept. 8). *U.S. energy consumption by the transportation sector*. Bureau of Transportation Statistics. Retrieved February 1, 2023, from <https://www.bts.gov/content/us-energy-consumption-transportation-sector>
- Walters, V. (1963). The trachipterid integument and an hypothesis on its hydrodynamic function. *Copeia*, 1963(2), 260. <https://doi.org/10.2307/1441341>
- Wainwright, D. K., & Lauder, G. V. (2016). Three-dimensional analysis of scale morphology in bluegill sunfish, *Lepomis macrochirus*. *Zoology*, 119(3), 182–195. <https://doi.org/10.1016/j.zool.2016.02.006>
- Wainwright, D. K., & Lauder, G. V. (2017). Mucus matters: The slippery and complex surfaces of fish. *Biologically-Inspired Systems*, 223–246. https://doi.org/10.1007/978-3-319-74144-4_10
- Wainwright, D. K., Karan, E. A., & Collar, D. C. (2022). Evolutionary patterns of scale morphology in damselfishes (Pomacentridae). *Biological Journal of the Linnean Society*, 135(1), 138–158. <https://doi.org/10.1093/biolinnean/blab140>
- White, F. M. (2016). Dimensional Analysis and Similarity. In *Fluid mechanics* (8th ed., p. 317). McGraw-Hill.
- White, F. M. (2016). Flow Past Immersed Bodies. In *Fluid mechanics* (8th ed., p. 450). McGraw-Hill.
- Wood, R. M. (2004). Impact of Advanced Aerodynamic Technology on Transportation Energy Consumption. *SAE Technical Paper Series*. doi:10.4271/2004-01-1306
- Wu, L. Y., Jiao, Z. B., Song, Y. Q., Ren, W. T., Niu, S. C., & Han, Z. W. (2017). Water-trapping and drag-reduction effects of fish ctenopharyngodon idellus scales and their simulations. *Science China Technological Sciences*, 60(7), 1111–1117. <https://doi.org/10.1007/s11431-016-0630-x>

- Xu, M., Grabowski, A., Yu, N., Kerezyte, G., Lee, J.-W., Pfeifer, B. R., & Kim, C.-J. (2020). Superhydrophobic drag reduction for turbulent flows in Open water. *Physical Review Applied*, 13(3). <https://doi.org/10.1103/physrevapplied.13.034056>
- Yanase, K., & Saarenrinne, P. (2016). Boundary Layer Control by a fish: Unsteady laminar boundary layers of rainbow trout swimming in turbulent flows. *Biology Open*, 5(12), 1853–1863. <https://doi.org/10.1242/bio.020008>
- Yu, C., Liu, M., Zhang, C., Yan, H., Zhang, M., Wu, Q., Liu, M., & Jiang, L. (2020). Bio-inspired drag reduction: From nature organisms to artificial functional surfaces. *Giant*, 2, 100017. <https://doi.org/10.1016/j.giant.2020.100017>
- Zhang, L., Shan, X., & Xie, T. (2020). Active control for wall drag reduction: Methods, mechanisms and performance. *IEEE Access*, 8, 7039–7057. <https://doi.org/10.1109/access.2020.2963843>

Chapter 4

4 Conclusions

4.1 Problem Overview

With several active and passive drag reduction techniques available, few are applicable in commercial applications. Applications targeting the transportation sector have a significant potential to reduce energy consumption and consequently greenhouse gas emissions. Passive techniques have shown promising results, in particular the application of fish scales. While studies have highlighted the potential for fish scale arrays to reduce surface drag, few have sought to understand the physics of the mechanisms driving the drag reduction. In particular, a lack of experimental quantification of the flow structures and mechanisms leading to drag reduction over biomimetic fish scale arrays was identified as a knowledge gap. Along with this, understanding of how scale shape impacts the development of flow structures over the scale surfaces has yet to be explored. Thus, the objectives of this research were to provide a detailed characterization of the near wall flow behaviour over biomimetic fish scale arrays contributing to a deeper understanding of the flow physics, as well as, to study the impact of scale shape on the observed flow structures. These objectives would help in determining the optimal scale geometry that could potentially be used commercially in the transportation sector to reduce the drag, thus, contributing to the efforts of mitigating greenhouse gas emissions.

4.2 Chapter 2

In chapter 2, the development of an experimental water channel enabled the detailed characterization of the flow behaviours in the near wall region over a biomimetic fish scale array. The circular scale geometry considered in this study contained an eight times scaling factor to enable measurement of velocity in the region behind the scale heights. Dynamic similarity was maintained ensuring that the Reynolds number based on boundary layer thickness and the boundary layer thickness to scale height ratio were of the same order of magnitude as for the real fish. PIV measurements were conducted in the vertical (wall normal) and horizontal (parallel to the wall) planes to characterize the

flow within the boundary layer over the scale array. Three vertical planes were considered corresponding to the scale centerline, midline (edge of the scale overlap), and middle of the overlapping region. Additionally, eight planes were considered in the horizontal configuration varying from 1.3 – 5 mm from the surface.

Velocity profiles throughout the width and height of the channel without the scale array validated the development of a consistent channel flow. Additionally, the wall normal streamwise velocity profiles upstream of the scale array were compared to the Blasius solution which validated the development of a laminar boundary layer. Detailed analysis in the vertical and horizontal planes led to a deeper understanding of the underlying flow behaviours over the scale array.

Results in the vertical plane revealed the presence of a recirculation zone behind the scale heights along the centerline plane. The reattachment length of the recirculation zone is found to be about 2.6 scale heights. The wall normal streamwise velocity profiles revealed that the midline and centerline regions exhibit a similar flow behaviour. Upward shifted wall normal profiles associated with the flow recirculation region were found to converge back to the Blasius solution at lower wall normal distances in the midline plane. The wall normal streamwise velocity profiles in the overlapping region showed a large downward shift compared to the Blasius solution. This behaviour was much different than that which was observed along the scale centerline revealing the variations in the streamwise velocity in the spanwise direction. Trends in the momentum thickness suggest that both the centerline and overlapping region result in a lower momentum deficit compared to that over the flat plate. Additionally, a lower shape factor is maintained along the overlapping region highlighting the smaller velocity deficit that is experienced in this region.

The spanwise dependence of the streamwise velocity manifests itself as streamwise velocity streaks across the scale array. Low-velocity regions align with the scale centerline while high-velocity regions align with the overlapping region. The amplitude of the streamwise velocity variation is found to exhibit an asymptotic behaviour close to the surface above which it quickly dissipates. The streamwise velocity variation is also

found to increase in the downstream direction suggesting the streamwise velocity streaks continue to grow in the streamwise direction.

The spanwise variation in the streamwise velocity results in the formation of wall normal vorticity streaks which appear between the centerline and overlapping regions. These vorticity streaks highlight the rotation of fluid from the centerline region towards the overlapping region. The close relation between the vorticity and the streamwise velocity streaks suggests that they are linked to a similar generation mechanism. The vorticity streaks are found to become weaker in the wall normal direction, while the vorticity streaks highlight little streamwise development.

While the overlapping region yields a greater streamwise velocity than the centerline region, it is also found to carry an alternating spanwise velocity component. The spanwise velocity variations are found to be linked to the streamwise position of the overlapping scales and becomes smaller with increasing distance from the surface. The flow pattern in opposite overlapping regions is found to be mirrored due to the opposite facing scale heights on either side of the scale centerline. While the flow is predominantly in the streamwise direction, the spanwise variations are found to dissipate quicker in the wall normal direction with no asymptotic behaviour suggested close to the surface. These spanwise oscillations are suggested to play a unique role in drag reduction over these fish scale arrays.

Finally, exploratory experiments were conducted investigating the impact of the free-stream flow conditions on the observed flow behaviours. Measurements were conducted 2 mm from the wall at multiple free-stream conditions. The results revealed the streamwise velocity streaks follow the trends in the free-stream velocity, whereas the spanwise velocity fluctuations remain the same percentage of the free-stream velocity at all flow conditions.

4.3 Chapter 3

In chapter 3, a numerical approach was used to study the impact of scale geometry. Three different scale shapes, circular, flat back and diamond were considered. ANSYS Fluent

was used with a laminar flow model to simulate the steady state flow behaviour over these scale arrays. The model was validated using the experimental data from Chapter 2, the theoretical laminar boundary layer (Blasius solution), and results from previous studies.

Simulations were conducted for the three scale geometries using the experimental velocity profile 5 cm upstream of the scale array as the inlet velocity profile. The results in the recirculation region revealed that the diamond scale array contained the smallest reattachment length. The spanwise width of the recirculation zone was also found to be smaller for the diamond scale shape compared to both the circular and flat back scales. The wall normal streamwise velocity profiles in the scale centerline revealed that the diamond scale resulted in a larger upward shift in the velocity profiles compared to the Blasius solution. These upward shifted velocity profiles were sustained up to a greater height in the boundary layer whereas the circular and flat back profiles were found to converge at smaller wall normal distances. In the overlapping region the opposite is found where the flat back scale shape contains the smallest downward shift from the Blasius profile. These differences in the spanwise direction would become streamwise velocity streaks above the scale array.

While all geometries resulted in the formation of streamwise velocity streaks, the diamond scale array produced a greater velocity variation compared to the circular and flat back geometries. Similarly, the wall normal vorticity streaks which are associated with the streamwise velocity variations showed the greatest vorticity magnitude in the diamond scale array. The peak vorticity also appears closer to the scale centerline suggesting the straight edges of the diamond scale contribute to modifying the vorticity magnitude over the scale arrays. All geometries result in a weakening of the induced flow behaviour in the wall normal direction while similar trends between geometries are maintained. This suggests that the wall normal extent of the observed flow behaviours is greater for the diamond geometry as it has more amplified flow behaviours.

The spanwise velocity fluctuations observed in all scale geometries were found to have similar magnitudes. The dependence of this flow behaviour on the overlapping scale

heights led to a phase shift for different scale shapes. The phase shift did not have any influence on the observed flow behaviour. Further investigation into the spanwise velocity above peak scale heights revealed an elongated spanwise velocity region along the edge of the diamond scale. Also, a second region of spanwise velocity below the peak scale heights in the diamond array was found to be linked to flow from the adjacent scale rows. The elongated spanwise velocity region in the diamond scale array was found to influence the reattachment length and spanwise width of the recirculation zone.

When the inlet flow conditions were varied, the streamwise velocity variations close to the surface were found to decrease with a decrease in the free-stream velocity. The smaller streamwise velocity variations were a result of the slower moving fluid generating a smaller velocity gradient in the near wall region. Meanwhile, the spanwise velocity variations in the overlapping region were found to exhibit a similar non-dimensional magnitude for all flow conditions, as a result of the dependency on the overlapping features in this region.

Investigation of the skin friction coefficient in the centerline and overlapping regions revealed a lower overall skin friction along the centerline contributes to a friction drag reduction in all scale geometries. The diamond scale array is found to have a greater friction drag reduction compared to the circular and flat back geometries as a result of the larger variations in the streamwise velocity and higher wall normal deviation of the wall normal streamwise velocity profiles along the scale centerline. The friction drag reduction of the diamond scale array remained almost constant for varying flow conditions highlighting the unique ability for this geometry to outperform the circular and flat back arrays across flow conditions.

4.4 Summary

The mechanism driving the variations in the velocities observed over the scale arrays is the local variation in the scale height as a result of the changing scale shape. The changing scale shape in the spanwise direction results in a variation in the local scale height. From the perspective of the fluid the scale topography appears with peaks along the centerline and valleys in the overlapping region. Due to this, the fluid moving along

the surface experiences the greatest resistance to streamwise motion along the scale centerline and takes a path of lower resistance towards the overlapping region. This generates the patterns observed in the wall normal vorticity which show the diversion of the fluid from the centerline of the scale towards the overlapping region.

When considering different scale shapes, the variations in height across the width of the scale also varies. Thus, the larger height variations in the diamond scale array result in greater wall normal vorticity and more fluid being pushed towards the overlapping region. The same is true for the flat back scale which results in less height variation compared to the circular scale and contains a smaller wall normal vorticity magnitude. This resistance to streamwise motion results in the diversion of fluid towards the overlapping region, but also influences the wall normal streamwise velocity profiles generating streamwise velocity streaks.

The largest surface variations are found along the scale centerline which lead to a flow recirculation zone. Flow recirculation is observed in the region directly behind the scale height in the centerline region and causes an upward shift in the wall normal streamwise velocity profile compared to the Blasius solution. These upward shifted profiles contribute to a lower wall shear stress and decreased skin friction drag. In addition to the direct influence the flow recirculation has on the wall shear stress, the rolling vortex also enables the higher velocity fluid layer above the scale height to interact with a moving fluid boundary as opposed to a stationary surface boundary. This is likely to reduce the surface drag as the shear stress associated with the rolling friction is smaller than what it would be under traditional sliding friction conditions.

After reattachment, the velocity profiles begin to recover, and the flow accelerates over the length of the scale. In general, the velocity along the scale centerline is found to be moving slower compared to the overlapping region. Given the overlapping region contains the smallest surface variations, the wall normal streamwise velocity profiles are all shifted downward from the Blasius solution highlighting the higher velocities experienced in this region. The differences in streamwise velocity between the centerline and overlapping regions manifest themselves as streamwise velocity streaks and are

generated as a result of the local variations in the surface height across the width of the scales. The influence of the scale features weakens at greater wall normal distances due to viscous dissipation.

When considering the impact these flow patterns have on the surface drag, it is found that the shifted wall normal streamwise velocity profiles along the scale centerline contribute to a smaller wall shear stress and lower skin friction coefficient. Given that friction drag reduction was observed in all scale geometries, the flow behaviour along the scale centerline is found to be the driving factor leading to drag reduction over the scale array. Between different geometries, the larger surface variations in the diamond scale array result in a greater streamwise velocity variation. The greater streamwise velocity variation is a result of a larger upward shifted wall normal streamwise velocity profile along the scale centerline which leads to a greater reduction in the skin friction. Thus, the variations in scale height across the width of a single scale were found to be a large contributor to not only the strength of the induced streamwise velocity streaks but also the skin friction coefficient and overall surface drag.

While the flow along the scale centerline contributes to the skin friction drag reduction over the surface, another unique flow behaviour is observed in the overlapping region. An alternating spanwise velocity in the overlapping region is found to be related to the scale geometry. As the scale heights converge in the overlapping region, scale heights are found facing opposite spanwise directions. The overlapping nature of the scale features in this region are found to induce the alternating spanwise velocity. When considering the change in scale shape, similar spanwise velocities are found in the overlapping region. However, the scale shape is found to have a large influence on the spanwise velocity below the peak scale height which extends into the centerline region. The spanwise velocity in this region is found to impact the flow recirculation zone generating a 3D rolling vortex which facilitates the movement of fluid towards the scale tip. In the diamond scale array, the presence of a large spanwise velocity component below the scale height results in the elimination of the flow recirculation zone along a portion of the scale centerline region.

While velocity profiles along the scale centerline are found to contribute to the reduction in friction drag, the streamwise velocity streaks and alternating spanwise velocity are hypothesized to contribute to drag reduction through the delay in transition to turbulence. The study of similar flow behaviours in other applications has shown the ability for both the finite amplitude streamwise velocity streaks and the spanwise oscillating flows to suppress turbulence generation mechanisms and delay the transition to turbulence. Thus, not only do fish scale arrays contribute directly to friction drag reduction, but they also produce a stabilizing flow behaviour which contributes to the suppression of flow instabilities which leads to the delay in transition to turbulence.

The trends in the underlying flow behaviours were found to be influenced by the free-stream conditions. Lowering the free-stream velocity resulted in a shorter reattachment length and less variation in the streamwise velocity across the scale array. With a smaller free-stream velocity, the viscous effects dominate over a larger wall normal distance, while the influence of the surface patterns is found to be confined closer to the surface. The streamwise velocity variation becomes smaller at lower free-stream velocities indicating that the behaviour of the velocity streaks and the free-stream conditions are related. Meanwhile, the spanwise velocity fluctuations are found to remain the same percentage of the free-stream velocity highlighting that only the magnitude of the velocity fluctuations is impacted by the changing free-stream velocity. Considering the changes in scale shape, the diamond scale array showed a continued drag reduction at smaller free-stream conditions related to the increased velocity variation and sustained upward shifted streamwise velocity profiles observed over this scale geometry.

Overall, the influence of the scale topography is found to have a profound impact on the near wall velocity field for different scale shapes and different free-stream conditions.

4.5 Novel Contributions

Given the summary of the research provided above, the novel contributions of this work are listed as follows:

- The first detailed experimental characterization of velocities formed over a biomimetic fish scale array.

- Experimental quantification of the reattachment length in the flow recirculation region behind the scale height along the scale centerline.
- Identified the formation mechanisms of the key flow behaviours over biomimetic fish scale arrays.
- Identified how the observed flow behaviours contribute to friction drag reduction through modification of the skin friction coefficient and the role different flow patterns play in delaying the transition to turbulence.
- The first investigation of the flow over biomimetic scale arrays for standardized scale geometries.

Based on the findings from this work, the following section will outline some recommendations for future work.

4.6 Future Recommendations

- Given the experimental results highlight the development of the streamwise velocity streaks in the downstream direction, further investigation into the rate of growth and development length of these streaks in the streamwise direction would help to understand the limitations of the induced flow behaviour.
- A more detailed experimental analysis of how the Reynolds number affects the induced flow behaviour is needed. Identifying the practical limits of the streamwise velocity streaks and the relationship between these streaks and Reynolds number is needed.
- Exploring the transition process over a continuous scale array will highlight the critical streak amplitude required for breakdown to turbulence. While different techniques of generating streamwise velocity streaks were found to have different critical thresholds for breakdown to turbulence, investigation of the critical threshold for fish scale arrays will help inform the limitations of this drag reduction mechanism.
- Experimental quantification of the friction drag over fish scale arrays is required to experimentally verify their potential for drag reduction. Focus on the relation to friction drag is required for comparison to the flat plate alternative. This should be

done for fish scale arrays with overlapping features to understand the full impact of a biomimetic fish scale array.

- While this study focused on understanding the physics of overlapping scale arrays, the literature review identified microfeatures on the scales (Ctenii and Circuli) which have yet to be explored in terms of their impact on the flow over fish scales.
- The second chapter of this thesis focused on the variations in the flow behaviour and performance for different scale geometries and identified a diamond scale shape which outperformed the circular scale from various aspects. Exploring how varying the angle of the diamond scale edges impacts the flow behaviour would be useful in terms of developing an optimized scale array.
- While shape optimization is one aspect that needs further exploration, geometry optimization in terms of the ideal spanwise and streamwise spacing, as well as scale height, is required to further inform the development of optimal scale arrays for improved performance.

Appendix A: Experimental Facilities Development

The original water channel design underwent several iterations and modifications before reaching the final setup used as the experimental facility. Modifications to sample mounting, channel outlet, channel inlet, and flow conditioning all contributed to improving the quality of the channel background flow and flow over the structured sample before conducting experiments. The purpose of this appendix is to describe and document the modifications that were made throughout the experimentation process to achieve the final experimental facility used for testing.

Original Design

The original water channel was designed to use a 2-hp pump to drive flow through test section with dimensions 10 cm wide \times 15 cm tall \times 30 cm long. The design is shown in Figure 89 along with a schematic of the closed-circuit water loop in Figure 90.

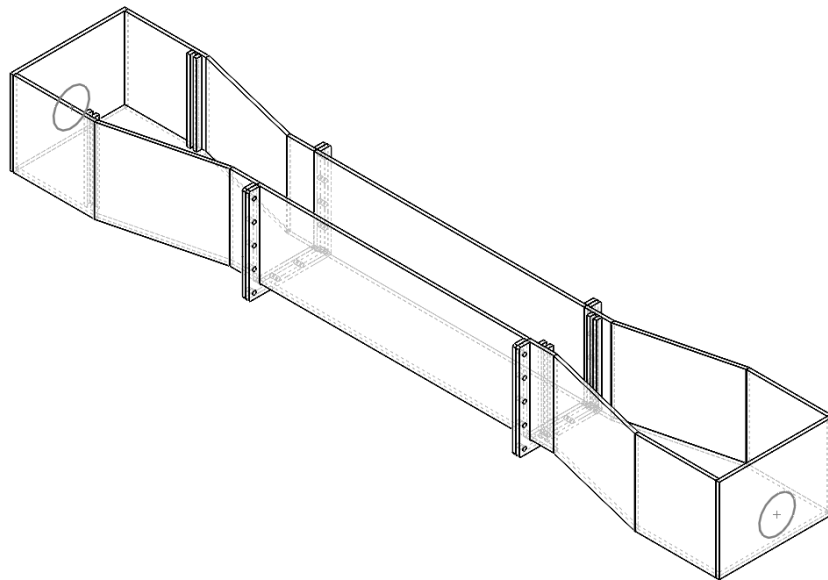


Figure 89: Original water channel CAD model. Inlet on the left, water flowing through the test section and into the outlet section of the right.

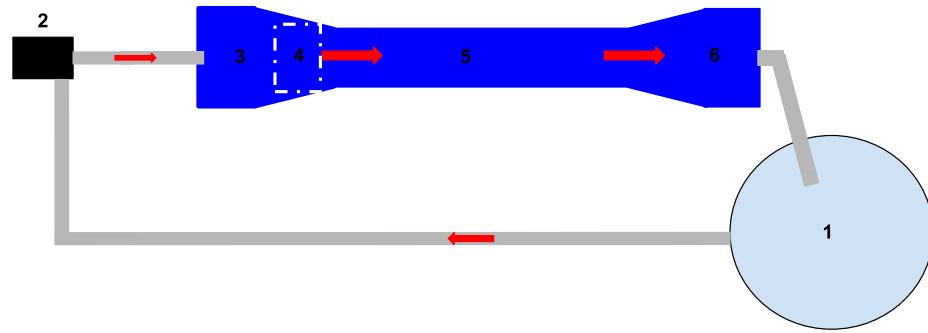


Figure 90: Closed circuit water channel layout. 1) Outlet reservoir; 2) Pump; 3) Inlet and contraction section; 4) Flow Conditioning; 5) Test Section; 6) Outlet and Diffusion Section

The channel consisted of three sections bolted together and sealed with silicone: the inlet (or contraction section), the test section, and the outlet (or diverging section). With a contraction ratio of 2:1, the converging and diverging section made use of a straight wall profiles for ease of manufacture. The design contained a 2-inch horizontal inlet that is connected directly to the 2hp centrifugal pump. The 2-hp pump was selected as it could support flow rates that would lead to velocities up to at least 0.5 m/s within the test section. A pair of slots were located near the inlet to hold a stilling plate⁵ designed to disperse the jet signature from the 2-inch horizontal pipe inlet. The stilling plate contained small holes of 8mm diameter, along with a larger approximately 3-inch blocked area directly in front of the horizontal jet inlet. Figure 91 shows the original stilling plate design.

⁵ A plate designed to act as a flow straightener downstream of a jet inlet.

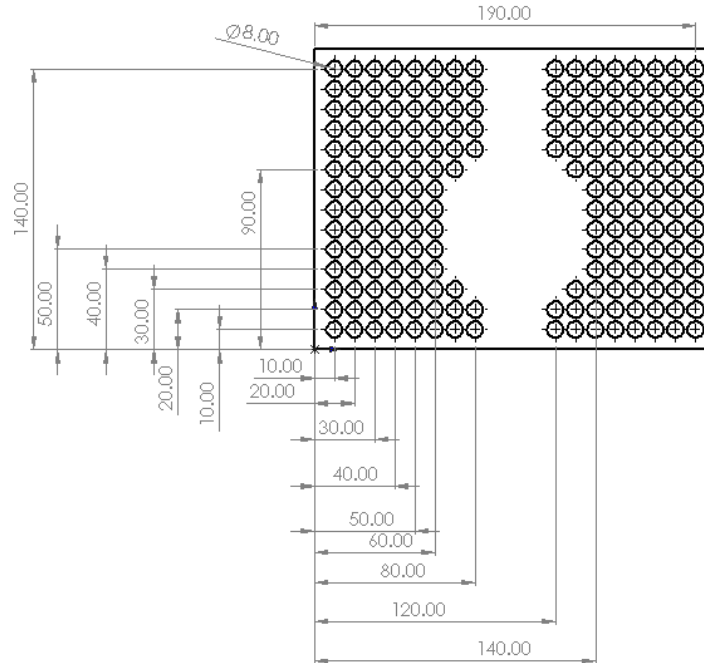


Figure 91: Original stilling plate design. Units are in mm.

The outlet of the water channel consisted of a 2-inch pipe that dumped water into a 45-gallon drum serving as an outlet reservoir. The channel also contained a pair of slots at the end of the test section that were used to hold a weir gate to control the height of the water level. The sample would be mounted to the top of the water channel walls using the mounting apparatus shown in Figure 92.

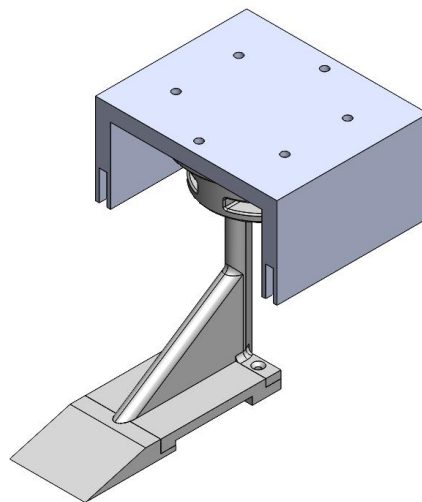


Figure 92: Sample Mounting Apparatus

This mounting apparatus allowed the sample to be suspended in the water channel from above to enable PIV imaging from below. The height of the sample in the channel could be modified by changing the length of the 3D printed mounting arm shown in Figure 92. While these are the key aspects of the original design, several modifications were made to improve the velocity profiles in the test section.

Outlet Modifications

The 2-inch pipe outlet that was included in the original design did not allow for a large enough outflow of water and resulted in the channel overflowing at higher flow rates. To resolve this, the end face of the outlet section was removed so that there was no constraint on the amount of water exiting the channel. See Figure 93 which shows the new outlet.

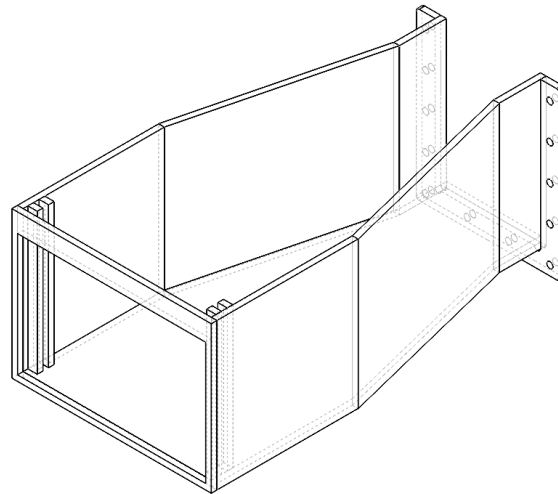


Figure 93: New flume outlet

In addition to removing the end of the outlet section, the pair of slots for the weir gate were moved from near the end of the test section to next to the outlet. The additional sharp contraction that the pair of weir gate slots made near the end of the test section was found to cause inconsistencies in the velocity profiles within the test section. These two modifications were the only modifications that were made to the outlet of the water channel. By opening the end of the outlet section and moving the weir gate slots, the channel flow in the test section became more consistent.

Inlet Modifications

Next, various modifications were made to the inlet section of the water channel to improve the consistency of the velocity profiles in the test section and reduce the amount of background turbulence present in the flow. First, the location of the 2-inch inlet pipe was varied. In the original horizontal inlet configuration with the stilling plate, the velocity profiles in the test section showed remnants of the inlet jet signature. To remove the jet signature a stilling plate with larger center blockage area was manufactured. However, this resulted in a large increase in pressure difference across the plate and decreased flow rate in the channel. As these outcomes were undesirable, a different inlet configuration was tested with a vertical 2-inch inlet from above. An inlet diffuser made of a closed end pipe with a series of holes facing away from the test section ensured sufficient mixing and that no jet signature would be propagated downstream (see Figure 94).



Figure 94: Vertical Inlet Configuration

In the vertical configuration, several different methods of flow conditioning were tested including a 0.5-inch-thick honeycomb core with cell size of 0.125 inches, and various wire mesh sizes from 20 mesh per inch to 120 mesh per inch. Although some combinations of these flow conditioning methods produced a relatively smooth horizontal velocity profile, the turbulent intensity present through the channel was still higher than what was desired. Given that the vertical inlet with diffuser created a large amount of

turbulence and was placed directly in the inlet section, there was no method for this turbulence to decay before the test section. Thus, to reduce the amount of background turbulence in the channel, the location of the inlet was moved to the bottom of the channel and two additional settling tanks were added between the pump and the inlet. This would create a gravity driven flow in the water channel. Figure 95 shows the final inlet configuration that produced the most consistent results.

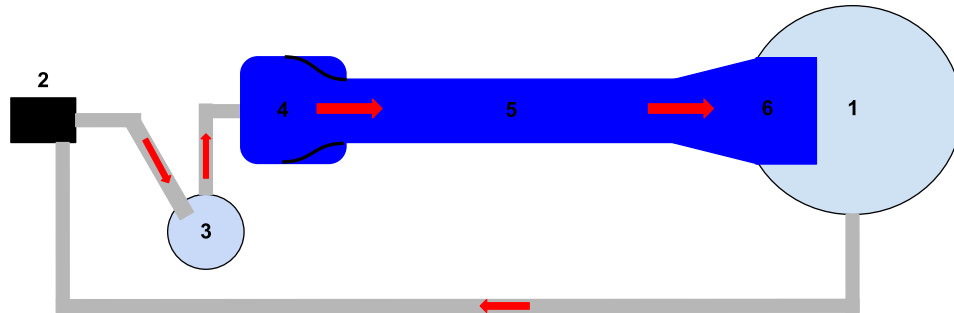


Figure 95: Stages 2, 3, and 4 show the water path through the pump into the inlet settling reservoir before entering the inlet and contraction section from below.

The two settling tanks allowed the turbulence introduced in the pump to decay before entering the test section. Additionally, having the inlet from the bottom of the channel removed the impact having the inlet diffuser in the inlet section itself. Initially, the contraction section of the inlet contained straight walls as is shown in Figure 89. However, it was found that the contraction shape given by a 5th order polynomial (Equation A.1) found in Bell and Mehta (1988) (from Lakshman & Basak, 2018) provided flow uniformity and prevented flow separation reducing the background turbulence in the test section.

$$y(x) = H_{inlet} - (H_{inlet} - H_{outlet}) * \left[6 \left(\frac{x}{L} \right)^5 - 15 \left(\frac{x}{L} \right)^4 + 10 \left(\frac{x}{L} \right)^3 \right] \quad (A.1)$$

Equation A.1 was used to determine the profile for the three-sided contraction section (bottom, left, and right). The H_{inlet} and H_{outlet} were specified based on the symmetry plane located at the center of the channel width and height. The values used for each

contraction profile are shown in Table 18 and Figure 96 shows the CAD model of the 3D printed contraction section that was used.

Table 18: Contraction Section Parameters.

Parameter	Left Profile	Right Profile	Bottom Profile
H_{inlet} (cm)	10.5	10.5	15
H_{outlet} (cm)	5	5	13
Total Length (L) (cm)	15	15	15

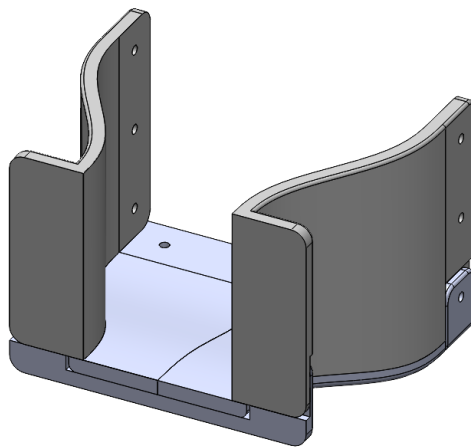


Figure 96: 3D Printed Inlet Contraction Section

As mentioned earlier, various combinations of flow straighteners and wire mesh screens were tested to improve the velocity profile within the test section. A 0.5-inch-thick honeycomb core with 0.125-inch cell size was used as a flow straightener preventing crossflow through the long honeycomb structures. In addition to this, wire mesh screens of varying sizes from 20 mesh per inch to 120 mesh per inch were used to break up turbulent structures before entering the test section. Not all combinations of wire mesh and honeycomb produced optimal results.

Through many iterations, the final inlet configuration minimized turbulence and produced consistent velocity results within the test section consisted of a vertical inlet from below with two settling tank stages and a curved contraction section. Two flow conditioning stages were used. The first contained an 80 mesh per inch and a 20 mesh per

inch wire screen located 12 cm from the entrance of the test section, and the second stage contained a 0.5-inch-thick honeycomb core with 0.125-inch cell size followed by a 20 mesh per inch wire screen located at the entrance to the test section. These screens and flow straighteners helped smooth the flow and remove any small turbulent structures before entering the test section. The final configuration of the inlet as described above can be viewed in Figure 97.



Figure 97: Final inlet configuration with two stages of flow conditioning and curved contraction section.

Sample Mounting Modifications

To suspend the surface inside the test section such that it was free from both sides of the channel and could be imaged from below, a sample fixture was designed to hold the structured surface from above. The surface would be mounted to a 3D printed leading edge and arm assembly. The height of the sample in the channel could be adjusted by modifying the length of the 3D printed arm. A machined backing plate and side supports are mounted in such a way that the entire structure can be attached to the upper edges of the test section. Figure 92 shows the original sample fixture.

Although this design of the sample fixture satisfied the primary needs of freely suspending the structured surface from above, it was not an ideal design. The vibrations from the pump were transferred through the walls of the water channel to the sample fixture and caused small undesirable oscillations of the surface. To decouple the sample fixture from the pump and water channel, a secondary independent support structure was built surrounding the water channel to enable independent mounting of the structured sample in the water channel. This structure proved effective at isolating the structured surface and removing any unwanted vibrations induced through the water channel itself.

In addition to the independent support structure, a machined acrylic leading edge of length 5 cm was originally used as a leading edge. The sharp acrylic leading edge was found to induce flow separation over the leading edge which became a significant issue when imaging in the horizontal plane. The varying nature of the vortices shedding from the leading-edge appeared as a low velocity region in the mean velocity field. Figure 98 shows the low velocity signature in the region behind the sharp leading edge of the plate.

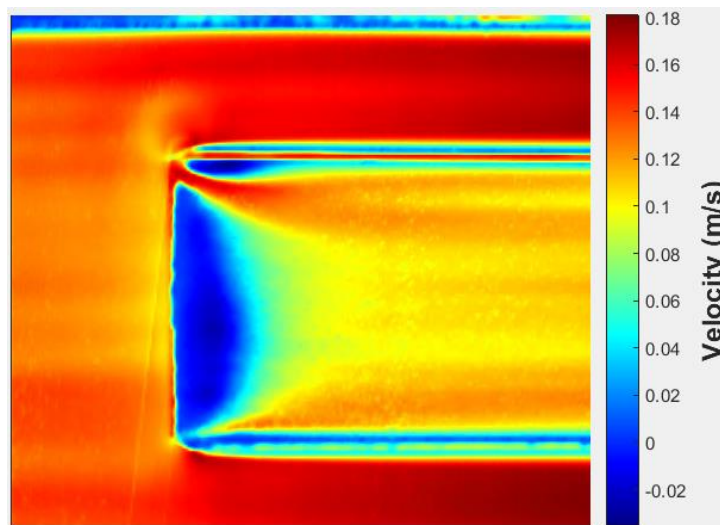


Figure 98: Streamwise velocity colourmap in the horizontal plane 1mm from the surface in the region of the sharp leading edge. Highlights the flow separation happening over the sharp leading edge. Flow is from the left to the right.

Upon further investigation, the issue of leading-edge flow separation is a common problem with boundary layer experiments at or near zero-incidence (Smith et al., 2021;

Fujiwara et al., 2020). A common approach to avoid this leading-edge flow separation is through the use of an asymmetrical or “curved” leading edge which suppresses the flow near the leading edge and prevents flow separation (Fransson, 2004; Hanson et al., 2012; Bhatia et al., 2020). The curved leading edge was made by heating a 1 mm thick piece of clear acrylic and placing it inside a 3D printed mould with a radius of about 36.5 mm. Once cooled, the curved piece of acrylic would be attached to the sample structure assembly using adhesive. Figure 99 shows the curved leading-edge mould and Figure 100 shows the colourmap of the streamwise velocity in the region of the new curved leading edge.

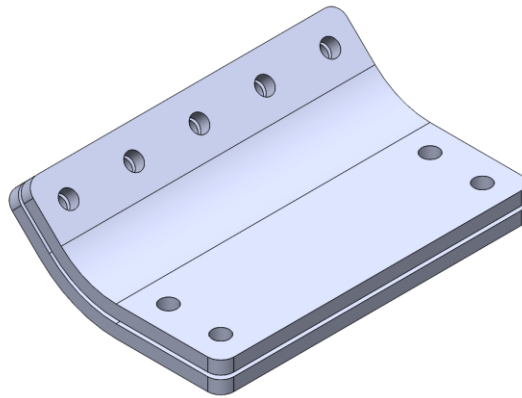


Figure 99: Curved leading-edge mould.

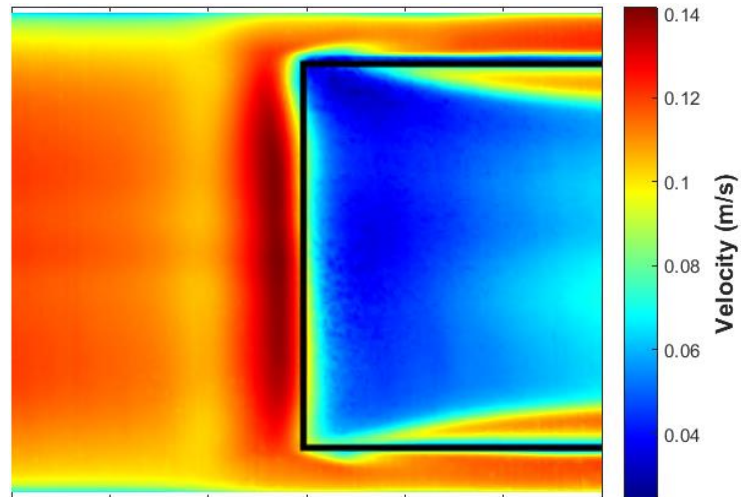


Figure 100: Streamwise velocity colourmap in the horizontal plane 1 mm from the surface in the region of the curved leading edge. Flow is from the left to the right.

Another modification to the sample mounting fixture that was tested was the impact of sidewalls mounted to the sample and leading edge to prevent spanwise fluid motion over the sides of the scale array. This solution proved inferior as the side walls created boundary layers and flow separation that proved to have a greater impact than no sidewalls at all.

Lastly, modifications to the overall sample size were made in an attempt to improve the strength and quality of the velocity results obtained. The overall sample size was increased from 5 cm \times 5 cm to 8 cm \times 16 cm. This was done by applying geometric and dynamic similarity using an eight-times scaling factor. This resulted in a scale height of 0.8 mm, with 4 scales across the sample width and 9 scales along the sample length. In summary, the final sample mounting fixture consisted of an independent wooden structure to support the sample from above the channel. A 3D printed mounting arm extends into the test section, and supports a curved acrylic leading edge, a 10 cm flat plate development length, and an 8 cm \times 16 cm sample area with no sidewalls.

Final Design

As described in each of the previous sections, the final water channel design consisted of a fully open outlet with a weir gate located at the end of the diffusion section. The inlet section consisted of two settling tank stages and inlet mounted from below providing a gravity driven flow through the channel. A curved contraction section was implemented to reduce flow separation and turbulence at the entrance of the test section. Flow conditioning takes place in the contraction section and makes use of one 80 and one 20 mesh per inch wire screens located 12 cm from the test section, along with one 0.5-inch-wide honeycomb core with 0.125-inch cell size followed by a 20 mesh per inch wire screen located at the entrance of the test section. The final setup contained a 0.9 m long test section with the sample structure located 0.55 m downstream from the inlet. The sample structure was mounted to an independent wooden structure and consisted of a 3D printed mounting arm, a curved leading edge, a 10 cm flat plate mounted in front of the scale array, and an 8 cm \times 16cm structured surface (scale array). Figure 101 shows a schematic of the final channel configuration including the inlet and outlet modifications, and the location of the sample in the test section. Figure 102 shows the final

configuration of the sample mounting structure including the flat plate, leading edge, and mounting arm.

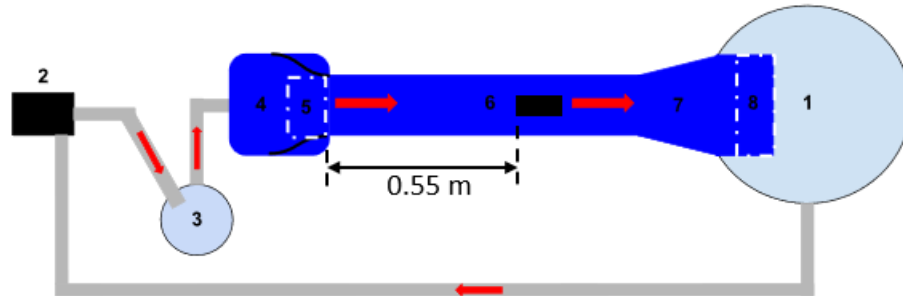


Figure 101: Schematic of Experimental Facility. 1) Outlet Reservoir 2) 2-hp Centrifugal Pump 3) Inlet Settling Reservoir 4) Inlet Contraction Section 5) Flow Conditioning 6) Test Section 7) Outlet Diffuser Section 8) Weir Gate

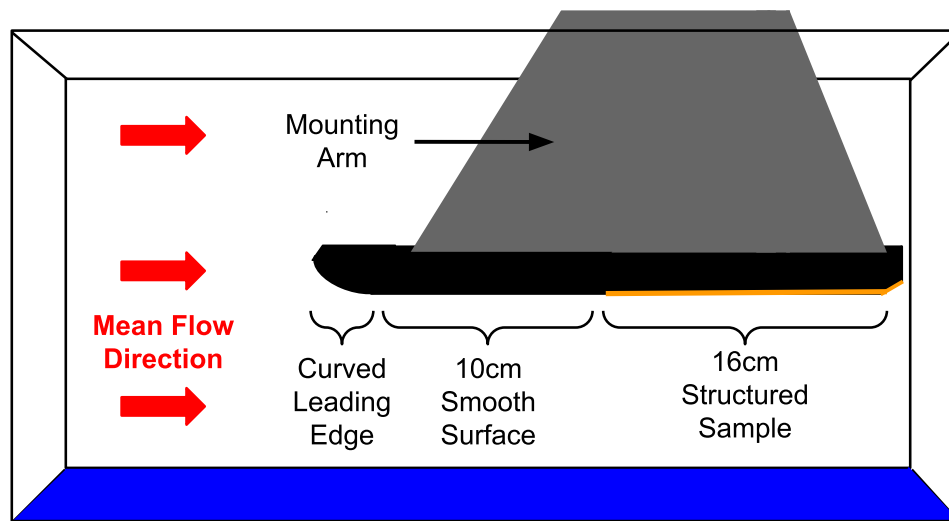


Figure 102: Schematic of the sample mounting structure including the curved leading edge, 10 cm flat plate, 16 cm structured sample, and 3D printed mounting arm.

Bibliography

- Bell, J. H., & Mehta, R. D. (1988). (tech.). *Contraction Design for Small Low-Speed Wind Tunnels*. National Aeronautics and Space Administration.
- Bhatia, D. D., Yang, G., Li, G., & Wang, J. (2020). Selection and impact of leading edge on boundary layer transition. <https://doi.org/10.21203/rs.3.rs-29913/v1>
- Hanson, R. E., Buckley, H. P., & Lavoie, P. (2012). Aerodynamic optimization of the flat-plate leading edge for experimental studies of Laminar and transitional boundary layers. *Experiments in Fluids*, 53(4), 863–871. <https://doi.org/10.1007/s00348-012-1324-2>
- Fransson, J. H. (2004). Leading edge design process using a commercial flow solver. *Experiments in Fluids*, 37(6), 929–932. <https://doi.org/10.1007/s00348-004-0858-3>
- Fujiwara, K., Sriram, R., & Kontis, K. (2020). Experimental investigations on the sharp leading-edge separation over a flat plate at zero incidence using particle image velocimetry. *Experiments in Fluids*, 61(9). <https://doi.org/10.1007/s00348-020-03039-w>
- Lakshman, R., & Basak, R. (2018). Analysis of transformed fifth order polynomial curve for the contraction of wind tunnel by using OpenFoam. *IOP Conference Series: Materials Science and Engineering*, 377, 012048. <https://doi.org/10.1088/1757-899x/377/1/012048>
- Smith, J. A., Pisetta, G., & Viola, I. M. (2021). The scales of the leading-edge separation bubble. *Physics of Fluids*, 33(4), 045101. <https://doi.org/10.1063/5.0045204>

Appendix B: PIV Uncertainties

The uncertainty associated with the PIV velocity computation was estimated based on the errors associated with particle size, AGW interpolation, image dynamic range, and out-of-plane motion (Cowen & Monismith, 1997).

1. The average seed particle diameter is 13 μm , and the minimum and maximum spatial resolution achieved were $527 \frac{\text{pixels}}{\text{cm}}$ and $2064 \frac{\text{pixels}}{\text{cm}}$, respectively. As such, the diameter of seed particles varies between 0.7 pixels and 2.7 pixels in all experiments. Using figure 5a from Cowen and Monismith (1997), it can be found that there is only a small variation in the rms error between a particle seed diameter of 0.7 pixels and 2.7 pixels, thus the average seed diameter size of 1.7 pixels was used to calculate the error. Taking the sum of the mean and rms errors for a seed particle diameter of 1.7 pixels the total error is found below.

$$\epsilon_{SP} = 0.05 \text{ pixels}$$

2. The dynamic range of the images captured from the Flare 48 mega-pixel camera was 255. Using figure 5b from Cowen and Monismith (1997), the total error is the sum of the mean and rms errors and is found below.

$$\epsilon_{DR} = 0.05 \text{ pixels}$$

3. The error associated with the out-of-plane motion was calculated based on the velocity in the spanwise and wall-normal directions for the vertical and horizontal planes, respectively. The out-of-plane velocity was found to be greatest in the horizontal plane measurements at 1.3 mm from the surface. The average spanwise velocity was found to be 0.0024 m/s in the overlapping region. Given the 1 milli-second time delay used in the horizontal plane measurements, the total spanwise displacement of particles in the overlapping region is 2.4 μm . While there is an out-of-plane motion for the horizontal planes as well, the average wall normal velocity in the vertical plane was found to be 0.000187 m/s and corresponds to a wall normal displacement of 0.0374 μm . Given the out-of-plane displacement in

both the horizontal and vertical planes is far less than 1 mm (or the thickness of the laser sheet) the error associated with the out-of-plane motion can be neglected.

4. The adaptive Gaussian window interpolation scheme utilized in this study has a known error found in Figure 5f of Cowen and Monismith (1997):

$$\epsilon_{AGW} = 0.08 \text{ pixels}$$

The total maximum error in the streamwise velocity for both the horizontal and vertical plane measurements is therefore:

$$\epsilon_{SP} + \epsilon_{DR} + \epsilon_{AGW} = 0.18 \text{ pixels}$$

When considering the vertical plane, converting this error to a velocity results in ≈ 0.436 cm/s. If the wall normal error is taken to be equal to the streamwise error, then the total maximum resultant error in the vertical plane measurements is ≈ 0.617 cm/s. Repeating the same calculations but using the spatial resolution and time delay for the horizontal plane results in a streamwise velocity error of ≈ 0.342 cm/s and a total maximum resultant velocity error of ≈ 0.483 cm/s. Given that the resultant error in the vertical plane is greatest, the error in all velocity measurements will be taken as ± 0.617 cm/s.

Two types of error not considered in this analysis are the seeding density and the velocity gradients. Seeding density is important because too little seed in the field will result in weak correlations peaks and a poor estimation of displacement. On the other hand, too much seeding can result in a greater signal to noise ratio. Therefore, a balance is required to obtain the optimal seed density to ensure strong displacement correlation peaks while not increasing the signal to noise ratio. The error associated with the velocity gradients arises due to the fact that some particles may not be found within the PIV interrogation window. This in-plane loss of correlation results in a bias towards slower moving particles as they are more likely to remain inside the interrogation window (Cowen & Monismith, 1997). The errors associated with both the seeding density and the velocity gradients were not quantified for this analysis but should be considered qualitatively for their influence on the overall velocity estimation.

Bibliography

- Cowen, E. A., Monismith, S. G., Cowen, E. A., & Monismith, S. G. (1997). A hybrid digital particle tracking velocimetry technique. *Experiments in Fluids*, 22(3), 199–211. <https://doi.org/10.1007/s003480050038>

Curriculum Vitae

Name: Isaac Clapp

Post-secondary Education and Degrees: The University of Western Ontario
London, Ontario, Canada
2016-2021 B.E.Sc. Mechanical Engineering

The University of Western Ontario
London, Ontario, Canada
2016-2021 B.A. Honors in Business

Honours and Awards: Natural Sciences and Engineering Research Council (NSERC)
Undergraduate Student Research Award
2020

Natural Sciences and Engineering Research Council (NSERC)
Master's Award
2021-2022

Ontario Graduate Scholarship
2022-2023

Related Work Experience Teaching Assistant
The University of Western Ontario
2021-2023

Research Assistant
The University of Western Ontario
2020

Publications:
Clapp, I., and Siddiqui, K., “Experimental investigation of the flow over biomimetic fish scale arrays”, ASME Fluids Engineering Conference, August 3-5, 2022, Toronto, Ontario

Clapp, I., and Siddiqui, K., “Numerical Investigation into the Influence of Scale Shape on the Hydrodynamics of Fish Scale Arrays”, CSME Computational Fluid Dynamics Summer Conference, May 28-31, 2023, Sherbrooke, Quebec (to appear)

Clapp, I., and Siddiqui, K., “Experimental Investigation of the Flow over a Biomimetic Fish Scale Array”, ASME-JSME-KSME Joint Fluids Engineering Conference, July 9-13, 2023, Osaka, Japan (to appear)